Threshold effect of local pulsed laser irradiation on the surface state of oxide layers deposited on real germanium surfaces

S. V. Vintsents and S. G. Dmitriev

Institute of Electrical Engineering and Electronics, Russian Academy of Sciences, 141120 Fryazino, Moscow Region, Russia

R. A. Zakharov, and G. S. Plotnikov

Physics Faculty, M. V. Lomonosov Moscow State University, 119899 Moscow, Russia
(Submitted June 10, 1996; accepted for publication July 1, 1996)
Fiz. Tekh. Poluprovodn. **31**, 513–514 (May 1997)

Data are presented from a study of changes in the spectra of surface states on real (with a thin oxide layer) germanium surfaces irradiated by localized (10–100 μm), pulsed (0.1–1 μs) laser light which heats the surface by an estimated ~20–40 K. It is shown that the thresholds for plastic deformation in the surface region of the semiconductor (due to the resulting local thermal stresses) correspond to threshold changes in the optical charging spectra of slow surface states of the insulator, while no threshold changes are observed for the fast states. The nature of this effect is discussed. © *1997 American Institute of Physics.* [S1063-7826(97)00505-X]

Damage is observed during repeated ($N \geqslant 10^3-10^5$) pulsed ($\tau = 0.1-1$ μs or less) laser irradiation of semiconductor (and metal) surfaces at extremely low absorbed irradiances $W_a < 0.1$ J/cm^2 (Refs. 1–3) and for spot diameters $a \approx 10-100$ μm it is characterized by the so-called size effect:[1,4] $W_a \propto a$. Models of deformation damage of the surface (based on a one-dimensional theoretical analysis) have been proposed to explain this phenomenon.[5,6] It has been shown[4] that the damage associated with dimensional effects must occur under the surface of a sample in the early stages of irradiation (with a small number of pulses).

In order to analyze this proposition, studies have been made of the instantaneous thermal deformation and displacement profiles of the surfaces of semiconductors (and metals) near (and below) the damage thresholds.[7,8] It has been shown that this damage involves the attainment of a plasticity threshold (due to shear stresses produced by local heating), while the surface heating is extremely low ($\Delta T \approx 20-40$ K).[7]

In this paper we study changes in the optical charging spectra of the slow states of the insulator and changes in the fast states, in Ge–GeO_2 structures when this threshold W_a is crossed within a fairly small number of pulses ($N \leqslant 10^3$), while there is still no visible (under an optical microscope) surface damage of the sample. In fact, sufficiently thin ($d \sim 30$ Å)[9] insulating films on real semiconductor surfaces, while having little effect on deformation and stress within the semiconductor,[10] can be sensitive to plastic (and elastic) photodeformation within it and can thereby serve as an effective sensor of small plastic deformations.

We have studied the (111) surfaces of high-ohmic single crystals of *n*-type germanium ($\rho = 25-30$ $\Omega \cdot$cm) etched in H_2O_2.[9,11] The surface potential Y, surface recombination rate S, and density N_{FS} of fast states were determined by the quasiequilibrium field method combined with the steady-state photoconductivity at a temperature of ~300 K.[11] The change in the surface charge on the slow states ΔQ_{SS} when the semiconductor was irradiated with photons having energies of $1.8 \leqslant h\nu \leqslant 4.0$ eV were detected by the field effect (the method for studying the optical charging spectra of the slow dielectric states described by Kashkarov *et al.*[12]).

The germanium surface (15×5 mm^2) was irradiated by the focussed ($2a \approx 70$ mm) beam of second harmonic ($\lambda = 0.53$ nm) emission from a pulsed[4] (rise time $\tau_c \sim 350$ ns and total duration ~1 μs) yttrium aluminum garnet laser with a pulse repetition rate of 10 kHz while scanning the beam over the surface with a step size of ~10 μm. Photothermal surface deformation[3] was used to determine the threshold irradiance $W_0 \approx 70$ mJ/cm^2 and the magnitude of the maximal elastic (fully reversible) shear deformations of the surface,[3,4] $\varphi = \partial u_z / \partial r \approx 4.7 \times 10^{-5}$, where u_z are the normal displacements of the surface, and r is the radial distance from the center of the laser beam.

The main changes in the system of surface states were observed in the insulating film. Figure 1 shows slow dielectric state optical charging spectra for an unirradiated surface (curve *1*), as well as on passing through W_0 (curves *2–4*). Both the overall growth in $\Delta Q_{SS}(h\nu)$ and the shifts in the optical charging thresholds toward lower photon energies due to additional threshold damage of GeO_2 are noteworthy.

During thermoelastic irradiation ($W < W_0$),[3,4] no qualitative changes took place in the optical charging spectra. There was only an increase in the number of slow states undergoing charge transfer, which indicates that the thresholds for the appearance of these states lie below W_0; i.e., the stresses which develop during local irradiation are mainly determined by the ''bulk'' germanium, while the deformations and displacements induced by these stresses in the film lead to lower-threshold changes in the GeO_2 due to the difference in the thermoelastic characteristics of the semiconductor and insulating film.

The shifts in the thresholds for slow insulating state optical charging occur on going to irradiances $W > W_0$ and are evidence of additional damage to the GeO_2 film. Here no noticeable threshold increase in the density of fast states

 1063-7826/97/050433-02$10.00

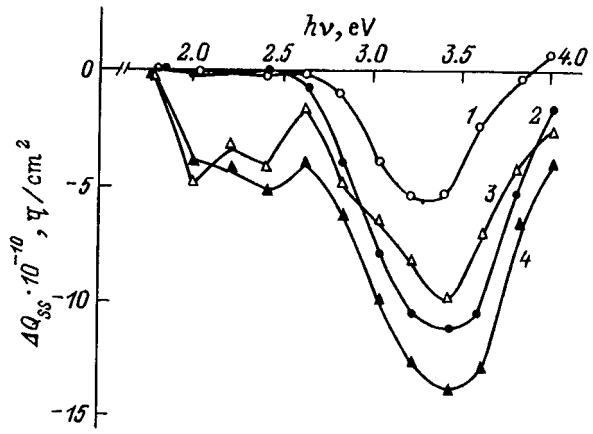

FIG. 1. Optical charging spectra of the slow states of the insulator on a real germanium surface prior to local pulsed irradiation (*1*) and after irradiation (*2–4*) at various irradiances W (in units of W_0, where $W_0=70$ mJ/cm^2 is the irradiance at the center of the laser spot at the threshold for plastic deformations): (*2*) 0.85, (*3*) 1.15, (*4*) 1.6.

($N_{FS}\approx 1\times 10^{11}$ electrons/eV·cm) localized in the Ge near the dielectric-semiconductor interface[11] (or increase in the surface recombination rate $S\approx 5\times 10^2$ cm/s) was observed. It is interesting to note that under other conditions (nonlocal irradiation by one or a few nanosecond pulses), there have been no significant changes in the slow dielectric states on real germanium surfaces.[13]

We believe that the observed threshold character of the change in the spectra of the slow states (in the oxide layer) and the absence of noticeable changes in the fast states confirm that the plastic deformations induced by thermal stresses (which develop[3,4] in germanium at shear stresses of several MN/m^3) take place in the volume of the semiconductor, rather than on its surface. These (plastic) deformations and the stress relaxation associated with them change the deformation on the Ge surface, which leads to additional damage of the insulating film, which is more sensitive to the residual deformations (and displacements).

In summary, we have measured the changes in the spectra of surface states when a germanium surface is locally irradiated by a pulsed laser with a threshold deformation amplitude of $\varphi\approx 4-5\times 10^{-5}$. It has been shown that the slow electronic states on a real semiconductor surface can serve as a sensitive probe of the resulting plastic deformations.

[1] C. S. Lee, N. Koumvakalis, and M. Bass, Appl. Phys. Lett. **47**, 625 (1982); Opt. Eng. **22**, 419 (1983).
[2] P. M. Fauchet, Phys. Lett. **93A**, 155 (1983).
[3] A. G. Barskov and S. V. Vintsents, Fiz. Tverd. Tela **36**, 2590 (1994) [Phys. Solid State **36**, 1411 (1994)].
[4] S. V. Vintsents and S. G. Dmitriev, Pis'ma Zh. Tekh. Fiz. **21** (19), 1 (1995) [Tech. Phys. Lett. **21**, 767 (1995)].
[5] C. S. Lee, N. Koumvakalis, and M. Bass, J. Appl. Phys. **54**, 5727 (1983).
[6] S. S. Cohen, J. B. Bernstein, and P. W. Wyatt, J. Appl. Phys. **71**, 630 (1992).
[7] S. V. Vintsents, S. G. Dmitriev, and O. G. Shagimuratov, Pis'ma Zh. Tekh. Fiz. **22** (8), 8 (1996) [Tech. Phys. Lett. **22**, 307 (1996)].
[8] S. V. Vintsents, S. G. Dmitriev, and O. G. Shagimuratov, Fiz. Tverd. Tela **38**, 993 (1996) [Phys. Solid State **38**, 552 (1996)].
[9] Yu. F. Novototskiĭ-Vlasov, Tr. FIAN SSSR **48** (1969).
[10] N. V. Karlov, N. A. Kirichenko, and B. S. Luk'yanchuk, in *Laser Thermochemistry* [in Russian], Nauka, Moscow (1971), Ch. 15, p. 269.
[11] A. V. Rzhanov, in *Electronic Processes on Semiconductor Surfaces* [in Russian], Nauka, Moscow (1971), p. 480.
[12] P. K. Kashkarov, V. F. Kiselev, and S. N. Kozlov, Surf. Sci. **75**, 251 (1978).
[13] P. K. Kashkarov and V. F. Kiselev, Izv. Akad. Nauk SSSR. Ser. Fiz. **50**, 435 (1986).

Translated by D. H. McNeill

Effect of manganese on radiation degradation of the electric and recombination parameters of a silicon single crystal

F. M. Talipov

Tashkent State University, 700095 Tashkent, Uzbekistan
(Submitted May 12, 1996; accepted for publication June 7, 1996)
Fiz. Tekh. Poluprovodn. **31**, 515–516 (May 1997)

The effect of manganese doping during the growth process on the γ-irradiation-induced degradation of the electric and recombination parameters of a silicon single crystal has been studied. It is shown that the rate of accumulation of radiation defects is lower in the presence of manganese, irrespective of the doping method. This is explained by the formation of manganese complexes which play the role of centers of indirect annihilation of radiation defects.
 [S1063-7826(97)00105-1]

One way to influence the radiation degradation of the electric and recombination parameters of a silicon single crystal is to dope the crystal with some impurities, specifically, manganese, by high-temperature diffusion.[1,2] However, doping with manganese can also be done as the silicon single crystal is being grown.

Our objective in this work was to study the effect of doping with manganese during the growth process on the degradation of the electric and recombination parameters of γ-irradiated silicon single crystals.

Silicon single crystals doped with high-quality manganese were used for the investigations. The crystals were grown by Czochralski's method in a Redmet-type apparatus in the flow of an inert gas. Quartz, 65 mm in diameter, crucibles with an initial charge consisting of 200 g of the initial silicon raw material were used. The total manganese concentration, determined by neutron-activation analysis, was equal to $10^{15}-10^{16}$ cm^{-3}. The manganese-doped silicon obtained was of *n* type with resistivity $\rho=15-20\ \Omega\cdot$cm and minority charge-carrier lifetime $\tau=9-15\ \mu$s. The change in the electric parameters was monitored by means of Hall effect measurements. The lifetime of the minority charge carriers was determined from investigations of the transient processes accompanying the passage of a large-amplitude sinusoidal signal through semiconductor structures.[3] Before each measurement, the samples were etched in SR-4 etchant. The samples were irradiated in the Issledovatel' apparatus with a dose rate of 2×10^6 R$\times$h^{-1} from a ^{60}Co source.

The experimental results on the effect of irradiating silicon single crystals, both doped with manganese and undoped, with γ rays with a dose of 2×10^9 R are presented in Table I. Comparing the experimental data presented in the table shows that the presence of manganese greatly decreases the degradation of the electric and recombination parameters of silicon, i.e., it decreases the rate of accumulation of radiation defects produced by irradiation with γ rays.

The data obtained therefore confirm the results of Ref. 2, where it was shown that the presence of manganese in diffusion-doped Si⟨Mn⟩ samples decreases the rate of accumulation of radiation defects. It can therefore be stated that, irrespective of the doping method (by diffusion or during the growth process), the presence of manganese in silicon substantially decreases the degradation of the electric and recombination parameters of the silicon. This affects, in particular, the charge-carrier lifetime. The results obtained are explained by the formation of manganese-atom complexes, which apparently play the role of effective centers of indirect annihilation of radiation defects.

TABLE I. Sample parameters.

Samples	ρ, $\Omega\cdot$cm	n, 10^{14} cm^{-3}	μ, cm^2/(V·s)	τ, μ
		Before irradiation		
Initial	18.8	2.8	1180	10−7
Si⟨Mn⟩-1	18.2	2.5	1367	
Si⟨Mn⟩-2	18.7	2.5	1338	9−15
Si⟨Mn⟩-3	18.6	2.4	1394	
		After irradiation with a dose of 2×10^9 R		
Initial	30.7	1.3	1527	0.3−0.7
Si⟨Mn⟩-1	19.1	2.3	1398	
Si⟨Mn⟩-2	20.5	2.3	1325	7−12
Si⟨Mn⟩-3	19.4	2.2	1337	

Note: n — carrier density, μ — mobility.

I wish to thank Yu. A. Karpov for assisting in the preparation of the samples and M. K. Bakhadyrkhanov for helpful discussions.

[1] M. K. Bakhadyrkhanov, S. Zaĭnabidinov, and A. T. Teshabaev, Fiz. Tekh. Poluprovodn. **11**, 285 (1977) [Sov. Phys. Semicond. **11**, 165 (1977)].
[2] F. M. Talipov, Fiz. Tekh. Poluprovodn. **24**, 1472 (1990) [Sov. Phys. Semicond. **24**, 921 (1990)].
[3] S. M. Gorodetskiĭ and M. A. Litovskiĭ, Fiz. Tekh. Poluprovodn. **23**, 580 (1989) [Sov. Phys. Semicond. **23**, 364 (1989)].

Translated by M. E. Alferieff

Faraday rotation angle anisotropy in a Fe-based diluted magnetic semiconductor

S. V. Mel'nichuk, O. S. Mel'nichuk, A. I. Savchuk, and D. N. Trifonenko

Yu. Fed'kovich Chernovtsy State University, 274012 Chernovtsy, Ukraine
(Submitted March 22, 1996; accepted for publication June 13, 1996)
Fiz. Tekh. Poluprovodn. **31**, 517–519 (May 1997)

The magnetic-field and temperature dependences of the Faraday rotation angle in the cubic crystal $Cd_{1-x}Fe_xTe$ has been investigated theoretically and experimentally. It is shown that by simultaneously taking into account the spin orbit and Zeeman interactions without use of perturbation theory the anisotropic nature of these dependences in strong magnetic fields can be explained in a unified approach. © *1997 American Institute of Physics.*
[S1063-7826(97)00205-6]

Semimagnetic semiconductors (SMSCs) containing iron, a magnetic component, are characterized by a number of distinguishing features. One is the manifestation of an anisotropic character of the magnetization, the anisotropy becoming especially large in strong magnetic fields at liquid-helium temperature. As shown in Ref. 1, this in turn results in an anisotropy of the Faraday effect in the cubic crystal $Cd_{1-x}Fe_xTe$. There exist different approaches for explaining the magnetization anisotropy in this material in strong magnetic fields.[2,3]

In the paper we report the results of an experimental and theoretical study of the Faraday effect in $Cd_{1-x}Fe_xTe$. Measurements of the Faraday rotation angle were performed on samples with Fe concentration $x=0.03$, which were preoriented along the [100] and [111] crystallographic axes, at temperatures in the range 4.2–100 K. A ~20% anisotropy of the temperature dependence of the Verdet constant was observed in strong magnetic fields up to 200 kG.

$Cd_{1-x}Fe_xTe$ ($x\leqslant 0.05$) single crystals were grown by a modified Bridgman method and the method of horizontally directed crystallization. The composition of the solid solutions was fixed by the charge of the initial components and checked by atomic-absorption and microprobe analysis. The composition of the samples employed was additionally checked by observing excitonic structure in the reflection spectra of the crystals at 4.2 K. Samples employed in the magneto-optic investigations consisted of (100) and (111) wafers with thickness $d=0.2-3.0$ mm.

The Faraday rotation angle (θ_F) measurements were performed in strong magnetic fields with maximum intensity up to 200 kOe, produced by a pulsed magnet consisting of a copper solenoid with an inside diameter of 6 mm and a capacitor bank with total capacitance $C=2400$ μF and working voltage up to 5 kV. The experimental sample was mounted at the center of the solenoid together with a magnetic test coil and a Ge sensor for monitoring the field intensity H and the temperature, respectively. A helium optical cryostat and a UTREKS temperature regulation system were used to conduct measurements in the temperature range 5–295 K.

The results of the measurements of the magnetic-field dependence of the Faraday rotation angle for different directions of the magnetic field are presented in Fig. 1. The temperature dependence of the Verdet constant is shown in Fig. 2. It was determined that the anisotropy of the angle θ_F and the Verdet constant V at low temperatures and in fields ~200 kG is approximately 20%.

To investigate this problem theoretically, we proceed from the fact that the ground state of an isolated Fe^{2+} ion, which possesses a $3d^6$ configuration, is the term ^5D. In a crystal field with T_d symmetry the term splits into a ^5E orbital doublet and a $^5T_2$ orbital triplet. The Hamiltonian of the Fe^{2+} ion in an external magnetic field, taking into account the spin-orbit interaction, is

$$H=H_0+H_{CF}+\lambda\mathbf{L}\cdot\mathbf{S}+\mu_B\mathbf{B}\cdot(\mathbf{L}+2\mathbf{S}), \tag{1}$$

where H_0 is the Hamiltonian of the isolated atom, H_{CF} takes

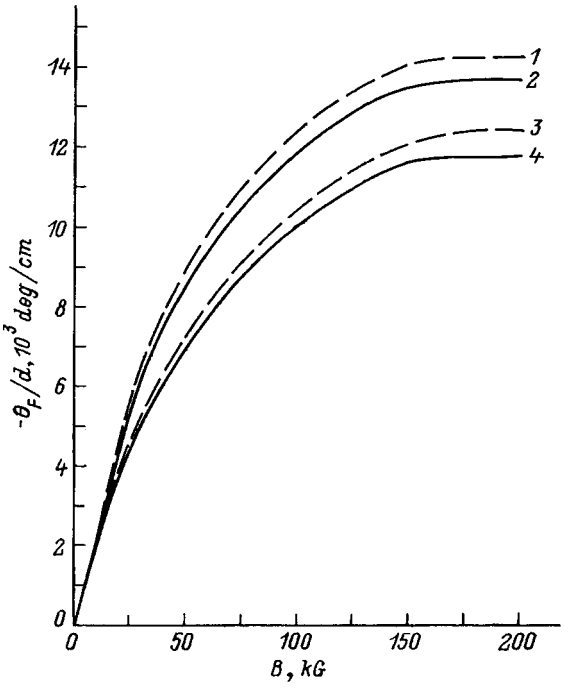

FIG. 1. Faraday rotation angle versus magnetic field in $Cd_{1-x}Fe_xTe$ ($x=0.03$) at temperature $T=5$ K with photon energy $E=1.459$ eV and different orientations of **B** relative to the crystallographic axes. *2, 4* — experimental results for [100] and [111] orientations, respectively; *1, 3* — computational results for the same orientations.

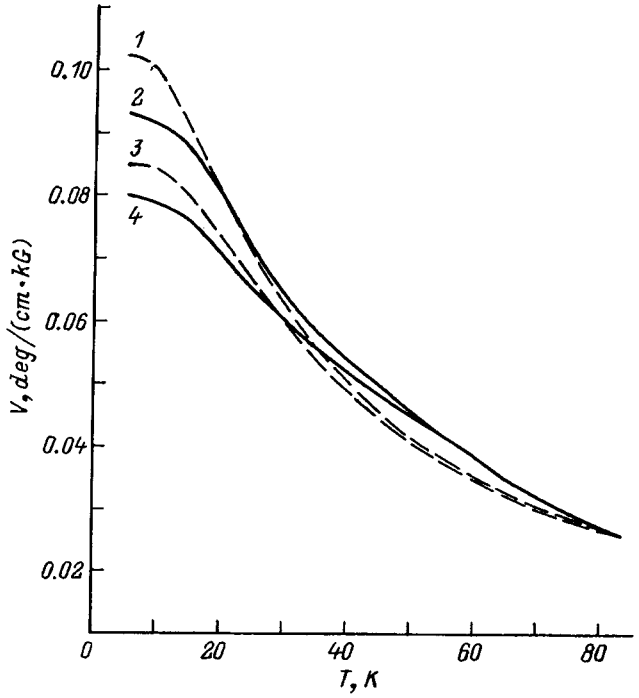

FIG. 2. Temperature dependence of the Verdet constant V in $Cd_{1-x}Fe_xTe$ ($x=0.03$) in a magnetic field $B=135$ kG and photon energy $E=1.459$ eV for different orientations of **B** with respect to the crystallographic axes. *2, 4* — Experimental results for [100] and [111] orientations, respectively; *1, 3* — computational results for the same orientations.

into account the crystal field, and λ is the spin-orbit interaction constant. In the approximation[4] of equivalent operators, H_{CF} is given by

$$H_{CF}=A\left[\frac{1}{8}(L_+^2+L_-^2)^2+\frac{3}{2}L_z^4-6L_z^2-\frac{12}{5}\right],$$

$$L_\pm=L_x\pm iL_y, \tag{2}$$

where A is a constant characterizing the interaction of the impurity ion Fe with its crystalline environment. The basis functions of the orbital terms ^5E and $^5T_2$ have the form[4]

$$\begin{aligned}
&^5E: \quad u_1=|0\rangle,\\
&\qquad u_2=(1/\sqrt{2})(|2\rangle+|-2\rangle);\\
&^5T_2: \quad \nu_1=|-1\rangle,\\
&\qquad \nu_2=(1/\sqrt{2})(|2\rangle-|-2\rangle),\\
&\qquad \nu_3=-|1\rangle.
\end{aligned} \tag{3}$$

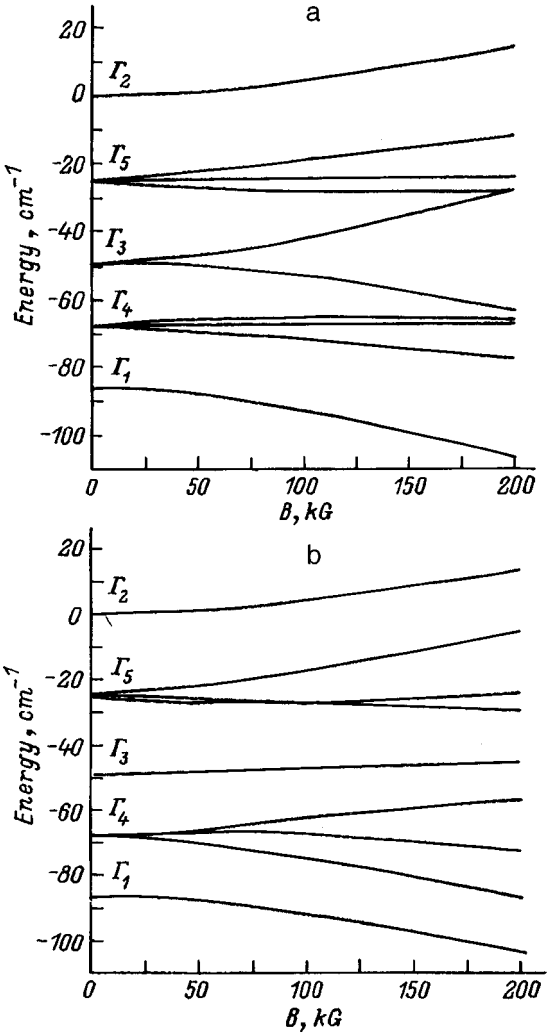

FIG. 3. Magnetic field dependence of the spin-orbit levels which originates from the orbital term E for **B** ∥ [100] (a) and **B** ∥ [111] (b).

In the absence of an external magnetic field the spin-orbit interaction splits the orbital doublet ^5E in second-order perturbation theory into the levels Γ_1, Γ_4, Γ_3, Γ_5, and Γ_2; the energy splitting between them $6\lambda^2/\Delta$ is ~ 24 cm^{-1} (for Fe $\Delta=6A=2500$ cm^{-1} and $\lambda=-100$ cm^{-1}). In strong magnetic fields $B\simeq 150$ kG, $\mu_B B\simeq 10$ cm^{-1}. Since the energy splittings presented are of the same order of magnitude, the spin-orbit and Zeeman interactions must be taken into account simultaneously.

In the basis (3) the Hamiltonian (1) has the form

$$H=\begin{bmatrix} E_0(^5E)+2\mu_B B\mathbf{n}\cdot\mathbf{S} & (\lambda\mathbf{S}+\mu_B B\mathbf{n})\cdot\mathbf{U} \\ (\lambda\mathbf{S}+\mu_B B\mathbf{n})\cdot\mathbf{U}^+ & E_0(^5T_2)+2\mu_B B\mathbf{n}\cdot\mathbf{S}-(\lambda\mathbf{S}+\mu_B B\mathbf{n})\cdot\mathbf{I}\end{bmatrix}, \tag{4}$$

where $E_0(^5E)$ and $E_0(^5T_2)$ are the eigenvalues of H_{CF} ($E_0(^5T_2)-E_0(^5E)=\Delta$), **n** is a unit vector in the direction of the magnetic field, and

$$\mathbf{U}_{\nu k}=\langle u_\nu \mathbf{L}\nu_k\rangle, \quad \mathbf{I}_{kk'}=-\langle \nu_k \mathbf{L}\nu_{k'}\rangle. \tag{5}$$

Substituting the explicit form of the matrix elements (5) with respect to the basis (3) and using the spin functions

($M_s = -2, -1, 0, 1, 2$), we obtain a 25×25 matrix of the Hamiltonian (4). This approach does not employ perturbation theory and makes it possible to take into account the mixing of the ^5E and $^5T_2$ terms. The magnetic-field dependence of the spin-orbit terms, which were obtained from the orbital doublet ^5E, is shown in Fig. 3.

We shall calculate the Faraday rotation angle according to Ref. 5:

$$\theta_F = \frac{F_0^{1/2} d}{2\hbar c} \frac{E^2}{(E_0^2 - E^2)^{3/2}} \frac{(J_h - J_e)}{g\mu_B} M. \quad (6)$$

Here J_e and J_h are the exchange interaction integrals for electrons and holes with the angular momenta of the Fe ions; E_0 is the excitonic transition energy; E is the photon energy; F_0 is a constant, which contains the oscillator strength of the excitonic transition; g is the g-factor of the Fe^{2+} ion; M is the magnetization per unit volume

$$M = x k_B T \frac{\partial}{\partial B} \ln Z, \quad (7)$$

x is the concentration of Fe^{2+} ions; and Z is the partition function, which is found with the aid of the energy spectra obtained in a magnetic field (Fig. 3).

In Figs. 1 and 2 the computational results for the magnetic-field and temperature dependences of the Faraday rotation angle are compared with the experimental data. As one can see from these curves, the experimental and theoretical results are in satisfactory agreement with one another. The Faraday rotation anisotropy is due to the characteristic behavior of the spin-orbit levels in strong magnetic fields (Fig. 3). The lower level Γ_1 is weakly anistropic, the magnitude of the splitting of the next level Γ_4 is substantially different for magnetic field orientations $\mathbf{B} \parallel [100]$ and $\mathbf{B} \parallel [111]$, and the Γ_3 level remains doubly degenerate with field orientation $\mathbf{B} \parallel [111]$, while in a field $\mathbf{B} \parallel [100]$ it is appreciably split.

We note that different variants of the perturbation theory, with allowance of the mixing of the different orbital levels and disregarding them in order to explain the anisotropy of the magnetization, were used in Refs. 4, 6, and 7. However, the energy spectrum obtained, for example, in Ref. 4, cannot be used to explain the indicated features from a unified standpoint. Taking into account simultaneously the spin-orbit and Zeeman interactions is therefore justifiable, this makes it possible to give a unified description of the Faraday rotation angle anisotropy and the characteristic features of the low-temperature dependence of the Verdet constant.

[1] A.I. Savchuk, O.R. Klichuk, and P.I. Nikitin, Japan. J. Appl. Phys. **32**, 393 (1993).
[2] C. Testelin, A. Mauger, C. Rigaux, M. Guillot, and A. Mycielski, Solid State Commun., **71**, 923 (1989).
[3] S. Rodrigues, M. Villeret, and E. Kartheuser, Phys. Scripta, **39**, 131 (1991).
[4] M. Villere, S. Rodrigues, and E. Kartheuser, Phys. Rev. B **41**, 10028 (1990).
[5] P. I. Nikitin and A. I. Savchuk, Usp. Fiz. Nauk **160**, 167 (1990) [Sov. Phys. Usp. **33**, 974 (1990)].
[6] M. Villeret, S. Rodrigues, and E. Kartheuser, Phys. Rev. B **43**, 3443 (1991).
[7] C. Testelin, C. Rigaux, A. Mauger, A. Mycielski, and M. Guillot, Phys. Rev. B **46**, 2193 (1992).

Translated by M. E. Alferieff

Photoelectric and radiation characteristics of silicon solar cells at high illumination levels and elevated temperatures

M. Ya. Bakirov

Radiation Research Division, Academy of Sciences of Azerbaĭdzhan, 370073 Baku, Azerbaĭdzhan
(Submitted October 3, 1995; accepted for publication July 1, 1996)
Fiz. Tekh. Poluprovodn. **31**, 520–522 (May 1997)

It has been established experimentally that the power of a cell increases and the rate of radiation degradation of the cell parameters decreases when concentrated solar radiation is used. In uncooled cells the temperature increases above 100 °C and the efficiency drops. © *1997 American Institute of Physics.* [S1063-7826(97)00305-0]

A great deal of attention has been devoted in recent years to the use of solar energy, specifically, the direct conversion of solar energy into electricity. Silicon solar cells are widely used for this purpose. They are the main source of electricity in space vehicles. However, the high cost of solar cells is holding back extensive use on earth. The cost of silicon solar cells is dropping mainly as a result of the decreasing cost of single-crystalline silicon and the development of cheap film cells based on amorphous silicon. The use of concentrated solar radiation is no less promising for this purpose.

Concentrated solar radiation is used in photoelectric devices mainly to improve the energy efficiency by increasing the specific power. However, as our investigations have shown, the rate of radiation degradation of cell parameters also decreases in the process. When concentrated solar radiation is used, a large amount of heat is released in the cells and, if no cooling is provided, the working temperature of the cells rises. A large increase in the temperature affects the charge-carrier density and the light-absorption process. As a result, the output parameters of the solar cells change. In cells operating under concentrated solar radiation conditions, in which the working temperature reaches 100 °C and higher, some radiation defects are found to be unstable due to the thermal activation. For this reason, the defect density, which determines the degree of degradation of the cell parameters, depends not only on the density of the integrated particle flux, but also on the temperature, which is determined by the solar radiation concentration factor. This motivated a study of the effect of temperature and illumination level on the photoelectric and radiation characteristics of silicon solar cells.

Our objective in this study was to determine the mechanisms of the change occurring in the main parameters at high temperature and to determine the effect of the illumination level and temperature on the rate of radiation-induced degradation of the parameters of silicon solar cells. We investigated cells with a p–n junction, which were prepared by diffusing phosphorus into p-Si with resistivity 5 $\Omega\cdot$cm. Under direct sunlight ($W=100$ mW/cm^2) these cells generate a photocurrent of about 25 mA/cm^2 and a photovoltage of 0.5 V. Their efficiency is $\sim$10%.

The temperatures of a cell exposed to concentrated solar radiation were measured. It was determined that as the power of the sunlight incident on a cell increases from 0.1 to 2.5 W/cm^2, the temperature of the cell increases monotonically from 30 to 220 °C.

Investigation of the temperature dependence of the main parameters of the solar cell showed that as the temperature increases above room temperature, the short-circuit photocurrent I_s increases slightly and the open-circuit voltage U_s, the maximum power P_m at optimal load, the filling factor γ of the current-voltage characteristic, and the efficiency η all decrease (Fig. 1). These dependences agree qualitatively with the results of Refs. 1 and 2. The increase in the photocurrent with increasing temperature is explained by the change in the light absorption. As the temperature of the cell increases, the absorption edge shifts as a result of band-gap narrowing in the crystal and the number of pairs generated in the bulk increases. On the other hand, the light absorption coefficient changes with increasing temperature. As a result, the photocurrent increases with temperature. In our samples the temperature coefficient of the photocurrent was equal to 40 μA/°C. The decrease in the open-circuit voltage with increasing temperature is due to the change in the intrinsic

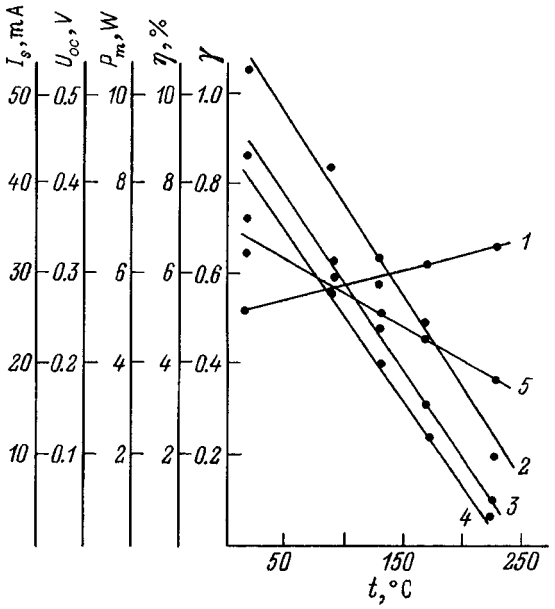

FIG. 1. Temperature dependences of the main parameters of a silicon solar cell at high temperatures: *1* — I_S, *2* — U_{oc}, *3* — P_m, *4* — η, and *5* — γ ($W=0.1$ W/cm^2).

 1063-7826/97/050439-02$10.00

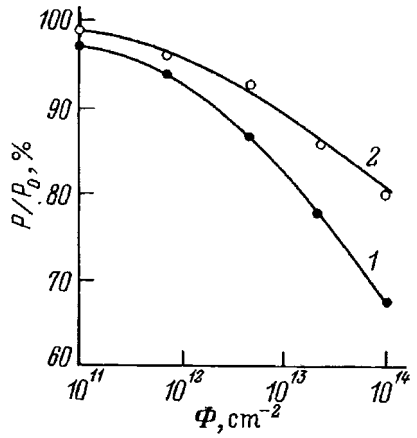

FIG. 2. Dose dependence of the power in silicon solar cells irradiated under different conditions: *1* — In the dark, $t=25$ °C; *2* — under illumination ($W=1$ W/cm^2, $t=80$ °C).

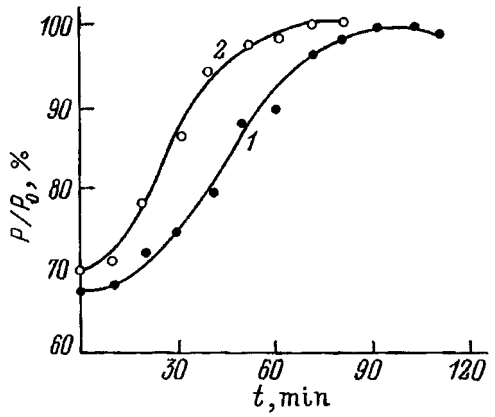

FIG. 3. Change in the power level as a result of isothermal annealing of irradiated silicon solar cells: *1* — In the dark, $t=150$ °C; *2* — under illumination ($W=1.7$ W/cm^2, $t=150$ °C).

charge-carrier density and band-gap in the crystal. In our case the open-circuit voltage is determined by the relation $U_{oc}\sim\ln(I_s/I_0)$, according to which U_{oc} should increase with I_s. But a sharp increase in the dark current I_0 flowing through the p–n junction decreases U_{oc}. The intrinsic density n_i varies exponentially with temperature, which gives $I_0/I_0\sim n_i$. Furthermore, narrowing of the band gap with increasing temperature increases the dark current and thereby reduces to a minimum the positive effect of increasing the light absorption coefficient in the long-wavelength region of the spectrum. As a result, U_{oc} decreases with increasing temperature and $\Delta U_{oc}/\Delta T=-2.3$ mV/°C. As the temperature is raised, the filling factor of the current-voltage characteristic decreases; this is explained by the increase in the dark current. The output power and efficiency decrease with increasing temperature mainly because of a decrease in the photovoltage and the filling factor of the current-voltage characteristic. In our samples $\Delta P/\Delta T=-0.4$ mW/°C and $\Delta\eta/\Delta T=-0.4\%/°$C.

We studied the effect of a high illumination and temperature on the rate of degradation and restoration of cell. The samples were irradiated with 5-MeV accelerated electrons in two regimes: at room temperature in the dark and in concentrated light with a power of 1 W. In the process the sample was heated to a temperature of 80 °C. The measurements showed that in the entire range of variation of the density of the integrated electron fluxes the degree of power degradation in illuminated and heated samples is much lower than in samples irradiated at room temperature in the dark (Fig. 2); this was observed in phototransducers based on GaAs–GaAlAs heterostructures irradiated with electrons and protons.[3]

To determine the effect of illumination on the rate of power restoration in irradiated cells after annealing, isothermal heating was conducted in the dark and in focused sunlight. The samples were irradiated in the dark with the same dose (10^{14} cm^{-2}). In both cases the temperature was maintained at 150 °C. It was established that power is restored much more rapidly with isothermal annealing under illumination conditions (Fig. 3); this attests to the effect of light on the process of annealing of radiation defects. The action of the illumination on parameter degradation and restoration in solar cells is explained by injection annealing.[4] Therefore the use of concentrated sunlight in photovoltaic setups will make it possible to improve the energy indicators of solar batteries not only by increasing the specific power but also by decreasing the rate of radiation degradation of the parameters.

[1] S. N. Borisov, S. M. Gorodetskiĭ, G. M. Grigor'eva, K. N. Zvyagina, and A. M. Kasymakhunova, Geliotekhnika, No. 4, 3 (1983).
[2] A. L. Fahrenbruch and R. H. Bube, *Fundamentals of Solar Cells: Photovoltaic Solar Energy Conversion*, Academic Press, N. Y., 1983 [Russian translation, Énergoizdat, Moscow, 1987].
[3] G. M. Grigor'eva, V. A. Grilikhes, K. N. Zvyagina, M. B. Kagan, T. L. Lyubashevskaya, and O. I. Chesta, Geliotekhnika, No. 1, 8 (1989).
[4] D. V. Lang and L. C. Kimerling, Phys. Rev. Lett. **33**, 489 (1979).

Translated by M. E. Alferieff

Distribution of a shallow donor impurity in a *p*-type CdTe wafer annealed in Cd vapors

V. N. Babentsov, Z. K. Vlasenko, A. I. Vlasenko,[1)] and A. V. Lyubchenko

Institute of Semiconductor Physics, Ukrainian National Academy of Sciences, 252650 Kiev, Ukraine
(Submitted April 4, 1996; accepted for publication July 1, 1996)
Fiz. Tekh. Poluprovodn. **31**, 523–525 (May 1997)

Experimental investigations and numerical modeling of the process of bilateral doping of a *p*-type CdTe wafer with shallow donors during annealing of the wafer in cadmium vapors have been performed. This process was found to have several features — a correlation in the low-temperature photoluminescence bands between the excitation of a line of a exciton bound on a donor and quenching of an acceptor line, which are characteristic of recombination on group-I impurities occupying interstices and Cd sites, respectively, and a strong effect of diffusion on the donor distribution profile. The results obtained by us make it possible to optimize the annealing process. © *1997 American Institute of Physics.* [S1063-7826(97)00405-5]

Cadmium telluride is widely used in infrared[1] and radiation[2] photoelectronics, optoelectronics,[3] laser technology,[4] and in other applications. Many applications require material with close to stoichiometric composition, highly accurate compensation, controllable doping level, absence of inclusions of a second phase, and a low density of residual, electrically active impurities. The latter are usually group-I elements (Li, Na, Cu, Ag), which are acceptors at cadmium sites and donors at interstices.[5,6] At the same time, because of the retrograde solubility of tellurium, cadmium vacancies predominate even in relatively stoichiometric material; the ratio of these concentrations of the impurities and vacancies, as a rule, determines the conductivity of the crystals. Post-growth annealing of *p*-type CdTe wafers in Cd vapors yields *n*-type material,[7,8] but the question of the donor impurity distribution over the thickness of the wafer requires additional study. This is because the gettering of point defects by surfaces, macrodefects of the lattice,[9] dissipation of clusters, and other processes must be taken into account.

We investigated experimentally the distribution profiles of shallow donors over the thickness of a *p*-type CdTe wafer when the wafer was annealed in saturated cadmium vapor and we performed numerical modeling of this process, taking into account the bilateral Cd diffusion and rediffusion of shallow donors from the wafer.

Plane-parallel *p*-type CdTe wafers, oriented with the large surfaces along the (111) plane, were annealed, after the damaged layer was removed at 600 °C for 1, 2, 3, 4, and 28 h in an evacuated cell containing a weighed portion of Cd.

The donor distribution profiles were measured on fresh cleavage faces by the low-temperature photoluminescence (LTPL) method (excitation with a He–Ne laser probe) according to the intensity of the radiation of excitons bound on donors.[10–12]

The formation of donor defects during annealing of a *p*-type CdTe wafer in Cd vapor can proceed mainly via the following reactions (disregarding thermal ionization of defects, the charge states of the defects, and complex formation):

$$\mathrm{Cd}_c \leftrightarrow \mathrm{Cd}_i^* , \tag{1a}$$

$$\mathrm{Te}_{\mathrm{Te}} \leftrightarrow \mathrm{Te}_i + V_{\mathrm{Te}}^* , \tag{1b}$$

$$\mathrm{Cd}_c + V_{\mathrm{Cd}} \leftrightarrow \mathrm{Cd}_{\mathrm{Cd}} \leftrightarrow V_{\mathrm{Cd}} + \mathrm{Cd}_i^* , \tag{1c}$$

$$\mathrm{Cd}_c \leftrightarrow \mathrm{Cd}_{\mathrm{Cd}} + V_{\mathrm{Te}}^* , \tag{1d}$$

$$\mathrm{Cd}_i + M_{\mathrm{Cd}}^I \leftrightarrow \mathrm{Cd}_{\mathrm{Cd}} + M_i^{I*} , \tag{1e}$$

$$M_c^I \leftrightarrow M_i^{I*} , \tag{1f}$$

where $\mathrm{Cd}_{\mathrm{Cd}}$, Cd_i, and Cd_c are cadmium impurity atoms, and M_{Cd}^I, M_i^I, and M_c^I are group-I metal impurity atoms at Cd sites, in interstices, and in clusters (on the surfaces), respectively; V_{Cd} and V_{Te} are Cd and Te vacancies; an asterisk denotes a donor state of the defects.

The Cd atoms, which diffuse in the bulk during annealing in Cd vapors, occupy A^{II} sites in the lattice. When an excess of Cd atoms is present and there are no free and weakly bound vacancies, the Cd atoms can occupy interstices and appear as donors (1a) or add to the Cd sublattice (primarily near structural macrodefects), the Te vacancies forming in the process (1d) also exhibit donor properties.

The spectral distribution of the LTPL intensity obtained from points on a cleavage face of the crystal, which are located at the same distance from the surfaces of the crystal, before and after annealing for $t=3$ h are shown in Fig. 1. The LTPL lines of excitons bound on shallow donors (I_2) and acceptors (I_1) are also indicated here. A comparison with the published data on the LTPL spectra of different types of defects in CdTe[6,8,9,11] shows that during the formation of shallow donors the most intensive reaction is the reaction (1e), the substitution of Cd atoms, which diffuse from the surface, for the M^I atoms, which occupy A^{II} sites (primarily weakly bound, for example, Li[13]), where they manifest themselves as acceptors, and displacement of the atoms into interstices, where they acquire donor properties.

The obvious correlation between the excitation of the donor line I_2 and the quenching of the acceptor line I_1 (see the inset in Fig. 1), which are associated with proportional changes in the concentration of M^I atoms at interstices and sites, respectively, with increasing annealing time (t) attests to the fact that this process predominates. As t increases, the

 1063-7826/97/050441-03$10.00

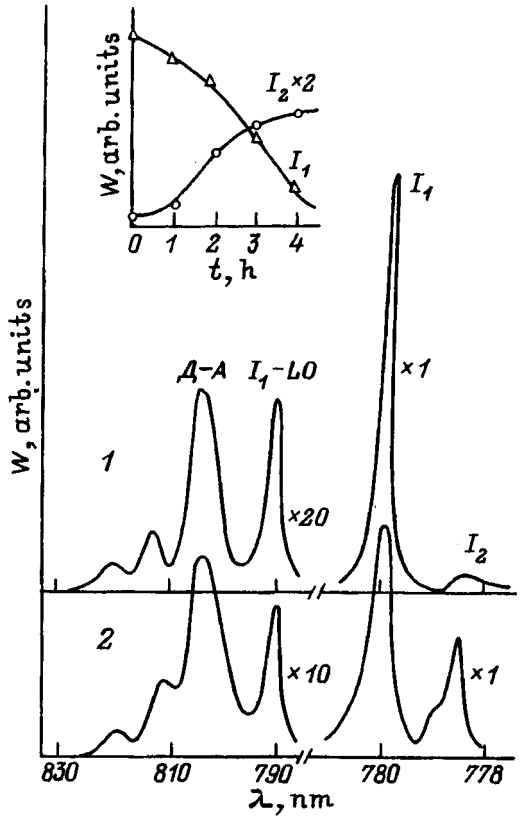

FIG. 1. Photoluminescence spectrum of CdTe at 4.2 K. *1* — Initial spectrum, *2* — at a depth of 100 μm after annealing for 3 h. Inset: Intensities of the lines of excitons bound on an acceptor (I_1) and donor (I_2) as a function of annealing time at a depth of 100 μm from the surface of the sample.

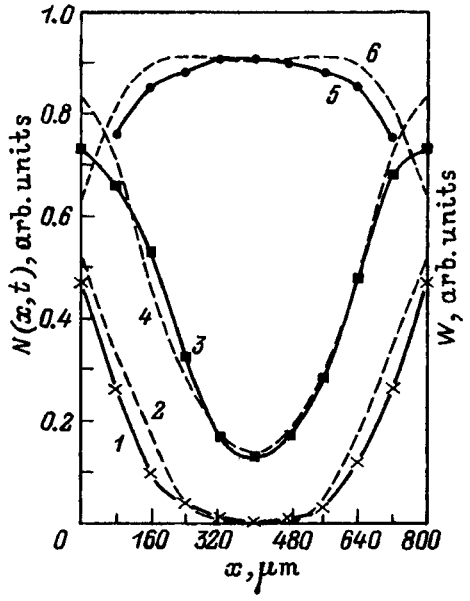

FIG. 2. Experimentally obtained profiles of the intensity distribution of a line of an exciton bound on a donor (W) over the thickness of a p-CdTe wafer after annealing at 600 °C for *1, 4,* and 28 h (*1, 3, 5*) and numerical calculation of the donor distribution density $N(x,t)$ for *1, 4,* and *28* h (dashed lines *2, 4, 6*).

curve I_2 for donors M_i^{I*} saturates; this could be due to the finiteness of the density of the residual impurity M^I. It should be noted that an increase in the donor density — Cd_i^*, V_{Te}^* — (1a), (1d) can preserve the increase in the electronic component in the conductivity.

For sufficiently long annealing times, one would expect a uniform distribution of the atoms M_i^* over the thickness of the wafer. However, despite the fact that a regime with a constant Cd vapor pressure above the CdTe wafer is established during the annealing process, the distribution profile of the residual donor impurity over the thickness of the plate remains complicated and does not level off even at long times t. The experimentally measured distribution profiles (shown in Fig. 2), of the line intensity I_2 over the thickness of the p-CdTe wafer for different times t attest to this fact.

This is due to the vaporization of the impurity atoms (primarily with small atomic radii) from the surface of the plate, which proceeds in parallel with diffusion, and their heterodiffusion from the volume toward the surfaces. The value of the self-diffusion coefficient CdTe determined for $t \leqslant 4$ h was $D_1 = 2.6 \times 10^{-8}$ cm^2/s. The value of the heterodiffusion coefficient determined for annealing time $T = 28$ h was $D_2 = 1.16 \times 10^{-9}$ cm^2/s.

The mathematical model describing the distribution of shallow donors occurring over the depth of the wafer annealed in Cd vapors as a result of the displacement of the residual impurity M^I from the Cd sites into interstices can be represented by two diffusion equations for the self-diffusion of Cd into the wafer and counterheterodiffusion of the impurity with the corresponding initial and boundary conditions.

A calculation of the resulting distribution profiles of the density of the donors M_i^{I*} is shown in Fig. 2 (dashed lines). The satisfactory agreement of the experimental data with the calculations for different values of t could attest to the correctness of the chosen physical and mathematical models.

Using the values obtained for D_1 and D_2, it is possible to calculate the process of long-time annealing of a p-type CdTe wafer. The results of the numerical modeling, taking into account bilateral diffusion of Cd atoms and counterhet-

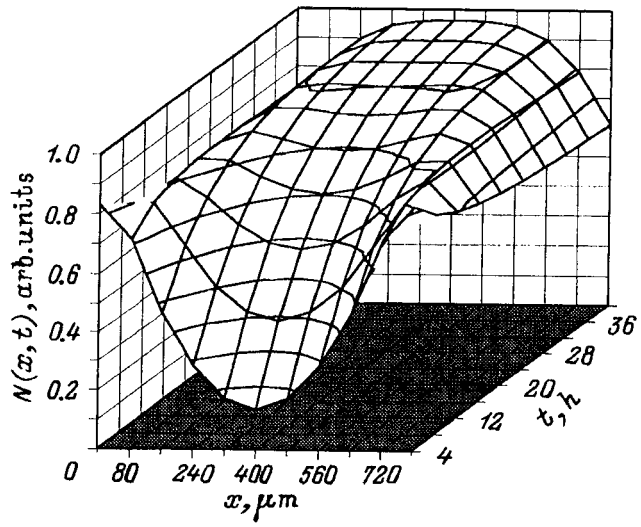

FIG. 3. Numerical modeling of the donor impurity density distribution over the thickness of a p-CdTe wafer ($a = 800$ μm) taking into account rediffusion during annealing at 600 °C for 40 h.

erodiffusion of impurity atoms toward the surfaces, are presented in Fig. 3 for annealing times up to 40 h. The results of the modeling show that under prolonged annealing in Cd vapors the surface regions become strongly depleted of the shallow donor impurity due to the evaporation into the exterior volume; i.e., the material is purified.

[1)]Electronic mail: mickle@semicond.kiev.ua; Fax: (044)-2658842

[1] R. Bean, K. Zanio, and J. Ziegler, J. Vac. Sci. Technol. A **7**, 343 (1989).
[2] M. R. Squilante, G. Entine, E. Frederic, and L. Cirignano, Instr. and Method in Phys. Research. A **283**, 323 (1989).
[3] A. Partovi, J. Millerd, E. Garmire, M. Ziari, W. Steier, S. B. Trivedi, and M. B. Klein, Appl. Phys. Lett. **57**, 846 (1990).
[4] W. J. Kim, M. J. Park, S. U. Kim, T. S. Lee, J. M. Kim, W. J. Song, and S. H. Suh, J. Cryst. Growth **104**, 677 (1990).
[5] P. Gheuvart, U. E. Hanani, D. Schneider, and R. Tribolet, J. Cryst. Growth **101**, 270 (1990).
[6] E. Molva, J. P. Chamonal, and J. L. Pautrat, Phys. St. Col. B **109**, 635 (1982).
[7] S. Seto, A. Tanaka, Y. Masa, S. Dairaku, and M. Kawashima, Appl. Phys. Lett. **53**, 1524 (1988).
[8] N. V. Agrinskaya and V. V. Shashkova, Fiz. Tekh. Poluprovodn. **22**, 1248 (1988) [Sov. Phys. Semicond. **22**, 790 (1988)].
[9] E. S. Nikonyuk, V. L. Shlyakhovyĭ, Z. I. Zakharuk, M. A. Kovalets, and N. I. Kuma, Neorg. Mater. **31**, 185 (1995).
[10] N. V. Agrinskaya, N. N. Zinov'ev, O. A. Matveev, and I. D. Yaroshetskiĭ, Fiz. Tekh. Poluprovodn. **14**, 172 (1980) [Sov. Phys. Semicond. **14**, 100 (1980)].
[11] V. N. Babentsov, L. V. Rashkovetskiĭ, E. A. Sal'kov, and N. I. Tarbaev, Fiz. Tekh. Poluprovodn. **26**, 1088 (1992) [Sov. Phys. Semicond. **26**, 608 (1992)].
[12] V. N. Babentsov, A. I. Vlasenko, and N. I. Tarbaev in *Inter. Workshop on Optical Diagnostics of Materials and Devices for Opto-, Micro-, and Quantum Electronics*, edited by S. V. Svechnikov and M. Ya. Valakh, Proc. SPIE **2113**, 104 (1993).
[13] V. V. Emtsov and T. V. Mashovets, *Impurities and Point Defects in Semiconductors* [in Russian], Radio i svyaz', Moscow, 1981.

Translated by M. E. Alferieff

Charge-carrier exclusion in InAs

S. S. Bolgov, V. K. Malyutenko, and A. P. Savchenko

Institute of Semiconductor Physics, Ukrainian National Academy of Sciences, 252650 Kiev, Ukraine
(Submitted June 11, 1996; accepted for publication July 1, 1996)
Fiz. Tekh. Poluprovodn. **31**, 526–527 (May 1997)

The first observation of contact exclusion in InAs-based p^+–p–p^+ structures at high temperatures is reported. To identify the process of nonequilibrium depletion of the base, attesting to exclusion of free charge carriers, the current-voltage characteristics, the kinetics of current establishment, and the negative luminescence in the spectral region of interband transitions were investigated. The practical aspect of this phenomenon is discussed. © *1997 American Institute of Physics.* [S1063-7826(97)00605-4]

There is now a large number of works in which the mechanisms of the exclusion phenomenon (bipolar exhaustion of an intrinsic semiconductor equipped with antiblocking contacts) are investigated and practical applications of this phenomenon are proposed. The investigations have been conducted mainly in well-purified or compensated wide-gap materials Ge and Si. However, in connection with the appearance of a number of new practical problems which contact exclusion can solve, specifically, the possibility of producing efficient photodetectors[1] and infrared (IR) range sources,[2] it is of special interest to investigate this phenomenon in materials conventionally employed in IR technology.[3] In Ref. 4 we showed that exclusion can be realized in $Cd_xHg_{1-x}Te$/CdTe heterostructures. In this paper we report the first observation of exclusion in InAs-based p^+–p–p^+ structures at high temperatures.

The investigations were conducted at temperatures in the range $T=300-400$ K on InAs-based p^+–p–p^+ samples prepared in the form of $3\times1.5\times0.4$-mm rectangular plates with hole density in the base $N_a-N_d=2\times10^{16}$ cm^{-3}, which exceeds the intrinsic charge carrier density $n_i=2\times10^{15}$ cm^{-3} at room temperature. The antiblocking contacts were produced by diffusing Zn in unsaturated As vapor. To decrease the surface recombination rate, the samples were etched in the mixture $5HNO_3$:1HF:$1CH_3COOH$. To identify the process of nonequilibrium exhaustion of the base, which attests to exclusion of electron–hole pairs, we investigated the current-voltage characteristics (IVC), the kinetics of current establishment, and the negative luminescence in the region of interband transitions of the material ($\lambda\leqslant3.8$ μm).

To avoid Joule heating, an electric field in the form of 10-μm square pulses (dc voltage regime) was applied to the p^+ contacts. A 1.0-mm-wide diaphragm, through which the nonequilibrium radiation was observed with a PbSe photodetector, was placed at the surface of the crystal near one of the antiblocking contacts. The current and voltage pulses were recorded with a stroboscopic oscillograph, and the IVC and field dependences of the negative luminscence were recorded on a recorder.

As expected, at $T=300$ K there was no exclusion effect in the experimental voltage range $V\leqslant30$ V: The IVC was ohmic, the current pulses were square, and a negative luminescence signal was not observed (the region of monopolar conductivity, bipolar exhaustion is very small).

As the temperature increased, typical indications of exclusion were observed as a result of an increase in the intrinsic charge carrier density n_i (bipolar conductivity region; see inset *2* in Fig. 1). A characteristic (for exclusion) region of sublinearity $V\sim I^{1/2}$ arose on the IVC; the current pulse with a square voltage pulse had the shape of a decreasing curve

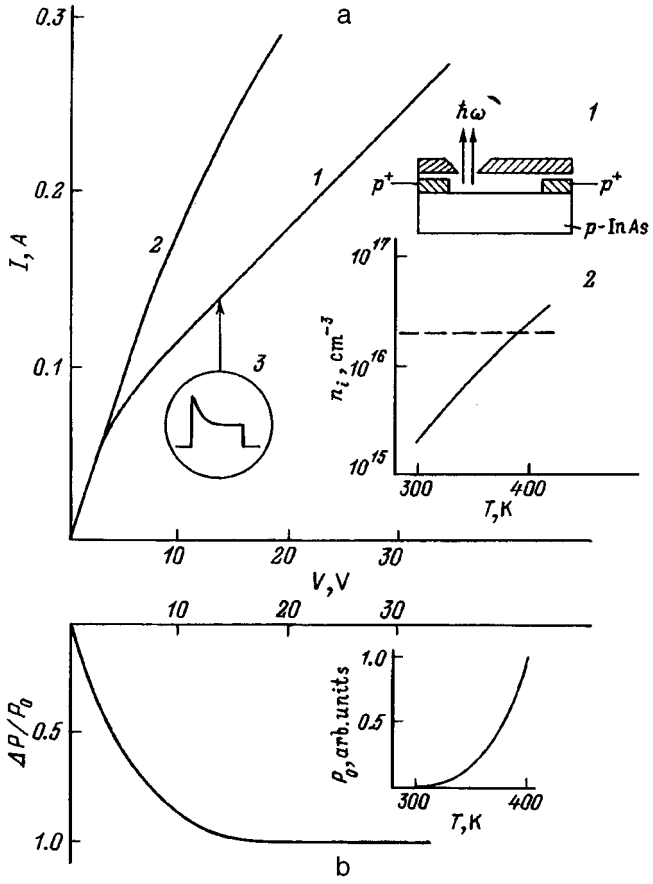

FIG. 1. a — Current-voltage characteristics of p^+–p–p^+ InAs structures at $T=360$ K: *1* — Etched surface of the sample, *2* — ground surface of the sample. Inset *1*: Arrangement of the experiment. Inset *2*: Temperature dependence of n_i in InAs, the dashed curve represents N_a-N_d. Inset *3* — Oscillogram of the current pulse. b — Field-dependence of negative luminescence in InAs under exclusion conditions at $T=360$ K. Inset: Temperature dependence of the maximum negative luminescence signal in InAs.

 1063-7826/97/050444-02$10.00

followed by saturation (see Fig. 1a). The field dependence of the negative interband luminescence signal ΔP also attests to a decrease in the charge carrier density in the base. As is well known, such a signal arises under conditions when the electron density n and the hole density p become less than the equilibrium values $np<n_i^2$ (Ref. 2 ; see Fig. 1b). The signal amplitude increases with voltage and then remains unchanged, attesting to complete exhaustion of the base.[1)] As T increases, the intensity of the negative luminescence signal ΔP in the saturation region increases.

An increase in the surface recombination rate in the base of the structure (polishing of the surface), as expected,[6] suppresses the exclusion effect because of a decrease in the effective charge carrier lifetime. As a result, the negative luminescence signal decreases, the IVC approaches an ohmic characteristic (see curve *2* in Fig. 1a), and the current pulse becomes square.

Considering the existence of the exclusion effect in InAs as proved, we present in conclusion several practical recommendations. From the IVC it is easy to estimate the lifetime of electron–hole pairs in the base of the structure. The region of sublinearity of the IVC characterizes the process of exhaustion of the base as a result of carrier removal to one of the p^+ contacts. The total exhaustion regime occurs at a voltage when the sublinearity region is replaced by a second ohmic section in the IVC (in the experiment $V=10$ V) and the extended diffusion length $L_d=\mu_n E\tau$ equals the distance d between the contacts. Since the electric field in this case is virtually uniform in the base of the structure (we ignore the accumulation layer, whose length is on the order of the carrier diffusion length near one of the p^+ contacts), the lifetime τ of electron–hole pairs can be easily estimated from the expression for L_d. Setting $\mu_n=27\,000$ cm^2/(V·s), for $V=10$ V we obtain $\tau=3.3\times10^{-7}$ s, which corresponds to the carrier diffusion length $L=\sqrt{D\tau}=28$ μm ($T=360$ K).

It could also be of practical interest to employ InAs p^+ structures as fast sources of IR radiation which operate at high temperatures. According to our estimates, the power of the maximum negative luminescence signal, equal to the power P_0 of the equilibrium radiation of the material in the spectral range of interband transitions $\lambda\leqslant\hbar c/E_g\leqslant3.8$ μm, is sufficiently high at high temperatures for practical applications. For example, $\Delta P=-P_0=1.2\times10^{-3}$ W/cm^2 for $T=400$ K (the temperature dependence of P_0 is shown in the inset in Fig. 1b).

[1)]See Ref. 5 for detailed information about the characteristic features of negative luminescence under the conditions of contact exclusion of charge carriers.

[1] T. Ashley, C. T Elliott, and A. M. White, SPIE Proc. **588**, 62 (1986).
[2] S. S. Bolgov, V. K. Malyutenko, and V. I. Pipa, Pis'ma Zh. Tekh. Fiz. **5**, 1444 (1979) [Sov. Tech. Phys. Lett. **5**, 610 (1979)].
[3] V. K. Malyutenko, Semicond. Sci. Technol. **8**, 390 (1993).
[4] S. S. Bolgov, V. K. Malyutenko, V. I. Pipa, and A. P. Savchenko, Pis'ma Zh. Tekh. Fiz. **15**, 49 (1989) [Sov. Tech. Phys. Lett. **15**, 268 (1989)].
[5] V. K. Malyutenko, A. G. Kollyukh, and A. M. Rybak, Zh. Prikl. Spektrosk. **47**, 299 (1987).
[6] S. A. Vigusevich, Yu. M. Malozovskiĭ, and V. K. Malyutenko, Fiz. Tekh. Poluprovodn. **20**, 1841 (1986) [Sov. Phys. Semicond. **20**, 1155 (1986)].

Translated by M. E. Alferieff

Nature of hole localization centers in sodium-doped lead chalcogenides

G. T. Alekseeva, E. A. Gurieva, P. P. Konstantinov, L. V. Prokof'eva, and Yu. I. Ravich

A. F. Ioffe Physicotechical Institute, Russian Academy of Sciences, 194021 St. Petersburg, Russia
(Submitted June 17, 1996; accepted for publication July 1, 1996)
Fiz. Tekh. Poluprovodn. **31**, 528–532 (May 1997)

The Hall coefficient R, thermoelectric power S, and electrical conductivity in Na-doped PbSe with lead-isovalent Cd and Mn impurities introduced in concentrations of up to 5 at. % have been investigated. The experimental data together with previously obtained results indicate that the acceptor action of Na in lead chalcogenides with isovalent impurities is weakened because of hole localization at defects. According to the proposed model of acceptor doping, such defects in lead chalcogenides can be chalcogen atoms in a metal sublattice. Increasing the temperature, and also introducing isovalent impurities with relatively small ionic radii, facilitates the formation of the defects. Antistructural defects produce resonance levels in the valence band, whose position depends on the Na concentration. © *1997 American Institute of Physics.* [S1063-7826(97)00705-9]

According to Refs. 1 and 2, the introduction of the isoelectronic substitution impurity Sn into lead chalcogenides, together with the acceptor impurity Na, strongly influences the doping mechanism: Carrier localization centers, which produce quasilocal levels in the valence band, form in addition to free holes. As the results of Mössbauer spectroscopy have shown, the role of Sn atoms in lead selenide and telluride is completely different. In Pb(Sn)Se⟨Na⟩ the Sn atoms are in two charge states Sn(+2) (neutral with respect to the lead ions) and Sn(+4)[3] and are thereby hole localization centers. In Pb(Sn)Te⟨Na⟩ the atoms Sn are only in the state Sn(+2).[2] Nonetheless, starting with a certain doping level, the concentration of localization centers in the solid solutions $Pb_{1-x}Sn_xTe$ with $x=0.005-0.01$ grows rapidly and at maximum Na density is close to the density of active centers, i.e., to half the total Na density. The following hypothesis was advanced to explain the weakening of the doping action of Na in these solid solutions: The Sn atoms create conditions for some Te atoms to occupy antistructural positions in the lattice, which results in hole localization.

A decrease of the acceptor action of Na in PbTe was also observed when the isovalent impurity Cd was added to this material.[4] The results noted suggest that such an effect can also be expected in PbSe⟨Na⟩ with the introduction of isovalent impurities which exhibit a valence of +2 in compounds with Se.

In the present work, to check and detail the foregoing ideas about the mechanism of formation of hole localization centers in lead chalcogenides, we investigated the changes occurring in the Hall coefficient R, the thermoelectric power S, and the electrical conductivity as a result of introduction of the lead-isovalent impurities Cd and Mn in concentrations up to 5 at. % in PbSe⟨Na⟩. Figure 1 shown the hole Hall coefficient p at 77 K as a function of the sodium density N for PbSe with different isovalent impurity contents. A strict correspondence between the indicated concentrations is not observed in the entire doping interval: At first, the hole density is less than the Na density, and then as the doping level increases, this ratio is reversed. The increase in the Hall density above the acceptor impurity density falls within the limits 0–20%. The appearance of values of p exceeding N can be explained by the fact that a Hall factor equal to 1, employed in the calculations, exceeds its real value in these materials at high hole densities.[5] Therefore, an exact relation between p and N cannot be established in the entire doping interval, but it can be stated confidently that the hole density lags behind the Na density with doping levels below 1×10^{20} cm^{-3}. Since the Na atoms, which substitute Pb in the lattice, do not exist in the form of Na(+2) ions and cannot be neutral with respect to the metal sublattice, the weakening of the acceptor action of Na means that the holes are localized on structural defects. As one can see from the figure, in the presence of neutral impurities the dependence $p(N)$ does not change qualitatively, but as far as the quantitative changes are concerned, it follows from experiment that the efficiency of the acceptor action of Na decreases and the value of p in solid solutions is less than in PbSe, although the effect is not as large as when Cd is added to PbTe.[4]

The temperature dependences of the Hall coefficient in PbSe with isovalent impurities also change: The temperature growth of the coefficient decreases (see inset in Fig. 2). As a comparison of the Hall data for PbSe in solid solutions with the same doping level (Fig. 2) shows, the discrepancy between the curves $R(T)$ is characteristic for low temperatures; near the temperature of the maximum the differences virtually vanish. If it is assumed that the increase in the Hall coefficient is due to the decrease in the free-hole density, i.e., hole localization, then the latter result means that the maximum number of localized holes in the experimental materials with constant N is the same. If in solid solutions some holes are localized even at 0 K and increasing T gives only an additional contribution, then in PbSe the activationless mechanism is ineffective in the strong-doping region and hole localization occurs mainly as a result of an increase in the temperature. The same result was obtained in Ref. 2 for PbTe and Pb(Sn)Te, the only difference being that in Pb(Sn)Te the fraction of holes localized at 0 K increases appreciably with the Na density, which results in pinning of the Fermi level and a large weakening of the temperature dependence of the Hall coefficient in strongly doped samples.

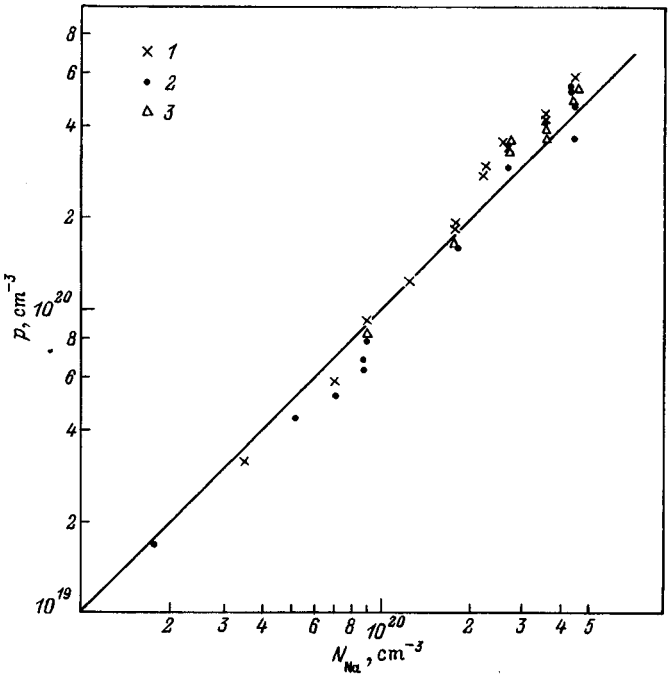

FIG. 1. Hall density versus sodium density (77 K): *1* — PbSe, *2* — $Pb_{0.95}Mn_{0.05}Se$, *3* — $Pb_{0.95}Cd_{0.05}Se$. Straight line — doping in a 1:1 ratio.

The thermoelectric power of PbSe increases in the presence of neutral impurities. Its value in the strong-doping region is presented in Fig. 3 for materials of different composition at 300 K. Temperature investigations of S showed that

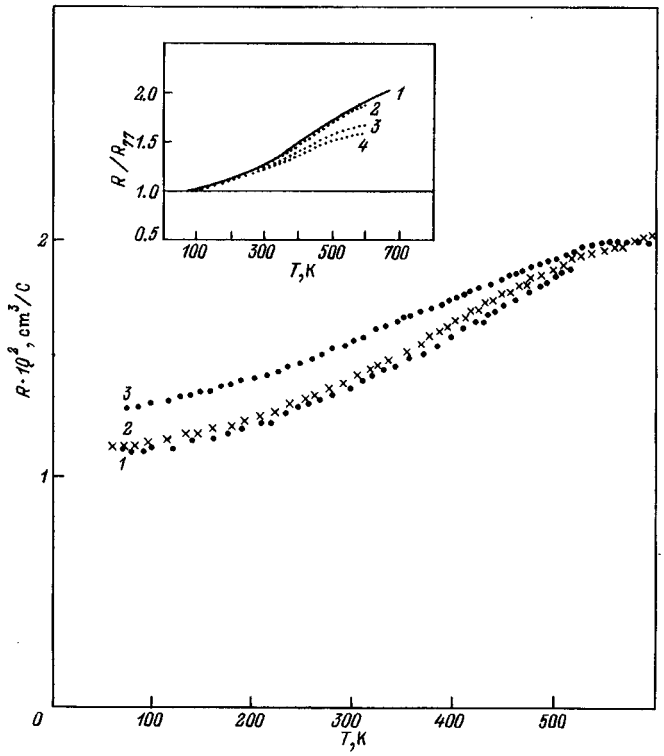

FIG. 2. Temperature dependence of the Hall coefficient: *1* — PbSe, *2* — $Pb_{0.99}Mn_{0.01}Se$, *3* — $Pb_{0.95}Cd_{0.05}Se$ ($N=2.5$ at.%). Inset: Temperature dependence of the ratio of the Hall coefficient to the value at 77 K: *1* — PbSe, *2* — $Pb_{0.99}Mn_{0.01}Se$, *3* — $Pb_{0.95}Mn_{0.05}Se$, *4* — $Pb_{0.95}Cd_{0.05}Se$ ($N=1.5$ at.%).

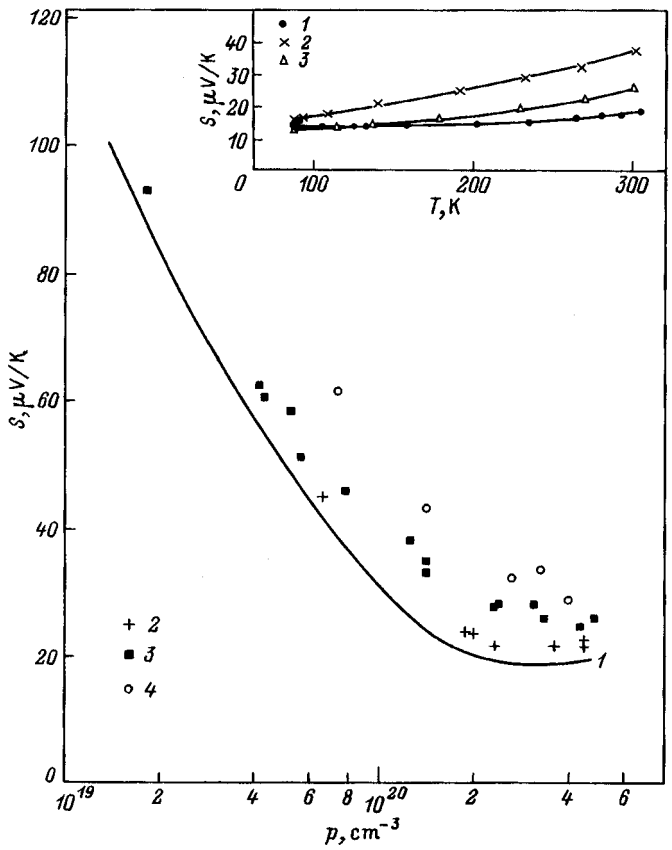

FIG. 3. Density dependence of the thermoelectric power at 300 K: *1* — PbSe, *2* — $Pb_{0.99}Mn_{0.01}Se$, *3* — $Pb_{0.95}Mn_{0.05}Se$, *4* — $Pb_{0.95}Cd_{0.05}Se$. Inset: Temperature dependence of the thermoelectric power: *1* — PbSe, *2* — $Pb_{0.95}Mn_{0.05}Se$, *3* — $Pb_{0.95}Cd_{0.05}Se$ ($N=2$ at. %).

at 85 K the increase in S in solid solutions is much smaller (see the inset in Fig. 3), and the maximum growth of the order of 350 K is noted at T. Values of S which are higher than the computed values at $T>300$ K are also characteristic of *p*-type PbSe. The decrease in the carrier density in accordance with the temperature increase of R cannot explain this effect.[6] The parameter which is most sensitive to the appearance of localized holes is the mobility. Its decrease in *p*-type PbSe (relative to the values for electrons)[6] and the even larger decrease in solid solutions were noted even at low temperatures and low doping levels.

The experimental data presented above combined with data obtained previously for other materials[1–4] give a systematic picture of the acceptor doping of PbTe-type materials with sodium. This picture can be briefly described as follows:

1. In lead chalcogenides, the acceptor action of the Na impurity, ordinarily described by the ratio of one free hole per impurity atom, is weakened, and together with free holes there exist holes which are localized at defects. The fraction of the latter is determined by the composition of the material (the presence of additional impurities), the acceptor doping level, and temperature.

2. The introduction of isovalent impurities, which substitute for lead (isovalent doping), increases the density of localized holes at low temperatures.

3. In the case of Cd and Mn in PbSe the relative fraction of localized carriers does not increase with the density N. In the case of Sn in PbTe, this fraction increases, which results in pinning of the Fermi level. Apparently, the hole density in PbTe changes similarly even when Cd is introduced.

4. An increase in the temperature gives rise to further hole localization in Na-doped materials. In the absence of isovalent impurities, this process proceeds more intensively at low temperatures. The Hall carrier density in a binary compound and in the solid solutions studied stops decreasing when the same temperature is reached; the value of the temperature is determined by the composition of the matrix (PbTe–400 K, PbSe–660 K), and only in weakly doped materials this occurs earlier as a result of the onset of the intrinsic conduction. At all doping levels the Hall carrier density decreases by not more than a factor of 2.

5. Hole localization gives rise to a decrease in the mobility and an increase in the thermoelectric power, i.e., a substantial change in the character of the hole scattering.

To explain the experimental data obtained by us, we invoke a model of acceptor doping of lead chalcogenides which was proposed in Ref. 2. When Na is introduced, two Na atoms in combination with a different number of chalcogen atoms can produce completely saturated bonds only at one chalcogen atom (according to a formula of the type $2NaTe = Na_2Te + Te$). It is possible that they occupy interstitial positions, which give rise to a metal vacancy, that forms together with Na atoms a neutral complex. Unsaturated bonds of a different chalcogen atom give rise to the acceptor action, which produces holes in the valence band: The isolated vacancies which are formed are double acceptors. Although metal vacancies can produce quasilocal states in the valence band,[7] they cannot be identified with observed localization centers, since the hole localization effect in this case would be equally characteristic of the binary compounds and the solid solutions under study.

The localization of two holes at a defect can be represented as the loss of two electrons from one of the chalcogen ions and the formation of a neutral atom. A neutral chalcogen atom occupies a metal vacancy, forming in this manner an antistructural defect. As a result of one such transition, two vacancies vanish in the metal sublattice (one occupied by a chalcogen atom and the other, from which this atom is lost, is compensated by the chalcogen vacancy which is formed). The radii of the neutral chalcogen atoms are relatively small (Te — 1.7 Å, Se — 1.6 Å) compared with the radii of the doubly charged ions, from which the sublattice of the chalcogen consists: Te(-2) — 2.1 Å, Se(-2) — 1.98 Å.[8] This facilitates the arrangement of these atoms in antistructural positions.

An increase in T and the introduction of isovalent impurities with relatively small ionic radii at metal sites produce such a rearrangement of the defects with the formation of an antistructural chalcogen. The ionic radii of Sn$(+2)$, Cd$(+2)$, and Mn$(+2)$ are 1.02 Å, 1.03 Å, and 0.91 Å, while the ionic radius of the Pb$(+2)$ ion which they replace equals 1.26 Å.[8]

Therefore, when the materials are doped with sodium, two types of structural defects are formed. Defects of one type (Pb vacancies) produce free holes and defects of the second type (antistructural) produce localized holes. As T increases, defects of one type restructure into defects of the other type; the total defect concentration in this case remains the same, being a function only of the sodium concentration. Each antistructural defect formed as a result of the introduction of four Na atoms binds two holes and two holes remain in the valence band. If antistructural defects predominate, then the efficiency of the acceptor action of Na decreases by a factor of 2, which agrees with experiment.

The antistructural defect which is formed is a hole localization center which forms resonance states that scatter holes if the energy of these states is split from the Fermi level by an amount of the order of kT. The number of such defects depends on the composition of the material and on the temperature. The experimental circumstance that the presence of localization centers is manifested in a wide range of Na densities suggests that as N increases, the resonance states shift into the valence band together with the Fermi level. Hole scattering by defects is of a resonance nature.[9]

Doping of lead chalcogenides with a different acceptor impurity, for example, thallium, has a different mechanism. Thallium doping of PbTe gives one hole per impurity atom, and no weakening of the activity of Tl in the presence of Sn is observed right up to densities of 10^{20} cm^{-3}, at which the filling of the impurity band of Tl starts.[10] The situation remains the same when 5 mol% PbS is added to PbTe.[11]

The new view of the hole conduction mechanism in Na-doped lead chalcogenides could also be helpful in discussing the properties of SnTe and GeTe, which previously were attributed, just as in lead chalcogenides, to the existence of a heavy-hole valence band.

[1] L. V. Prokof'eva, M.N. Vinogradova, and S. V. Zarubo, Fiz. Tekh. Poluprovodn. **14**, 2201 (1980) [Sov. Phys. Semicond. **14**, 1304 (1980)].

[2] G. T. Alekseeva, B. G. Zemskov, P. P. Konstantinov, L. V. Prokof'eva, and K. T. Urazbaeva, Fiz. Tekh. Poluprovodn. **26**, 358 (1992) [Sov. Phys. Semicond. **26**, 202 (1992)].

[3] L. V. Profof'eva, S. V. Zarubo, F. S. Nasredinov, and P. P. Seregin, JETP Lett. **33**, 12 (1981).

[4] A. J. Crocker and L. M. Rogers, J. de Physique, Suppl. 11–12, 4 (1968).

[5] A. J. Crocker, J. Phys. Chem. Sol. **28**, 1903 (1967).

[6] E. A. Gurieva, L. V. Prokof'eva, Yu. I. Ravich, and Kh. R. Maĭlia, Fiz. Tekh. Poluprovodn. **20**, 1823 (1986) [Sov. Phys. Semicond. **20**, 1144 (1986)].

[7] B. A. Volkov and O. A. Pankratova, Zh. Éksp. Teor. Fiz. **88**, 280 (1985) [Sov. Phys. JETP **61**, 164 (1985)].

[8] G. V. Voĭtkevich *et al.*, *Short Handbook of Geochemistry* [in Russian], Nedra, Moscow, 1970.

[9] V. I. Kaĭdanov, S. A. Nemov, and Yu. I. Ravich, Fiz. Tekh. Poluprovodn. **26**, 201 (1992) [Sov. Phys. Semicond. **26**, 113 (1992)].

[10] V. I. Kaĭdanov, S. A. Nemov, and A. M. Zaĭtsev, Fiz. Tekh. Poluprovodn. **19**, 268 (1985) [Sov. Phys. Semicond. **19**, 165 (1985)].

[11] S. A. Nemov, F. S. Nasredinov, R. V. Parfen'ev, M. K. Zhitinskaya, A. V. Chernyaev, and D. V. Shamshur, Fiz. Tverd. Tela (St. Petersburg) **38**, 550 (1996) [Phys. Solid State **38**, 301 (1996)].

Translated by M. E. Alferieff

Effect of fast-neutron irradiation on the photoluminescence of *n*-type GaAs(Te) crystals

K. D. Glinchuk and A. V. Prokhorovich

Institute of Semiconductor Physics, Ukrainian National Academy of Sciences, 252028 Kiev, Ukraine
(Submitted April 3, 1996; accepted for publication July 8, 1996)
Fiz. Tekh. Poluprovodn. **31**, 533–535 (May 1997)

The effect of neutron irradiation ($\Phi = 10^{14} - 10^{15}$ cm^{-2}) and subsequent anneals ($T = 100 - 750$ °C) on the photoluminescence of strongly tellurium-doped *n*-type GaAs crystals ($n_0 \simeq 2 \times 10^{18}$ cm^{-3}) has been investigated. It is shown that the indicated radiation-thermal action with increasing anneal temperature results at first (at $T \simeq 300$ °C) in the appearance of an intense luminescence band with a radiation maximum near 1.35 eV and then (at $T > 550$ °C) in a decrease of the intensity of the band. This is due to radiation-stimulated production of $V_{Ga}Te_{As}V_{As}$ pairs at moderate heating temperatures and subsequent dissociation of these pairs at elevated heating temperatures. © *1997 American Institute of Physics.* [S1063-7826(97)00805-3]

Studying the effect of fast-neutron irradiation and subsequent anneals [referred to below as radiation-thermal action (RTA)] on the photoluminescence (PL) of *n*-type GaAs(Te) crystals, we discovered nontrivial changes in their PL spectra (RTA stimulated appearance of a luminescence band with a radiation maximum near 1.35 eV and nonmonotonic variation of its intensity with heating temperature). In the present paper we shall examine these effects as well as a model which explains them.[1)]

1. EXPERIMENTAL PROCEDURE

In the experiments we used *n*-type GaAs crystals (equilibrium electron density $n_0 \simeq 2 \times 10^{18}$ cm^{-3}) which were strongly doped with tellurium ($N_{Te} \simeq 2 \times 10^{18}$ cm^{-3}).

The *n*-type GaAs crystals were irradiated with fast neutrons [average neutron energy $E = 2$ MeV, integrated irradiation dose $\Phi = 10^{14} - 10^{15}$ cm^{-2}, density of irradiation-produced point defects (also isolated in clusters) $n_d(0) \simeq (50\ \text{cm}^{-1})\Phi$] at 20 °C. The temperature of the crystals could reach 60 °C at the maximum irradiation dose. Isochronous annealing for 1 h followed by quenching of the irradiated and unirradiated control *n*-GaAs(Te) crystals were performed at $T = 100 - 750$ °C under conditions which prevented different contaminants, including copper atoms, from entering the crystals [the density of radiation defects (RDs) in the annealed irradiated crystals $n_d < n_d(0)$]. Irradiation and subsequent annealing changed n_0 very little, because $n_d(0) \ll N_{Te}$.

The PL of the *n*-type GaAs crystals (its intensity I) was excited with a He–Ne laser radiation (photon energy $h\nu_e = 1.96$ eV, excitation intensity $L = 10^{18}$ photons/cm$^2 \cdot$s). The excitation did not change the conductivity of the crystals much. The PL spectra were measured at 77 K in the region where I is a linear function of L, i.e. in the region of linear recombination of the excess current carriers.[2]

The changes occurring in the PL spectra of *n*-type GaAs(Te) crystals at different neutron-irradiation doses and subsequent anneal temperatures were studied. Annealing of the unirradiated *n*-type GaAs(Te) crystals produced virtually no changes in their PL spectra, i.e., it changed little the density of the ''growth'' centers of radiative and nonradiative recombination of excess current carriers in the crystals and did not produce new centers (Fig. 1). In analyzing the data we focused our attention mainly on the most interesting region of the RTA, associated with the generation of new centers of luminescence. The radiation itself did not produce such centers (Fig. 1). Therefore, we shall not study the trivial changes produced by the indicated RTA in the PL intensities of *n*-GaAs(Te) crystals as a result of the generation and annihilation of radiation defects consisting of efficient centers of nonradiative recombination of excess current carriers (see, for example, Refs. 1–3).

2. RESULTS AND DISCUSSION

The low-temperature ($T = 77$ K) PL spectra of the control and fast-neutron irradiated *n*-GaAs(Te) crystals after heating at 500 °C for 1 h are shown in Fig. 1. As one can see, irradiation and subsequent annealing of *n*-GaAs(Te) crystals result in the appearance of an intense ''impurity'' luminescence band with a radiation maximum $h\nu_m$ near 1.35 eV (this PL band is not observed in heated unirradiated crystals) and very small changes in the intensities of the impurity luminescence band with $h\nu_m \simeq 1.20$ eV and the ''intrinsic'' luminescence band with $h\nu_m \simeq 1.52$ eV. As is well known,[4–6] these impurity luminescence bands are due to the radiative recombination of electrons in pairs, which consist of a gallium vacancy V_{Ga}, arsenic vacancy V_{As}, and tellurium atoms Te_{As} in an arsenic sublattice of gallium arsenide, namely, the pairs $V_{Ga}Te_{As}V_{As}$ and $V_{Ga}Te_{As}$, respectively. Therefore, annealing of *n*-GaAs(Te) crystals irradiated with fast neutrons results in the production of $V_{Ga}Te_{As}V_{As}$ pairs and changes little the density of $V_{Ga}Te_{As}$ pairs [the density of RTA stimulated pairs $V_{Ga}Te_{As}$ (the latter undoubtedly form as a result of the interaction of RD gallium vacancies freed from clusters with isolated tellurium atoms; see below) is lower than the density of growth (''congenital'') $V_{Ga}Te_{As}$ pairs].

The changes in the densities $N_{1,2}$ and $N_{1.35}$ of $V_{Ga}Te_{As}$ and $V_{Ga}Te_{As}V_{As}$ pairs, respectively, during isochronous annealing of *n*-GaAs(Te) crystals irradiated with different

 1063-7826/97/050449-03$10.00

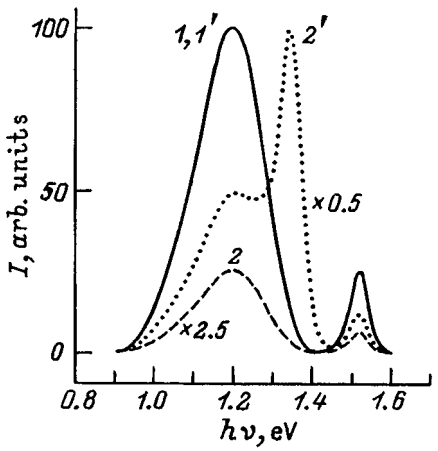

FIG. 1. PL spectra of *n*-type GaAs(Te) crystals: Initial (*1*), heated at 500 °C for 1 h (*1′*), irradiated with a fast-neutron flux $\Phi=10^{15}$ cm^{-2} (*2*), and then heated at 500 °C 1 h (*2′*). The measurements were performed at a temperature of 77 K.

fluxes of fast neutrons are shown in Fig. 2.[2)] As one can see, annealing of irradiated *n*-GaAs(Te) crystals changes the density of $V_{Ga}Te_{As}$ pairs very little; the growth pairs $V_{Ga}Te_{As}$, whose density $N_{1,2}(0)\simeq 10^{16}$ cm^{-3} at any T, dominate. Annealing at high heating temperatures results in the production of $V_{Ga}Te_{As}V_{As}$ pairs. A quasistationary density of $V_{Ga}Te_{As}V_{As}$ pairs was reached in practice for the heating times employed. The maximum production of $V_{Ga}Te_{As}V_{As}$ pairs is observed at $T=T^*\simeq 550$ °C [$N_{1.35}(\max)\simeq 2\times 10^{16}$ cm$^{-3}\ll n_d(0)$ with $\Phi=10^{15}$ cm^{-2}], and at $T>T^*$ thermal dissociation of the pairs starts to play a role, resulting in a corresponding decrease in the density of these pairs. The generation of $V_{Ga}Te_{As}V_{As}$ pairs increases with increasing neutron irradiation dose, confirming their radiation-stimulated nature.

Let us now discuss the results presented above.

Undoubtedly, under the RTA which we are studying $V_{Ga}Te_{As}V_{As}$ pairs can form as a result of interaction of the neutron-irradiation stimulated mobile arsenic vacancies with growth pairs $V_{Ga}Te_{As}$ or mobile arsenic and gallium vacancies with isolated tellurium atoms. Evidently, isolated mobile arsenic and gallium vacancies appear when neutron-irradiation-produced RD clusters decompose, because the radiation-produced point defects are concentrated mainly[3)] in the latter.[1,3,7–9]

Apparently, the first process (the pair conversion process $V_{Ga}Te_{As}+V_{As}\rightarrow V_{Ga}Te_{As}V_{As}$) is inefficient because of the following factors. As estimates show (see footnote 2), the density of growth pairs $V_{Ga}Te_{As}$ is comparable to the density of RTA stimulated pairs $V_{Ga}Te_{As}V_{As}$, specifically, their maximum density $N_{1.35}(\max)$. For this reason, a direct conversion of $V_{Ga}Te_{As}$ pairs into $V_{Ga}Te_{As}V_{As}$ pairs as a result of their interaction with arsenic vacancies should result in an appreciable decrease in the density of $V_{Ga}Te_{As}$ during RTA. However, this is not observed experimentally — the density of the pairs $V_{Ga}Te_{As}$ remains nearly constant (Fig. 2). We consider the second process ($Te_{As}+V_{As}+V_{Ga}\rightarrow V_{Ga}Te_{As}V_{As}$) to be more efficient (this process dominates, because $N_{Te}\gg N_{1,2}$). In this case isolated tellurium atoms at first act as sinks for RD arsenic vacancies freed from *R* clusters and then for RD gallium vacancies freed from *Q* clusters. This is confirmed by the fact that the decomposition of RD *R* and *Q* clusters (this occurs for $T\geqslant 300$ and 450 °C, respectively[1,3,7–9]) and radiation-stimulated production of the pairs $V_{Ga}Te_{As}V_{As}$ occur in the same temperature ranges.

The comparatively narrow temperature range of the stability of the RTA stimulated pairs $V_{Ga}Te_{As}V_{As}$ (Fig. 2) is due to the relatively weak coupling between their constituent components.[11]

We can therefore draw the following conclusion.

Neutron irradiation and subsequent annealing of *n*-type GaAs crystals doped with tellurium atoms results in the production in them of relatively thermally unstable pairs $V_{Ga}Te_{As}V_{As}$. This is due to the trapping of mobile arsenic and gallium vacancies from RD *R* and *Q* clusters trapped by isolated tellurium atoms and the low binding energy between the components of the pairs $V_{Ga}Te_{As}V_{As}$. This is important for determining the nature and the migration rate of the neutron-irradiation-produced RD in gallium arsenide.[3,7–9]

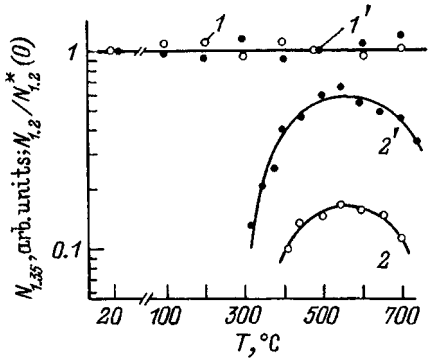

FIG. 2. Change in the density of the pairs $V_{Ga}Te_{As}$ (*1*, *1′*) and $V_{Ga}Te_{As}V_{As}$ (*2*, *2′*) during isochronous annealing ($t=1$ h) of *n*-GaAs(Te) crystals irradiated with a fast-neutron flux $\Phi=10^{14}$ (*1*,*2*) and 10^{15} cm^{-2} (*1′*, *2′*). The curves *1* and *1′* are normalized with respect to the $V_{Ga}Te_{As}$ pair density in annealed unirradiated crystals $N^*_{1,2}(0)\simeq N_{1,2}(0)$. $T=20$ °C corresponds to the unannealed crystals.

[1)] In Ref. 1 we presented data on the effect of neutron irradiation on the PL of *p*-GaAs(Zn, Te) crystals.

[2)] The relative densities of the $V_{Ga}Te_{As}$ and $V_{Ga}Te_{As}V_{As}$ pairs were found (within ±15%) by comparing the corresponding changes in the intensities of the impurity luminescence bands due to them, and the intensity of the ''intrinsic'' radiation.[1,6] The absolute values of the densities of the degenerate pairs $V_{Ga}Te_{As}$ and the maximum densities of the RTA stimulated pairs $V_{Ga}Te_{As}V_{As}$ were determined (within ±30%) by analyzing the kinetics of the quenching of the PL impurity bands induced by them.[4]

[3)] The migration rates of the radiation-stimulated arsenic and gallium vacancies for the temperatures and heating durations employed are sufficient for diffusion-limited production of $V_{Ga}Te_{As}V_{As}$ pairs.[10]

[1] E. V. Vinnik, K. D. Glinchuk, V. I. Guroshev, and A. V. Prokhorovich, Fiz. Tekh. Poluprovodn. **25**, 82 (1991) [Sov. Phys. Semicond. **25**, 48 (1991)].

[2] E. V. Vinnik, K. D. Glinchuk, V. I. Guroshev, and A. V. Prokhorovich, Fiz. Tekh. Poluprovodn. **27**, 1030 (1993) [Semiconductors **27**, 560 (1993)].

[3] L. S. Smirnov, *Problems of Radiation Technology of Semiconductors* [in Russian], Novosibirsk, 1980.

[4] K. D. Glinchuk, K. Lukat, and V. E. Rodionov, Fiz. Tekh. Poluprovodn. **15**, 1337 (1981) [Sov. Phys. Semicond. **15**, 772 (1981)].
[5] K. D. Glinchuk, A. V. Prokorovich, and N. S. Zayats, Phys. Status Solidi A **82**, 503 (1984).
[6] K. D. Glinchuk, V. F. Kovalenko, and A. V. Prokhorovich, Optoélektron. Poluprovodn. Tekhn. **22**, 46 (1992).
[7] R. Coates and F. W. Mitchell, Adv. Phys. **24**, 593 (1975).
[8] G. Dlubek and A. Krause, Phys. Status Solidi A **102**, 443 (1987).
[9] G. Dubek, A. Dlubek, R. Krause, and O. Brümer, Phys. Status Solidi A **107**, 11 (1988).
[10] K. D. Glinchuk and A. V. Prokhorovich, Kristallografiya **41**, 324 (1996) [Crystallography Rep. **41**, 306 (1996)].
[11] E. V. Vinnik, K. D. Glinchuk, V. I. Gurovev, and A. V. Prokhorovich, Fiz. Tekh. Poluprovodn. **24**, 1363 (1990) [Sov. Phys. Semicond. **24**, 856 (1990)].

Translated by M. E. Alferieff

On the relaxational characteristics and stability of a Si:H films grown at high temperatures

I. A. Kurova and N. N. Ormont

M. V. Lomonosov Moscow State University, 119899 Moscow, Russia

O. A. Golikova and V. Kh. Kudoyarova

A. F. Ioffe Physicotechnical Institute, Russian Academy of Sciences, 194021 St. Petersburg, Russia
(Submitted July 1, 1996; accepted for publication July 8, 1996)
Fiz. Tekh. Poluprovodn. **31**, 536–538 (May 1997)

Some characteristics of the photo- and thermal stability in *a*-Si:H films, which were deposited in a triode reactor at 300–390 °C and which possess different hydrogen concentrations C_{H}, have been investigated. It has been found that the equilibration temperature T_E increases as C_{H} decreases. Under prolonged illumination the photoconductivity decreases as $t^{-1/3}$ in films with high values of C_{H}. In films with a low hydrogen content the photoconductivity drops more slowly. © *1997 American Institute of Physics.* [S1063-7826(97)00905-8]

The properties of amorphous hydrated silicon (*a*-Si:H) are determined by the conditions under which the silicon is obtained, specifically, the substrate temperature T_s during film deposition. At high growth temperature the hydrogen concentration and its distribution over the volume in the films decrease.[1] Since it is indicated in a number of studies that the distribution over the volume is correlated with an increase in the stability of the material,[2,3] it is of great practical interest to investigate material obtained at high temperatures.

In the present work we investigated films prepared by rf decomposition of silane in a triode reactor with $T_s = 300-400$ °C.[4,5] Some data on the Staebler–Wronski effect for such films are presented in Refs. 6 and 7, but such investigations of the metastability of the films have not been previously performed. For comparison, an *a*-Si:H film obtained in a diode reactor with $T_s = 310$ °C and weakly compensated with boron with total density $N_{\mathrm{B}} = 2\times10^{17}$ cm^{-3} (N_{B} was determined by the SIMS method) was also investigated.

Some parameters of the experimental films are presented in Table I: ΔE_d and σ_0 were determined from the temperature dependence of the dark conductivity σ_d in the temperature range $T = 380-300$ K in accordance with $\sigma_d = \sigma_0 \exp(-\Delta E_d/kT)$ after the films were annealed at 185 °C for 60 min. The photosensitivity K, equal to the ratio of the photoconductivity σ_{ph} to the dark conductivity σ_d of an annealed film, are presented for $T = 300$ K and illumination by a halogen lamp with an infrared (IR) filter (the power density $W = 90$ mW/cm^2); the total hydrogen concentration C_{H} in the film was determined by IR spectroscopy.

The temperature dependences of the dark conductivity and photoconductivity of the experimental films are shown in Fig. 1. The measurements of σ_d were performed with decreasing temperature and the measurements of σ_{ph} were performed with increasing temperature. We see that the temperature dependence of the photoconductivity for films 1–4 has a region of weak temperature quenching, as is characteristic of *n*-type films. The photoconductivity of film 5 does not have a characteristic region of temperature quenching and increases monotonically with temperature, as is characteristic of *p*-type films. The curve $\sigma_d(T)$ for films 1 and 2 contains regions of equilibrium conductivity at temperatures $T > T_E$ (T_E is the temperature at which the measurement times and the structural relaxation times are equal to one another).[8] For these films $T_E = 110$ and 185 °C, respectively. Above these temperatures $\sigma_d(T)$ varies exponentially, irrespective of the direction and rate of change of the temperature, with a lower activation energy, and the preexponential factor σ_0 is close to the value $\sigma_{\min} = 1.5\times10^2\ \Omega^{-1}\cdot\ \mathrm{cm}^{-1}$. For film 5 only a transition to a region of equilibrium conductivity is observed; i.e., for this film $T_E > 185$ °C. For films 3 and 4 the dark conductivity varies exponentially with the same activation energy in the entire experimental temperature range. This signifies that T_E for these films lies in the region of higher temperatures: $T_E > 200$ °C. Therefore, T_E

TABLE I. *a*-Si:H film parameters.

Sample	T_s, °C	C_{H}, at. %	ΔE_d, eV $T<T_E$	σ_0, $\Omega^{-1}\cdot$cm^{-1} $T<T_E$	ΔE_d, eV $T>T_E$	σ_0, $\Omega^{-1}\cdot$cm^{-1} $T>T_E$	T_E, °C	$K=\sigma_{\mathrm{ph}}/\sigma_d$ (T=290 K)	σ_d, $\Omega^{-1}\cdot$cm^{-1} (T=290 K)
1	300	9	0.82	3×10^5	0.56	1.7×10^2	185	4.5×10^4	4×10^{-9}
2	340	20	0.71	1×10^5	0.49	1.4×10^2	110	1×10^4	1.2×10^{-7}
3	340	6	0.83	5×10^5	–	–	>200	1.5×10^5	5×10^{-10}
4	390	4	0.86	5×10^5	–	–	>200	1×19^5	1.8×10^{-10}
5	310	7	0.83	3×10^5	–	–	>185	8×10^4	2.2×10^{-10}

Note: (*1–4*)—Undoped films; *5*—boron-doped film.

 1063-7826/97/050452-03$10.00

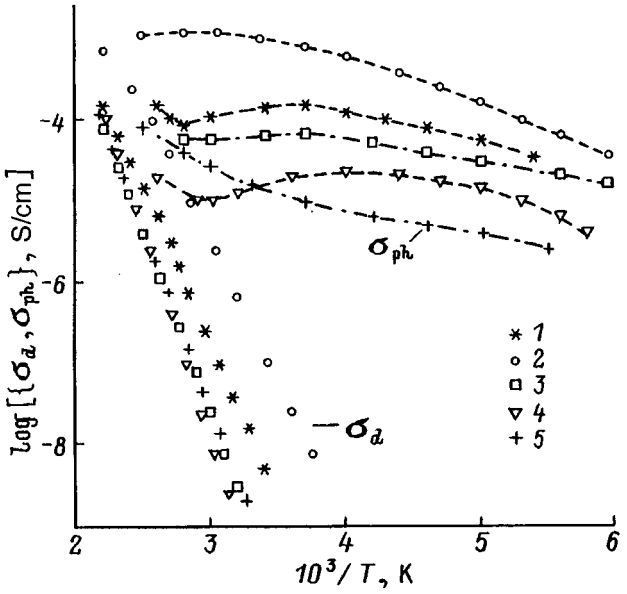

FIG. 1. Temperature dependences of the dark conductivity and photoconductivity of *a*-Si:H films. The designations correspond to the numbers of the samples in Table I.

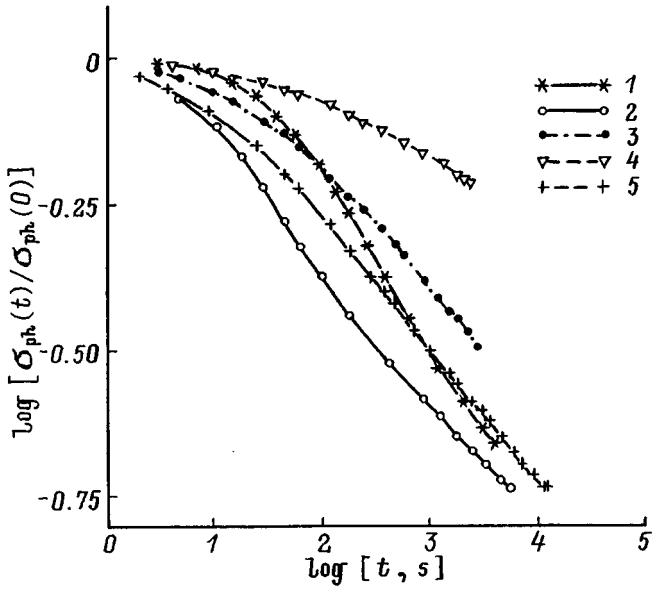

FIG. 2. Kinetics of the variation of the reduced photoconductivity for *a*-Si:H films under illumination by a halogen lamp with intensity $W=90$ mW/cm^2. The designations corresponds to the numbers of the samples in Table I.

increases with decreasing hydrogen concentration, as above in Ref. 9 on *a*-Si:H films after implantation of B and P with hydrogen concentration from 0.06 to 12 at. %. This also agrees with the increase in the rate of hydrogen diffusion in undoped *a*-Si:H films with increasing C_{H}, as observed in Ref. 10.

It can be assumed that the structural relaxation times as a function of the temperature and under the influence of light are determined by the same hydrogen diffusion process[11] and therefore the rate of formation of photoinduced dangling bonds (BBs) Si–Si in our films will be correlated with the value of T_E. The variation of the reduced photoconductivity $\sigma_{\mathrm{ph}}(t)/\sigma_{\mathrm{ph}}(0)$ with time for the experimental films in a regime of illumination at room temperature with a quartz halogen lamp with an IR filter is shown in Fig. 2. According to Ref. 12, for undoped films $\sigma_{\mathrm{ph}}(t)\sim N(0)/N(t)$, which reflects the change in the density N of dangling Si–Si bonds in time t. One can see from Fig. 2 that the rate of formation of BBs is lowest in film 4 and highest in film 2. This correlates with the structural equilibration time: This time is longest in film 4 (T_E is high) and shortest in film 2 (T_E is lowest). We note that film 2 was deposited under nonoptimal conditions and for this reason the hydrogen content in it is much higher than in other films deposited at $T_s=300-400$ °C (see Table I and Ref. 5).

The photostability of a film is estimated by the stationary density N_{st} of BBs that appears under prolonged illumination, when the rate of formation and annihilation of BBs are equal to one another. To achieve N_{st} prolonged illumination of the film is required, under our conditions up to 150–200 h. In Ref. 1 it is shown that in the model of formation of BBs by breaking of weak Si–Si bonds with recombination of electrons and holes N_{st} correlates with the initial rate of formation of BBs. According to this model, $\sigma_{\mathrm{ph}}(t)$ varies in some range of BB density as $t^{-1/3}$. We see such a dependence only for films 1 and 2, and film 2 is more stable than the film 1, since the initial rate of change of σ_{ph} in film 2 is lower. For films 3–5 $\sigma_{\mathrm{ph}}(t)\sim t^{-n}$, where $n<1/3$.

For *p*-type films the condition of inverse proportionality between the photoconductivity and the density of dangling bonds is not satisfied,[13] and therefore the time dependence $\sigma_{\mathrm{ph}}(t)$ does not reflect the rate of formation of BBs and a $t^{-1/3}$ dependence is not observed. The Fermi level E_f lies much deeper in *n*-type films 3 and 4 than in films 1 and 2. Under illumination E_f moves to the center of the band gap, which makes films 3 and 4 similar to *p*-type films, where a section with $\sigma_{\mathrm{ph}}\sim t^{-1/3}$ is not observed. However, additional investigations are being performed in order to understand more clearly the characteristic features of the kinetics of σ_{ph} in these films.

We thank A. G. Kazanskiĭ for useful discussions of the results. This work was supported by INTAS Grant N 931916 and was performed in accordance with a joint research program of Moscow State University and the A. F. Ioffe Physicotechnical Institute of the Russian Academy of Sciences.

[1] D. Caputo, G. de Cesare, F. Irrera, F. Palma, M. C. Rossi, G. Conte, G. Nobile, and G. Fameli, J. Non-Crust. Sol. **170**, 278 (1994).
[2] D. E. Carlson, Appl. Phys. A **41**, 305 (1986).
[3] M. Rondo and R. H. Morigaku, J. Non-Cryst. Sol. **137/138**, 247 (1991).
[4] O. A. Golikova, M. M. Kazanin, M. M. Mezdrogina, V. Kh. Kudoyarova, K. L. Sorokina, and U. S. Babakhodzhaev, Fiz. Tekh. Poluprovodn. **23**, 1737 (1989) [Sov. Phys. Semicond. **23**, 1076 (1989)].
[5] O. A. Golikova, M. M. Kazanin, O. I. Kon'kov, V. Kh. Kudoyarova, and E. I. Terukov, Fiz. Tekh. Poluprovodn. **27**, 263 (1993) [Semiconductors **27**, 260 (1993)].
[6] O. A. Golikova, R. G. Ikramov, M. M. Kazanin, and M. M. Mezdrogina, Fiz. Tekh. Poluprovodn. **27**, 263 (1993) [Semiconductors **27**, 265 (1993)].
[7] O. A. Golikova, R. G. Ikramov, and M. M. Kazanin, J. Non-Cryst. Sol. **164–166**, 395 (1993).
[8] R. A. Street, J. Kakalios, and T. M. Hayer, Phys. Rev. B **34**, 3030 (1986).

[9] S. M. Pietruszko, S. Olszewski, and A. V. Zherzdev, Solid Status Phenom. **44–46**, 695 (1995).
[10] R. Shinaz, J. Shinaz, H. Sia, and X. L. Wu, Phys. Rev. B **47**, 9361 (1993).
[11] R. A. Street. Physica B **170**, 69 (1991).
[12] M. Stutzmann, W. B. Jackson, C. C. Tsai, Phys. Rev. B, **32**, 23 (1985).
[13] A. G. Kazanski and S. V. Kuznetsov, Phys. Status Solidi B **168**, k19 (1991).

Translated by M. E. Alferieff

The properties of low-threshold heterolasers with clusters of quantum dots

S. V. Zaĭtsev,[a] N. Yu. Gordeev, V. M. Ustinov, A. E. Zhukov, A. Yu. Egorov, M. V. Maksimov, A. F. Tsatsul'nikov, N. N. Ledentsov, P. S. Kop'ev, and Zh. I. Alferov

A. F. Ioffe Physicotechnical Institute, Russian Academy of Sciences, 194021 St. Petersburg, Russia

D. Bimberg

Institute for Festkorperphysik, Technische Universitat Berlin, D-10623 Berlin, Germany
(Submitted July 4, 1996; accepted for publication July 8, 1996)
Fiz. Tekh. Poluprovodn. **31**, 539–544 (May 1997)

The properties of GaAs–AlGaAs injection heterolasers with (In, Ga)As quantum dots (QDs) depend principally on the number N of planes with quantum dots imbedded in the active region. Lasing via the ground state of an exciton in a quantum dot at room temperature has been realized in structures with $N>3$. For $N=1$ at 300 K lasing occurs via an excited state of an exciton in a quantum dot or via a state of the wetting layer. As the number of planes with quantum dots increases, the threshold current density decreases and the differential quantum efficiency increases. The lowest threshold current density 97 A/cm^2 ($\lambda=1.05$ μm, 300 K) was obtained in structures with maximum N ($N=10$). © *1997 American Institute of Physics.* [S1063-7826(97)01005-3]

The advent of a new generation of injection lasers — quantum dot (QD) lasers — has opened up new possibilities for radically decreasing the threshold current and increasing its temperature stability and improving the dynamical and spectral characteristics of heterostructure lasers. In Ref. 1 it was shown that in injection heterolasers with a single plane of QDs at low temperatures it is possible to achieve lasing via the ground state of an exciton in a quantum dot and ultrahigh temperature stability of the threshold current (the characteristic temperature $T_0=350$ K) in a wide temperature range (50–150 K). By increasing the radiation exit losses, the possibility of narrowing the gain spectrum has been demonstrated in these structures and a lasing regime in a single longitudinal mode has been achieved.[2]

At the same time, the thermal emission of carriers from quantum dots at near-room temperatures made it necessary, under conditions of the same losses, to increase the injection current in order to maintain the lasing regime and to shift the lasing wavelength in the direction of high energies relative to the ground state of an exciton in a QD. Lasing was realized at room temperature at energies near the energy of the so-called wetting layer, unavoidable for a Stronskiĭ–Krastanov growth mechanism characteristic of InGaAs/GaAs. In a preceding work[3] it was shown that increasing the number of planes with QDs to three in a structure with an array of vertically coupled quantum dots makes it possible to achieve lasing via the ground state of a QD right up to room temperature. At the same time, the threshold current density obtained at 300 K in the indicated work was quite high ($\sim$700 A/cm^2).

In the present work we investigated the possibilities for further improving the characteristics of heterolasers based on structures with quantum dots by optimizing the geometry of the structures. The structures were grown by molecular-beam epitaxy on GaAs (100) substrates doped with silicon. The growth conditions corresponded to those described in Refs. 4 and 5. Laser structures with InAs and InGaAs quantum dots were investigated. The number N of planes with quantum dots was equal to 1, 3, 6, and 10. Samples with a strip geometry and samples with total internal reflection with a reentrant mode (quadricleaved samples) were investigated.

The PL spectra of a sample with vertically coupled QDs with $N=10$ planes are shown in Fig. 1. At low excitation

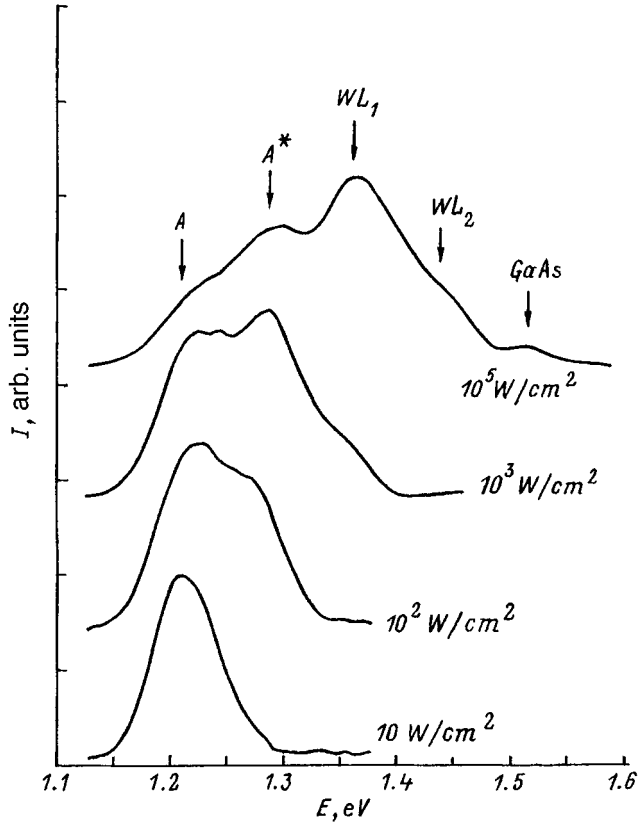

FIG. 1. Photoluminescence spectra of a sample with vertically coupled quantum dots.

 1063-7826/97/050455-05$10.00

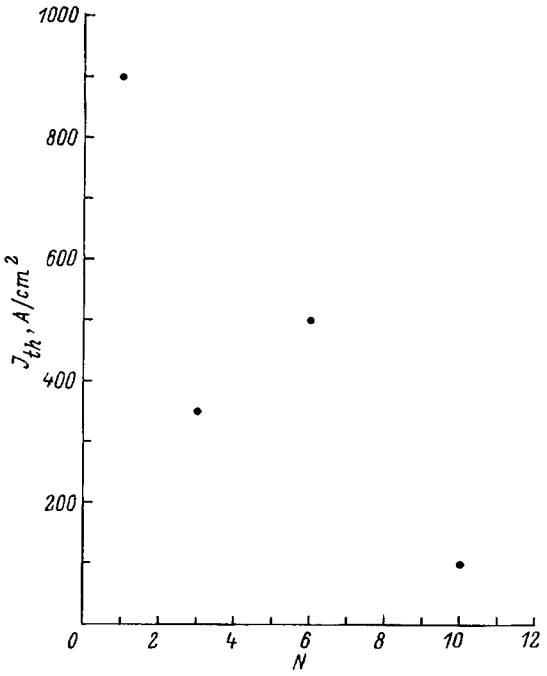

FIG. 2. Threshold current density versus the number of layers in samples with a re-entrant mode.

densities the PL spectrum contains an intense line (A) due to recombination via the ground state of an exciton in vertically coupled quantum dots. The half-width of the line, 40–60 meV, and is determined by the statistical size distribution of the dots. The position of the PL peak is shifted strongly in the long-wavelength direction compared with the computed energy of the optical transition for an InGaAs well of equivalent thickness. The line A remains dominant right up to room

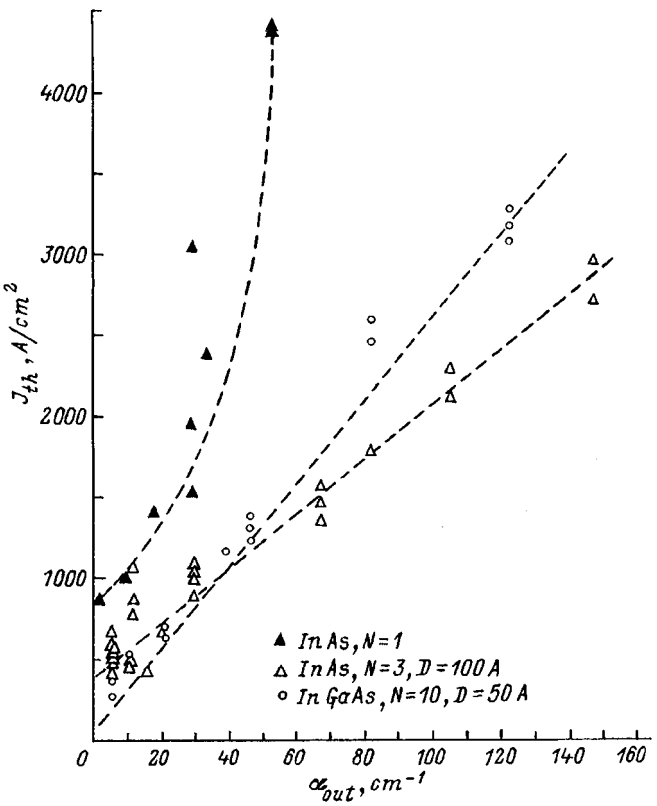

FIG. 4. Threshold current density versus radiation exit losses from the cavity.

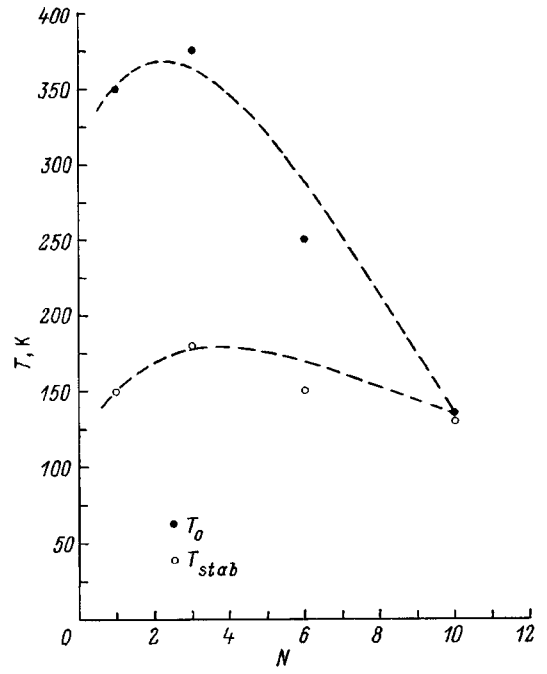

FIG. 3. T_0 in a temperature range of high threshold current density stability and the upper limit of this range (T_{stab}) versus the number of layers in samples with a re-entrant mode.

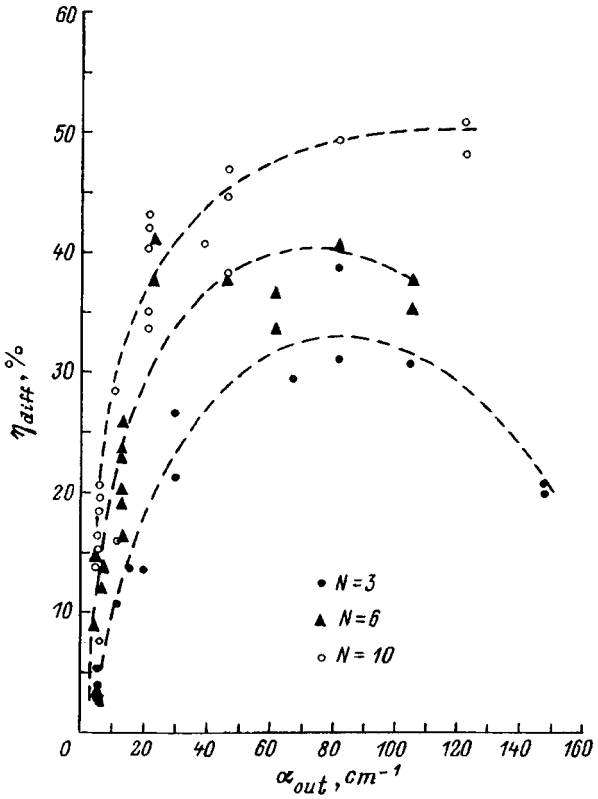

FIG. 5. Differential quantum efficiency versus radiation exit losses from the cavity.

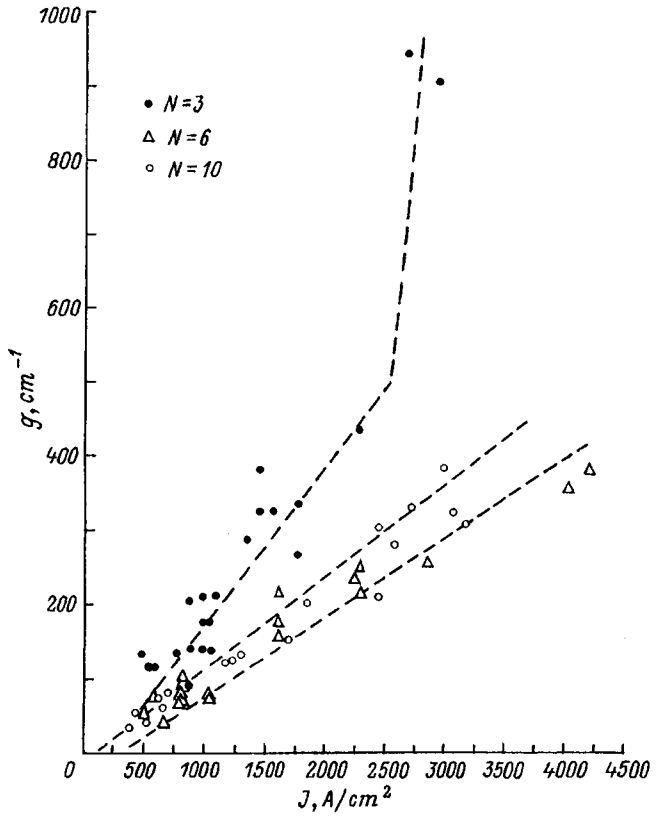

FIG. 6. Gain versus pump current density.

temperature even at high excitation densities (10^2 W/cm^2). At higher excitation densities (10^3 W/cm^2) a line A^* which is associated with the excited state of an exciton, appears in the spectrum. At ultrahigh excitation densities (10^5 W/cm^2) luminescence from quantum dots saturates and lines due to optical transitions associated with excitons localized in the wetting layer ($WL1$ and $WL2$) start to dominate in the spectrum. The interpretation of the nature of the lines A, A^*, $WL1$, and $WL2$ is confirmed by comparing the luminescence, luminescence excitation, and calorimetric absorption spectra, as well as the computational results.[6–8]

The threshold current density J_{th} of the lasers as a function of N is shown in Fig. 2. We attribute some of the increase in J_{th} for $N=6$ to a decrease in the GaAs interlayer thickness to 5 nm. For the InAs dots employed in the present structure this apparently resulted in extreme stresses in the active region and local formation of defects and some irreproducibility of the results for the present structure.

A further increase in the number of planes with QDs up to 10 but using InGaAs based dots made it possible to achieve in the lasers with a re-entrant mode a record high, for lasers of this spectral range (1.05 μm), threshold current density at 300 K (97 A/cm^2). By growing self-aligned QDs it is possible to obtain clusters of tunneling-coupled quantum dots, where the dots lying above one another comprise a single quantum-mechanical object.

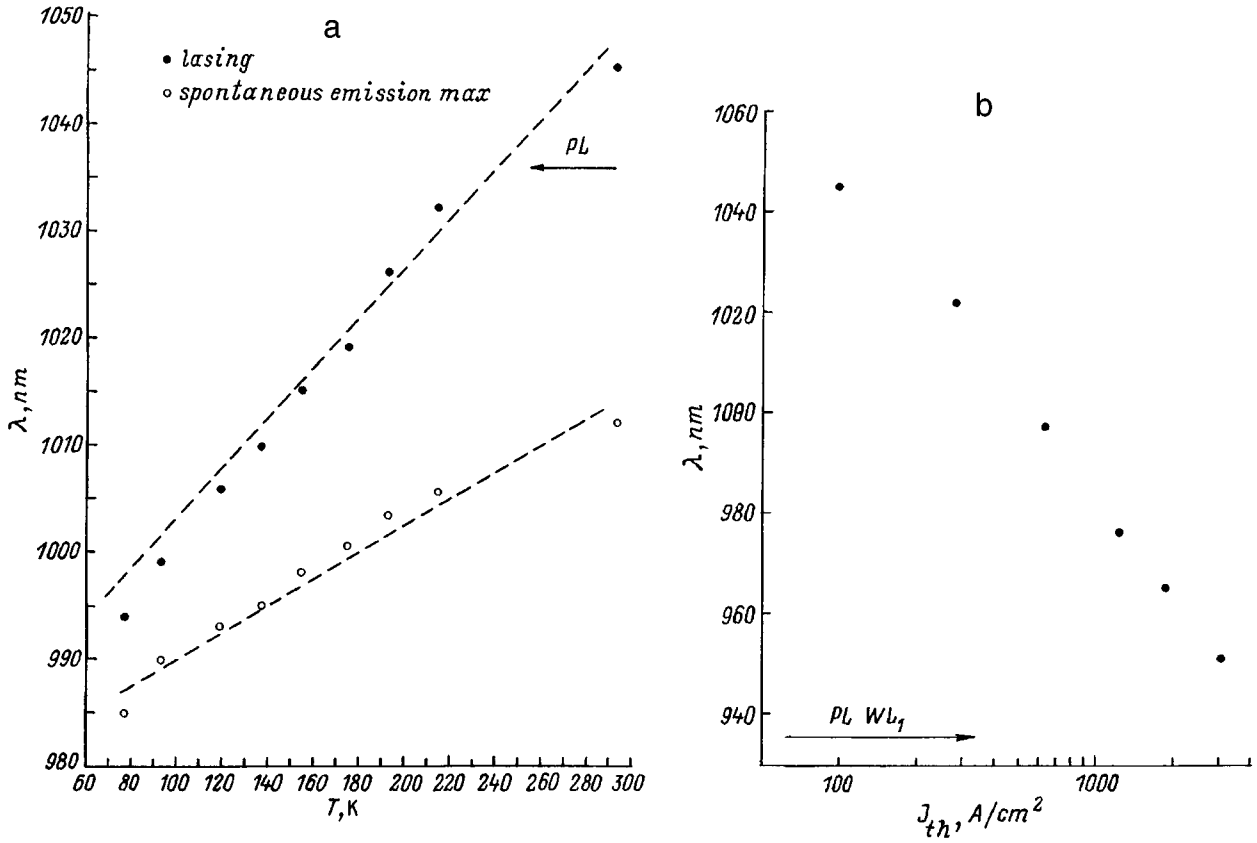

FIG. 7. a — Lasing wavelength and spontaneous emission maximum versus temperature in a sample with a re-entrant mode based on a structure with $N=10$. b — Lasing wavelength versus threshold current density for a strip laser based on a structure with $N=10$.

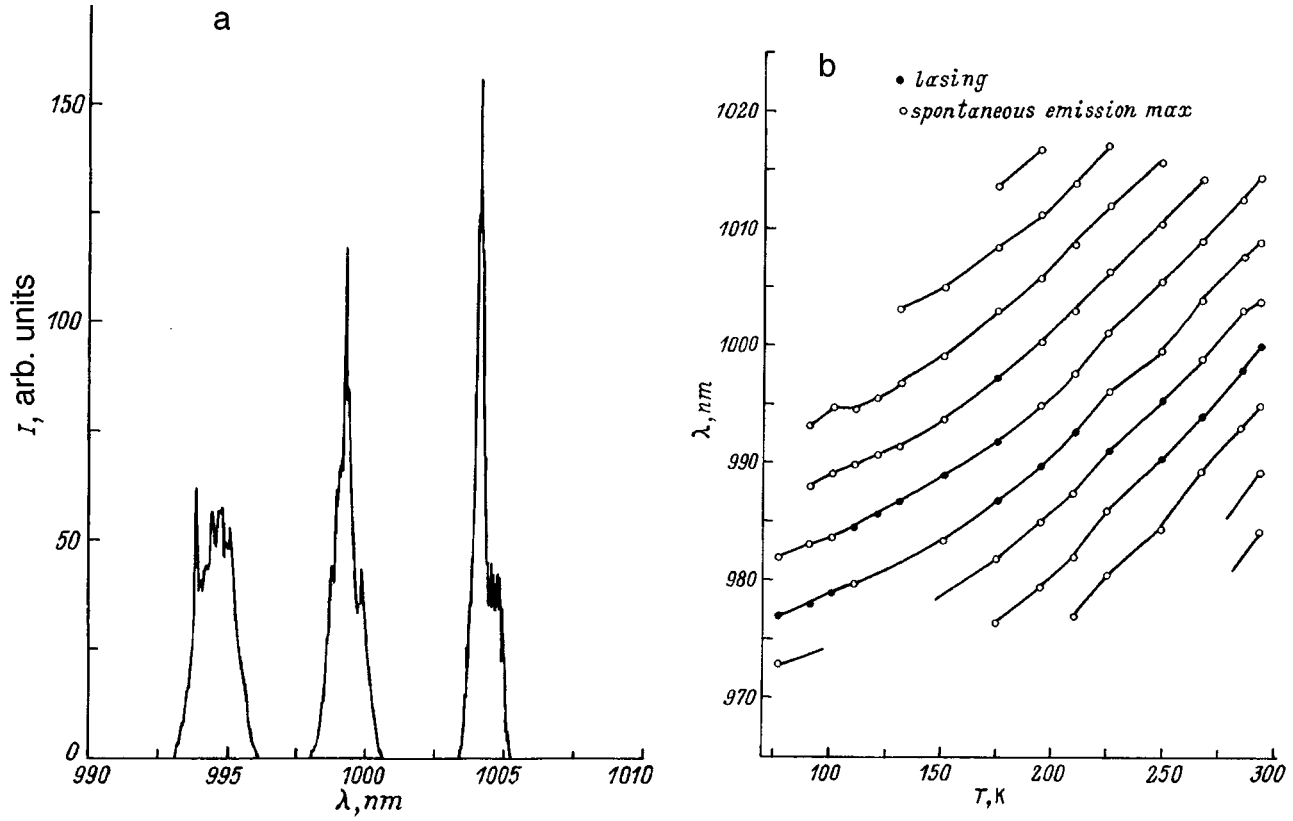

FIG. 8. a — Emission spectrum of a strip laser based on a structure with $N=6$ and $J=1.1J_{th}$ at room temperature. b — Lasing wavelength versus temperature for a strip laser based on a structure with $N=6$.

As follows from Fig. 3, increasing N to 3 slightly increases the characteristic temperature T_0 (from 350 to 380 K) at low observation temperatures. A further increase in the number of layers and (or) decrease of the distance d between the planes, however, results in a narrowing of the range of high stability temperature. This effect is directly related to the appearance of a miniband of allowed states instead of discrete levels, characteristic of single quantum dots. The values of T_0 in this range become less reproducible or meaningless. For example, for $N=6$ and $N=10$ even a section of negative T_0 (decrease of J_{th} with increasing T) is observed in the low-temperature region; we attribute this to carrier evaporation from small dots and carrier recapture by large dots. As a result, the gain for lasing through the ground state increases slightly. At $T=120$ K we obtained for a structure with $N=10$ a threshold current density $J_{th}=18$ A/cm^2, which is an absolute record-high value for a quantum-dot laser.

Curves of the threshold current density versus radiation exit losses are shown in Fig. 4. As one can see, a sharp superlinear growth of J_{th} with increasing losses is observed in a structure with $N=1$. In contrast, in structures with multiplied dots the dependence is linear in nature right up to large losses. It should be noted that this character is atypical of structures with a quantum well, where superlinear growth is also observed. A structure with ten quantum-dot planes gives the largest slope.

Curves of the differential quantum efficiency versus the radiation exit losses are shown in Fig. 5. It should be noted that as the number of planes with quantum dots increases, the differential quantum efficiency also increases. The best values were obtained for a structure with $N=10$.

The integrated gain at the lasing threshold, estimated by the method described in Ref. 2, is shown in Fig. 6. It follows from the calculation that structures with $N=3$, 6, and 10 demonstrate much larger gains than a structure with $N=1$. For $N=6$ and 10 the dependence is monotonic, and for $N=3$ a characteristic break associated with a transition to lasing via a state of the wetting layer at a wavelength near 933 nm is observed, just as previously for lasers with a single plane with QDs obtained from organometallic compounds by gas-phase epitaxy (OM GPE).[3] This transition is not observed for structures with $N=6$ and 10. Therefore, the maximum achieved gain in structures with a set of planes with QDs equals about 300 cm^{-1}. For $N=6$ and 10 gain saturation is not observed at least up to 4.5 kA/cm^2.

To calculate the integral gain we proceeded from the standard assumption made for laser structures that the internal quantum yield of radiative recombination is close to 1. Since the waveguide and emitter layers were identical in all structures described, the degree of localization of the optical radiation in the waveguide region was not varied.

The temperature dependence of the lasing wavelength for a structure with $N=10$ with long cavity lengths or in samples with a re-entrant mode is always monotonic. The lasing energy equals, within several meV, the energy of the maximum of the photoluminescence line of quantum dots with low and moderate densities of excitation due to recom-

bination of the ground state of excitons in QDs (Fig. 7a). As already mentioned, an increase the radiation exit losses increases J_{th}. Furthermore, a monotonic short-wavelength shift of the lasing line is observed. The dependence of the lasing wavelength on J_{th} is shown in Fig. 7b. The monotonic character of these dependences shows that in the lasers investigated lasing occurs through the state of a QD in a wide range of temperatures (right up to room temperature) and in the entire range of threshold current densities.

The short-wavelength shift of the lasing line agrees with the monotonic shift of the photoluminescence line observed at high excitation densities. This shift is related to the filling of the excited states of an exciton in QDs, which give rise to radiation in a shorter wavelength range of the spectrum. As follows from Fig. 7b, however, the lasing wavelength for a structure with $N=10$, in contrast to structures with $N=1$ and $N=3$, does not reach the wavelength corresponding to the wetting layer (933 nm) even for $J=4$ kA/cm^2.

In Ref. 2, narrowing of the radiation spectrum with decreasing cavity length and therefore with high threshold current densities was observed in a laser with a single plane of QDs. For low current densities the gain spectrum remains wide. As already noted for lasers with QDs,[3] this could result in an unusually wide lasing spectrum at room temperature. The effect is explained by the absence of exciton and carrier transport between neighboring quantum dots and their size dispersion. For MBE lasers, the broadening of the lasing spectrum is more strongly expressed for structures with large N, since for such lasers a regime of lasing via the ground state of an exciton in QDs, which has the highest spatial localization, is realized.

Since the waveguide of strip lasers of width 40–60 μm admits the existence of many transverse modes, in separate cases lasing in several transverse modes arises simultaneously near the lasing threshold. The radiation spectrum of a laser based on a structure with $N=6$ with $J=1.1J_{th}$ is shown in Fig. 8a. The temperature dependence of the lasing wavelength at threshold for the same sample is shown in Fig. 8b. The maxima of the spontaneous emission spectrum, which correspond to transverse modes of the laser, are indicated separately. Their temperature dependence can be explained by the characteristic features of the transverse spreading of carriers in the top layers of the laser with oxide–strip construction.

In summary, structures with vertically coupled quantum dots can be used to overcome the gain saturation effect, to increase T_0 near room temperature, and to realize low threshold current densities and a regime of lasing via the ground state of an exciton in QDs right up to room temperature.

We wish to thank V. B. Khalfin for helpful discussions of the results obtained.

[a)]E-mail: sergey@zaitsev.ioffe.rssi.ru

[1] N. Kirstaedter, N. N. Ledentsov, M. Grundmann, D. Bimberg, V. M. Ustinov, S. S. Ruvimov, M. V. Maximov, P. S. Kop'ev, Zh. I. Alferov, U. Richter, P. Werner, U. Gosele, and J. Heydenreich, Electron. Lett. **30**, 1416 (1994).

[2] S. V. Zaitsev, N. Yu. Gordeev, M. P. Soshnikov, A.Yu. Egorov, A. E. Zhukov, V. M. Ustinov, N. N. Ledentsov, and P. S. Kop'ev, Proc. of SPIE's Optical Dimension and Materials (OPTDIM) Conf., Kiev, Ukraine, 1995 p. 287.

[3] S. V. Zaitsev, N. Yu. Gordeev, M. P. Soshnikov, V. M. Ustinov, A. Yu. Egorov, A. E. Zhukov, N. N. Ledentsov, I. N. Kochnev, V. P. Komin, and P. S. Kop'vev in *Abstract of SPIE's Int. Symp. Photonics West*, San Jose, USA, 1996, proc. N2693-80.

[4] V. M. Ustinov, A. Yu. Egorov, A. E. Zhukov, N. N. Ledentsov, M. V. Maksimov, A. F. Tsatsul'nikov, N. A. Bert, A. A. Kosogov, P. S. Kop'ev, Zh. I. Alferov, and D. Bimberg in *Proc. Mater. Research Society*, Boston, USA, 1995, Vol. 417. P. 141.

[5] N. N. Ledentsov, J. Bohrer, D. Bimberg, S. V. Zaitsev, V. M. Ustinov, A. Yu. Egorov, A. E. Zhukov, M. V. Maksimov, P. S. Kop'ev, Zh. I. Alferov, A. O. Kosogov, U. Gosele, and S. S. Ruvimov [to be published in Proc. Mater. Research Society (San Francisko, USA, 1996)].

[6] A. F. Tsatsul'nikov, N. N. Ledentsov, M. V. Maksimov, A. Yu. Egorov, A. E. Zhukov, V. M. Ustinov, B. V. Volovik, I. L. Krestnikov, A. R. Kovsh, A. V. Sakharov, N. A. Bert, P. S. Kop'ev, D. Bimberg, and Zh. I. Alferov, Fiz. Tekh. Poluprovodn. **31**, 1822 (1996) [Semiconductors **31**, 938 (1996)].

[7] A. F. Tsatsul'nikov, N. N. Ledentsov, M. V. Maksimov, A. Yu. Egorov, A. E. Zhukov, S. S. Ruvimov, V. M. Ustinov, V. V. Komin, I. V. Kochnev, P. S. Kop'ev, D. Bimberg, and Zh. I. Alferov, Fiz. Tekh. Poluprovodn. **31**, 1793 (1996) [Semiconductors **31**, 949 (1996)].

[8] N. N. Ledentsov, M. Grundmann, N. Kirstaedter, O. Schmidt, R. Heitz, J. Bohrer, D. Bimberg, V. M. Ustinov, V. A. Shchukin, P. S. Kop'ev, Zh. I. Alferov, S. S. Ruvimov, A. O. Kosogov, P. Werner, U. Richter, U. Gosele, and J. Heydenreich in *7th Int. Conf. on Modulated Semiconductor Structures*, Madrid, Spain, June 1995 [to be published in Solid Status Electron.].

Translated by M. E. Alferieff

Deep vacancy levels in $(AlAs)_1(GaAs)_3$ superlattices

S. N. Grinyaev and G. F. Karavaev

V. D. Kuznetsov Siberian Physicotechnical Institute, 634050 Tomsk, Russia
(Submitted January 24, 1996; accepted for publication September 9, 1996)
Fiz. Tekh. Poluprovodn. **31**, 545–555 (May 1997)

The pseudopotential and augmented unit cell ($4\times4\times4$) methods are used to study deep levels created by neutral, unrelaxed vacancies in AlAs, GaAs, and the $(AlAs)_1(GaAs)_3$ (001) superlattice. The symmetry of the electronic states of defective crystals as a function of the location of the vacancies in the superlattice layers is analyzed by group theory. Calculations of the band structure of an ideal superlattice show that it is a straight-band, many-valley semiconductor with a 1.79-eV band gap. Competing valleys in the lower band are found near the X, M, and Z points of the Brillouin zone and they originate in the L_1^c, X_3^c, and Δ_1^c sphalerite states, respectively. The size of the chosen augmented unit cell ensures good isolation of the wave functions of neighboring deep centers and the calculated level energies of the t_2 vacancies in the band gaps of GaAs and AlAs agree with published data. In the superlattice, a tetragonal component of the potential leads to partial (complete) removal of the degeneracy of these levels for vacancies lying in the intermediate (extreme) layers relative to Al. The biggest changes (~0.1 eV) occur for As vacancies lying on the heterojunction. The symmetry of the deep level states and the orientation of the planes in which they are localized depend on the geometrical position of the vacancy, which may be manifested in a polarization dependence of the optical characteristics. © *1997 American Institute of Physics.* [S1063-7826(97)01105-8]

In recent decades increasing attention has been drawn to superlattices, a new semiconductor material. By controlling the composition and dimensions of the layers of a superlattice, it is possible to vary the energy spectrum of the electrons and purposefully change the properties of materials with important practical applications. Various defects play an important role in bulk semiconductors.[1–4] In superlattices the role of different types of defects is also significant. Because of the reduced symmetry of the crystal potential in superlattices, additional singularities show up in the impurity states (such as a dependence of the level energies on the positions of defect centers within the superlattice layers, splitting of the degenerate levels, an anisotropy in the charge distribution near a defect, etc.), which may lead to new effects.

The scientific literature includes publications on this topic which are based on different methods. The effective mass method has been justified as a description of shallow, hydrogen-like centers in doped superlattices.[5] This method, however, is poorly suited to the study of deep centers, whose wave functions are strongly localized near defects. In order to calculate the spectra of such states in bulk materials, the Green's function method, the augmented unit cell method, and cluster method have been used in combination with fundamental and semiempirical approaches to account for the crystal potential.[1–4] The fundamental methods (pseudopotential, associated plane waves, etc.) require large amounts of computation, even for binary compounds, so that studies of this type for superlattices have thus far only been based on the strong coupling method.

The energy spectrum of deep levels associated with gallium vacancies and As_{Ga} antistructural defects near the AlAs/GaAs (001) heterojunction has been studied[6] using a recursion method with clusters containing up to 512 atoms. It was shown that the interaction energy of an intrinsic defect with the interface depends on the location of the Fermi level and this may lead to deviations from stoichiometry near the heterojunction. At the same time, the influence of the heterojunction on the local density of states and on the position of the deep levels in the band gap was negligible, apparently because of the small valence band gap (0.035 eV) used there.

Deep donor levels created by DX centers in some alloys and superlattices of III–V compounds have been studied[7] using the Green's function method. It was found that for a realistic barrier potential it plays an important role in the formation of bound and resonance deep levels: donors lying near the heterojunction create states with energies which differ substantially from those in the bulk.

It is known[2] that the strong coupling method can yield distorted defect potentials because of the limited basis that is used. This is manifested, in particular, in a lowering of the splitting energy of the deep a_1 and t_2 levels. A correct description of all the levels can be achieved in principle by using fundamental methods. When they are used, however, problems arise in connection with the self-consistent field. The magnitude of the gap obtained by the widely used approximation of a local electron density has a large systematic error (~0.5–1 eV), which may have a major effect on the location of the deep levels (up to 0.2–0.3 eV).[2] The more exact quasiparticle method is extremely cumbersome and has only been used for rather simple materials.

In this paper we examine the levels of neutral, unrelaxed vacancies in a $(AlAs)_1(GaAs)_3$ superlattice using the pseudopotential and augmented unit cell methods.[8] In the augmented unit cell method one actually studies the band structure of a crystal in which the impurities being studied are located at sublattice sites with periods large enough to exclude interactions of the defects with one another. However,

TABLE I. Compatibility relations of the irreducible representations of the T_d^2, D_{2d}^5, and T_d^2 groups (augmented unit cell) (the standard notation is given in parentheses).

T_d^2	D_{2d}^5	T_d^2 (Augmented unit cell)	T_d^2	D_{2d}^5	T_d^2 (Augmented unit cell)
Γ_1	Γ_1	Γ_1	Σ_1	$\Sigma_1+\Sigma_2+X_1+X_2$	$\Gamma_1+\Gamma_3+2\Gamma_4+2\Gamma_5$
Γ_2	Γ_4	Γ_2	Σ_2	$\Sigma_1+\Sigma_2+X_2+X_4$	$\Gamma_2+\Gamma_3+\Gamma_4+2\Gamma_5$
$\Gamma_3(\Gamma_{12})$	$\Gamma_1+\Gamma_4$	Γ_3	L_1	X_1+X_3	$\Gamma_1+\Gamma_4$
$\Gamma_4(\Gamma_{15})$	$\Gamma_3+\Gamma_5$	Γ_4	L_2	X_2+X_4	$\Gamma_2+\Gamma_5$
$\Gamma_5(\Gamma_{25})$	$\Gamma_2+\Gamma_5$	Γ_5	L_2	$X_1+X_2+X_3+X_4$	$\Gamma_3+\Gamma_4+\Gamma_5$
X_1	$\Gamma_1+M_1+M_4$	$\Gamma_1+\Gamma_3$	$2\Lambda_1$	$2U_1$	$2\Gamma_1+2\Gamma_4$
X_2	Γ_2+M_5	Γ_5	$2\Lambda_2$	$2U_2$	$2\Gamma_2+2\Gamma_5$
X_3	Γ_3+M_5	Γ_4	$2\Lambda_3$	$2(U_1+U_2)$	$2\Gamma_3+2\Gamma_4+2\Gamma_5$
X_1	$\Gamma_1+M_1+M_4$	$\Gamma_1+\Gamma_3$	$2\Lambda_1$	$2U_1$	$2\Gamma_1+2\Gamma_4$
X_2	Γ_2+M_5	Γ_5	$2\Lambda_2$	$2U_2$	$2\Gamma_2+2\Gamma_5$
X_4	$\Gamma_4+M_1+M_4$	$\Gamma_2+\Gamma_3$	$2F_1$	$2U_1+2(\Gamma_1+\Gamma_2)$	$2\Gamma_1+2\Gamma_3+4\Gamma_4+2\Gamma_3$
X_5	$\Gamma_5+M_1+M_2+M_5$	$\Gamma_4+\Gamma_5$	$2F_2$	$2U_2+2(\Gamma_1+\Gamma_2)$	$2\Gamma_2+2\Gamma_3+2\Gamma_4+4\Gamma_5$
Δ_1	$\Gamma_1+\Gamma_3+\Sigma_1$	$\Gamma_1+\Gamma_3+\Gamma_4$	Δ_1'	$Z_1+Z_3+\Sigma_1$	
Δ_2	$\Gamma_2+\Gamma_4+\Sigma_1$	$\Gamma_2+\Gamma_3+\Gamma_5$	Δ_2'	$Z_2+Z_4+\Sigma_1$	
Δ_3	$\Gamma_5+\Sigma_2$	$\Gamma_4+\Gamma_5$	Δ_3'	$Z_5+\Sigma_2$	
Δ_4	$\Gamma_5+\Sigma_2$	$\Gamma_4+\Gamma_5$	Δ_4'	$Z_5+\Sigma_2$	
W_1	$M_1+M_2+\Sigma_1$	$\Gamma_1+\Gamma_3+\Gamma_5$			
W_2	$M_5+\Sigma_2$	$\Gamma_4+\Gamma_5$			
W_3	$M_3+M_4+\Sigma_1$	$\Gamma_2+\Gamma_3+\Gamma_4$			
W_4	$M_5+\Sigma_2$	$\Gamma_4+\Gamma_5$			

Note: The points Δ have coordinates $\pi/a(001)$ and the points Δ' have coordinates, $\pi/(2a)(001)$ and $3\pi/(2a)(001)$. The factor 2 with the representations Λ_1 and F_1 of the T_d^2 group of sphalerite means that one representation refers to the star $\{\mathbf{k}\}$ and the other to the star $\{-\mathbf{k}\}$.

because of the rapid rise in the order of the matrices as the size of the augmented unit cells is increased, until now only comparatively small augmented unit cells containing a few tens of atoms have been used.[9,10] Here we have been able to reduce substantially the number of required basis functions due to the symmetry of the augmented unit cells; thus, we have been able to increase the volume of the augmented unit cell by a factor of 64 compared to the primitive cell of sphalerite and thereby reduce the overlap of the states of neighboring defects and the dispersion of the impurity band. The deep levels have been calculated using empirical pseudopotentials that have been found[11] recently on the basis of a large set of experimental data and self-consistent band spectrum calculations. These pseudopotentials yield a rather accurate description of the electronic states in ideal crystals, which should ensure a correct form for the wave functions of the deep centers.

1. GROUP THEORETICAL ANALYSIS

We employ the traditional notation for describing the crystal structure of GaAs and AlAs. Let us take the coordinate origin at a cation site and direct the axes along the edges of a elementary cube. The symmetry group of this lattice is T_d^2 with elementary translation vectors $\mathbf{a}_1=a/2(011)$, $\mathbf{a}_2=a/2(101)$, and $\mathbf{a}_3=a/2(110)$, where a is the lattice constant, which is assumed, for simplicity, to be the same in GaAs and AlAs. Let us place vacancies in sites denoted by integral combinations of the vectors $\mathbf{A}_1=2a(011)$, $\mathbf{A}_2=2a(101)$, and $\mathbf{A}_3=2a(110)$. The resulting new crystal has a unit cell that is magnified 64 times compared to those of GaAs or AlAs. The symmetry group of this crystal with the defects is, as before, T_d^2, but with the elementary translation vectors $\mathbf{A}_i$. Thus, the Brillouin zone for the defective crystal is a copy of the Brillouin zone of the original crystal reduced by a factor of 64. As a result of convolution, 64 different points of the large Brillouin zone fall at each point of the small Brillouin zone. The wave functions of the defective crystal can be classified according to their symmetry properties. The states of the isolated vacancy a_1 and t_2 transform[4] in accordance with the irreducible representations Γ_1 and Γ_{15} of the T_d^2 group of the point Γ of the small Brillouin zone, into which the points from the stars Γ, L, X, Δ, W, Σ, Λ, and F of the large Brillouin zone that are equivalent to it turn. Table I shows the compatibility relations of the representations at these points with the representations at the point Γ of the small Brillouin zone in Kovalev's notation.[12] These relations can be used to analyze quantitatively the contributions of the different states of the original crystal to the vacancy states.

For the ideal $(AlAs)_1(GaAs)_3$ (001) superlattice in a coordinate system coincident with the coordinate system for GaAs(AlAs) we can choose the following as the basis translation vectors: $\boldsymbol{\alpha}_1=a/2(110)$, $\boldsymbol{\alpha}_2=a/2(\bar{1}10)$, and $\boldsymbol{\alpha}_3=a/2(002)$. The corresponding reciprocal lattice vectors have the form $\boldsymbol{\beta}_1=2\pi/a(110)$, $\boldsymbol{\beta}_2=2\pi/a(\bar{1}10)$, and $\boldsymbol{\beta}_3=2\pi/a(001/2)$. The high symmetry points in the Brillouin zone of the superlattice are given by the vectors $\mathbf{k}_\Gamma=0$, $\mathbf{k}_M=1/2(\boldsymbol{\beta}_1+\boldsymbol{\beta}_2)$, $\mathbf{k}_\Sigma=1/4(\boldsymbol{\beta}_1+\boldsymbol{\beta}_2)$, $\mathbf{k}_U=1/4(\boldsymbol{\beta}_2+\boldsymbol{\beta}_3)$, $\mathbf{k}_X=1/2\boldsymbol{\beta}_2$, $\mathbf{k}_Z=1/2\boldsymbol{\beta}_3$, $\mathbf{k}_T=1/4(\boldsymbol{\beta}_1+2\boldsymbol{\beta}_2+2\boldsymbol{\beta}_3)$, and $\mathbf{k}_R=1/2(\boldsymbol{\beta}_2+\boldsymbol{\beta}_3)$. The spatial group of the superlattice symmetry is the D_{2d}^5 group. The volume of its unit cell is a factor of 4 greater than that of the GaAs or AlAs cell, while the Brillouin zone is correspondingly 4 times smaller than that of sphalerite. Sixteen points of the Brillouin zone of the superlattice from the Γ, M, X, Δ, U, and T stars turn into the point Γ of the small Brillouin zone. The compatibility relations for the representations of the T_d^2 and D_{2d}^5 symmetry groups are also shown in Table I. Here it is

TABLE II. Compatibility relations for the representations of the D_{2d}^5 group of an ideal $(AlAs)_1(GaAs)_3$ superlattice and of the D_{2d}^9 and C_{2v}^{20} groups of a superlattice with defects in the augmented unit cell at the point Γ of the small Brillouin zone. The type of atom chosen as the coordinate origin is indicated in the top row.

D_{2d}^5 Al	D_{2d}^9 Al_3,Ga($a\nu$)	Ga(ed)	C_{2d}^{20} As(ed)	As($a\nu$)
Γ_1	Γ_1	Γ_1	Γ_1	Γ_1
Γ_2	Γ_2	Γ_2	Γ_2	Γ_2
Γ_3	Γ_3	Γ_1	Γ_1	Γ_1
Γ_4	Γ_4	Γ_2	Γ_2	Γ_2
Γ_5	Γ_5	$\Gamma_3+\Gamma_4$	$\Gamma_3+\Gamma_4$	$\Gamma_3+\Gamma_4$
M_1	Γ_1	Γ_2	Γ_4	Γ_3
M_2	Γ_2	Γ_1	Γ_3	Γ_4
M_3	Γ_3	Γ_2	Γ_4	Γ_3
M_4	Γ_4	Γ_1	Γ_3	Γ_4
M_5	Γ_5	$\Gamma_3+\Gamma_4$	$\Gamma_1+\Gamma_2$	$\Gamma_1+\Gamma_2$
Σ_1	$\Gamma_1+\Gamma_4+\Gamma_5$	$\Gamma_1+\Gamma_2+\Gamma_3+\Gamma_4$	$\Gamma_1+\Gamma_2+\Gamma_3+\Gamma_4$	$\Gamma_1+\Gamma_2+\Gamma_3+\Gamma_4$
Σ_2	$\Gamma_2+\Gamma_3+\Gamma_5$	$\Gamma_1+\Gamma_2+\Gamma_3+\Gamma_4$	$\Gamma_1+\Gamma_2+\Gamma_3+\Gamma_4$	$\Gamma_1+\Gamma_2+\Gamma_3+\Gamma_4$
U_1	$\Gamma_1+\Gamma_3+\Gamma_5$	$2\Gamma_1+\Gamma_3+\Gamma_4$	$2\Gamma_1+\Gamma_3+\Gamma_4$	$2\Gamma_1+\Gamma_3+\Gamma_4$
U_2	$\Gamma_2+\Gamma_4+\Gamma_5$	$2\Gamma_2+\Gamma_3+\Gamma_4$	$2\Gamma_2+\Gamma_3+\Gamma_4$	$2\Gamma_2+\Gamma_3+\Gamma_4$
X_1	$\Gamma_1+\Gamma_3$	$\Gamma_3+\Gamma_4$	$\Gamma_1+\Gamma_4$	$\Gamma_1+\Gamma_3$
X_2	$\Gamma_2+\Gamma_4$	$\Gamma_3+\Gamma_4$	$\Gamma_2+\Gamma_3$	$\Gamma_2+\Gamma_4$
X_3	Γ_5	$2\Gamma_1$	$\Gamma_1+\Gamma_3$	$\Gamma_1+\Gamma_4$
X_4	Γ_5	$2\Gamma_2$	$\Gamma_2+\Gamma_4$	$\Gamma_2+\Gamma_3$
T_1	$\Gamma_1+\Gamma_3+\Gamma_5$	$2\Gamma_2+2\Gamma_4$	$\Gamma_1+\Gamma_2+2\Gamma_4$	$\Gamma_1+\Gamma_2+2\Gamma_3$
T_2	$\Gamma_2+\Gamma_4+\Gamma_5$	$2\Gamma_1+2\Gamma_3$	$\Gamma_1+\Gamma_2+2\Gamma_3$	$\Gamma_1+\Gamma_2+2\Gamma_4$

noted that the D_{2d}^5 group is described in Ref. 12 in a coordinate system that is rotated relative to the coordinate system of sphalerite so that the X axis is directed along the vector $\boldsymbol{\alpha}_1$ and the Y axis, along $\boldsymbol{\alpha}_2$. In order for the coordinate origin in these two crystals to coincide, we have placed it in a site occupied by a cation in the case of sphalerite. In the case of the $(AlAs)_1(GaAs)_3$ superlattice, the description of the D_{2d}^5 group given in Ref. 12 corresponds to choosing the coordinate origin at an Al atom or at a Ga atom lying in an intermediate layer equally distant from the Al layers. It is evident from Table I that the Γ_{15} upper valence level in GaAs(AlAs) is split in the superlattice into a double Γ_5 level and a single Γ_3 level. The levels Γ_1, X_1, and X_3 of the lower conduction band of GaAs transform in the superlattice into the levels Γ_1, $\Gamma_1+M_1+M_4$, and Γ_3+M_5, respectively, and the additional extremum L_1 of the conduction band of GaAs(AlAs) is split into two levels X_1+X_3. In the lower conduction band of the superlattice there is also a competing valley near the point Z whose state originates from the sphalerite levels on the Δ line.

In studying the $(AlAs)_1(GaAs)_3$ superlattice defect states we have retained the mutual positions of the defects specified by means of the vectors $\mathbf{A}_i$. On placing the coordinate origin at a site occupied by a defect, we obtain five different possible structures for a superlattice with defects. In these crystal structures the basis vectors $\mathbf{A}_i$ describe the translation group, while the choice of position of the defect determines the point symmetry. If the defect to which the reference system origin is attached is placed at an Al site or at a site in the middle of the Ga layers ($a\nu$), then the symmetry group of the defective superlattice is D_{2d}^9, while if the defect is located at an As site (in an intermediate layer $a\nu$ or in the nearest ed layers to Al), then the symmetry group is C_{2v}^{20}. Table II lists the compatibility relations of the group representations for states corresponding to the center of the Brillouin zone of a defective superlattice with different locations for the defect sites. It can be seen that lowering the point symmetry of the potential leads to splitting of the volume defect levels t_2. For Al and Ga($a\nu$) vacancies it splits into a single Γ_3 level and a double Γ_5 level, while for As and Ga (ed) levels the degeneracy is removed completely $(\Gamma_1+\Gamma_3+\Gamma_4)$.

2. COMPUTATIONAL TECHNIQUE

In the augmented unit cell method the problem of finding the electronic states in a crystal with a single defect reduces to determining the band structure of a crystal with periodically sited defects. The Hamiltonian of this type of crystal can be written as the sum of the Hamiltonian H_0 of an ideal crystal and the potential V of the defect sublattice. Its spectrum can then be determined from the single-electron Schrödinger equation:

$$(H_0+V)\Psi_{\mathbf{q}}=E_{\mathbf{q}}\Psi_{\mathbf{q}},$$

$$V=\sum_1 \nu_d(\mathbf{r}-\mathbf{R}_1), \tag{1}$$

where ν_d is the potential of a single defect, $\mathbf{R_1}$ are the vectors of the lattice constructed from the basis vectors $\mathbf{A}_i$, and $\mathbf{q}$ is the wave vector inside the small Brillouin zone. This equation can be solved most efficiently by using a basis of Bloch wave functions for an ideal crystal, $\varphi_{n\mathbf{k}}$, which, in turn, are expanded in terms of plane waves:

$$H_0\varphi_{n\mathbf{k}}=\varepsilon_{n\mathbf{k}}\varphi_{n\mathbf{k}}$$

$$\varphi_{n\mathbf{k}}(\mathbf{r})=1\Big/\sqrt{V_0\sum_{\mathbf{g}} C_n(\mathbf{k}+\mathbf{g})e^{i(\mathbf{k}+\mathbf{g})\mathbf{r}}}, \tag{2}$$

where n is the zone number, and $\mathbf{k}$, $\mathbf{g}$, and V_0 are the wave vector, the inverse lattice vector, and the volume of the ideal crystal, respectively. We represent the function $\Psi_{\mathbf{q}}$ in the form of a superposition of symmetrized combinations of the states $\varphi_{n\mathbf{k}}$:

$$\Psi_{\mathbf{q}}^{\alpha,j}=\sum_{n\mathbf{k}_i} B_{n\mathbf{k}_i}^{\alpha,j} O_{jm}^{\alpha}\varphi_{n\mathbf{k}_i}. \tag{3}$$

Here Q_{jm}^{α} is the projection operator which projects onto the subspace which transforms through the jth row of the mth column of the αth irreducible representation of the space group of the defective crystal, and $\mathbf{k}_i$ are the wave vectors satisfying the equation $\mathbf{k}_i=\mathbf{q}+\mathbf{G}$, in which the $\mathbf{G}$ are the reciprocal lattice vectors corresponding to the augmented unit cell, and the summation is taken over one of the representatives of each star. Substituting Eq. (3) in Eq. (1) yields a system of equations whose order is determined by the number of bands taken into account and the number of stars of the vectors $\mathbf{k}_i$. In general, the projection operator does not ensure orthogonality of the projected functions, so that they were Schmidt orthogonalized in the cases which arose here. Because the phases were specified consistently, the symmetrized combinations of Bloch functions can be fairly well localized within the confines of small regions of the augmented unit cells; this is yet another advantage of this basis for the study of defective materials.

The band spectra of the ideal AlAs and GaAs crystals and of the $(AlAs)_1(GaAs)_3$ superlattice were calculated in a basis of plane waves with the pseudopotentials taken from Ref. 11 in accordance with the lattice parameters, method for cutoff of the kinetic energy, and pseudopotential form factor assumed there, and with allowances for the dependence of the pseudopotential of arsenic on the type of nearest surrounding atoms.

The electronic states of the crystals with vacancies were calculated with an augmented unit cell $(4\times4\times4)$. In the basis of wave functions with a sphalerite structure (GaAs, AlAs), the number of irreducible stars of $\mathbf{k}_i$ in this case is 10 and the expansion (3) ensures rapid convergence in terms of the number of bands from the initial problem that are included. When 30 such bands are included, the maximum order of the matrices is 400 for all the representations. In order to obtain the deep vacancy levels in the binary crystals with an accuracy of about 0.1 eV it was sufficient to take about 15 bands. On going to the superlattice, the number of symmetrized wave functions in the basis increases because of the reduced symmetry. To construct them we have used as the $\varphi_{n\mathbf{k}}$ the Bloch wave functions of GaAs for the lowest 15 bands. In this basis the band energies of the ideal superlattice near the band gap were obtained with an accuracy of better than 0.02 eV.

The pseudopotentials[11] correspond to neutral atoms. By treating these potentials (assumed to have the opposite sign) as seed perturbation potentials created by distant atoms, we have taken the relaxation of the electron density into account with the aid of the Penn model dielectric permittivity function of an ideal crystal calculated[13] including corrections for exchange and for correlation in the Hubbard–Sham approximation.[14] The potentials of the neutral vacancies constructed in this way are, as will be shown below, in good agreement with the potentials obtained from self-consistent calculations.

TABLE III. Band energies in GaAs and AlAs relative to the ceiling of the valence band Γ_{15}^{ν} (eV).

	AlAs	GaAs
Γ_1^{ν}	−11.69	−12.13
Γ_1^{c}	3.03	1.52
Γ_{15}^{c}	4.21	4.01
X_1^{ν}	−9.51	−10.01
X_3^{ν}	−5.79	−6.25
X_5^{ν}	−2.29	−2.34
X_1^{c}	2.24	2.00
X_3^{c}	3.04	2.31
L_1^{ν}	−10.15	−10.66
L_1^{ν}	−5.53	−5.96
L_3^{ν}	−0.94	−0.97
L_1^{c}	2.87	1.80

Effects related to relaxation and distortion of the lattice can also affect the position of the deep levels.[4] For vacancies in GaAs, however, the corresponding shifts turn out to be small.[15] Thus, in this paper we only study neutral, unrelaxed vacancies in order to clarify the basic features of the deep levels which they induce in a superlattice compared to its binary components.

3. COMPUTATIONAL RESULTS

The calculated band energies of GaAs and AlAs (Table III) are in good agreement with experimental data. On an absolute scale the valence band energy gap of the two compounds is 0.50 eV. The calculations of the band spectra of the $(AlAs)_1(GaAs)_3$ superlattice are illustrated in Table IV and Fig. 1. This superlattice is a straight band semiconductor with a band gap energy $E_g(\Gamma_1^c-\Gamma_5^{\nu})=1.79$ eV, which is 0.1 eV below the energy obtained by linear interpolation between $E_0(\Gamma_1^c-\Gamma_{15}^{\nu})$ for GaAs and AlAs. This is related to the influence of the tetragonal component of the crystal potential, which also causes the appearance of multiple valleys in the lower conduction band. The valleys near the points X, M, and Z lie close in energy to the valley Γ in the conduction band. According to the compatibility relations (Table I), the superlattice states X_3 and X_1 originate from the sphalerite L_1 state, the M_5 (doubly degenerate) and Γ_3 (sec-

TABLE IV. Band energies in a $(AlAs)_1(GaAs)_3$ superlattice near the band gap relative to the ceiling of the valence band Γ_5^{ν} (eV).

Γ_3^{ν}	−0.013	M_5^{ν}	−2.33	U_2^{ν}	−0.67
Γ_1^{c}	1.79	M_2^{ν}	−2.27	U_1^{ν}	−0.62
Γ_3^{c}	2.05	M_5^{c}	2.05	U_1^{ν}	−0.55
Γ_1^{c}	2.49	M_4^{c}	2.38	U_2^{ν}	−0.49
Γ_3^{c}	2.64	M_1^{c}	2.58	U_1^{c}	2.31
X_2^{ν}	−0.98	Z_5^{ν}	−0.64	U_1^{c}	2.52
X_3^{ν}	−0.94	Z_5^{ν}	−0.47		
X_2^{ν}	−0.90	Z_3^{c}	2.14		
X_4^{ν}	−0.90	Z_1^{c}	2.15		
X_3^{c}	1.86				
X_1^{c}	2.20				

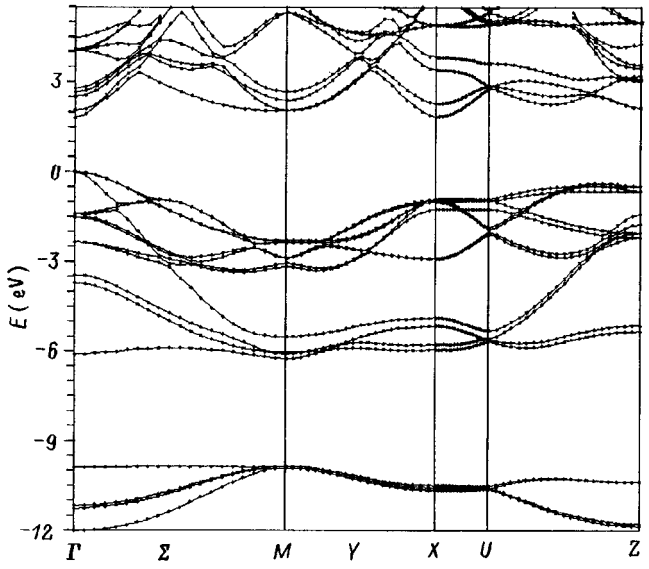

FIG. 1. Band structure of the $(AlAs)_1(GaAs)_3$ superlattice.

ond conduction band) states originate from the X_3 levels, and the Z_3 and Z_1 states orginate from levels on the Δ line in GaAs and AlAs.

Thus, this superlattice is of interest for observing phenomena related to the intervalley structure of its electronic spectrum.

Let us now discuss the computational results for defective crystals. Figure 2, for example, shows the Fourier transforms (assumed to have the opposite sign and cut off for $q>3.53$ atomic units, in accordance with Ref. 11) of the form factors of the original and screened (with the parameters for GaAs, and according to the method described

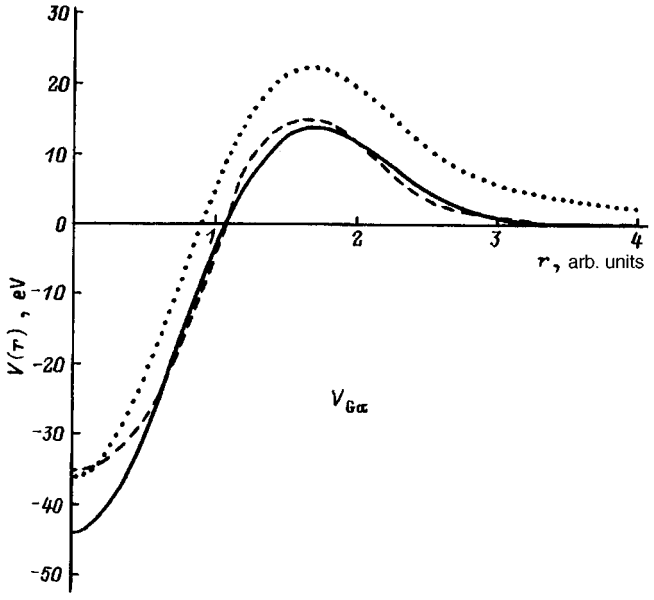

FIG. 2. The potential of a Ga vacancy in GaAs: the dotted curve is the original atomic pseudopotential of Ga from Ref. 11 (with opposite sign), the smooth curve is the same potential but screened as described in the text, and the dot–dashed curve is the spherically averaged self-consistent potential from Ref. 16.

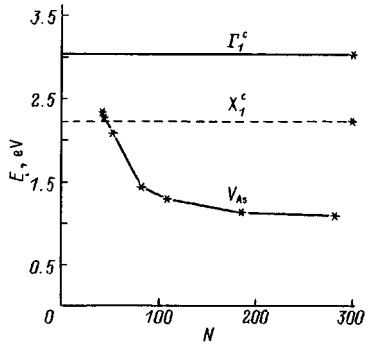

FIG. 3. The dependence of the energy of the deep level t_2 created by an As vacancy in AlAs on the number N of symmetrized Bloch wave functions for an ideal crystal that are included.

above) atomic pseudopotential of Ga, together with the spherically averaged potential of Ga vacancies in GaAs found[16] by a self-consistent calculation. The anisotropy in the defect potential[16] is relatively small ($\sim$10 %). It is clear that the vacancy potentials are in rather good agreement with one another. Note especially their almost identical asymptotic behavior at $r>2$ atomic units, where the ionic pseudopotential transforms to a Coulomb potential and essentially no longer has the indeterminacy that is intrinsic to it in the central cell region. This ''tail'' on the vacancy potential has a strong effect on the position of the deep level t_2. The coincidence of the two potentials is evidence of linear screening of the atomic potential in this region. The existing slight difference in the defect potentials in the neighborhood of the central cell may be related either to the difference in the choice of the form of the pseudopotentials in Refs. 11 and 16 or to nonlinear screening effects.[3] Previous calculations[17] of the deep vacancy levels have been done without screening of the atomic pseudopotentials and this led to excessively high values for the energies of these levels.

The $4\times4\times4$ augmented unit cell that we have used reduces the dispersion of the impurity band T_2 by roughly a factor of 2 compared to the dispersion obtained in a calculation[18] with a $3\times3\times3$ cell. Here the energy of the intermediate level of the impurity band calculated as in Ref. 18 from the two points Γ and X of the small Brillouin zone differs from the energy of the level at the point Γ in our case by less than 0.1 eV. Thus, the results given below are just for the point Γ ($\mathbf{q}=0$).

We have examined the convergence of the energy of the deep levels as a function of the number of symmetrized functions employed. This dependence is shown in Fig. 3 for the example of the t_2 level for arsenic vacancies in AlAs. Here the 300 symmetrized functions correspond to roughly the 30 lower states of the band structure of ideal AlAs. Evidently, an acceptable accuracy (about 0.1 eV) is reached by the time 15 bands from the initial problem have been included. For the shallower levels (in energy) of the cation vacancies, this accuracy is obtained with slightly fewer bands ($\sim$10). It is clear that when too few bands are included, as is often the case in the strong coupling method, the correct location of the local levels can be obtained only by distorting the potential of the defect (in this case by attenuating it).

TABLE V. t_2 vacancy levels in the band gap of AlAs and GaAs relative to the ceiling of the valence band (eV). The results of a calculation including 15 ideal crystal bands are given in parentheses.

	AlAs		GaAs	
Theory	V_{Al}	V_{As}	V_{Ga}	V_{As}
Our calculation	0.28(0.30)	1.09(1.15)	0.11(0.12)	0.93(1.00)
[6]	0.81	1.58	0.44	1.21
[16]			0.06	1.08
[20]	0.19	1.71	0.01	1.47
[21]			0.02	1.47
[22]			0.55	1.33
[17]			0.15	1.75
[23]			0.168	1.295
Experiment			0.042 [Ref. 25]	1.38 [Ref. 24]

Table V shows the energies of the deep t_2 levels lying in the band gap of GaAs and AlAs calculated using 30 bands. The energies of these levels obtained using the 15 lowest bands of the initial problem are given in parentheses to characterize the accuracy of the calculations. All the levels are taken relative to the energy of the top of the valence band of the ideal crystals. The states a_1 closest to it lie in the valence band and are resonance states. The t_2 levels of Ga and Al vacancies are half filled, while only one electron is found in the t_2 level of an As vacancy. Thus, these states are unstable with respect to the Jahn–Teller effect.[3] However,[19] the Jahn–Teller splitting energy in GaAs is small (<0.03 eV). In Table V data are given for comparison from other calculations using other methods. The discrepancies between them are as much as 0.5 eV, which reflects the substantial dependence of the deep levels on the way the defect potential is parametrized. For AlAs the earlier calculations were carried out only by the strong coupling method.[6,20] For GaAs our results are closest to a self-consistent pseudopotential calculation[16] using the Green's function method. This is related to the correlation between the vacancy potentials noted previously. In order to interpret the experimental data[24,25] it is necessary to know the dependence of the deep level on the charge state. Further studies are needed to eliminate the re-

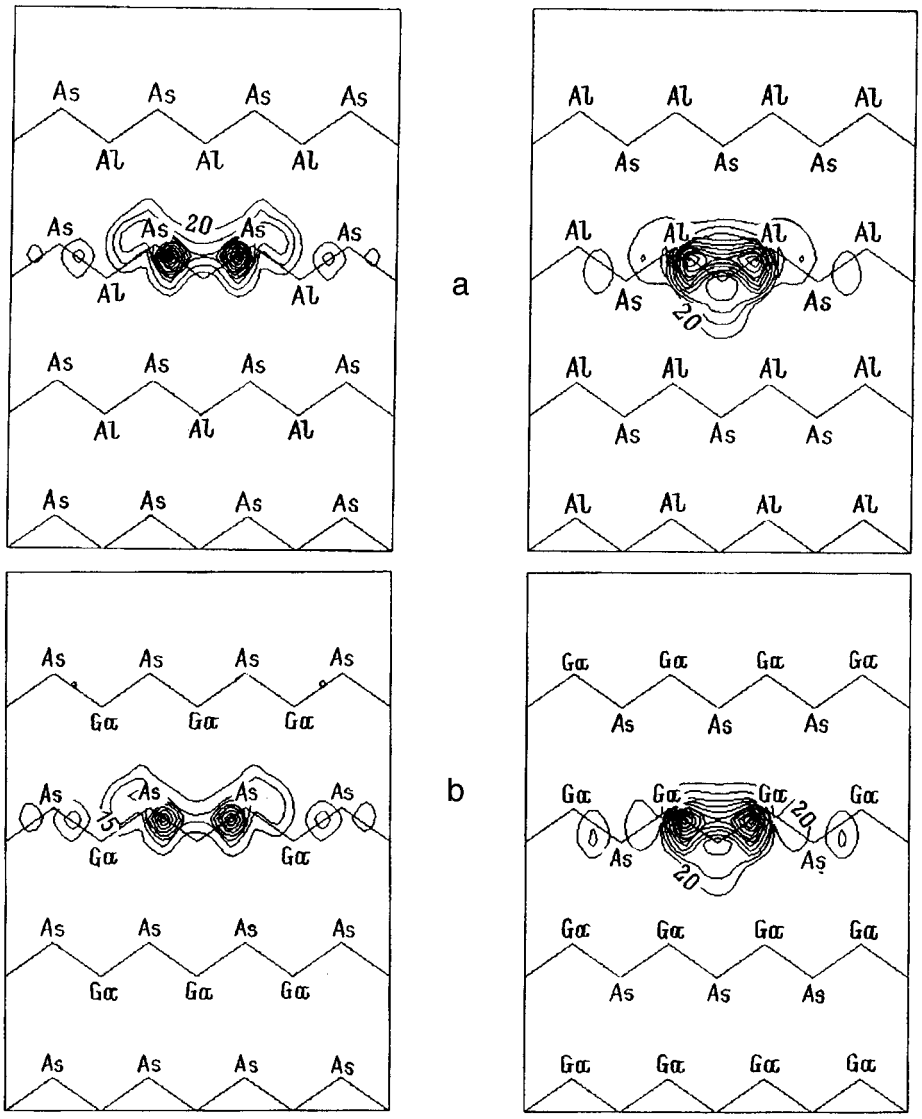

FIG. 4. Contours of the charge density of states of t_2 deep levels in: (a) AlAs created by V_{Al} (left) in the (110) plane and V_{As} (right) in the $(1\bar{1}0)$ plane in units of e/Ω_0 (Ω_0 is the unit cell volume); (b) GaAs created by V_{Ga} (left) and V_{As} (right) in the same units and planes. The zigzag lines indicate the directions of the bonds.

TABLE VI. Vacancy levels in the forbidden band gap of the $(AlAs)_1(GaAs)_3$ superlattice relative to the ceiling of the valence band (eV).

V_{Al}	$V_{Ga}^{a\nu}$	V_{Ga}^{ed}	$V_{As}^{a\nu}$	V_{As}^{ed}
0.18 (Γ_3)	0.14 (Γ_5)	0.14 (Γ_4)	1.03 (Γ_4)	1.03 (Γ_3)
0.15 (Γ_5)	0.12 (Γ_3)	0.12 (Γ_1)	0.99 (Γ_1)	1.00 (Γ_4)
		0.12 (Γ_3)	0.99 (Γ_3)	0.96 (Γ_4)

sulting ambiguities in the explanation of the observed spectra.[19]

Figure 4 shows contour plots of the charge density distributed around Ga, Al, and As vacancies in GaAs and AlAs for local t_2 states in the (110) plane for cations and in the 1–10 plane for arsenic within the confines of the periodic units of the augmented unit cell in these cross sections. It is clear that the size of the $4\times4\times4$ augmented unit cell are already sufficient to eliminate any significant overlap of the defect states from neighboring large unit cells. The wave

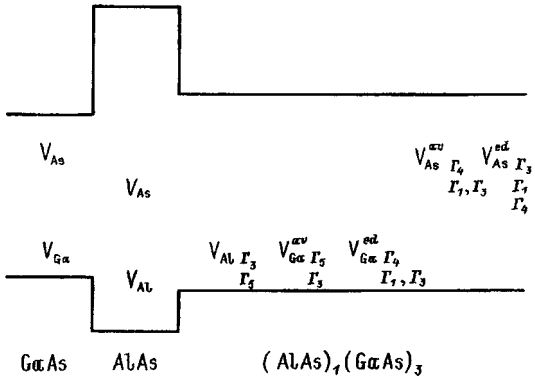

FIG. 5. Level scheme of vacancy levels in GaAs, AlAs, and $(AlAs)_1(GaAs)_3$ superlattice including the real band gaps.

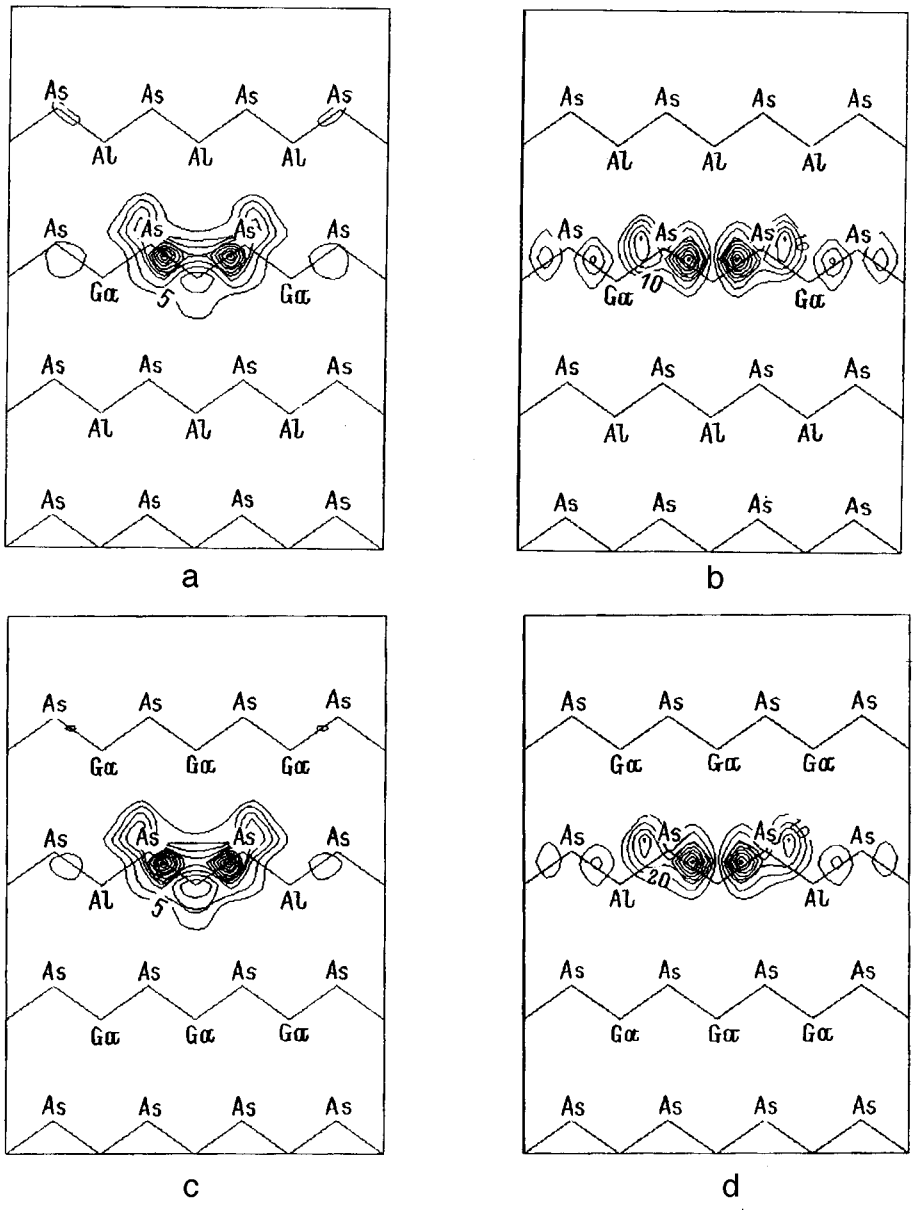

FIG. 6. Contours of the charge density of superlattice deep level states in the (110) plane created by Ga($a\nu$) (a, b) and Al (c, d) vacancies: (a, c) for the Γ_3 representation in units of e/Ω_0 and (b, d) for the Γ_5 representation in units of $e/(2\Omega_0)$.

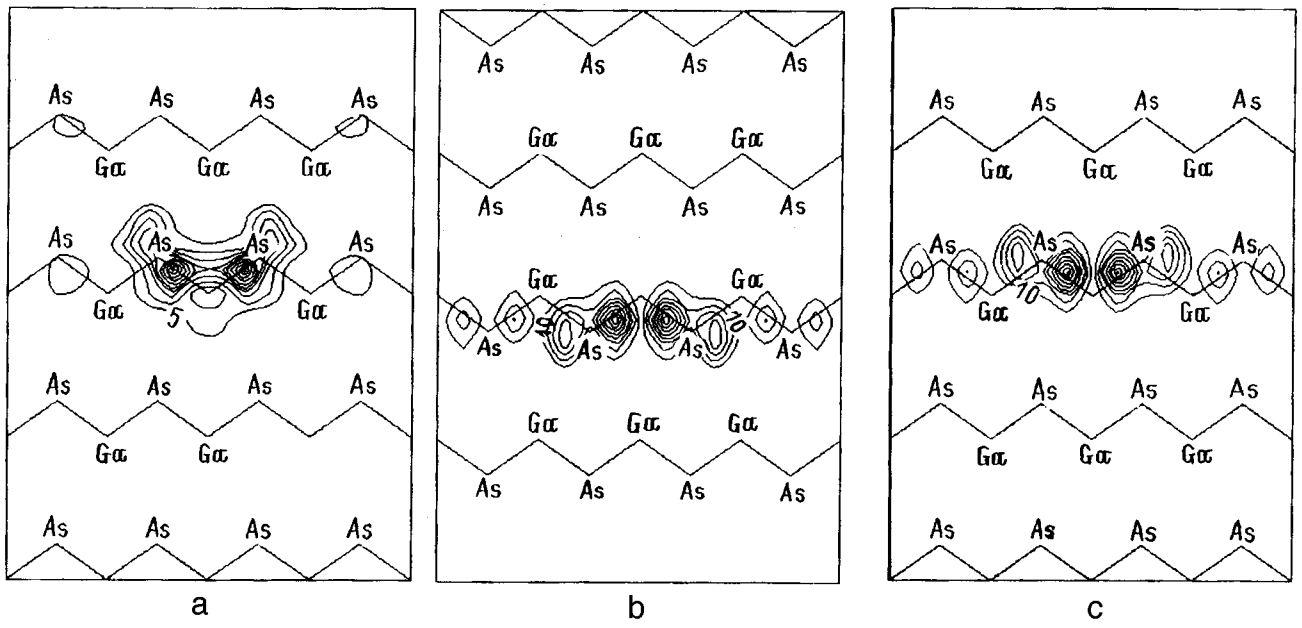

FIG. 7. Contours of the charge density (in units of e/Ω_0) of superlattice deep level states created by Ga(ed) vacancies for the representations (a) Γ_1 (110), (b) Γ_2 ($1\bar{1}0$), (c) Γ_4 (110). The orientations of the planes are indicated in parentheses.

functions of the deep levels are mainly localized in the dangling bonds of the vacancies with atoms of the nearest surroundings; the deeper (in energy) states V_{As} and V_{Al} in the wide band AlAs are localized somewhat more strongly than V_{As} and V_{Ga} in GaAs. A greater ''spreading out'' of the defect wave function is also observed in the direction of the bonds. For GaAs our charge density profiles are in good agreement with an earlier study.[16] An analysis of the coefficients $B_{n\mathbf{k}_i}^{\alpha,j}$ in the expansion (3) shows that the vacancy wave functions are mainly constructed from states of the upper valence band with the largest contribution from the central Γ valley. However, even for the shallowest of these t_2 levels, which is created by a gallium vacancy in GaAs and for which the weight of the Γ_{15}^{v} state in the expansion (3) is as high as 0.8, the conduction bands play an important role in determining the location of this level, so that ignoring their contribution will lead to a significant excess in its energy ($\sim$0.3 eV). This is caused by the large amplitude ($\sim$40 eV) of the perturbing vacancy potential (Fig. 2).

Calculations of the deep levels in the $(\mathrm{AlAs})_1(\mathrm{GaAs})_3$ superlattice as a function of the location of the defect are shown in Table VI. It is clear that the differences in the pseudopotentials of Al and Ga, as well as in the geometric positions of the Ga and As vacancies, show up in the energies of the corresponding levels only within a range of 0.1 eV. However, the resulting behavior differs qualitatively from that of the binary compounds and is, therefore, of interest. The triply degenerate t_2 levels in AlAs and GaAs were split in the superlattice and shifted by amounts consistent with the change in the band gap. Complete splitting of the levels occurs for defects with C_{2v} point symmetry, although the energy of the Ga(ed) and As($a\nu$) levels with Γ_1 and $\Gamma 3$ symmetry differ by less than 0.01 eV. For an arsenic vacancy located immediately at the heterojunction, As(ed), the amounts of splitting are greatest and the lowest Γ_4 level is nondegenerate, so that, given the estimates of Ref. 19, it is entirely probable that for such a defect there may be no distortion due to the Jahn–Teller effect. At Ga($a\nu$) and Al vacancies the splitting of the t_2 level into single Γ_3 and double Γ_5 levels due to the tetragonal component of the potential is of different sign and magnitude. At the same time, for an Al vacancy the deep Γ_3 level is higher than the Γ_5 level, while for a Ga vacancy the Γ_3 level is somewhat lower than the Γ_5 level. This change in the ordering of the levels is explained by the difference in sign (and magnitude) of the tetragonal perturbation that splits the t_2 level. In fact, at an Al vacancy the nearest Ga atoms are second neighbors, while at a Ga vacancy the nearest Al atoms are fourth neighbors. In addition, at them there is a change in the order of the As atoms from the first and third coordination spheres, which have somewhat different pseudopotentials.

Figure 5 shows a sketch of the deep levels (on an absolute energy scale) in the band gaps of these crystals calculated using the same number of basis functions. Here the edge of the conduction band corresponds to the Γ_1^c state. The distributions of the charge density of states of the deep levels are shown in Figs. 6–8. As in the case of vacancies in the binary compounds, the wave functions are mostly localized at the dangling bonds with nearest atoms. It should be noted that when a Ga vacancy is moved from an intermediate layer to an outer one, the lower level corresponds to states localized at bonds directed toward the heterojunction [in the $(1\bar{1}0)$ plane], while the upper level corresponds to states at bonds oriented away from the heterojunction [in the (110 plane]. These states have different symmetries Γ_3 or Γ_4. Thus, depending on which of the outer layers a vacancy lies, the upper level will have Γ_3 or Γ_4 symmetry. An optical transition from this local level out of the Γ_3 or Γ_4 states and into the band state Γ_1^c is allowed for different polarizations of

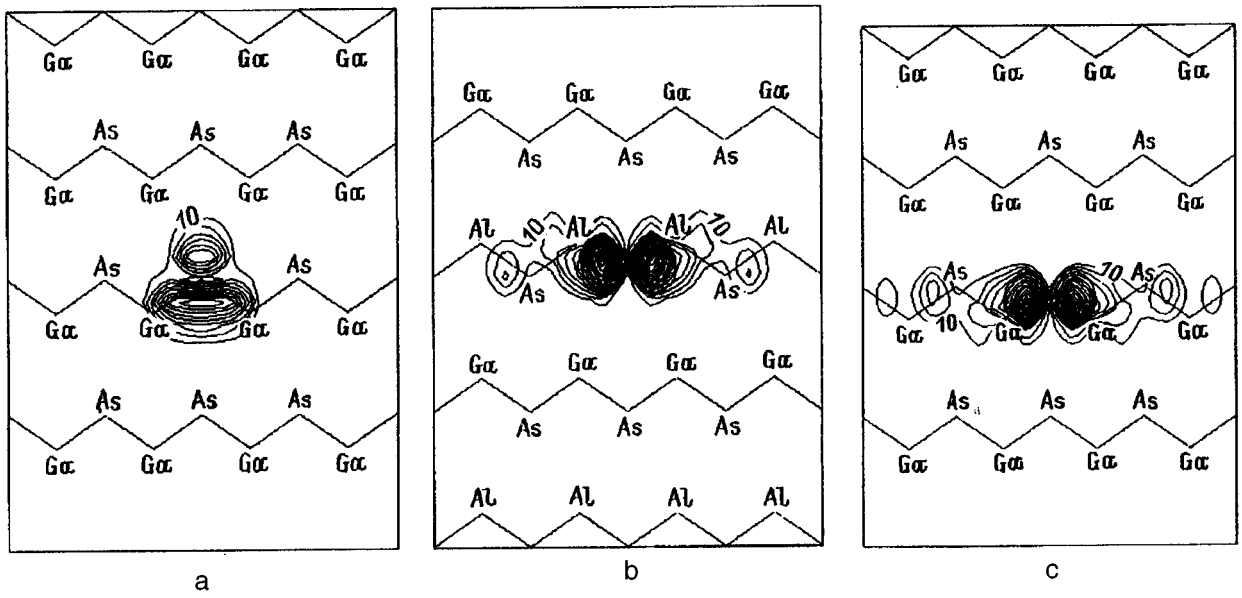

FIG. 8. Contours of the charge density (in units of e/Ω_0) of superlattice deep level states created by an As(ed) vacancy for the representations (a) Γ_1 (110), (b) Γ_3 (1$\bar{1}$0), (c) Γ_4 (110). The contours are essentially the same for an As($a\nu$) vacancy and in order to obtain the corresponding figures for the same representations in the same planes it is sufficient to replace the Ga atoms in the first (lower) and third chains with Al atoms (a, c) and, vice versa, Al atoms by Ga atoms in the same order of chains (b).

light incident normally on the plane of the superlattice. Thus, by observing the polarization dependence of the absorption on these transitions it is possible to determine the predominant geometrical distribution of the Ga vacancies. A different behavior is observed for the Γ_3 and Γ_4 vacancies of As (ed). Here the lower energy level corresponds to a state that is localized on bonds directed toward Ga atoms and the higher level, to a state localized on bonds directed toward Al atoms. At the same time, there was essentially no difference between the charge densities due to the anisotropy of the crystal potential for the Γ_3 states of Ga($a\nu$) vacancies and the Γ_1 states of Ga(ed) vacancies associated with the compatibility relations (Table II). This also happens for all states with the same symmetry in the case of the two As vacancies. In the latter case, however, the higher states (Γ_3 or Γ_4) are localized in planes containing Al atoms, which have pseudopotentials with a stronger repulsive core than do the Ga atoms.

4. CONCLUSIONS

In this paper we have shown that when symmetry is taken into account in the augmented unit cell method, rather large cells, which make it possible to describe localized states in defective crystals with acceptable accuracy, can be used. For the $4\times4\times4$ augmented unit cell employed by us this accuracy is about 0.1 eV. Including relaxation of the electron density around a vacancy in terms of the linear theory of dielectric screening with a suitable choice of the seed potential yields a defect potential which is close to the self-consistent potential in the most important region. As in the binary components, in the $(AlAs)_1(GaAs)_3$ superlattice considered here the energies of the deep vacancy levels depend on the band structure of the ideal crystal and on the defect potential, and their wave functions are localized on dangling bonds with nearest neighbor atoms. Additionally, in the superlattice there is a dependence on the geometric location of the defect (its local symmetry), which shows up as a splitting (partial or complete) of the degenerate states and as different orientations in their charge densities. This should be observed in the form of a polarization dependence of the absorption at transitions involving deep levels and can be used to analyze the geometric distribution of the vacancies. The small splitting of the deep levels indicates that perturbation theory can be used to account for the tetragonal component of the crystal potential. This may be used to develop simplified models of defects in other superlattices.

Further refinements in the calculations and development of this method will require simultaneous inclusion of all the effects which influence the location of the deep levels (lattice relaxation and distortion, defect charge state, spin–orbit interactions, self-consistent determination of the electron density, etc.).

This work was supported by the Russian Fund for Fundamental Research, Grant No. 94-02-04765.

[1] G. A. Baraff, Acta Phys. Polon. **A82**, 599 (1992).
[2] M. Lanno, Acta Phys. Polon. **A73**, 897 (1988).
[3] M. Jaros, Adv. Phys. **28**, 409 (1980).
[4] M. Lanno and J. Bourgoin, *Point Defects in Semiconductors. I*, Springer-Verlag, New York (1981).
[5] M. Herman, *Semiconducting Superlattices* [Russian trans., Mir, Moscow (1989)].
[6] P. J. Lin-Chung and T. L. Reinecke, Phys. Rev. B **27**, 1101 (1983).
[7] E. Yamaguchi, J. Phys. Soc. Japan **56**, 2835 (1987).
[8] R. A. Évarestov, *Quantum Chemical Methods in Solid State Theory* [in Russian], Leningrad (1982).
[9] R. W. Jansen, Phys. Rev. B **41**, 7666 (1990).
[10] J. Dabrowsky and M. Scheffler, Phys. Rev. B **40**, 10391 (1989).
[11] K. A. Mader and A. Zunger, Phys. Rev. B **50**, 17393 (1994).
[12] O. V. Kovalev, *Irreducible and Induced Representations and Corepresentations of the Fedorov Groups* [in Russian], Nauka, Moscow (1986).

[13] R. D. Grimes and E. R. Cowley, Can. J. Phys. **53**, 2549 (1975).
[14] L. Sham, Proc. Roy. Soc. A **283**, 33 (1965).
[15] A. P. Seitsonen, R. Virkkunen, M. J. Puska, and R. M. Nieminen, Phys. Rev. B **49**, 5253 (1994).
[16] G. B. Bachelet, G. A. Braff, and M. Schluter, Phys. Rev. B **24**, 915 (1981).
[17] M. Jaros and S. Brand, Phys. Rev. B **14**, 4494 (1976).
[18] S. G. Louie, M. Schluter, J. R. Chelikowsky, and M. L. Cohen, Phys. Rev. B **13**, 1654 (1976).
[19] C. Delarue, Phys. Rev. B **44**, 10525 (1991).
[20] W. Potz and D. K. Ferry, Phys. Rev. B **31**, 968 (1985).
[21] J. Bernhole and S. T. Pantelides, Phys. Rev. B **18**, 1780 (1978).
[22] A. Fazzio, J. R. Leite, and M. L. de Siqueira, J. Phys. C **12**, 3469 (1979).
[23] H. Xu and U. Lindefelt, Phys. Rev. B **41**, 5979 (1990).
[24] K. Saarinen, P. Hontojorvi, P. Lanki, and C. Corbel, Phys. Rev. B **44**, 10585 (1991).
[25] A. Jorio, A. Wang, M. Parentean, C. Carlone, N. L. Rowell, and S. M. Khanna, Phys. Rev. B **50**, 1557 (1994).

Translated by D. H. McNeill

Infrared absorption in porous silicon obtained in electrolytes containing ethanol

A. A. Kopylov and A. N. Kholodilov

St. Petersburg State Electronics University, 197376 St. Petersburg, Russia
(Submitted May 24, 1996; accepted for publication September 10, 1996)
Fiz. Tekh. Poluprovodn. **31**, 556–558 (May 1997)

The effect of treatments in hydrofluoric acid and annealing at $T=350$ °C on the optical properties of porous silicon in the infrared region of the spectrum has been investigated. An interpretation is given for the observed absorption bands. The index of refraction and thickness of the porous layer are estimated. © *1997 American Institute of Physics.* [S1063-7826(97)01205-2]

Molecular spectroscopy methods are helpful for studying the properties of porous silicon.[1–5] The use of these methods is explained by the fact that the conditions of preparation in an electrolyte are conducive to the adsorption of quasimolecular groups on an extended surface.

We investigated porous-silicon layers obtained in an electrolyte consisting of equal parts of a 48% HF solution and 96% C_2H_5OH on *p*-type [111] silicon substrates with current density 7.5 mA/cm^2 and an etch time of 30 min. The layers exhibited efficient photoluminescence in the visible region of the spectrum. The experimental samples were treated in a 40% HF solution for 15–20 min. After each treatment, the samples were washed in distilled water and dried in air for one day. The operations listed above were conducted at room temperature. Annealing was performed at a temperature of 350–400 °C in air for 3 h.

The IR transmission spectra were measured at room temperature with a LAFS-02 Fourier spectrometer in the range 450–4000 cm^{-1} and a LAFS-1000 Fourier spectrometer in the range 100–650 cm^{-1}. The spectral resolution was equal to 4 cm^{-1}. The chambers of the apparatus were evacuated to a pressure of 1 Torr in order to decrease the effect of atmospheric absorption.

Examples of the spectra obtained are shown in Figs. 1 and 2. Curve *1* shows the transmission spectrum of the initial sample. Together with the lines observed previously by other investigators, in our case additional lines are present in the spectrum primarily in the regions 1200–1500 and 2800–3000 cm^{-1}. Data on the positions of the lines and their interpretation are presented in Table I. Analysis of the lines which were not observed in previous studies shows that most of these lines belong to molecular complexes containing carbon.

Repeated measurements performed after the samples were stored in air for 6 months (curve *2*) showed an appreciable change in the large-scale structure of the spectrum while the intensity of most absorption lines associated with quasimolecular complexes remained constant. One possible explanation of this behavior could be a change in the properties of the porous layer as a result of natural oxidation by the oxygen in air.[11] The form of the spectra in the region 150–650 cm^{-1} remained practically the same at all stages of the treatments.

After treatment in HF (curve *3*), besides changes in the large-scale structure of the spectrum, a substantial decrease in the absorption on complexes containing carbon is observed. A subsequent analogous treatment (curve *4*) substantially restored the shape of the spectrum observed prior to treatment in HF (curve *2*). Further treatments of porous silicon did not produce any large changes in the transmission spectra. The annealing of the sample performed next resulted in almost complete vanishing of the absorption lines associated with carbon-containing molecular complexes (curve *5*) and in a strong weakening of the photoluminescence.

The observed large-scale structure of the spectra shown in Fig. 1, is due to interference in a layer on the surface of the experimental structure substrate–porous silicon. This is especially clearly seen for curve *5*. To obtain a quantitative estimate of the parameters of this layer we used a model of a uniform nonabsorbing layer on a high-resistivity silicon substrate. In this case the amplitude reflection coefficient of the surface of the sample on the side of the layer is

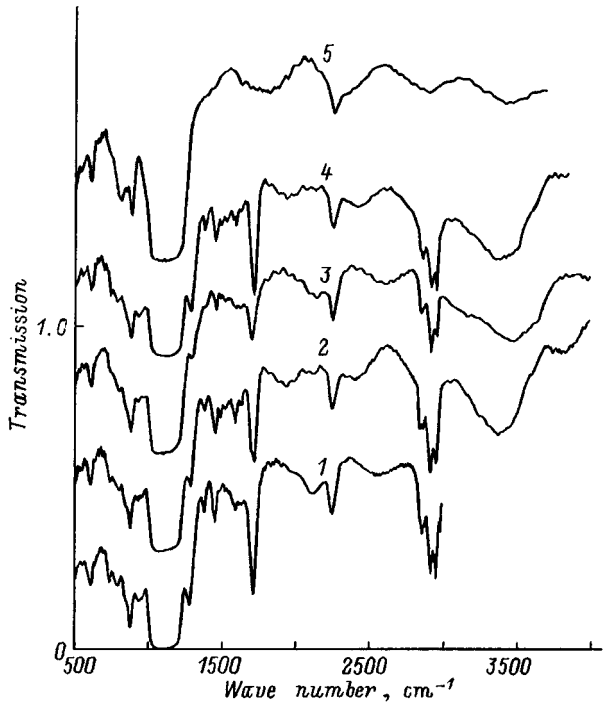

FIG. 1. Optical transmission spectra of porous-silicon samples. *1* — Initial sample, *2* — *6* months storage in air, *3* — first treatment in HF, *4* — second treatment in HF, *5* — after annealing. The spectra *2*—*5* are shifted along the vertical axis.

 1063-7826/97/050470-03$10.00

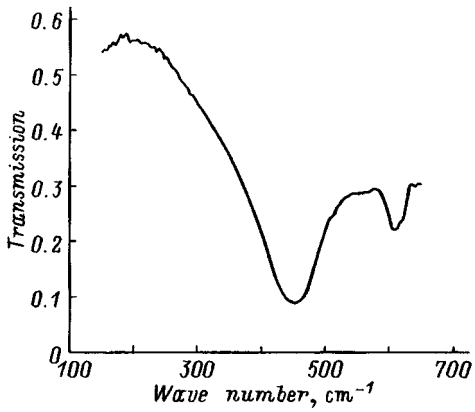

FIG. 2. Optical transmission spectrum of a porous-silicon sample in the region 150–650 cm^{-1}. The spectrum corresponds to the initial sample.

$$r=\frac{r_l+r_{ls}\exp(i4\pi n_l h\sigma)}{1+r_l r_{ls}\exp(i4\pi n_l h\sigma)}, \tag{1}$$

where

$$r_l=(1-n_l)/(1+n_l), \quad r_{ls}=(n_l-n_s)/(n_l+n_s),$$

n_l is the index of refraction of the layer, and n_s is the index of refraction of the substrate (for silicon $n=3.42$). The transmission of the structure was calculated according to the formula

$$T=\frac{(1-R)(1-R_s)}{1-RR_s}, \tag{2}$$

where

$$R=r^*r, \quad R_s=r_s^*r_s, \quad r_s=(n_s-1)/(n_s+1).$$

TABLE I. Spectral position and interpretation of absorption lines associated with adsorbed molecular complexes.

Position of absorption lines, cm^{-1}	Interpretation	References
450	δ(Si—O—Si)	6
664	δ(Si—H_2), δ(Si—H)	1
744	ν_{as}(Si—C)	7
800	ν_s(Si—O—Si)	6
882	Si—H, Si—OH, Si—O	3,6
908	Si—H_2, scissors mode	1,3
940	Si—OH	6
1070	ν_{as}(Si—O—Si)	1,6
1288	δ_s(Si—CH_3), δ_s[Si—$(CH_3)_2$]	8,9
1385	δ_s(C—CH_3)	8,9
1460	δ_{as}(C—CH_3)	8,9
1578	Probably δ(H—OH)	10
1705	ν(C═O) bound groups	10
1725	ν(C═O) free groups	10
2120	Si—H, Si—H_2	1,3
2250	Si—H, O_3—Si—H	3,6
2850	ν_s(C—H_2), ν_s(C—H_3)	9
2925	ν_{as}(C—H_2)	8,9
2959	ν_{as}(C—H_3)	8,9
3400	H_2O, Si—OH	6

Note: ν—stretching vibration; δ—bending vibration; *s*—symmetric vibration; *as*—antisymmetric vibration.

TABLE II. Results of an analysis of the parameters of the porous-silicon layer.

	Set No. 1		Set No. 2	
State of the sample	h, μm	n_l	h, μm	n_l
Initial sample	3.35	2.9	8.45	1.15
6 months in air	3.95	2.65	8.05	1.3
1st treatment in HF	3.3	2.9	8.35	1.15
2nd tretment in HF	3.73	2.8	8.15	1.28
3rd treatment in HF	4.11	2.55	7.87	1.33
Annealing at 350 °C	3.15	2.7	6.6	1.28

Equation (2) takes into account the interference inside the layer and the multiple incoherent reflections in the substrate.

The results of the analysis of the interference structure of the transmission spectra are summarized in Table II and examples of the transmission spectra corrected with allowance for the interference are shown in Fig. 3. The errors in determining the thickness and index of refraction of the layer are ~ 0.1 μm and 0.1, respectively. As shown in Table II, there exist two sets of physically realizable values of the thickness and the index of refraction of the layer which give equivalent descriptions of the shape of the spectra. A unique solution can be chosen only by using additional information about the experimental structures.

It is known that efficiently luminescing porous-silicon layers possess comparatively low refractive indices, for example, $n=1.4$, according to Ref. 12. Moreover, as follows from the transmission spectra, the experimental structures have a high content of silicon oxides whose refractive index is $n\approx 1.4$. Of the two available variants, the lower values of

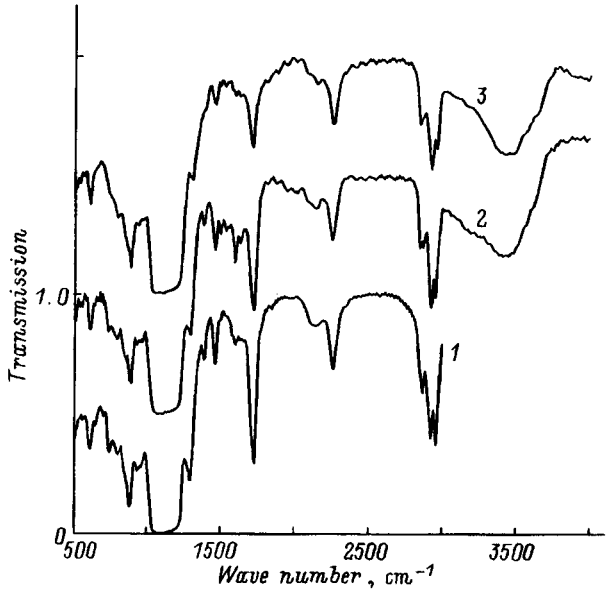

FIG. 3. Optical transmission spectra of porous-silicon samples. The spectra are corrected for interference. The spectra were obtained by dividing the initial transmission spectra by the result of the calculation according to Eq. (2) for the values of the parameters presented in Table II. The numbers on the curves correspond to Fig. 1. The spectra 2 and 3 are shifted along the vertical axis.

the refractive index should therefore be chosen, i.e., set 2 (Table II).

We note that in the spectra presented the lines of the carbon-containing complexes are much weaker than the lines of hydrogen-containing complexes (2120 and 2250 cm^{-1}). An estimate of the effective thickness of the layer of carbon-containing compounds, according to the absorption band 2850–2960 cm^{-1}, gives a value of the order of 1 μm. The changes in the effective thickness of the porous layer as a result of treatment are of the same order of magnitude. The presence of a large quantity of carbon-containing compounds could be due to the electrochemical oxidation of ethanol on the porous-silicon surface, which results in the appearance of C = O groups which interact with hydroxyl groups. This is indicated by the substantial intensity of the 1705 and 1725-cm^{-1} lines and the weak absorption on the 744-cm^{-1} (Si–C) and 1288-cm^{-1} (Si–CH_3) lines.

The data obtained suggest that the morphology of the porous layer changes during the treatments, which can result in a redistribution of the adsorbed molecules of the products of oxidation of ethanol on the modified surface of the porous layer and therefore it can influence the contribution of molecular complexes to the optical absorption. This assumption agrees with the observed character of the changes in the intensity of the absorption lines, which indicates that the concentration of the molecular complexes changes very little right up to annealing.

We thank A. V. Andrianov for a helpful discussion of the questions considered in this paper.

[1] C. Tsai, K.-H. Li, J. Sarathy, S. Shih, and J. C. Campbell, Appl. Phys. Lett. **59**, 2814 (1991).
[2] M. A. Tischler, R. T. Collins, J. H. Stathis, and J. C. Tsang, Appl. Phys. Lett. **60**, 639 (1992).
[3] N. Ookubo, H. Ono, Y. Ochiai, Y. Mochizuki, and S. Matsui, Appl. Phys. Lett. **61**, 940 (1992).
[4] R. Kumar, Y. Kiton, and K. Hara, Appl. Phys. Lett. **63**, 3032 (1993).
[5] H. D. Fuchs, M. Stutzmann, M. S. Brandt, M. Rosenbauer, J. Weber, A. Breischwerdt, P. Deak, and M. Cardona, Phys. Rev. B **48**, 8172 (1993).
[6] A. C. Adams, F. B. Alexander, C. D. Capio, and T. E. Smith, J. Electrochem. Soc. **128**, 1545 (1981).
[7] I. F. Kovalev, L. A. Ozolin, M. G. Voronkov, and L. A. Zhagat, *Collection of Works on Optics and Spectroscopy, III Molecular Spectroscopy* [in Russian], Nauka, Leningrad, 1987, p. 301.
[8] S. P. Mukherjee and P. E. Evans, Thin Sol. Films **14**, 105 (1972).
[9] L. H. Little, *Infrared Spectra of Adsorbed Species*, Academic Press, N. Y., 1966 [Russian translation, Mir, Moscow, 1969].
[10] A. V. Kiselev and V. I. Lygin, *Infrared Spectra of Surface Compounds*, Wiley, N. Y., 1975 [Russian original, Nauka, Moscow, 1972].
[11] F. Kozlowski and W. Lang, J. Appl. Phys. **72**, 5401 (1992).
[12] G. W.'t Hooft, Y. A. R. R. Kessener, G. L. J. A. Rikken, and A. H. J. Venhuizen, Appl. Phys. Lett. **61**, 2344 (1992).

Translated by M. E. Alferieff

Inelastic electron scattering in strongly doped $Bi_{0.88}Sb_{0.12}$

S. A. Aliev, A. A. Movsum-zade, and S. S. Ragimov

Institute of Physics, Azerbaĭdzhan Academy of Sciences, 370143 Baku, Azerbaĭdzhan
(Submitted November 27, 1995; accepted for publication September 10, 1996)
Fiz. Tekh. Poluprovodn. **31**, 559–562 (May 1997)

Experimental investigations of the Maggi–Righi–Leduc, Righi–Leduc, and Nernst–Ettingshausen thermomagnetic effects have been performed on three samples of the solid solution $Bi_{0.88}Sb_{0.12}$, doped with tellurium from 0.01 to 0.2 at.%, in the temperature interval 20–230 K. The quantity $L(T)$ is calculated from the experimental values of κ_e and the thermomagnetic effects. It is found that in the interval 40–220 K $L_{\exp}$ is less than its Sommerfeld value L_0. Comparing $L(T)$ with the existing theory showed that the low value of L is due to inelastic electron–electron interaction. © *1997 American Institute of Physics.* [S1063-7826(97)01305-7]

It is well known that in narrow-gap semiconductors with a degenerate electron gas and low lattice thermal conductivity, besides elastic scattering, there is also inelastic scattering of electrons.[1–4] To see it, it is necessary to separate experimentally the electronic component κ_e of the thermal conductivity or to investigate thermomagnetic effects.[1,3,5] The Lorentz number L in the Wiedemann–Franz relation ($\kappa_e = L \cdot \sigma \cdot T$) can be determined from these data, and in the presence of inelastic scattering it turns out to be less than the Sommerfeld value $[L_0 = (\pi 2/3)(k/e)^2]$. This has been done for pure bismuth.[6] The value of κ_e was separated in the interval 2–100 K under the action of a strong magnetic field and the temperature dependence $L(T)$ was determined. It was shown that in pure bismuth the bipolar thermal conductivity κ_{bp} is also substantial because of the mixed conductivity. It was found that the Lorentz number is less than L_0 only for $T < 30$ K. It was assumed that the low value of L is due to the inelastic intervalley or electron–electron scattering. However, the nature of the scattering in Bi and in systems of solid solutions based on Bi has not been settled, especially since additional sources of scattering, both elastic and inelastic, can arise in solid solutions.

In the present paper we analyze the results of an experimental study of the electronic thermal conductivity and the Maggi–Righi–Leduc (MRL) $\Delta\kappa$, Righi–Leduc (RL) $(-S \cdot H)$, and the Nernst–Ettingshausen (N–E) $\mathcal{E}_y$ thermomagnetic effects in the solid solutions $Bi_{0.88}Sb_{0.12}$ doped with tellurium up to 0.2 at. %.

1. EXPERIMENTAL RESULTS

The investigations were performed parallel and perpendicular to the C_3 axis on three $Bi_{0.88}Sb_{0.12}$ samples doped with tellurium in amounts of 0.01, 0.1, and 0.2 at. %. Tellurium dissolves in the system Bi–Sb, creating shallow donor levels with density from 5×10^{18} up to 5×10^{19} cm^{-3}. To analyze the main results, measurements of the electric conductivity σ, the Hall coefficient R, and the thermo emf α, and the thermo emf α_∞ in a strong magnetic field were also required. These data showed that up to room temperature the conductivity in the experimental samples is determined by the degeneracy of the electron gas $\mu^* \geqslant 5$. The electron mobility for a sample with $n = 5\times10^{18}$ cm^{-3} at 100 K reaches 20 000 cm^2/(V·s). In the magnetic fields accessible to us (up to 2.2 T) such a high mobility made it possible to achieve almost limiting values of the longitudinal thermomagnetic coefficients. Figure 1 is a plot of $\Delta\kappa$ as a function of uH/c (u is the electron mobility, and c is the speed of light), in which $\nabla\mathbf{H}$ and the magnetic field $\mathbf{H}$ are directed along the length of the samples and along the C_3 axis. Since the bipolar thermal conductivity is negligible in samples with such high electron density, the maximum value $\Delta\kappa_\infty$ can be taken as the purely electronic value κ_e ($\Delta\kappa_\infty = \kappa_0 - \kappa_{H\to\infty}$). In samples with $n = 2\times10^{19}$ cm^{-3} and $n = 5\times10^{19}$ cm^{-3} the mobilities reach much lower values, and for this reason $\Delta\kappa(H)$ did not saturate. For these samples the limiting value $\Delta\kappa_\infty$ was determined by the well-tested method of graphical and analytic extrapolation.[1,2] The temperature $L(T)$ was calculated from the data on κ_e. It was found that in the interval 40–220 K $L_{\exp}$ is less than its Sommerfeld value L_0 (for elastic scattering), and at $T \leqslant 40$ K $L_{\exp} \to L_0$ (Fig. 2).

The dependences of the transverse thermomagnetic effects NE ($\mathcal{E}_y$) and RL ($-S \cdot H$) on the magnetic field intensity uH/c are shown in Figs. 3 and 4. We see that $\mathcal{E}_y$ and $-SH$ pass through a maximum not for $(uH/c) = 1$, as should be the case in the presence of elastic scattering, but rather at $(uH/c) \simeq 1.4-1.5$.

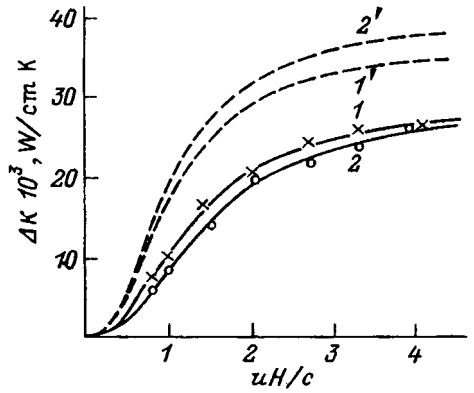

FIG. 1. $\Delta\kappa$ versus uH/c for a sample of the alloy $Bi_{0.88}Sb_{0.129}$ with electron density $n = 5\times10^{18}$ cm^{-3}. Dots — experiment. Curves — calculation according to Eq. (1) taking into account elastic (dashed lines) and inelastic (solid lines) electron scattering. T, K: *1, 1′* — 93; *2, 2′* — 205.

 1063-7826/97/050473-03$10.00

These investigations were also repeated in the case $\Delta T \| C_3$ and H parallel to the layers. It was found that the longitudinal and transverse thermomagnetic effects are substantially weaker when H is parallel to the layers (the anisotropy factor reaches 1.6).

2. ANALYSIS OF THE RESULTS

Undoubtedly, the presence of some inelasticity, irrespective of its nature, in the scattering of charge carriers should also affect other transport phenomena. Several theoretical studies[4,7,8] have been examining this question. The mobility, thermoemf, and the NE effect are analyzed in Ref. 7 . In solving the transport equation, two relaxation times are introduced: τ_{el} for isothermal effects and τ_{ee} for effects due to the temperature gradient. Specifically, it was shown that the degree of inelasticity can be defined as

$$r_\alpha / r_\mu = L/L_0 = \tau/\tau_{el},$$

where r_α and r_μ are the parameters of the scattering mechanisms, determined from the thermo-emf and mobility data. It is noted that the inelastic electron-electron interaction influences only the effects caused by the presence of a temperature gradient. The effect of inelasticity on other transport phenomena is studied in Ref. 5 .

Specifically, it was found that

$$\Delta\kappa = \Delta\kappa_\infty \frac{(uH/c)^2 (L/L_0)^2}{1+(uH/c)^2(L/L_0)^2}, \tag{1}$$

$$-SH = \frac{(uH/c)(L/L_0)}{1+[\kappa_r/(L_0\cdot\sigma\cdot T)][1+(uH/c)^2(L/L_0)^2][L_0/L]}, \tag{2}$$

$$\mathcal{E}_y = \frac{\Delta\alpha_\infty (uH/c)(L/L_0)}{(k/e)[1+(uH/c)^2(L/L_0)^2]}, \tag{3}$$

where $\mathcal{E}_y = \frac{k}{e} H \cdot Q_\perp$, $Q_\perp$ is the Nerust–Ettinghausen effect, and κ_r is the lattice thermal conductivity.

As one can see from Eqs. (1)–(3), the degree of inelasticity (L/L_0) can be determined from data on the indicated coefficients in arbitrary magnetic fields, from the value of uH/c corresponding to the maximum of the transverse effects $\mathcal{E}_y$ and $-SH$, and with the aid of definite relations between these effects

$$\Delta\alpha/H\cdot Q_\perp = L/L_0, \quad Q_\perp/R\cdot\sigma\cdot\Delta\alpha_\infty = L/L_0.$$

The experimental data are compared in Figs. 1, 3, and 4 with the curves computed according to Eqs. (1)–(3) for different values of L/L_0. It is found that there is good agreement for $(L/L_0)<1$. The values obtained for L/L_0 are presented in Table I together with other data.

It follows from the computed data on $\Delta\kappa(H)$ (Fig. 1) that in the case of elastic interactions between charge carriers or interactions with optical phonons $\Delta\kappa(H)$ saturates at much lower values $uH/c = 5-6$ than in the case of inelastic interactions (8–9), i.e. inelasticity seemingly decreases the effect of the Lorentz force, produced by the same value of H, on an electron.

As one can see from Fig. 3, the curves $\mathcal{E}_y$ pass through a maximum for $(uH/c)=1$ in the case of inelastic scattering and $(uH/c)>1$ in the case of inelastic scattering.

It is interesting that the curves of the field dependences of the transverse NE effect, which were calculated for elastic and inelastic scattering, cross after the maximum. The crossing after the maximum is due to the fact that in the case of an inelastic scattering the effective value of $(uH/c)(L/L_0)$ decreases less with H than in the case of elastic scattering. The

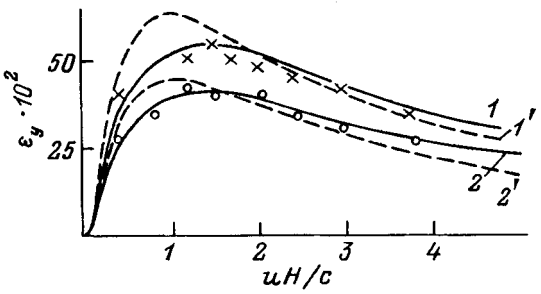

FIG. 3. $\mathcal{E}_y$ versus uH/c for a sample of the alloy $Bi_{0.88}Sb_{0.12}$ with electron density $n=5\times10^{18}$ cm^{-3}. Dots — experiment. Curves — calculation according to Eq. (2) taking into account elastic (dashed lines) and inelastic (solid lines) electron scattering. T, K: *1*, *1′* — 205; *2*, *2′* — 105.

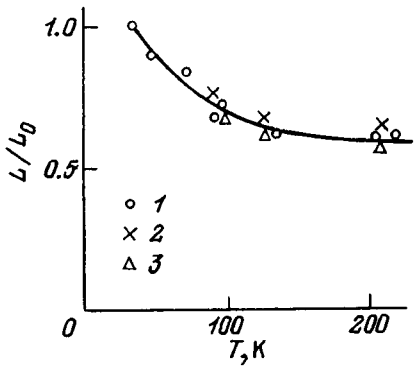

FIG. 2. Temperature dependence of L/L_0 for samples with different electron densities, cm^{-3}: *1* — 2×10^{19}, *2* — 5×10^{18}, *3* — 5×10^{19}.

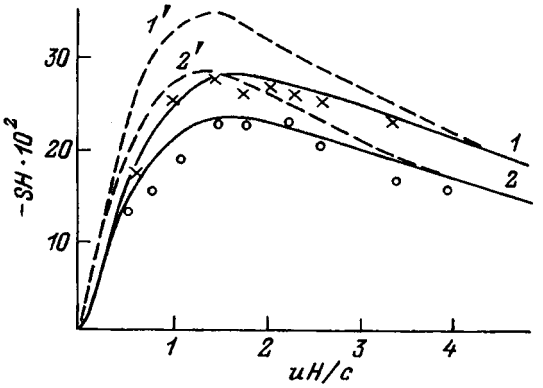

FIG. 4. $-SH$ versus uH/c for a sample of the alloy $Bi_{0.88}Sb_{0.12}$ with electron density $n=5\times10^{18}$ cm^{-3}. Dots — experiment. Curves — calculation according to Eq. (3) taking into account elastic (dashed lines) and inelastic (solid lines) electron scattering. T, K: *1*, *1′* — 205; *2*, *2′* — 93.

TABLE I. Values obtained for the fraction (L/L_0) of inelasticity in electron scattering in $Bi_{0.88}Sb_{0.12}$ from data on different thermomagnetic effects.

Sample No.	T, K	n, 10^{18} cm^{-3}	U, cm^2/(V·s)	L/L_0					
				$\Delta\kappa_\infty$	$\Delta\kappa$	$-S\cdot H$	$\mathscr{E}_y$	$\frac{\Delta\alpha}{H\cdot Q_\perp}$	$\frac{Q_\perp}{R\cdot\sigma\cdot\Delta\alpha_\infty}$
	93			0.81	0.80	0.76	0.75	0.72	0.75
1	120	5	20000	0.78	0.76	0.72	0.70	0.65	0.71
	205			0.75	0.71	0.60	0.65	0.62	0.60
	35			1.01	1	–	–	–	–
	70			0.88	0.85	–	–	–	–
2	102	20	8000	0.72	0.76	0.70	0.70	0.68	0.065
	130			0.69	0.70	0.68	0.65	0.61	0.61
	205			0.66	0.65	0.60	0.60	0.60	0.55
	97			0.77	0.75	0.71	0.70	0.70	0.65
3	115	50	3800	0.71	0.70	0.68	0.70	0.70	0.65
	200			0.62	0.60	0.60	0.65	0.65	0.65

$-SH$ maximum is reached for $(uH/c)>1$ even in the case of elastic scattering. However, in the case of inelastic scattering the $-SH$ maximum shifts in the direction of even larger values of uH/c. The displacement of the $-SH$ maximum in the direction of high fields is determined by the value of the factor $\kappa_r/(L_0\cdot\sigma\cdot T)$ in Eq. (2) and the magnitude of its displacement to the right in the case of inelastic scattering is determined by the degree of inelasticity L/L_0.

The nature of the inelastic mechanism of the interactions is described more completely in Ref. 8 . According to this theory, if for strong electron degeneracy $(\mu^*\gg kT)$ the energy of the longitudinal optical phonons $(\mu_0=\hbar\omega_0)$ is much less than the electron energy μ but is of the order of kT $(\mu\gg\hbar\omega_0,\ \mu_0\sim kT)$, then the Lorentz number, in general, has the form

$$\frac{L}{L_0}=\left[1+\frac{W_{ll}}{W_0}+\frac{u}{u_{0p}}\left(\frac{L_0}{L}-1\right)_{0p}\right]^{-1}. \tag{4}$$

In Eq. (4) the term $(u/u_{0p})((L_0/L)-1)_{0p}$ takes into account the inelasticity caused by the polar scattering of electrons by optical phonons and the term W_{ll}/W_0 takes into account the electron–electron interaction.[9,10]

The computational results are compared in Fig. 2 with the experimental data.

The calculations make it possible to conclude that the inelasticity of charge-carrier scattering in the solid solution $Bi_{0.88}Sb_{0.12}$ under the conditions of strong degeneracy is due mainly to the electron–electron interaction. The fraction of the inelasticity which is due to polar scattering by optical phonons does not exceed 5–7%.

As noted above, in pure Bi in the temperature interval 80–100 K electron scattering is elastic, and scattering inelasticity appears only at $T<30$ K.[6] It can be assumed that the purely elastic electron scattering in pure Bi at high temperatures is due to the simultaneous participation of electrons and holes in the heat flux and the low electron density. This fact is in accord with the results of Refs. 1–3 on the fact that in narrow-gap semiconductors with a degenerate electron gas at moderate temperatures, when scattering by phonons occurs, an electron–electron collision contains some measure of inelasticity. The absence of inelastic scattering in the alloys $Bi_{0.88}Sb_{0.12}$ at low temperatures is also due to the high electron density. As is well known, at low temperatures a high electron density gives rise to elastic scattering by ionized impurities. Evidently, even in the case of $Bi_{0.88}Sb_{0.12}$ at high values of n this mechanism prevails over the intervalley mechanism.

[1] S. A. Aliev, L. L. Korenblit, and S. S. Shalyt, Fiz. Tverd. Tela (Leningrad) **8**, 705 (1966) [Sov. Phys. Solid State **8**, 565 (1966)].
[2] S. A. Aliev, U. Kh. Suyunov, D. D. Arasly, and N. I. Aliev, Fiz. Tekh. Poluprovodn. **7**, 1086 (1973) [Sov. Phys. Semicond. **7**, 737 (1973)].
[3] S. A. Aliev, U. Kh. Suyunov, and N. I. ALiev, in *International Conffer-ence on Phonon Scattering in Solids*, Paris, 1972.
[4] S. A. Aliev, D. A. Bagirov, É. R. Iskenderov, É. I. Zul'fugarov, and S. I. Safarova, Neorg. Mater. **29**, 4 (1993).
[5] L. L. Korenblit, and V. E. Sherctobitov, Fiz. Tekh. Poluprovodn. **2**, 688 (1968) [Sov. Phys. Semicond. **2**, 573 (1968)].
[6] I. Ya. Korenblit, M. E. Kuznetsov, V. M. Muzhdaba, and S. S. Shalyt, Zh. Éksp. Teor. Fiz. **57**, 1867 (1969) [Sov. Phys. JETP **30**, 1009 (1970)].
[7] B. Ya. Moĭzhes and Yu. I. Ravich, Fiz. Tekh. Poluprovodn. **1**, 188 (1967) [Sov. Phys. Semicond. **1**, 149 (1967)].
[8] Yu. I. Ravich, B. A. Efimova, and V. T. Tamarchenko, *Semiconducting Lead Chalcogenides*, Plenum Press, N. Y., 1970.
[9] Yu. I. Ravich, B. A. Efimova, and V. T. Tamarchenko, Phys. Status Solidi B **43**, 11 (1971).
[10] V. I. Tamarchenko, Yu. I. Ravich, L. Ya. Morgovskiĭ, and I. E. Dubrovskaya, Fiz. Tverd. Tela (Leningrad) **11**, 3206 (1969) [Sov. Phys. Solid State **11**, 2599 (1969)].

Translated by M. E. Alferieff

Photoelectric effect in GaAs-based surface-barrier structures: Temperature dependence of the short-wavelength quantum efficiency

Yu. A. Gol'dberg, O. V. Konstantinov, O. I. Obolenskiĭ, E. A. Posse, and B. V. Tsarenkov

A. F. Ioffe Physicotechnical Institute, Russian Academy of Sciences, 194021 St. Petersburg, Russia
(Submitted July 11, 1996; accepted for publication September 10, 1996)
Fiz. Tekh. Poluprovodn. **31**, 563–566 (May 1997)

The temperature dependences of the short-wavelength photoelectroconversion quantum efficiency of GaAs-based surface-barrier structures were studied in the temperature range 78–300 K and photon energy range 1.8–4.7 eV. It was shown experimentally that the quantum efficiency γ increases with temperature T. The dependence of γ on T saturates at high temperatures. A model based on the idea of fluctuation traps in the space-charge layer of the structure is used to explain the temperature increase of the photoelectroconversion quantum efficiency of GaAs-based surface-barrier structures. This model, which agrees quite well with experiment, makes it possible to distinguish the dependence of the quantum efficiency on the temperature and on the photon energy, i.e., to separate explicitly the temperature dependence of the quantum efficiency. © *1997 American Institute of Physics.* [S1063-7826(97)01405-1]

1. PRELIMINARY REMARKS

This work continues our investigations of the short-wavelength photoelectric effect in III–V semiconductors,[1] i.e., the photoelectric produced by photons with energy much greater than the band gap in the semiconductor.

The temperature dependence of photoelectroconversion in GaP-based surface-barrier structures in the region of direct optical transitions was studied in Ref. 1 . It was shown that the short-wavelength quantum efficiency of the structures increases with temperature, and it was concluded that this increase is due to the temperature increase of the internal quantum yield of the photoelectric in GaP and not a temperature change in the losses of nonequilibrium charge carriers.

In this paper we report the results of an experimental study of the temperature dependence of the short-wavelength photoelectroconversion in GaAs-based surface-barrier structures which are used as visible-radiation detectors. The investigations of the short-wavelength quantum efficiency of GaAs-based surface-barrier structures, which are known to us, involve only experiments performed at room temperature (see, for example, Refs. 2–4).

2. OBJECT OF INVESTIGATION

The objects of investigation were Ni–*n*-GaAs surface-barrier structures. A structure consisted of a strongly doped GaAs substrate (electron density $n \simeq 10^{17}$ cm^{-3} and 300 K) coated with a 10-μm-thick, weakly doped, epitaxial layer of GaAs ($n = 1 \times 10^{15}$ cm^{-3}) with a half-transmitting barrier contact (Ni layer) on one side and containing an ohmic contact (In) on the opposite side. The substrate was oriented along the (100) crystallographic plane. The ohmic contact was produced by alloying In into the substrate, and the barrier contact was produced by chemical deposition of Ni on the epitaxial layer.[5] The structure was ~ 0.02 cm thick and the illuminated surface area was equal to 6×10^{-2} cm^2.

3. SUBJECT OF INVESTIGATION

The subject of the investigation was the temperature dependence of the short-wavelength quantum efficiency of GaAs-based surface-barrier structures in the temperature range 78–300 K and photon energy range $h\nu = 1.8 - 4.7$ eV. The effective light absorption length $L_\nu \equiv \alpha_\nu^{-1}$ (where α_ν is the absorption coefficient) in this spectral interval varies from 4000 Å at $h\nu = 1.8$ eV up to 60 Å at $h\nu = 4.7$ eV. This length is much less than the width of the space-charge layer of the structure ($W_0 = 10^4$ Å).

The quantum efficiency γ was determined with respect to the incident light and calculated according to the standard formula $\gamma = Ih\nu/P$, where I is the photocurrent (in A), P is the incident light flux (in W), and $h\nu$ is the photon energy (in eV).

4. EXPERIMENTAL RESULTS

The results of the study of the temperature dependences of the short-wavelength quantum efficiency of photoelectroconversion in surface-barrier structures are as follows (Fig. 1): The quantum efficiency increases with temperature and the temperature dependence of the quantum efficiency saturates at high temperatures.

The effect under study was already reported by us in a study of the temperature dependence of the photoelectroconversion in GaP-based surface structures.[1] Comparing the temperature dependences of the quantum efficiency of GaAs-based surface-barrier structures obtained in the present work and GaP-based structures obtained in Ref. 1 shows that the dependence $\gamma = \gamma(T)$ for GaAs structures is much stronger than for GaP structures. For example, at $h\nu = 3.98$ eV an increase in the temperature by a factor of 3 (from 100 to 300 K) increases γ for GaAs structures by a factor of 6, while for GaP structures γ increases only by a factor of 1.4. The reason for this difference is still unclear — the chemical composition of the semiconductor or the doping level of the semiconductor, since the GaP-based structure had a doping

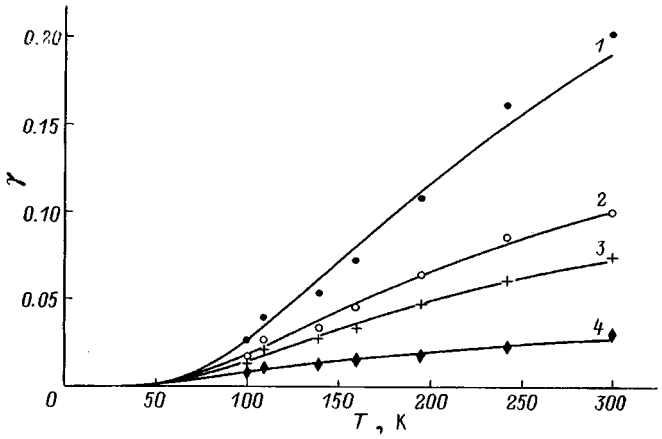

FIG. 1. Short-wavelength quantum efficiency of photoelectroconversion versus temperature for different photon energies $h\nu$, eV: *1* — 1.8, *2* — 4.11, *3* — 4.18, and *4* — 4.68.

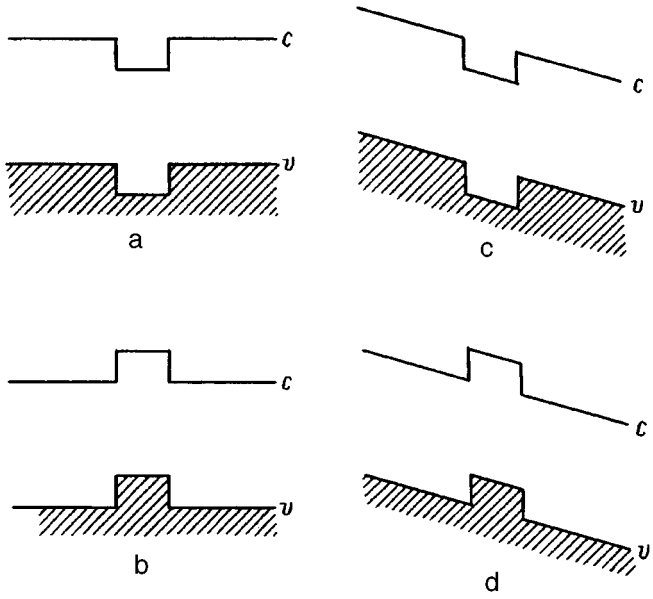

FIG. 2. Fluctuations of the conduction-band bottom (c) and valence-band top (υ) in the absence (A, b) and presence (a′, b′) of an electric field.

level of the order of $\sim 10^{17}$ cm^{-3} and the doping level of the GaAs-based structure was equal to $\sim 10^{15}$ cm^{-3}.

In our work Ref. 1 an excitonic model of the photoelectric was used to explain the temperature dependence $\gamma = \gamma(T)$ in GaP-based structures. However, the excitonic model of the photoelectric cannot be used for GaAs-based surface-barrier structures, since the exciton binding energy in GaAs is four times smaller than in GaP.

We therefore propose a different model to explain the temperature variation of photoelectroconversion in semiconductor surface-barrier structure.

5. MODEL

To construct a model of the experimentally observed dependence of the quantum efficiency on temperature and incident photon energy, we shall analyze all stages of photoelectroconversion.

We assume that radiation is not absorbed in the metal (Ni) and that all photons which have not been reflected from the surface enter the semiconductor. Indeed, absorption losses in the given wavelength range with Ni layer thickness $\leqslant 100$ Å do not exceed 10% and cannot greatly affect the observed characteristics.

We also assume that all photons which have entered the semiconductor are absorbed and that one electron-hole pair is produced in each case.

Photons with energy $h\nu \geqslant 1.8$ eV generate photocarriers in the space-charge layer, and to some extent they are subjected to the action of a barrier electric field. The barrier field separates some of these photoelectrons and photoholes.

If the energy of a photocarrier is sufficient for the carrier to overcome the potential barrier, then there is some probability that the photoelectron will escape into the metal and (or) a photohole will escape into the volume of the semiconductor; i.e., these photocarriers will be excluded from the photoelectroconversion process. Therefore, the higher the photon energy, i.e., the higher the kinetic energy of the photocarrier produced, the lower is the photoelectroconversion quantum efficiency. If there is sufficient time for the produced photocarriers to be thermalized, then their future fate will be determined by the barrier field.

It is ordinarily assumed that if the surface recombination and thermionic emission of photoelectrons into the metal is neglected, then the barrier field separates all thermalized photoelectrons and photoholes. In this case the quantum efficiency of photoelectroconversion should not depend on the temperature.

As follows from the experiment, however, the quantum efficiency of photoelectroconversion in a surface-barrier structure does depend, and quite strongly, on the temperature.

We assume that the losses of hot photocarriers do not depend on temperature. We need than only to study the possibility of recombination losses of thermalized (cooled) carriers in the space-charge layer and the relation of these losses to the temperature.

Recombination of thermalized free electrons to free holes in the space-charge layer is unlikely. In order for recombination to occur, the electron and hole must be spatially localized, i.e., traps for carriers must exist, and a trap must simultaneously localize an electron and a hole in a small region of space. It was natural to assume at first that the traps are allowed states in the band gap (impurity centers and defects). However, the results of a theory constructed for traps of this type do not agree with experiment. This is due to their high activation energy. For this region, we propose a different model: Potential wells and (or) humps formed by fluctuations of the conduction-band bottom and the valence-band top can serve as traps.

In the absence of an electric field, fluctuations of the conduction-band bottom and the valence-band top lead to localization of carriers of only one type: In Fig. 2a an electron is localized and in Fig. 2 a hole is localized. However, an electric field converts this fluctuation into a trap for an

electron and a hole simultaneously (see Figs. 2a′ and 2b′). An electron–hole pair trapped by such a capture center recombines after some time as a result of the tunneling effect.

A change in temperature results in a change in the density of free thermalized photocarriers because some carriers are trapped by fluctuation capture centers, i.e., the quantum efficiency of photoelectroconversion changes.

As the temperature increases, the density of free thermalized photocarriers will increase as a result of thermal dissociation of electron-hole pairs trapped by the capture centers and therefore the higher the temperature, the higher is the quantum efficiency of photoelectroconversion; this occurs until the traps are completely emptied.

We shall describe everything that has been said above in an expression for the quantum efficiency of photoelectroconversion.

Before a photon incident on the structure contributes to the photocurrent, there occur several events, each of which is characterized by a corresponding probability. Since these events all occur gradually, the resulting quantum efficiency equals the product of the probabilities of all events.

The probability that a photon enters a semiconductor equals $1-R$, where R is the reflection coefficient; we assume that the probability β of the production of an electron-hole pair by the photon (the quantum yield of the internal photoeffect) equals 1; the probability that the produced electron-hole pair will stop in the space-charge layer and will thereby be able to participate in the photoelectroconversion process equals $1-\delta_{\text{hot}}$, where δ_{hot} is the loss factor for hot photocarriers; the probability that a thermalized electron-hole pair is separated by the electric field and the photoelectroconversion process is completed equals $1-\delta_{\text{therm}}$, where δ_{therm} is the coefficient of recombination losses of thermalized photocarriers.

The quantum efficiency of photoelectroconversion, therefore, is given by

$$\gamma=(1-R)\beta(1-\delta_{\text{hot}})(1-\delta_{\text{therm}}). \tag{1}$$

The loss factor δ_{hot} of hot photocarriers is determined by the light absorption depth, i.e., the position of the produced photocarriers with respect to the boundaries of the space-charge region, and by their energy. We assume that δ_{hot} does not depend on temperature.

The loss factor δ_{therm} for thermalized carriers does not depend on the photon energy; it depends only on the ratio of the densities n_{loc} and n_{f} of photocarriers trapped in capture centers and free photocarriers, respectively:

$$\delta_{\text{therm}}=\frac{n_{\text{loc}}}{n_{\text{f}}+n_{\text{loc}}}. \tag{2}$$

Assuming that carriers are freed from traps with increasing temperature according to a simple exponential law, we obtain

$$1-\delta_{\text{therm}}=e^{-\Delta E/kT}, \tag{3}$$

where ΔE is the activation energy, k is Boltzmann's constant, and T is the temperature.

Therefore,

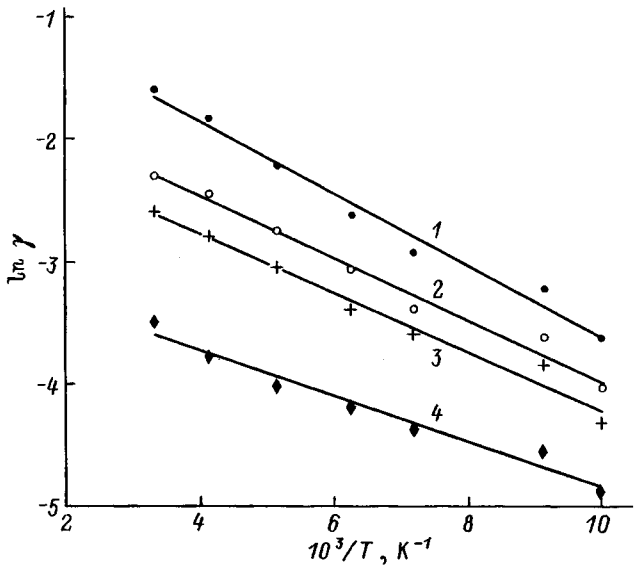

FIG. 3. $\ln\gamma$ versus $1/T$: Comparison of theory with experiment. Photon energy $h\nu$, eV: *1* — 1.8, *2* — 4.11, *3* — 4.18, *4* — 4.68.

$$\gamma=(1-R)(1-\delta_{\text{hot}})e^{-\Delta E/kT}. \tag{4}$$

6. COMPARISON OF THE MODEL WITH EXPERIMENT

Equation (4) which we have proposed gives a linear relation between $\ln\gamma$ and $1/T$. The activation energy ΔE determines the slope of this straight line, and the loss factor δ_{hot} for hot carriers determines the cutoff at the ordinate (the reflection coefficient for any energy can be found from the appropriate — see, for example, Ref. 6).

The experimental dependences of γ on $1/T$ turned out to be linear on a semilogarithmic scale, in accordance with the model, for all photon energies (Fig. 3), and the activation energy and loss factor for hot carriers determined from the experimental data are presented in Table I. As expected, the loss factor for the hot photocarriers increases with photon energy, and the activation energy does not depend on the photon energy. The activation energy can be assumed to be 20 meV with an error of no more than 25%.

We have thus reduced the experimental results of a study of the temperature dependence of the quantum efficiency of photoelectroconversion in GaAs-based surface-barrier structures to rather simple empirical laws. We proposed a simple model to explain these laws. To a first approximation, this model makes it possible to assume that the temperature dependence of the quantum efficiency of photoelectroconversion is determined by recombination losses of thermalized photocarriers in fluctuation traps located in the space-charge

TABLE I.

$h\nu$, eV	ΔE, meV	δ_{hot}	R
1.8	25.4	0.23	0.34
4.11	22.0	0.58	0.44
4.18	20.8	0.70	0.46
4.68	15.9	0.88	0.57

layer, and that the photon-energy dependence of the quantum efficiency of photoelectroconversion is determined by the losses of hot photocarriers which are not separated by the barrier field.

This work was supported by the Russian Fund for Fundamental Research (Grant No. 95-02-04121).

[1] Yu. A. Gol'dberg, O. V. Konstantinov, E. A. Popov, and B. V. Tsarenkov, Fiz. Tekh. Poluprovodn. **29**, 421 (1995) [Semiconductors **29**, 215 (1995)].
[2] R. Kalibijan and K. Mayeda, Solid–State Electron. **14**, 529 (1971).
[3] A. A. Gutkin, N. V. Dmitriev, D. N. Nasledov, and A. V. Pashkovskiĭ, Fiz. Tekh. Poluprovodn. **5**, 1927 (1972) [Sov. Phys. Semicond. **5**, 1673 (1972)].
[4] Yu. A. Gol'dberg, T. V. L'vova, O. A. Merzin, S. I. Troshkov, and B. V. Tsrenkov, Fiz. Tekh. Poluprovodn. **24**, 1835 (1990) [Sov. Phys. Semicond. **24**, 1143 (1990)].
[5] Yu. A. Gol'dberg and B. V. Tsarenkov, Inventor's Certificate SSSR No. 392845 (1975).
[6] Landolt-Burnstein, *Numerical Data and Functional Relationships in Science and Technology*, Springer-Verlag, N. Y., 1982, Vol. 17, *Semiconductors, Physics of Group IV Elements and III–V Compounds*.

Translated by M. E. Alferieff

Contact phenomena in two-dimensional electronic systems

V. B. Shikin and N. I. Shikina

Institute of Solid-State Physics, Russian Academy of Sciences, 142432 Chernogolovka, Russia
(Submitted March 13, 1996; accepted for publication September 16, 1996)
Fiz. Tekh. Poluprovodn. **31**, 567–570 (May 1997)

Unusual oscillations of the conductivity of a two-dimensional Corbino disk in a magnetic field, which were recently observed experimentally, are discussed on the basis of existing ideas about the specific properties of the contacts of a two-dimensional electronic system with ''external'' metallic electrodes. © *1997 American Institute of Physics.*
[S1063-7826(97)01505-6]

In an interesting experiment[1] it was shown that the conductivity of a low-density two-dimensional electronic system, which in a magnetic field oriented normal to its surface possesses a filling factor less than one, nonetheless undergoes oscillations as a function of the magnetic field. The amplitude of the oscillations increases as the average density of the two-dimensional electron gas (2DEG) in the central part of the Corbino disk, on which the experiments of Ref. 1 were performed, decreases. These two effects cannot be explained by using the standard ideas about the conductivity of an infinite two-dimensional (2D) electronic system in a magnetic field. This paper proposes an interpretation of the effects observed in Ref. 1 that takes into account the contact phenomena which occur in devices containing low-dimensional conducting systems and ''external'' metallic electrodes. Such setups also include the Corbino disk employed in the investigations performed in Ref. 1.

Contact phenomena (below called the Coulomb proximity effects), which destroy the spatial uniformity of the electron density in the contact zone of two metals with different work functions, have been known for a long time in classical three-dimensional electrostatics (see, for example, Ref. 2, the section entitled ''Contact potential difference''). The same phenomena also occur in low-dimensional conducting systems, where they are more pronounced. The recent review[3] serves as a good introduction to the physics of two-dimensional contact phenomena. It makes sense to underscore that virtually all low-dimensional contact phenomena studied in this review presuppose depletion of the low-dimensional system and the appearance of different depletion layers, Schottky layers, directly in the contact zone in the process. The central problem of the theory is to describe the Schottky layer accurately. The oscillations of interest to us develop under conditions of nonuniform enrichment of the 2D system and depend mainly on the characteristics of the electronic system in the bulk, at a large distance from the contacts. As a rule, this requires taking into account the relative position of the contacts. This is the technical novelty of the problem discussed below.

In the absence of Coulomb proximity effects the total resistance of a Corbino disk from Ref. 1 should not oscillate as a function of the magnetic field (the resistance is determined mainly by the central part of the disk, where the filling factor is less than 1 and therefore there are no oscillations). If, however, the Coulomb proximity effects are substantial, then the oscillations of the total resistance can appear as a result of the oscillatory behavior of the chemical potential in the metallic edges which have a high (compared with the central part of the disk) electron density and correspondingly a quasiclassically large filling factor. The effect of such oscillations on the equilibrium electron density in the central part of the disk is transferred from the metallic edges because of the Coulomb proximity effect.

1. To investigate the proposed mechanism of the specific oscillations in the conductivity of the Corbino disk as a function of the magnetic field, we shall employ a simplified model of the structure: metal–2DEG–metal. The model contains only qualitatively important details of the contact problem under discussion, so that we do not claim to explain the data of Ref. 1 quantitatively. The problem, nonetheless, remains essentially the same.

We are talking about a specially prepared, unscreened, degenerate heterostructure which possesses a stepped donor density distribution $n_d(x)$. The donors are distributed in the plane $z=-d$ according to the law

$$n_d(x)=N_d,\ \ |x|>w;\quad n_d(x)=n_d,\ \ |x|<w. \tag{1}$$

Here $2w$ is the width of a step in the donor distribution along the x axis. This step plays the role of the central part of the Corbino sample in the one-dimensional approximation.

Regions with high donor density N_d act as metallic contacts.

The quasi-one-dimensionality of the Corbino disk, which makes it possible to interpret the data in Ref. 1 on the basis of our model, arises under the conditions

$$R_2-R_1\ll(R_2+R_1)/2, \tag{2}$$

where R_2 and R_1 are the outside and inside radii of the two-dimensional region of the Corbino disk. It is obvious that the main property of the Corbino geometry — the closed nature of the current lines in the Hall direction — is also preserved in the quasi-one-dimensional approximation (all functions of the problem are independent of the coordinate y, which is also the direction of the Hall current).

In general, the electrons occupy the plane $z=+d$, i.e., they are separated from the donors by a spacer layer of thickness $2d$. The existence of a spatial separation between electrons and holes, as is characteristic of real heterostructures, must be taken into account in our model as well. However, the discussion below shows that the oscillations of the con-

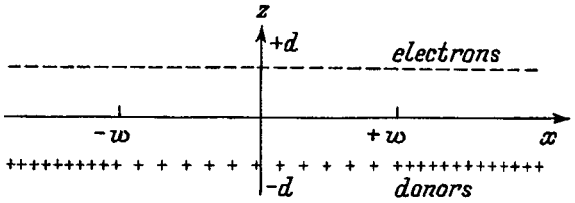

FIG. 1. Diagram of a heterostructure with modulated donor density. The crosses represent the distribution of the donors occupying the plane $z=-d$; the dashes represent the plane of 2D electrons $z=+d$. The jumps in the donor density are located at the points $x=\pm w$. The magnetic field is directed along the z axis. All spatial quantities are independent of the coordinate y.

ductivity are insensitive to this separation if $d \ll w$. The structure under discussion is shown schematically in Fig. 1.

The model (1) is suitable from the formal standpoint becuase of its simplicity. It contains singularities of the electron density, which are known from Ref. 2, in the contact zones [see the definition of $\delta n_0(x)$ given by expression (14) of Ref. 2] and it can be used to regulate the singularities by the methods described in Ref. 3. The properties of the model (1), as compared with the existing results from Ref. 3, suggest that the behavior of the perturbed electron density at large distances from the contact zones is insensitive to their geometry. Finally, in model (1) it is possible to give a self-consistent description of a two-dimensional electronic system bounded on two sides. This solves the problem of the integral divergence of the total effective charge near the contact zones, as is the case within the one-contact approximation, and (which is important for the conductivity problem in which we are interested) there arises a reasonable definition of the perturbed electron density in the central part of the system at large distances from the metallic edges. On this basis we consider the proposed model of a Corbino disk to be acceptable for a qualitative description of oscillatory magneto-Coulomb proximity effects in bounded 2D systems with metal contacts.

2. The finiteness of the spacer thickness $2d$ makes it much more difficult to solve the problem of equilibrium in an electronic system. For this reason, it is desirable to determine its role at least under simplified conditions, for example, for a purely electrostatic equilibrium in a nonuniformly doped heterostructure where the equilibrium condition has the form

$$\varphi(x,z=+d)+\varphi_d(x,z=+d)=\text{const}. \tag{3}$$

Here $\varphi(x,z)$ and $\varphi_d(x,z)$ are the electric potentials associated with the electron density $n(x)$ and donor density $n_d(x)$ distributions along the heterostructure. The electron density $n(x)$ can be represented in the form

$$n(x)=N_d+\delta n(x). \tag{4}$$

Here the correction $\delta n(x)$ must vanish in the limits $\pm\infty$. Taking into account Eq. (4), the requirement (3) reduces to an equation for $\delta n(x)$:

$$e\varphi_d'(x)+\frac{2e^2}{\kappa}\int_{-\infty}^{+\infty} ds\,\delta n(s)/(x-s)=0, \tag{5}$$

$$e\varphi_d'(x)=\frac{2e^2}{\kappa}(N_d-n_d)\ln\sqrt{\frac{(w+x)^2+4d^2}{(w-x)^2+4d^2}}, \tag{6}$$

where κ is the permittivity.

The solution of Eqs. (5) and (6) is

$$\delta n(x)=\gamma\left[\pi S+\arctan\frac{4dw}{4d^2-w^2+x^2}\right], \tag{7}$$

$$\gamma=(n_d-N_d)/\pi, \quad S=\begin{cases}0, & (4d^2-w^2+x^2)>0\\ 1, & (4d^2-w^2+x^2)<0\end{cases}. \tag{7a}$$

In the region $|x| \gg w$ the quantity $\delta n(x)$ is of the order of

$$\delta n(x)\sim 4\gamma dw/x^2; \tag{8}$$

i.e., the perturbation (8) is integrable.

If, however, $x\to 0$ and $d/w \ll 1$, then

$$\delta n(0)\cong\pi\gamma\left(1-\frac{4d}{\pi w}\right); \tag{8a}$$

i.e., the additional density in the central part of the 2D system is proportional to d/w. It is obvious that the effect of the finiteness of d/w on the conductivity of the system can be disregarded in the region $d/w \ll 1$, especially since this channel of nonuniformity $\delta n(x)$ is insensitive to the magnetic field.

3. Now let $d/w\to 0$; i.e., the spacer thickness is zero, and

$$N_d \gg n_d. \tag{9}$$

This means, specifically, that the resistance of the structure is determined mainly by its central part. We now introduce into the problem a magnetic field oriented perpendicular to the plane of the system. Here the magnetic filling factor ν_a is quasiclassically large for regions with electron density $n(x)\sim N_d$; i.e., $\nu_a \gg 1$, and small ($\nu_b<1$) for the central part of the system:

$$\nu_a=\pi l_h^2 N_d \gg 1, \quad \nu_b=\pi l_h^2 n_d<1, \quad l_h^2=c\hbar/eH, \tag{10}$$

where H is the intensity of the magnetic field. How will the total resistance of the heterostructure behave as a function of the magnetic field?

As noted above, when the Coulomb proximity effects are taken into account, the total resistance of the system can oscillate because of the oscillatory behavior of the chemical potential in the metallic edges and because of the effect of these oscillations on the equilibrium electron density in the central part of the disk. This idea was realized in the experiments of Ref. 1, where the electron density of the disk was modulated with the aid of auxiliary controlling electrons. Qualitatively, the experimental answer is that the total resistance of the disk, with the ''suppressed'' electron density in the central part of the disk, does indeed oscillate as a function of the magnetic field with quasiclassical frequency characteristic of ''edges'' with a high electron density. The amplitude of the oscillations increases with decreasing electron density in the central part of the disk. However, a detailed interpretation of the data of Ref. 1 is impeded by the abundance of auxiliary electrons. Our model of a Corbino disk makes it possible to analyze the details of this effect.

The condition of equilibrium for the modulated electronic system $n(x)$ in a magnetic field and with zero spacer thickness is [instead of Eq. (3)]

$$\mu = e\varphi(x,z=0) + \zeta\,[n(x)] = \text{const}. \tag{11}$$

Here

$$\zeta_a(n) = \epsilon_f + \frac{4T\cos(2\pi\epsilon_f/\hbar\omega_c)}{\sinh(2\pi T/\hbar\omega_c)}, \quad \epsilon_f \gg \hbar\omega_c \tag{11a}$$

or

$$\zeta_b(n) = \frac{1}{2}\hbar\omega_c - T\ln\left(\frac{1}{\nu} - 1\right), \quad \epsilon_f \ll \hbar\omega_c, \tag{11b}$$

where

$$\varepsilon_f \simeq \hbar^2 n(x)/m^*, \quad \nu(x) = \pi l_h^2 n(x),$$

ω_c is the cyclotron frequency, and m^* is the effective electron mass. We do not present here the general definition of $\zeta(n)$ in the form of a series in the eigenvalues of the electron energy in the magnetic field. We shall restrict the discussion to the asymptotic relations (11a) and (11b). We assume that the problem of equilibrium is solved approximately.

The idea of the approximation is suggested by the structure of the definition (11). In this formula the ''chemical'' part $\zeta(n)$ is sensitive to the total electron density $n(x)$ and its Coulomb component contains only $\delta n(x)$. We now assume that in the zeroth approximation the electronic density $n(x)$, which appears in the definition of $\zeta(n)$, reproduces the donor distribution (1), i.e.,

$$n_0(x) = n_d(x), \tag{12}$$

where $n_d(x)$ is obtained from the initial condition (1). In this case the equilibrium condition (11) along the system assumes the form

$$e\varphi_a + \zeta_a(N_d) = e\varphi_b + \zeta_b(n_d) \tag{13}$$

or, equivalently,

$$e\varphi_{ab} \equiv e\varphi_b - e\varphi_a = \zeta_a(N_d) - \zeta_b(n_d), \quad -w \leqslant x \leqslant +w. \tag{13a}$$

If the distribution $n(x)$ of the type (12) were an equilibrium solution (11), then the electrical part of the problem would be zero. In reality, however, Eq. (13) implies the presence of a jump φ_{ab}, which is determined by the asymptotic expressions for $\zeta(n)$ [Eqs. (11a) and (11b)]. This behavior of $\varphi(x)$ is possible only if there exists a deviation $\delta n(x)$ of the equilibrium electron density from $n_d(x)$ [Eq. (12)]. Denoting this deviation in the zeroth approximation as $\delta n_0(x)$ and using Eq. (13a), we obtain

$$\delta n_0(x) = \frac{\kappa w \varphi_{ab}}{\pi^2 e(w^2 - x^2)}, \tag{14}$$

where φ_{ab} is given by Eq. (13a). The power-law dependences at the ends of the interval $2w$ are similar to the divergences of the normal component of the electric field at the joint of the free faces of the metals in contact with one another in the problem of the contact potential difference of Ref. 2. The presence of these singularities is not very important for the effective conductivity of the system of interest to us, since the critical feature here is the region with the minimum electron density, i.e., the central part of the 2D system. From this reasoning follows the criterion for the applicability of the perturbation theory which we are using

$$\delta n_0(0) \ll n_d \tag{15}$$

or, using Eq. (14), we have

$$l \ll w, \quad l = \kappa\varphi_{ab}/\pi^2 e n_d. \tag{15a}$$

It is obvious that the requirement (15a) can always be satisfied in any case by making a suitable choice of w.

The next approximation for $n(x)$ is formulated, when necessary, as

$$n_1(x) = n_0(x) + \delta n_0(x), \quad n_0(x) \equiv n_d(x). \tag{15b}$$

The density distribution (15) must be substituted into $\zeta(n_1)$, after which a new boundary condition [which replaces the condition (13)] for the distribution $\varphi(x)$ along 2DEG arises from Eq. (11):

$$\varphi_1(x) = \text{const} - \zeta\,[n_1(x)]. \tag{16}$$

Using the new boundary condition (16) instead of the condition (13a), we can find the distribution $\varphi_1(x,z)$ in all the space around the 2DEG and hence also $\delta n_1(x)$:

$$2\pi e\,\delta n_1(x) = \kappa\frac{\partial\varphi_1(x,0)}{\partial z}, \tag{17}$$

etc.

4. We now introduce the correction $\delta n(x)$ into Ohm's law for the current between the metallic edges of the system under discussion. Here we confine our attention to the simplest possibility — the Drude approximation

$$j = \frac{n(x)e^2\tau}{m^*}\frac{d\varphi}{dx}, \quad n(x) = n_d + \delta n_0(x), \tag{18}$$

where τ is the momentum relaxation time, and $\delta n_0(x)$ is taken from Eq. (14). Assuming now that the current density j is conserved along the x axis, we can determine the effective relation between j and the potential difference V at the edges of the high-resistance part of the system

$$V = \int_{-w}^{+w} ds\,(d\varphi/ds) = \frac{m^* j}{e^2\tau}\int_{-w}^{+w}\frac{ds}{n_d + \delta n_0(s)}. \tag{19}$$

The definition (19) indicates, in particular, that the singular points of the function $\delta n_0(x)$ from Eq. (14) do not contribute to the integral. The expression (19) can be reduced ultimately to the following effective Ohm's law:

$$j = \sigma V/2w, \quad \sigma = \sigma_0 f(\delta), \quad \sigma_0 = e^2\tau\, n_d/m^*, \tag{20}$$

$$f(\delta) = \frac{\delta}{\delta - 0.5(1-\delta^2)\ln[(1+\delta)/(1-\delta)]},$$

$$\delta = (1 + l/w)^{-1/2}, \quad l = \kappa e\varphi_{ab}/\pi^2 e^2 n_d.$$

If $\delta = 1 - \epsilon$, $\epsilon \ll 1$, then

$$f(\delta) \simeq \frac{1}{1 - \varepsilon\,\ln(2/\epsilon)}, \quad \epsilon = 0.5 l/w. \tag{21}$$

In the opposite limiting case $\delta \to 0$ ($l \gg w$), which we present only as an alternative to Eq. (21) (our perturbation theory ''does not work'' in this limit),

$$f(\delta) \simeq 3/2\delta^2. \tag{22}$$

Equations (20) and (21) contain the main qualitative features of the experiment of Ref. 1; specifically, for small ε the effective conductivity of the system possesses a component which oscillates as a function of the magnetic field. Here the period of these oscillations is determined by the density N_d and the amplitude is inversely proportional to n_d. Taking into account the definitions of σ [Eq. (20)] and of φ_{ab} [Eq. (13a)], we can write the definition of the oscillatory part $\delta\sigma$ in the form

$$\delta\sigma/\sigma_0 = \delta\varepsilon \ \ln(2/\varepsilon_0),$$

$$\delta e = \frac{2\kappa\hbar\omega_c \cos[(2\pi\hbar N_d)/(m^*\omega_c]}{\pi^3 e^2 n_d w}, \quad \hbar\omega_c \gg T, \tag{23}$$

$$\varepsilon_0 \simeq \kappa\hbar N_d/(\pi e^2 n_d w),$$

where ε from Eq. (21) is divided into monotonic ε_0 and oscillatory δe components. For $\kappa \simeq 10$, $w \geqslant 10^{-2}$ cm, $H \geqslant 1$ T, $N_d \geqslant 10^{11}$ cm^{-2}, and $n_d \leqslant 10^9$ cm^{-2}, the amplitude $\delta\sigma/\sigma_0 \geqslant 10^{-2}$.

This estimate is approximately an order of magnitude smaller than the experimental result of Ref. 1. However, it should be kept in mind that in the density interval of interest to us the conductivity of a Corbino disk exhibits a pronounced percolation character (see, for example, Ref. 4), i.e., it is determined mainly by local saddle points with low electron density, and the capacitance measurements of the density from Ref. 1 give an idea only about the average electron density along the central part of the Corbino disk. Furthermore, a direct comparison of the numerical data in Ref. 1 and our results is only moderately correct, since the presence of an additional controlling electrode in Ref. 1 influences the experimental results.

In summary, we call attention to the existence of specific oscillations of the conductivity as a function of the magnetic field in bounded, low-dimensional, charged systems with metallic contacts, when the oscillations of the chemical potential in the low-resistance part of the system, which makes a negligible contribution to the total resistance, influence the electron density in the high-resistance part of the system — which accounts for the oscillations of the total resistance. A relationship between the low- and high-resistance parts of the problem can be established because of the Coulomb proximity effects.

This work is supported by INTAS Grant No. 93-933 and RFFR Grant No. 95-02-06108.

[1] V. T. Dolgopolov, A. A. Shashkin, G. V. Kravchenko, I. M. Mukkhamedzhanov, M. Vendel', J. P. Cotthouse, L. V. Molencamp, and S. T. Foxson, JETP Lett. **63**, 63 (1996).
[2] L. D. Landau and E. M. Lifshitz, *Electrodynamics of Continuous Media*, Pergamon Press, N. Y. [Russian original, Gostekhizdat, Moscow, 1957, p. 133).
[3] A. Ya. Shik, Fiz. Tekh. Poluprovodn. **29**, 1345 (1995) [Semiconductors **29**, 697 (1995)].
[4] A. A. Shashkin, V. T. Dolgopolov, and G. V. Kravchenko, Phys. Rev. B **49**, 14 486 (194).

Translated by M. E. Alferieff

Exchange energy of a free electron in a semiconductor

O. V. Konstantinov, O. I. Obolenskiĭ, and B. V. Tsarenkov

A. F. Ioffe Physicotechnical Institute, Russian Academy of Sciences, 194021 St. Petersburg, Russia
(Submitted April 25, 1996; accepted for publication September 16, 1996)
Fiz. Tekh. Poluprovodn. **31**, 571–576 (May 1997)

A general expression is obtained for the exchange interaction energy of an electron in a semiconductor for arbitrary degree of degeneracy of an electron gas. The single-particle exchange energy is expressed in terms of an integral function that depends only on the ratio of the Fermi energy, measured from the conduction-band bottom, to the thermal energy of the electron. For a strongly degenerate Fermi gas and zero temperature, this expression transforms to Slater's formula for the exchange energy of an electron in a metal. As the temperature is raised, the exchange energy decreases monotonically. The general expression acquires a simple analytic form in the limit of a nondegenerate electron gas. On the insulator side of a Mott transition the exchange energy varies nonmonotonically with increasing temperature: It has a maximum at a temperature of the order of the donor ionization energy. It is shown that the anistropy of the isoenergy surface of the electrons has virtually no effect on the magnitude of the exchange energy. The concentration dependences of the narrowing of the band gap at several temperatures for silicon and gallium arsenide are presented. [S1063-7826(97)01605-0]

1. INTRODUCTION

It is well known that in the theory of metals it is important to take into account the exchange energy of the free-electron gas when calculating the shape of the Fermi surface. The exchange energy is also found to be important in some problems of semiconductor physics. Examples are the theory of impuirty-concentration narrowing of the band gap of a semiconductor[1] and the theory of a insulator–metal phase transition in semiconductors.[2]

The effect of the exchange interaction can be taken into account when finding either the total energy of the system or the single-particle energy levels of the electrons. The contribution of the exchange energy to the total energy of the system was first obtained by Wigner and Seitz[3–5] in a calculation of the lattice parameters of a crystal. Wigner and Seitz work with the exchange energy per electron; this quantity is obtained by dividing the total exchange energy by the number of electrons in the system. However, in applications, including in the calculation of the band gap of a semiconductor, it is necessary to know the single-particle eigenenergies. The single-particle exchange energy, as shown by Slater,[6] is two times greater than the exchange energy per electron. The expression used by Slater is

$$U_{\mathrm{ex}}=-\frac{3}{2\pi}\frac{e^2}{\varepsilon}\,k_F, \tag{1}$$

where e is the elementary charge, ε is the dielectric constant of the medium (assumed to be 1 in Ref. 6), and k_F is the Fermi quasiwave vector, which in the case of a semiconductor is given by the expression

$$k_F=\left(\frac{3\pi^2 n}{M}\right)^{\frac{1}{3}}. \tag{2}$$

Here n is the free-electron density, and M is the number of equivalent valleys in the energy spectrum of the electrons in the k space of an anisotropic semiconductor.

Slater's formula (1) is widely used not only in the theory of metals[7] but also in the theory of atoms.[8] Using this formula, the complicated nonlocal Fock term was replaced by a simple local potential. This idea was the basis of the so-called local-density approximation.[9] This approximation takes into account, in addition to the exchange energy, the correlation energy responsible for the interaction of Fermi particles with antiparallel spins.[10] This correlation term for semiconductors is no more than 1/8 of the exchange term. Here we disregard this term since for a concentration shift of the conduction-band bottom another correlation term[11] is found to be much more important — the Debye–Hückel energy

$$U_{DH}=\frac{e^2}{2\varepsilon}\,\kappa, \tag{3}$$

where κ is the reciprocal of the Debye screening length

$$k^2=\frac{4\pi n e^2}{\varepsilon E_s}. \tag{4}$$

Here E_s is the screening energy

$$E_s=k_B T\,\frac{F_{-\frac{1}{2}}(\eta)}{F^{\frac{1}{2}}_{\frac{1}{2}}(\eta)},\qquad \eta=\frac{E_F}{k_B T}. \tag{5}$$

Expression (1) was obtained for an isotropic dispersion relation and for a Fermi gas with the maximum degeneracy. In semiconductors the state of the electron gas can vary from strongly degenerate to nondegenerate. In addition, the isoenergy surfaces in many semiconductors are anisotropic.

Our objective was to obtain an expression suitable for determining the single-particle exchange energy in a semiconductor.

2. CALCULATION OF THE EXCHANGE INTERACTION ENERGY OF AN ELECTRON IN A SEMICONDUCTOR

2.1. *General method for obtaining the exchange corrections to the total energy of a particle.* Let us consider the first-order correction to the energy of an electron in a state with quasiwave vector $\mathbf{k}$ and some definite direction of the spin which arises as a result of the exchange interaction of the given electron with another electron located in the state $\mathbf{k}'$ and with the same direction of the spin. It is known[12] that the exchange interaction decreases the total energy of a particle by the amount of the exchange integral

$$\Delta\varepsilon_{\mathbf{k}'}(\mathbf{k})=V_{\mathbf{kk}'}^{\mathbf{k}'\mathbf{k}}. \tag{6}$$

The expression for the exchange integral $V_{\mathbf{kk}'}^{\mathbf{k}'\mathbf{k}}$ will be presented below.

If the exchange interaction is summed over all states $\mathbf{k}'$ with fixed $\mathbf{k}$, taking into account the probability of filling these states, then the total energy of a quasiparticle in a state with quasiwave vector $\mathbf{k}$ and a definite direction of the spin can be written in the form

$$\varepsilon(\mathbf{k})=E_k-\sum_{\mathbf{k}'} V_{\mathbf{kk}'}^{\mathbf{k}'\mathbf{k}}f_{k'}, \tag{7}$$

where

$$E_k=\frac{\hbar^2}{2}\left(\frac{k_\parallel^2}{m_\parallel}+\frac{k_\perp^2}{m_\perp}\right) \tag{8}$$

is the kinetic energy, $m_\parallel$ and $m_\perp$ are the longitudinal and transverse effective masses, and $k_\parallel$ and $k_\perp$ are the analogous components of the quasiwave vector;

$$f_k=\frac{1}{e^{\frac{E_k-E_F}{k_BT}}+1} \tag{9}$$

is the Fermi distribution, where E_F is the Fermi energy level, and k_BT is the thermal energy.

The exchange integral $V_{\mathbf{kk}'}^{\mathbf{k}'\mathbf{k}}$ in Eq. (6) is determined by the expression

$$V_{\mathbf{kk}'}^{\mathbf{k}'\mathbf{k}}=\frac{e^2}{\varepsilon}\int d^3r_1 d^3r_2 \frac{\Psi_{\mathbf{k}}^*(\mathbf{r}_1)\Psi_{\mathbf{k}'}^*(\mathbf{r}_2)\Psi_{\mathbf{k}}(\mathbf{r}_2)\Psi_{\mathbf{k}'}(\mathbf{r}_1)}{|\mathbf{r}_1-\mathbf{r}_2|}. \tag{10}$$

In the effective-mass approximation the Bloch wave functions $\Psi_{\mathbf{k}}(\mathbf{r})$ can be replaced by plane waves

$$\Psi_{\mathbf{k}}(\mathbf{r})=\frac{1}{\sqrt{V}}\,e^{i\mathbf{k}\cdot\mathbf{r}}, \tag{11}$$

where V is a normalization volume. In this approximation it must be assumed that all wave functions appearing in the integral (10) refer to the same valley of the energy spectrum of the electron.

We make the following substitution of integration variables in Eq. (10):

$$\mathbf{r}=\mathbf{r}_1-\mathbf{r}_2, \tag{12}$$

$$\mathbf{r}'=\frac{\mathbf{r}_1+\mathbf{r}_2}{2}. \tag{13}$$

Then the integration over $\mathbf{r}'$ gives the volume of the system V and the exchange integral becomes

$$V_{\mathbf{kk}'}^{\mathbf{k}'\mathbf{k}}=\frac{e^2}{\varepsilon V}\int d^3r\frac{e^{i(\mathbf{k}-\mathbf{k}')\cdot\mathbf{r}}}{r}. \tag{14}$$

Replacing in Eq. (7) the summation over $\mathbf{k}'$ by integration, we obtain the single-particle energy

$$\varepsilon(\mathbf{k})=E_k-\frac{2e^2}{\pi\varepsilon}Q_{\mathbf{k}}, \tag{15}$$

where

$$Q_{\mathbf{k}}=\frac{1}{16\pi^2}\int d^3k' f_{k'}\int d^3r\,\frac{e^{i(\mathbf{k}-\mathbf{k}')\cdot\mathbf{r}}}{r}. \tag{16}$$

The second term in Eq. (15) gives the single-particle exchange energy,[13,14] which depends on the quasiwave vector $\mathbf{k}$. In the literature (see, for example, Ref. 15), the single-particle exchange correction to the total energy of a quasiparticle is, as a rule, averaged over the quasiwave vector:

$$Q=g^{-1}(0)\int d^3kQ_{\mathbf{k}}f_k, \tag{17}$$

where the normalization constant is

$$g(0)=\int d^3kf_k. \tag{18}$$

Therefore, the averaged single-particle exchange energy is

$$U_{\text{ex}}=-\frac{2e^2}{\pi\varepsilon}Q. \tag{19}$$

The quantity Q, defined in Eq. (17), can be put into the form

$$Q=\frac{1}{16\pi^2}g^{-1}(0)\int\frac{d^3r}{r}|g(\mathbf{r})|^2, \tag{20}$$

where $g(\mathbf{r})$ is the inverse Fourier transform of the Fermi distribution function:

$$g(\mathbf{r})=\int d^3ke^{i\mathbf{k}\cdot\mathbf{r}}f_k. \tag{21}$$

2.2. *General expression for the single-particle exchange energy in a semiconductor.* Equations (19)–(21) completely determine the single-particle energy. We shall further transform them in order to decrease the multiplicity of the integration by separating the angular part and representing the final expression for the exchange energy in a form convenient for practical applications.

In the general case of ellipsoidal or spherical valleys in a semiconductor, the problem of finding the single-particle exchange energy can be reduced to a calculation of a double integral which depends only on a single parameter η — the ratio of the Fermi energy (measured from the conduction-band bottom) to the thermal energy k_BT:

$$U_{\text{ex}}=-\frac{e^2}{\pi\varepsilon}Ak_T\frac{K(\eta)}{\frac{\sqrt{\pi}}{2}F_{\frac{1}{2}}(\eta)},\quad \eta=\frac{E_F}{k_BT}. \tag{22}$$

Here $K(\eta)$ is a function defined as

$$K(\eta)=\int_0^\infty \rho J^2(\rho)\,d\rho,$$

$$J(\rho)=\int_0^\infty \cos(q\rho)\ln(e^{\eta-q^2}+1)\,dq; \tag{23}$$

k_T is the characteristic thermal momentum of the carriers

$$k_T=\sqrt{\frac{2m_c k_B T}{\hbar^2}}; \tag{24}$$

$F_{\frac{1}{2}}(\eta)$ is the Fermi integral

$$F_{\frac{1}{2}}(\eta)=\frac{2}{\sqrt{\pi}}\int_0^\infty \frac{\sqrt{\gamma}\,d\gamma}{e^{\gamma-\eta}+1}; \tag{25}$$

A is the anisotropy factor in the dispersion relation

$$A=\frac{m_c}{\sqrt{m_\perp(m_\parallel-m_\perp)}}\arcsin\left(\sqrt{1-\frac{m_\perp}{m_\parallel}}\right),$$

$$m_\perp<m_\parallel; \tag{26}$$

$$A=\frac{m_c}{\sqrt{m_\perp(m_\perp-m_\parallel)}}\ln\left(\sqrt{\frac{m_\perp}{m_\parallel}-1}+\sqrt{\frac{m_\perp}{m_\parallel}}\right),$$

$$m_\perp>m_\parallel, \tag{27}$$

where

$$m_c^3=m_\perp^2 m_\parallel. \tag{28}$$

It is obvious that for an isotropic dispersion relation ($m_\perp=m_\parallel$) the factor $A=1$. But the value of A is found to be close to 1 even for the common anisotropic semiconductors. For example, for silicon, which has a comparatively high anisotropy, $A=0.94$. It can be assumed, therefore, that the anisotropy of the isoenergetic surface of electrons has virtually no effect on the magnitude of the exchange energy.

The representation given above for the final result is useful for practical calculations, since it is sufficient to calculate once and tabulate the function $K(\eta)$ in order to obtain the single-particle energy for different ratios of the Fermi energy (measured from the conduction-band bottom) and the thermal energy k_BT.

The integrals appearing in the function $K(\eta)$ can be calculated analytically in two limiting cases — for strongly degenerate and nondegenerate electron gases.

2.3. *Strongly degenerate electron gas.* In the limiting case of strong degeneracy

$$K(\eta)=\eta^2, \tag{29}$$

$$F_{\frac{1}{2}}(\eta)=\frac{4}{3\sqrt{\pi}}\eta^{\frac{3}{2}}, \tag{30}$$

and therefore

$$U_{\text{ex}}=-\frac{3e^2}{2\pi\varepsilon}Ak_F. \tag{31}$$

For an isotropic dispersion relation Eq. (31) transforms into the Slater equation (1). The expression for Q_k, which is obtained in this case from Eq. (16), is identical to the quasiparticle dispersion relation presented in Refs. 13 and 14:

$$Q_k=k_F F(x),\quad x=\frac{k}{k_F}; \tag{32}$$

$$F(x)=\frac{1}{2}\left(1+\frac{1-x^2}{2x}\ln\left|\frac{1+x}{1-x}\right|\right). \tag{33}$$

We note that the anisotropy of the isoenergy surface of the electrons in a semiconductor (for the case $m_\perp<m_\parallel$) was first taken into account in Ref. 16; the expression obtained in Ref. 16 for U_{ex} was then refined in Ref. 17.

2.4. *Nondegenerate electron gas.* In the case of a nondegenerate electron gas

$$K(\eta)=\frac{\pi}{4}e^{2\eta}, \tag{34}$$

$$F_{\frac{1}{2}}(\eta)=e^\eta, \tag{35}$$

and therefore

$$U_{\text{ex}}=-\frac{e^2}{2\sqrt{\pi}\varepsilon}Ak_T e^{\frac{E_F}{k_BT}}. \tag{36}$$

This formula will be discussed in the next section.

3. RELATION OF THE EXCHANGE INTERACTION WITH THE PARAMETERS OF THE SYSTEM OF ELECTRONS

3.1. *Transformation of the final asymptotic expressions.* The single-particle exchange interaction energy is represented in a simple analytical form for two limiting states of an electron gas in a semiconductor: degenerate state (Eq. 31) and nondegenerate state (Eq. 36). These formulas can be transformed into a clear and symmetrized form by introducing into the analysis the characteristic de Broglie wavelength of an electron ($\lambda=2\pi/k$, where k is the characteristic quasiwave vector) and the average distance between electrons ($a=n^{-\frac{1}{3}}$). The quantity a determines the Coulomb interaction energy between two electrons $e^2/\varepsilon a$ and the ratio λ/a determines the degree of overlapping of the wave functions, i.e., the intensity of the exchange interaction. Equations (31) and (36) can then be written in the unified form

$$U_{\text{ex}}\sim-\frac{A}{M}\frac{e^2}{\varepsilon a}\left(\frac{\lambda}{a}\right)^2. \tag{37}$$

The numerical factor equals $9/8\pi$ for a degenerate electron gas and $1/2\pi$ for a nondegenerate gas. In the expression (37) λ is the electron de Broglie wavelength associated with the characteristic electron energy:

$$\lambda=\lambda_F\left(1-\frac{5\pi^2}{24}\left(\frac{k_BT}{E_F}\right)^2\right),\quad \lambda_F=\frac{2\pi}{k_F},\quad T\to 0 \tag{38}$$

for a degenerate gas and

$$\lambda=\lambda_T=\frac{2\pi}{k_T} \tag{39}$$

for a nondegenerate electron gas.

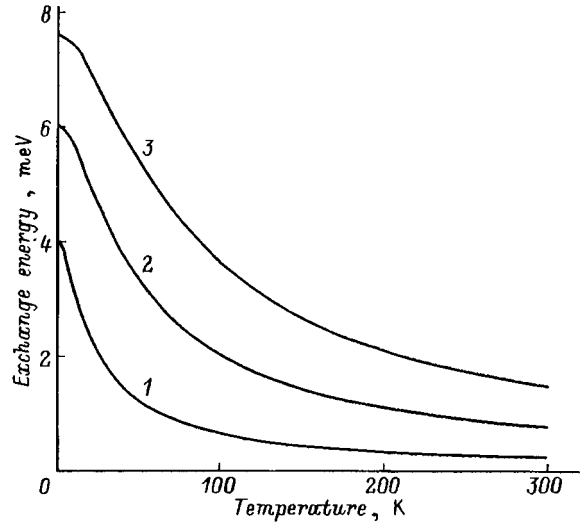

FIG. 1. Temperature dependence of the single-particle exchange energy in degenerate GaAs with different doping levels N_D, 10^{16} cm^{-3}: *1* — 1.5, *2* — 5, *3* — 10. Parameters: Electron effective mass $m_c=0.067m_0$; dielectric constant $\varepsilon=12.9$.

Equation (37) reflects the fact that the greater the electron wavelength and the shorter the distance between the electrons, the stronger is the exchange interaction.

3.2. *Temperature dependence of the single-particle exchange interaction energy.* We shall now consider the temperature dependence of the single-particle exchange energy in a semiconductor in the case of degenerate and nondegenerate gallium arsenide. It was calculated according to formula (22) and is presented in Figs. 1 and 2. To understand these dependences clearly, it is sufficient to analyze Eq. (37) for the exchange energy in two limiting states of the electron gas.

In a degenerate semiconductor the single-particle exchange energy decreases monotonically with inceasing temperature (Fig. 1). This decrease is due to the temperature decrease of the characteristic de Broglie wavelength λ of the electrons, since a does not depend on the temperature (the electron density in the conduction band is constant).

In a nondegenerate semiconductor the exchange energy varies nonmonotonically with increasing temperature (Fig. 2). At low temperature the exchange interaction energy increases as a result of a decrease in a (the electron density increases) and reaches a maximum at the ionization temperature of all donors, when the increase in the carrier density saturates. Then the exchange energy starts to decrease, but now it does so as a result of the temperature decrease in λ, i.e., a decrease in the overlapping of the wave functions. The effect of such a temperature dependence of the exchange energy in a nondegenerate semiconductor is that the exchange correction to the band gap in a nondegenerate semiconductor is much smaller than the exchange correction in a degenerate semiconductor.

4. CONCENTRATION NARROWING OF THE BAND GAP

The electron–electron interaction decreases the width of the band gap in a semiconductor. There are several mechanisms for this narrowing, which we shall examine for the example of a *n*-type semiconductor. The Debye–Hückel lowering (3) of the conduction-band bottom and the rising of the valence-band top equivalent to it (if it is assumed that electrons and holes are screened by the electron gas identically; see, for example, Ref. 11) and the lowering of the conduction-band bottom by the amount of the exchange interaction (22) make the main contribution. The total narrowing of the band gap will then be

$$\Delta E_g=2U_{DH}+U_{\rm ex}. \tag{40}$$

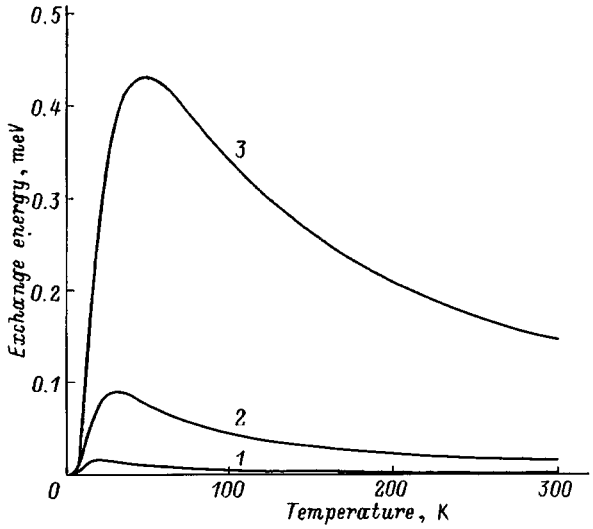

FIG. 2. Temperature dependence of the single-particle exchange energy in nondegenerate GaAs for different doping levels N_D, 10^{15} cm^{-3}: *1* —0.1, *2* — 1, *3* — 10. The parameters of the semiconductor are the same as in Fig. 1.

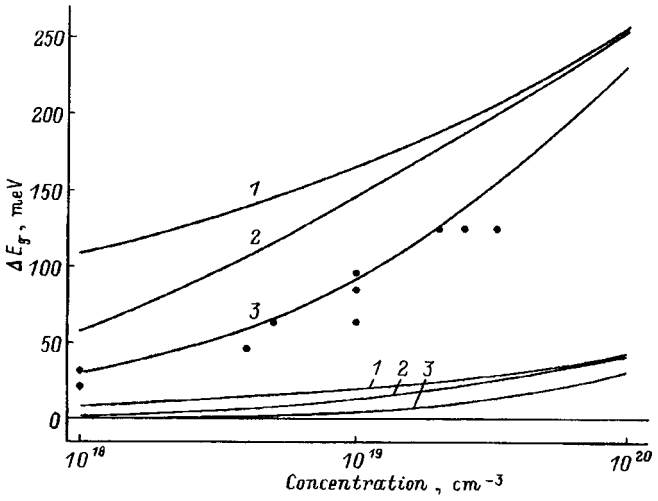

FIG. 3. Narrowing of the band gap in Si as a function of the free carrier density at different temperatures T, K: *1* — 4, *2* — 77, *3* — 300. Heavy lines — total narrowing; thin lines — exchange term. Experimental data are available for temperature $T=300$ K (indicated in the figure by dots).[19] Parameters: effective masses $m_\parallel=0.98m_0$, $m_\perp=0.9m_0$; dielectric constant $\varepsilon=11.9$.

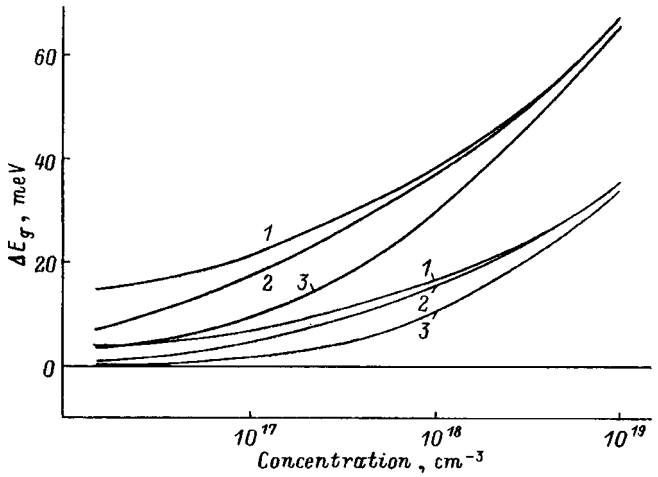

FIG. 4. Narrowing of the band gap in GaAs as a function of the free carrier density at different temperatures T, K: *1* — 4, *2* — 77, *3* — 300. Heavy lines — total narrowing; thin lines — exchange term. The parameters of the semiconductor are the same as in Figs. 1 and 2.

This formula was used to calculate the concentration dependences of the narrowing of the band gap for *n*-type silicon and gallium arsenide; these curves are presented in Figs. 3 and 4. The computational results agree well with the experimental data only for silicon. For gallium arsenide our values of the narrowing of the band gap are 1.5–2 times smaller than the available experimental values.[8] This could be due to different methods of performing the experiment: In gallium arsenide the measurements were performed according to the photoluminescence spectra, whereas in silicon the data on band-gap narrowing were obtained by measuring the transport coefficient in transistors with a different degree of doping of the emitter.[19] This method seems to us to be more reliable since in practice the tails of the density of states cannot affect the carrier transport coefficient, but at the same time they can play a substantial role in the formation of the photoluminescence spectrum.

The heavy lines in Figs. 3 and 4 represent the total narrowing of the band gap and the thin lines represent the contribution of the exchange energy which we are studying here. We see from Fig. 3 that in silicon the effect of the exchange mechanism is small compared with the Debye–Hückel correlation mechanism. In gallium arsenide, on the other hand, the effect of the exchange interaction is found to be substantial, as one can see from Fig. 4. For free electron density 10^{19} cm^{-3} the exchange term becomes the same as the correlation term. This stems from the fact that the exchange interaction arises only between electrons located in the same valley of k space. The presence of six valleys in silicon in the calculation of the exchange energy is therefore equivalent to a decrease in the electron density by a factor of 6. Conversely, the correlation energy depends only on the total electron density in the conduction band and therefore the relative contribution of the exchange interaction to the total narrowing of the band gap decreases as the number of valleys increases.

[1] K. E. Berggren and B. E. Sernellius, Phys. Rev. B **24**, 1971 (1981).
[2] D. N. Bychkovskiĭ, O. V. Konstantinov, and B. V. Tsarenkov, Fiz. Tekh. Poluprovodn. **29**, 152 (1995) [Semiconductors **29**, 80 (1995)].
[3] E. Wigner and F. Seitz, Phys. Rev. **43**, 804 (1933).
[4] E. Wigner and F. Seitz, Phys. Rev. **46**, 509 (1934).
[5] E. Wigner, Trans. Faraday Soc., **34**, 678 (1938).
[6] J. C. Slater, Phys. Rev. **81**, 385 (1951).
[7] A. P. Cracknell and K. Wong, *The Fermi Surface* [Russian trans., Atomizdat, Moscow, 1978].
[8] F. Herman and Sh. Skillman, *Atomic Structure Calculations*, Prentice-Hall Inc., 1963.
[9] S. Lundqvist and N. M. March [Eds.], *Theory of the Inhomogeneous Electron Gas*, Plenum Press, N. Y., 1983 [Russian trans., Mir, Moscow, 1987].
[10] O. Gunnarsson and B. I. Lundqvist, Phys. Rev. B **13**, 4274 (1976).
[11] D. N. Bychkovskiĭ, O. V. Konstantinov, and B. V. Tsrenkov, Fiz. Tekh. Poluprovodn. **24**, 1848 (1990) [Sov. Phys. Semicond. **24**, 1151 (1990)].
[12] L. D. Landau and E. M. Lifshitz, *Quantum Mechanics*, Pergamon Press, N. Y. [Russian orig., Nauka, Moscow, 1989].
[13] N. W. Ashcroft and N. D. Mermin in *Solid State Physics*, Holt, Rhinehart, and Winston, N. Y., 1976 [Russian trans., Mir, Moscow, 1979].
[14] F. Seitz, *Modern Theory of Solids*, McGraw-Hill, N. Y., 1940 [Russian trans., GTTL, Moscow, 1949].
[15] J. Slater, *Insulators, Semiconductors, and Metals* [Russian trans., Mir, Moscow, 1969].
[16] V. L. Bonch-Bruevich and R. Rozman, Fiz. Tverd. Tela (Leningrad) **6**, 2535 (1964) [Sov. Phys. Solid State **6**, 2016 (1964)].
[17] A. A. Rogachev, Author's Abstract of Doctoral Dissertation, A. F. Ioffe Physicotechnical Institute of the USSR Academy of Sciences, Leningrad, 1967.
[18] Huade Yao and A. Compaan, Appl. Phys. Lett. **57**, 147 (1990).
[19] S. M. Sze, *Physics of Semiconductor Devices*, Wiley, N. Y. [Russian trans., Mir, Moscow, 1984, Vol. 1, Chap. 3, Fig. 8].

Translated by M. E. Alferieff

Electron transport under Wannier–Stark localization conditions in silicon carbide polytypes

V. I. Sankin and I. A. Stolichnov

A. F. Ioffe Physicotechnical Institute, Russian Academy of Sciences, 194021 St. Petersburg, Russia
(Submitted May 13, 1996; accepted for publication September 16, 1996)
Fiz. Tekh. Poluprovodn. **31**, 577–584 (May 1997)

A detailed study is made of electron transport in high electric fields in natural superlattices of the $6H$ and $4H$ polytypes of silicon carbide. The electron behavior indicates the appearance and development of Wannier-Stark quantization over a wide range of electric fields, 100–2000 kV/cm. Direct measurements of the electron current as a function of the average electric field reveal a number of regions with negative differential conductivity. An analysis of these data shows that the observed effects are caused by different mechanisms which come into effect as the electric field is raised: (1) Bragg reflection of electrons from the boundary of the first miniband, (2) jump conduction between levels of a Wannier–Stark staircase induced by resonant electron–phonon interactions, and (3) resonant inter-miniband tunnelling from the first miniband into the second. © *1997 American Institute of Physics.* [S1063-7826(97)01705-5]

INTRODUCTION

Applying an electric field to a crystal is known to lead to a number of interesting effects. Many of these effects, such as the Frank–Keldysh effect, tunnelling, and others, received early experimental confirmation and have found widespread practical application. In this paper we examine one of the most interesting effects, for which this cannot be said: Wannier–Stark localization. A qualitative picture of this phenomenon can be obtained using the basic principles of the band theory of solids; this has been done most clearly by Gurevich.[1] The result of solving this problem is widely known to be the transformation, under the influence of the electric field, of the continuous band structure into discrete levels which are localized in space and which form a so-called Wannier–Stark staircase.[2] The distance between the levels (the Stark energy) is determined by

$$\Delta E = eFa. \tag{1}$$

Here e, F, and a are the electronic charge, the electric field, and the lattice period, respectively.

Since then the Wannier–Stark localization problem has been discussed widely in scientific publications. It should be noted that the correctness of Wannier's solution leading to Wannier–Stark localization has been questioned by some[3] because his model used a single-band approximation which did not take into account the possibility of mixing of states from different bands by the electric field. It was later shown[4] that even if interband tunnelling is taken into account, the Wannier–Stark localization remains, but the later result has itself generated an active controversy.[5] This is evidence of the theoretical complexity of the problem and of the need for experimental data for the entire range of related questions. The great practical interest in experimental data on this topic arises in the possibility, in principle, of obtaining a negative differential conductivity, which is very important for many applications.

Practical observation of Wannier–Stark localization is possible only with use of a superlattice which has a charge carrier spectrum consisting of narrow bands known as minibands. A number of Wannier–Stark localization effects related to the appearance of a negative differential conductivity have been predicted theoretically for this type of structure.

The possibility, in principle, of obtaining a negative differential conductivity on an artificial superlattice due to the field-induced localization was predicted by Esaki.[6] The threshold field for its appearance is determined by

$$eFd > h/\tau. \tag{2}$$

Here h and τ are Planck's constant and the electron scattering time, respectively; and d is the superlattice period. The criterion (2) means that negative differential conductivity associated with this effect arises when the frequency eFd/h of the Stark oscillations exceeds the scattering frequency.

In the effect considered above the Stark energy is still small as long as the quasicontinuity of the first miniband is preserved, i.e., many Stark levels fit into its width. As the field is increased further, the region $l \sim E_1/eF$ in which the electron is localized becomes smaller. Here E_1 is the width of the first miniband. The miniband is then destroyed and the spectrum takes the form of discrete energy levels. Electron transport in a system of this sort has been described by Emin and Hart.[7] Conduction becomes possible in this range of electric fields due to jumps between the discrete Stark levels with the participation of phonons. A negative differential conductivity associated with resonances of phonon transitions was predicted.[7] The field corresponding to these resonances is given by

$$eFdn = \hbar\omega. \tag{3}$$

Here $\hbar\omega$ is the energy of the corresponding phonon, and n takes the values 1,2,3, ...

At still higher fields, the Stark energy becomes high enough that only one level fits within the width of the miniband. This case has been discussed theoretically elsewhere.[8] A negative differential conductivity effect was predicted with a threshold field

$$F = E_1/2ed. \quad (4)$$

Yet another possible mechanism for the conductivity in the Wannier-Stark localization regime is interminiband resonant tunnelling.[9] It occurs when the height of the step in the Wannier–Stark staircase eFd equals the energy gap E_{12} between the first and second minibands; i.e.,

$$eFd = E_{12}. \quad (5)$$

As note above, in a number of theoretical papers[3,5] doubts have been raised about the correctness of the solutions implying the existence of Wannier–Stark staircases. This largely stems from the absence of convincing experimental confirmation of this phenomenon.

For a rather long time, studies of Wannier–Stark localization were carried out exclusively on artificial heterojunction superlattices, mainly of the type AlAs–GaAs, as proposed by Esaki.[6] The first manifestations of Wannier–Stark quantization were found in luminescence and optical spectra,[10] and after a few years observations of negative differential conductivity were reported.[11,12]

In this paper we propose to study Wannier–Stark localization on an object which differs substantially from those used previously: a natural superlattice which contains most of the polytypes of silicon carbide. From the standpoint of crystalline structure, the natural superlattice is defined rather simply. Silicon carbide is known to consist of a set of crystals which differ from one another in structure (i.e., polytypes). The simplest polytypes are cubic $3C$-SiC and hexagonal $2H$-SiC. There are no purely cubic or purely hexagonal polytypes among the more complicated polytypes. Each of them consists of layers ordered in a specific way with cubic and hexagonal surroundings. The best known polytypes are $4H$, $6H$, $8H$, $15R$, $21R$, and $27R$. The number denotes the number of atomic layers contained in a unit cell along the selected symmetry axis of the crystal, C, while the letter defines the symmetry of the unit cell: hexagonal (H) or rhombohedral (R). It is clear, therefore, that the size of the unit cell of most of the polytypes along the C axis exceeds the size of the cell for the simplest polytypes. For example, in the hexagonal series $4H$, $6H$, and $8H$ it exceeds the size for $2H$ by factors of 2, 3, and 4. In this sense, this series of polytypes has a natural one-dimensional superlattice.

How does this affect the energy of the crystals? Specifically, is it possible to isolate a one-dimensional superpotential in it with a period along the axis of the superlattice that exceeds the period of the primary crystal potential? It has been found experimentally that the band gap in the purely hexagonal polytype $2H$ is greater than that in the cubic $3C$ by 1 eV. Evidently, this means that the amplitude of the crystal potential of an atomic layer with a hexagonal surrounding is substantially greater than the amplitude of a layer with a cubic surrounding. These hexagonal layers have a fixed periodicity with a period that exceeds the primary period of the crystal. For the series $4H$, $6H$, $8H$ this excess is same: by factors of 2, 3, and 4, respectively. Thus, there is reason to assume in these polytypes the existence of a superlattice with a period that exceeds the period of the primary lattice by the corresponding number of factors. In terms of this model, we can say in accordance with the Kronig–Penney solution that the energy structure of the allowed band for $4H$ contains two minibands, that for $6H$, three, and that for $8H$, four.

Two bands have been observed previously in the optical spectra of many polytypes in the region from 1 to 2.7 eV,[13,14] i.e., well below the intrinsic absorption edge. Both bands were justifiably attributed to direct allowed electronic transitions at the localization point of the minimum of the conduction band from the ground state of the conduction band into higher conduction bands. A hypothesis was advanced.[14] According to this hypothesis, these bands were explained by transitions from the first into the second and third minibands.

Rather convincing confirmation of the presence of a narrow electronic band in a number of polytypes, such as $4H$, $6H$, $8H$, $15R$, $21R$, $27R$, and $33R$, has been obtained[15–17] in studies of collisional ionization in silicon carbide. It was found that the character of the collisional ionization depends strongly on the direction of the electric field. The following conclusions were drawn from the collisional ionization data:

(1) In uniaxial silicon carbide polytypes there is a narrow electron band in the direction of the superlattice axis and Wannier–Stark localization processes develop in that band under the action of high electric fields.

(2) The hole band has no features associated with the presence of a superlattice, or they are so small that they do not show up during collisional ionization.

The next natural step in the development of these studies was an attempt at direct observation of Wannier–Stark localization effects in electron transport by studying the current voltage characteristics of superlattice crystals in high fields.

EXPERIMENTAL TECHNIQUE

For studying electron transport in high fields we have developed an experimental apparatus that satisfies the following requirements: (1) the measured current in the sample is purely electronic, (2) the electric field in the sample is uniform, and (3) the current in the sample can be controlled independently of the field. The triode structure developed for these purposes has a number of important differences from a traditional transistor which should be considered separately.

The main element of this structure is a base that is doped with a deep acceptor impurity (scandium) with an ionization energy $E > 0.5$ eV. This makes it possible to achieve a hole concentration $p \sim 10^{10}$ cm^{-3} at room temperature. The characteristic deionization times for such an impurity in the space charge region when $p \sim 10^{10}$ cm^{-3} exceeds 10^{-2} s. This means that the forward-biased emitter $n^+ - p$ junction can be opened only by a constant voltage or by pulses of duration $t > 10^{-2}$ s. After the potential barrier has been lowered, however, injection (which is a fast process) can be realized with short pulses of duration $t < 10^{-6}$ s.

We now consider the collector $p - n^+$ junction. With reverse bias, the establishment of an electric field in the base is determined by the ionization process for the deep acceptor impurity, which takes place over a rather long time. Thus, if the reverse bias is created by sufficiently short pulses, the acceptor levels in the base remain neutral and the hole concentration, as stated above, is no more than 10^{10} cm^{-3},

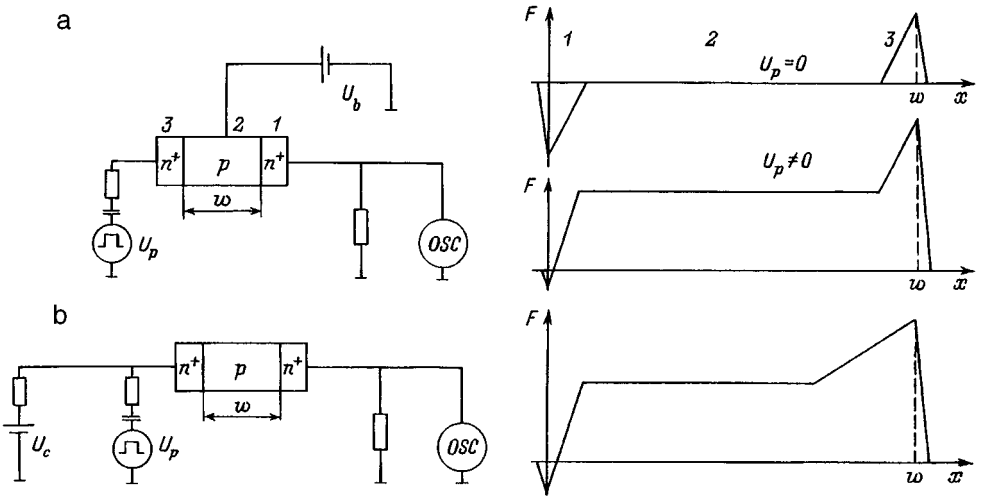

FIG. 1. The measurement setup and distribution of the electric field in the experimental device structure for the cases of a high uniform field (a) and a very high nonuniform field (b).

which corresponds to screening of the electric field over a distance of less than 10^{-1} cm. Thus, for a base width of 5–10 μm, screening of the field will be very weak and the field in the base may be assumed to be essentially uniform Fig. 1a. Its magnitude is given by $F=V/w$, where V is the magnitude of the voltage pulse, and w is the width of the base region.

The operating principle of this structure is as follows: a pulsed reverse bias V_p with a period $t_p \sim 10^{-7}$ s is applied between the collector and emitter. A constant forward bias V_b is applied to the emitter-base junction. The associated emitter-base current essentially has no effect on the injection magnitude due to the large (10^7-10^8 Ω) resistance of the p-region. The task of this bias is to reduce the height of the contact barrier. A pulsed voltage applied between the collector and emitter ensures a uniform electric field which, on propagating through the base, reaches the open emitter junction and gives rise to injection. The injection current increases together with V_p, but is can be limited by changing V_b. The resistance of the base region decreases by a factor of 10^3-10^4 during the pulsed current flow, because the electrons injected into the base are captured by the field and pass through the base to the collector. Thus, an injection-transition mechanism for current flow is realized in the experimental device. This electrical circuit corresponds to a transistor incorporated with a common emitter.

All the conditions enumerated above as necessary for studying electron transport in high field under Wannier–Stark localization conditions are realized in this experimental structure. A pure electron current, controlled by a constant bias which has no effect on the magnitude of the field in the base, flows through the base. The field over the entire width of the base is then essentially uniform. We have described this experimental structure elsewhere for the first time.[18] A triode structure was used later[12] and its use was justified by the same considerations.

This experimental structure was created by growing films of two scandium-doped polytypes, 4H and 6H, by means of the sublimation sandwich method on an n-type substrate. It should be noted that the problem of controlled growth of a given polytype has not been solved in practice and the required object is found by selection from a large number of samples. Then an n-type layer with a thickness of 1–2 μm was grown on the p-type film. The thickness of the base layer was determined by direct measurements of the width of the luminescence region seen at the end of the fabricated three-layer structure. Usually the thickness of the base layer was 5–10 μm. After this, the experimental structure was prepared by photolithography. The diameters of the collector, base electrode, and emitter were 420, 400, and 200 μm, respectively.

The measurement scheme is shown in Fig. 1a. The current in the emitter circuit was recorded during the measurements. When the pulsed voltage was changed, the base bias was usually held constant. In addition, in order to observe the states of the experimental structure, the constant currents in the emitter and base circuits were recorded.

RESULTS AND DISCUSSION

The measured N-shaped current voltage characteristics for the 4H and 6H polytypes are shown in Fig. 2. This sort of characteristic was first obtained for the 6H polytype.[19,20] The threshold field at the beginning of its falling portion was $1.2-1.7\times 10^5$ V/cm in the various samples with an error of about 10% due primarily to the inaccuracy in determining the width of the base layer. Somewhat later this effect was obtained in a second polytype, 4H.[21] Figure 2 shows that the current voltage characteristics are qualitatively similar, but the threshold field for 4H is almost a factor of 2 higher than for 6H at $2.7-3\times 10^5$ V/cm. Figure 2 shows structures for which the N-shaped current voltage characteristic showed up most distinctly. In some of the samples the current drop was less than 20% and in many cases observation of the effect was inhibited by uncontrolled current losses and microplasma breakdown. In some of the samples, even when there

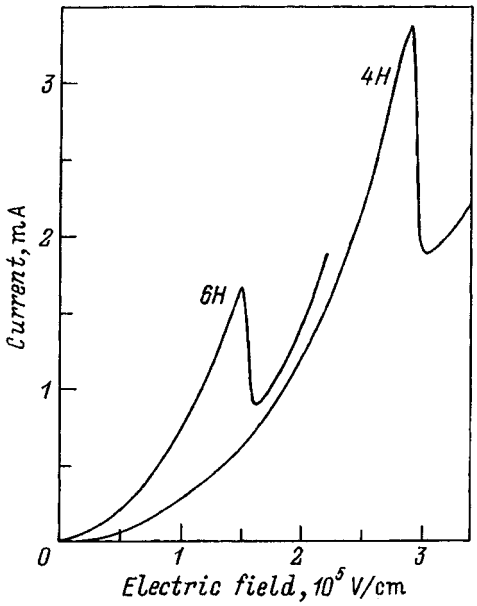

FIG. 2. Current as a function of field in experimental structures based on the $6H$ and $4H$ polytypes.

were no losses of this kind, the current voltage characteristic retained its monotonic character up to the breakdown field.

For numerical calculations in the course of interpreting the data we have used the following parameters: $d=7.5\times10^{-8}$ cm for $6H$-SiC, $d=5\times10^{-8}$ cm for $4H$-SiC, $m=m_0$, and $\mu=100$ cm^2/(V·s). Here m, μ, and m_0 are, respectively, the mass of the electron mass, its mobility along the superlattice axis, and the mass of the free electron.

Condition (2) implies that the threshold field for negative differential conductivity associated with the Esaki–Tsu effect depends directly on the superlattice period. An estimate of the scattering time τ according to the formula

$$\tau=m\mu/e \tag{6}$$

yields $\tau=6\times10^{-14}$ s, which is in fair agreement with the estimate given by Eq. (2). The estimate of τ given by that formula is 4.4×10^{-14} s for $4H$ and 5.5×10^{-14} s for $6H$.

The other condition for this effect is

$$eFl>E_1, \tag{7}$$

where l is the mean free path, and E_1 is the width of the first miniband. Evidently, the width of the first miniband in $4H$ should be considerably greater than in $6H$, since the superlattice period of the former is a factor of 1.5 shorter. Thus, the threshold field for appearance of negative differential conductivity in the $4H$ and $6H$ polytypes corresponds to the conditions for the Esaki–Tsu effect, while the observed difference in the threshold fields for these polytypes are also consistent with these conditions. This allows us to interpret the negative differential conductivity observed in these polytypes as the initial phase of a Wannier–Stark localization process, specifically, as Bragg reflection of electrons from the edge of the first miniband.

The observed negative differential conductivity also can obviously be explained by other causes. An N-shaped current voltage characteristic is also known to arise during a recombination instability, when the current carriers are captured at repulsive centers.[22] The time of flight of the electrons through the base layer, $t<10^{-10}$ s, however, is much shorter than the recombination time, so the probability of this process is reduced. Furthermore, in the case of a recombination instability the threshold fields for $4H$ and $6H$ would be essentially the same.

It thus seems reasonable to interpret the observed effects in terms of a theory of Wannier–Stark localization. The parameters of these effects satisfy the criteria for Wannier–Stark localization and the difference in the threshold fields for the two polytypes is consistent with the difference in their superlattice parameters. The rising branch of the current voltage characteristic to the right of the threshold point can be explained by increased injection as the field is raised, as well as by transverse heating of the electrons. In addition, not all the electrons which participate in the current flow are subject to Wannier–Stark quantization. Because of the geometry of the experimental structure, current can flow in it in directions other than along the superlattice axis.

STUDIES OF WANNIER–STARK LOCALIZATION IN VERY HIGH ELECTRIC FIELDS

Until now, we have been concerned with Wannier-Stark localization effects in strong fields, but only such that the distances between the levels in the Stark staircase are so small that the miniband can be regarded as quasicontinuous; i.e., $E_1\gg eFd$. When the electric field is increased further, the continuity of the electron spectrum is broken and the region in which an electron is localized becomes smaller. We define very high fields as the fields in which the size of this region is much smaller than the mean free path, i.e.,

$$l\gg E_1/eF. \tag{8}$$

The experimental procedure was modified slightly in order to study the further development of the Wannier–Stark localization process in these high fields. This was necessary because the technique described above does not permit attainment of fields above 5×10^5 V/cm because of local breakdown. The main change in the experimental conditions was that, in addition to the pulsed voltage, a constant voltage was applied to the collector junction in order to bias it in the reverse direction. This meant that, besides a pulsed voltage that was uniform over the entire base region, a much higher constant field was concentrated in the space charge region at the collector junction. The measurement scheme and field distribution in the structure for this case are shown in Fig. 1b. Obviously, the field in the space charge layer is nonuniform. Since this junction is formed by a heavily doped n^+ region with $N_d-N_a=3-5\times10^{18}$ cm^{-3} and a p region with $N_a-N_d<2\times10^{17}$ cm^{-3}, it can be regarded as sharp and asymmetric, while the electric field inside it varies linearly with position. The maximum field at the $p-n^+$ boundary is then

$$F_m=2V(eN/2\varepsilon V)^{1/2}, \tag{9}$$

where ε is the dielectric constant, and $N=N_a-N_d$. The average field within each of the regions is equal to half the

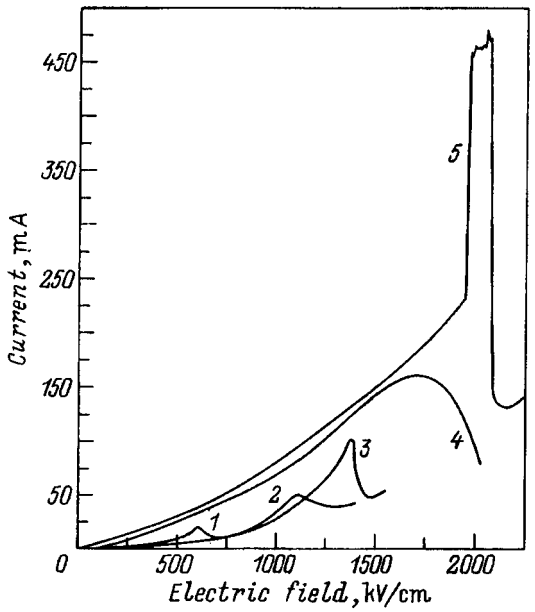

FIG. 3. Current as a function of field for the experimental structures based on the 6*H* polytype (very high electric field case). See comments on this figure in the text.

maximum. In this experimental setup the pulsed field serves to ensure injection of electrons into the base and make them drift into the high field region.

This experimental technique made it possible to investigate the current voltage characteristics of structures based on the 4*H* and 6*H* polytypes at fields ranging from 100 to 2000 kV/cm. The main results are shown in Figs. 3 and 4. The characteristics for the two polytypes have a number of structural features, of which there are many more for 6*H* than for 4*H*. Here we propose an interpretation of these data in terms of the theory of Wannier–Stark localization.

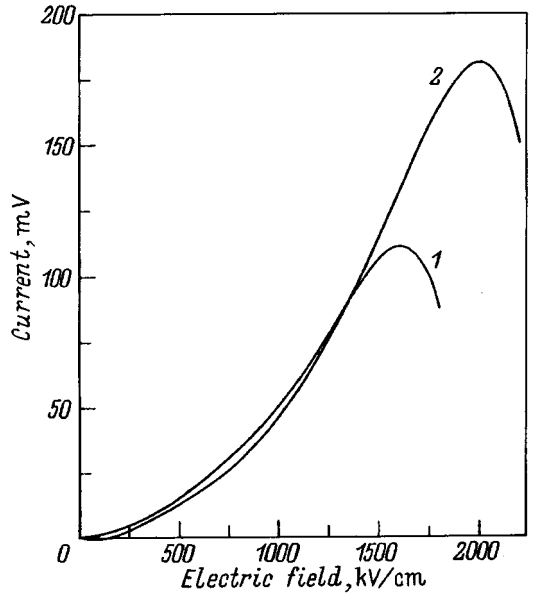

FIG. 4. Current as a function of field for the experimental structures based on the 4*H* polytype (very high electric field case). See comments on this figure in the text.

The current–voltage characteristics for the 6*H* polytype contain five structural features (denoted by the labels *1*–*5*), of which four have a segment with a negative differential conductivity, while the fifth has a sharp current burst, as well as a segment with a negative differential conductivity (Fig. 3). Region *1* is characterized by a threshold field of 600 kV/cm. It is unlikely that this effect is caused by Bragg reflection of electrons, i.e., that it is the initial stage of a Wannier–Stark localization process. As noted above, the threshold field for Bragg reflection is about 150 kV/cm. In this experimental setup it was not possible to produce such low fields, since even without an external field the $p-n$ junction contact barrier is 2.7 V, which corresponds to an average field in the space charge region of over 150 kV/cm. In order to lower the field further it would be necessary to reverse the external voltage at the collector junction, but then the three-electrode structure can no longer function.

The threshold field of 600 kV/cm for the 6*H* polytype corresponds to a Stark energy of 45 meV, which suggests strong localization leading to failure of the quasicontinuity condition for the electron spectrum in the first miniband. Then conduction can occur through jumping of electrons between quasidiscrete levels with the participation of phonons. This mechanism for conduction has been examined theoretically in two papers.[7,8] The physical models upon which the calculation is based were different in these two papers, so the predicted results were different. Both papers do conclude that the current voltage characteristic must have the form of resonances with threshold fields for the appearance of negative differential conductivity given by the equation

$$eFdn = \text{const}. \tag{10}$$

In Ref. 7 the constant was the phonon energy and in Ref. 8, the width E_1 of the first miniband. The factor $n = 1,2,3, \ldots$ corresponds to the number of superlattice layers through which an electron jumps.

In the current voltage characteristic for the 6*H* polytype the features labelled *1*, *2*, and *3* correspond to Stark energies of 45, 80, and 103 meV, respectively. These are close to the transverse (46 meV) and longitudinal (77 meV) acoustic phonon energies, and to the longitudinal optical phonon energy (103–112 meV) at the conduction band minimum.[23] Thus, the negative differential conductivity observed in regions *1*, *2*, and *3* can be interpreted as phonon assisted electron jumps between neighboring levels of a Stark staircase. Here the threshold fields for negative differential conductivity satisfy Eq. (3) with $n=1$, i.e., for transitions between neighboring superlattice sites. Transitions with $n>1$ are not observed, since they take place at substantially lower fields which were not technically attainable in our experiment. Low fields can also lead to failure of the strong localization condition (8), which will make it impossible to observe this effect. It should also be noted that transitions with $n>1$ are more subtle effects and it may be hard to see them because of the different loss mechanisms in the bulk and on the surface, since the problem of crystal quality becomes crucial in high field studies. Thus, it is doubtful, in principle, whether it is possible to observe multiplicative series with $n>1$.

The Stark energy corresponding to the threshold field in region *4* is 125–130 meV, or substantially higher than the known phonon energies at the conduction band minimum. Thus, there is reason to interpret the observed effect in terms of the model considered in Ref. 8, where the width of the first miniband must be a multiple of the Stark energy. The Stark energy at the threshold field is $1/2E_1$.[8] This easily yields $E_1 = 250-260$ meV. Thus, the width E_1 has been estimated directly for the first time and this value is consistent with other qualitative estimates of the width of the first miniband,[24] as well as with the line of reasoning introduced above in connection with the interpretation of the data for homogeneous fields.

Region *5* is distinguished from the other four in that the negative differential conductivity segment is preceded by a sharp current rise. In itself, a sharp rise in the current at high fields is an ordinary event which accompanies breakdown phenomena. The distinctive feature of the present situation is that the current falls after it has risen. During the observations, we recorded both a pulsed current associated with the electron current from the emitter and a constant current caused by local breakdown and uncontrolled leakage into the collector junction region. A drop was observed only in the current voltage characteristic of the pulsed current. In addition, the emission accompanying the sharp rise in the pulsed current was quenched at the threshold field for the negative differential conductivity.

The experimental observations can be explained as follows: the section with a rapid rise in the electron current is associated with resonant tunnelling of electrons from states in the discrete spectrum of the first miniband into the second miniband, which is still quasicontinuous. The subsequent current drop can be attributed to Bragg reflection of electrons in the second miniband. Based on the simplest rule for the increase in the size of the first miniband as the band number rises, we can assume that the second miniband is roughly four times wider than the first and that it is still quasicontinuous at the available fields. Thus, electron Bragg reflection can occur in it. Interminiband resonant tunnelling is possible when condition (5) is met.[9] It is correct to characterize the resonant tunnelling process by the maximum, rather than the average, field in the space charge region. Thus, the Stark energy corresponding to interminiband tunnelling is about 300 meV. Here the sum $E_1+E_{12}+E_2<1.55$ eV, in good agreement with the spectral location of the interminiband absorption band due to transitions between the first and second minibands.[14]

These results make it possible to refine the scheme for electron heating proposed earlier.[24] This scheme was used to interpret data on collisional ionization and was based on the assumption that there is no tunnelling between the first and second minibands, while transitions into the second miniband are caused by an increase in the energy of the electrons through transverse heating as they are scattered by phonons. Our data show that electrons can tunnel into the second miniband and that this occurs at a field 20% below the avalanche breakdown field.

Similar measurements were made for the $4H$ polytype. The resulting current voltage characteristics are shown in Fig. 4. Only two features containing a negative differential conductivity were observed at threshold fields of $(1.6-1.7)\times 10^6$ V/cm and $(1.9-2)\times 10^6$ V/cm, which correspond to Stark energies of 80–85 and 96–100 meV. These values are close to the energies of the longitudinal acoustic and optical phonons.[25] No other features associated with resonant interactions of phonons with Wannier–Stark staircase states were observed in $4H$. This can be explained by the fact that the condition for strong localization in the $4H$ polytype, which has a much wider first miniband than $6H$, is satisfied at higher fields. In particular, this condition cannot be satisfied at a Stark energy corresponding to the energy of the transverse acoustic phonon.

The absence of a feature associated with complete localization of the first miniband can be explained by the fact that, because of the large width of the first miniband in $4H$, condition (4) is satisfied only at very high electric fields in excess of the limit imposed by avalanche breakdown. In addition, we cannot say that our measurements provide a complete picture of the evolution of the Wannier–Stark localization process in the $4H$ and $6H$ polytypes. Further improvements in the experimental technique and in the quality of the experimental device structures may lead to the observation of new effects.

CONCLUSION

In this paper for the first time we have obtained a most detailed characterization of electron transport during the evolution of Wannier–Stark localization. It is not by chance that these data were obtained on a natural superlattice of silicon carbide, which is free of serious deficiencies of the type intrinsic to even the most perfect artificial superlattices.

We might expect that the picture of Wannier–Stark localization obtained here is not complete and that it will be enriched by new effects in the future. Probably, it will be more complicated and largely unpredictable in the rhombohedral polytypes of SiC. At the same time, detection of a number of the electron transport effects is extremely problematic. This applies first of all to transitions between levels of the Stark staircase caused by electron jumps between distant layers of the superlattice involving phonons (the multiplicative series with $n>1$). We have shown in this paper that the strong localization condition (8) fails for these transitions and that this occurs even for the very narrow first miniband, since its narrowing is, as a rule, accompanied by a reduction in the mean free path.

We note in concluding that superlattices of the different polytypes of silicon carbide are thus far the only natural objects in which Wannier–Stark localization effects have been observed over a wide range of electric fields. Our data suggest the possibility of creating microwave devices, including oscillators and amplifiers, based on the effects observed here.

We consider it our pleasant duty to thank E. N. Mokhov for help in growing the heavily doped n^+ layers of silicon carbide.

This work was supported by the Russian Fund for Fundamental Research (Project 94-06258-a), as well as by the Program on the Physics of Solid State Nanostructures of the

Ministry of Scientific and Technological Industries (Project 1-003).

[1] L. É. Gurevich, *Materials from the VIth Winter School of the A. F. Ioffe Physicotechnical Institute* [in Russian], Leningrad (1971), p. 175.
[2] G. D. Wannier, Phys. Rev. **11**, 432 (1960).
[3] A. Rabinovitch and J. Zak, Phys. Rev. B **4**, 2358 (1971).
[4] D. Emin and C. F. Hart, Phys. Rev. B **36**, 7353 (1987).
[5] L. Kleiman, Phys. Rev. B **41**, 3857 (1990).
[6] L. Esakv and R. Tsu, IBM J. Res. Dev. **14**, 61 (1970).
[7] D. Emin and C. F. Hart, Phys. Rev. B **36**, 2530 (1987).
[8] R. Tsu and G. Dohler, Phys. Rev. B **12**, 680 (1975).
[9] R. F. Kazarinov and R. A. Suris, Fiz. Tekh. Poluprovodn. **6**, 148 (1972) [Sov. Phys. Semicond. **6**, 120 (1972)].
[10] P. Voisin, J. Bleuse, C. Blouch, S. Gailard, C. Alibert, and A. Regreny, Phys. Rev. Lett. **61**, 1639 (1988).
[11] A. Sibille, J. F. Palmier, H. Wong, J. C. Esanault, and F. Mollot, Phys. Rev. Lett. **64**, 52 (1990).
[12] F. Bettram, F. Capasso, D. Sivco, A. Hutchinson, S. Chu, and A. Cho, Phys. Rev. Lett. **64**, 3167 (1990).
[13] E. Biderman, Solid Status Commun. **3**, 343 (1965).
[14] G. B. Dubrovskiĭ, A. A. Lepneva, and E. I. Radovanova, Phys. Status Solidi B, **57**, 423 (1973).
[15] A. P. Dmitriev, A. O. Konstantinov, D. P. Litvin, and V. I. Sankin, Fiz. Tekh. Poluprovodn. **17**, 1093 (1983) [Sov. Phys. Semicond. **17**, 686 (1983)].
[16] V. I. Sankin, Yu. A. Vodakov, and D. P. Litvin, Fiz. Tekh. Poluprovodn. **18**, 2146 (1984) [Sov. Phys. Semicond. **18**, 1339 (1984)].
[17] Yu. A. Vodakov, D. P. Litvin, V. I. Sankin, E. N. Mokhov, and A. D. Roenkov, Fiz. Tekh. Poluprovodn. **19**, 814 (1985) [Sov. Phys. Semicond. **19**, 502 (1985)].
[18] V. I. Sankin, A. V. Naumov, A. A. Vol'fson, M. G. Ramm, L. M. Smerklo, and A. V. Suvorov, Pis'ma Zh. Tekh. Fiz. **15**, 43 (1989) [Sov. Phys. Tech. Phys. Lett. **15**, 98 (1989)].
[19] V. I. Sankin and A. V. Naumov, Pis'ma Zh. Tekh. Fiz. **16**, 91 (1990) [Sov. Phys. Tech. Phys. Lett. **16**, 922 (1990)].
[20] V. Sankin and A. Naumov, Superlat. Microstruct. **10**, 353 (1991).
[21] V. I. Sankin, A. V. Naumov, and I. A. Stolichnov, Pis'ma Zh. Tekh. Fiz. **17**, 38 (1991) [Sov. Phys. Tech. Phys. Lett. **17**, 328 (1991)].
[22] A. F. Volkov and Sh. M. Kogan, Usp. Fiz. Nauk **96**, 633 (1968).
[23] V. I. Sankin, Fiz. Tverd. Tela **17**, 1191 (1975) [*sic*].
[24] V. I. Sankin, D. P. Litvin, and Yu. A. Vodakov, Springer Proc. in Phys. **56**, 225 (1991).
[25] G. B. Dubrovskiĭ and V. I. Sankin, Fiz. Tverd. Tela **17**, 1847 (1975) [*sic*].

Translated by D. H. McNeill

Low-frequency Hall conductance of a semi-infinite two-dimensional system

V. B. Shikin

Institute of Solid-State Physics, Russian Academy of Sciences, 142432 Chernogolovka, Russia
Submitted May 23, 1996; accepted for publication September 16, 1996)
Fiz. Tekh. Poluprovodn. **31**, 585–586 (May 1997)

A contact theory of the current-voltage characteristic at finite frequencies is constructed for a semi-infinite two-dimensional electronic system with two point contacts. It is noted that the relative arrangement of the contacts substantially influences the structure of the current-voltage characteristic. The relation between the current-voltage characteristic and the properties of edge magnetoplasmons in this system is discussed. © *1997 American Institute of Physics.* [S1063-7826(97)01805-X]

The study of the frequency dependence of the Hall conductivity in bounded two-dimensional (2D) systems can be divided into two parts. First, the conductivity tensor itself depends on the frequency of the alternating electric field. For 2D systems this problem has been solved, with different degrees of accuracy, by many authors (see, for example, Refs. 1 and 2). Furthermore, the conductance (i.e., the electrical conductivity of this system with allowance for its geometry and the arrangement of the contacts in the linear region of the current-voltage characteristic) can additionally and nontrivially depend on the frequency of the external signal for geometric reasons. For example, in bounded 2D systems the position of the cyclotron resonance is shifted relative to its value for an infinite two-dimensional electron gas (2DEG) by the so-called depolarization effect.[3] As will be shown below, the size factor is also present in the semi-infinite problem, when the traditional depolarization effects are not important. In this case there is the question of the excitation of specific edge magnetoplasmons (EMPs), whose spectrum has no threshold and softens with increasing magnetic field, along the edge of the 2DEG between the contacts.

The objective of this note is to calculate the conductance for a semi-infinite 2D system with two point contacts, which determine the position of the source and sink along the edge of the 2D system. Obviously, the current-voltage characteristic (IVC) of the problem in the linear approximation has the form of Ohm's law. However, the effective conductance is by no means correspond to the conductivity tensor for the given 2D system.

This problem is also interesting from the standpoint of the excitation of EMPs in bounded 2D systems. The point is that the ''soft'' EMPs propagate along the boundary of the 2DEG only in one direction. Such oscillations do not form standing waves, and as a result the question of how traveling EMPs are excited with the aid of external contacts fixed along the boundary of the sample remains open. Existing experiments on the excitation of EMPs with the aid of fixed contacts[4–6] are interpreted in terms of free (i.e. traveling along the unperturbed boundary) EMPs, which is not entirely correct.

1. In presenting specific results, we shall examine the semi-infinite 2DEG occupying the region $x \geqslant 0$ with a free boundary extended along the y axis. The magnetic field is oriented in a direction normal to the plane of the 2DEG. The input contacts are located at the points $x=0$, $y=\pm b$ symmetrically relative to the origin of the coordinates. The boundary of the 2D electronic system is assumed to be quite sharp. Its presence will be taken into account by the effective boundary conditions on the current density.

The system of definitions which relates the potential difference $V(t)=V \exp i\omega t$ between the contacts and the corresponding current $I(t)=I \exp i\omega t$ is as follows:

$$j_i=\sigma_{ik}E_k, \quad E_k=\partial\phi/\partial x_k, \tag{1}$$

$$i\omega e\,\delta n=\sigma_{xx}\Delta\phi, \tag{2}$$

$$\phi(x,y)=\frac{2e}{\kappa}\int_{-\infty}^{+\infty}d\sigma\int_{0}^{+\infty}ds\,\frac{\delta n(s,\sigma)}{[(x-s)^2+(y-\sigma)^2]^{1/2}}, \tag{3}$$

$$j_n(y)=I(t)[\delta(y-b)-\delta(y+b)], \tag{4}$$

$$V(t)=\phi(x=0,y=+b,t)-\phi(0,-b,t), \tag{5}$$

$$\delta n(x\to+\infty,y\to\pm\infty,t)\to 0. \tag{6}$$

Here $\delta n(x,y,t)$ and $\phi(x,y,t)$ determine the deviation of the electron density and the corresponding potential from its values, κ is the dielectric constant, and σ_{ik} is the local conductivity tensor, whose structure (including the frequency dependence) is assumed to be given.

Switching in Eqs. (1)–(6) to Fourier components in the variable y, we have

$$\delta n(x,y,t)\propto\delta n(x,q)\exp iqy \exp i\omega t,$$

$$\phi(x,y,t)\propto\phi(x,q)\exp iqy \exp i\omega t, \tag{7}$$

$$i\omega e\,\delta n(x,q)=\sigma_{xx}[d^2\phi(x,q)/dx^2-q^2\phi(x,q)], \tag{8}$$

$$\phi(x,q)=\frac{2e}{\kappa}\int_{0}^{+\infty}\delta n(s,q)K_0(q|x-s|)ds, \tag{9}$$

$$j(q)=\sigma_{xx}d\phi(0,q)/dx+iq\sigma_{xy}\phi(0,q),$$

$$j(q)=2iI \sin qb \exp i\omega t, \tag{10}$$

$$\delta n(+\infty,q)\to 0, \quad \phi(+\infty,q)\to 0. \tag{11}$$

$$V=\int_{-\infty}^{+\infty}\phi(0,q)dq, \tag{12}$$

$$\sigma_{xx}/\sigma_{xy}\ll 1. \tag{13}$$

Here $K_0(x)$ is a Bessel function; the transformation of the condition (5) to (12) is valid only if the inequality (13) is satisfied. This inequality limits somewhat the generality of our analysis, but it makes it possible to simplify the calculation substantially, remaining in so doing in the parametrically most interesting region close to the quantum Hall effect (QHE).

The combination (8) and (9) leads to an integral equation for $\delta n(x,q)$ which is typical of the theory of EMPs. Solving this equation approximately by the method described in Ref. 7, we find from Eqs. (8)–(11)

$$\phi(0,q)=j(q)\Big/\left[iq\sigma_{xy}+\sigma_{xx}\frac{1+2\sigma_{xx}qK/i\kappa\omega}{2\sigma_{xx}K_0(ql)/i\kappa\omega}\right], \quad (14)$$

$$\phi(0,q)=-\phi'(0,q)l, \quad K=\int_0^{+\infty}K_0(s)ds, \quad ql\ll 1, \quad (15)$$

The desired relation between V and I arises when $\phi(0,q)$ (14) is substituted into Eq. (12). The characteristic length l appearing in the course of the solution of the system (8)–(11) [see the definition of l (15)] ultimately has the following asymptotic forms:

$$j(q)=0, \quad l=\sigma_{xx}/iq\sigma_{xy}; \quad (16)$$

$$j(q)\neq 0, \quad l=2\sigma_{xx}K_0(ql)/[1+\pi\sigma_{xx}q/i\kappa\omega]. \quad (16a)$$

In the case $j(q)=0$, in order for the quantity $\phi(0,q)$ (16) to be finite, the denominator from Eq. (15) must vanish. This requirement leads to the standard dispersion relation for EMPs in an electronic system with a sharp boundary

$$\kappa\omega=2q\sigma_{xy}K_0(ql), \quad ql\ll 1. \quad (17)$$

Here the length l is given in Eq. (16). If, however, $j(q)\neq 0$, the quantity l acquires the form (16a) and the pole of the expression (15) for $\phi(q)$, which arises with a purely imaginary σ_{xx}, is no longer a characteristic of free EMPs. Furthermore, the observed quantity — the IVC from Eq. (12) — contains an integral over all wave numbers. Therefore, the resonance excitation of the EMPs at the wavelength $\lambda=2b$ for $\kappa\omega=2\pi\sigma_{xy}K_0(\pi l/b)/b$ is impossible. Using $\phi(0,q)$ (16), the I–V characteristic of this system can be calculated with the aid of Eq. (12).

If in addition $\sigma_{xx}\ll b\omega$, then

$$V=\frac{I}{\sigma_{xy}}\cos\left[\frac{\kappa b\omega}{2\sigma_{xy}K_0(l/b)}\right], \quad (18)$$

where l is taken from Eq. (16a).

Therefore, the conductance $\Sigma=I/V$ of the system under discussion has the form

$$\Sigma=\frac{\sigma_{xy}}{\cos[\kappa b\omega/2\sigma_{xy}K_0(l/b)]}. \quad (19)$$

In the limit $\omega\to 0$ the quantity $\Sigma\to\sigma_{xy}$. However, at finite frequencies $\Sigma\neq\sigma_{xy}$.

The results obtained can be compared with the data of Ref. 8 on the frequency dependence of the Hall voltage for a MOS structure in the range from zero to several kHz. These experiments attest to the increase in the conductance with increasing frequency and the appearance of additional oscillations of Σ near the Hall plateau. Both observations can be qualitatively explained in the above-proposed picture of the formation of low-frequency conductance.

This work was supported by the Russian Fund for Fundamental Research grants Nos. 95-02-06108a and 96-02-19568.

[1] T. Ando, A. Fowler, and F. Stern, Rev. Mod. Phys. **54**, 437 (1982).
[2] S. M. Apenko and Yu. E. Lozovik, Zh. Éksp. Teor. Fiz. **89**, 573 (1985) [Sov. Phys. JETP **62**, 328 (1985)].
[3] G. Dresselhaus, A. F. Kip, and C. Kittel, Phys. Rev. **98**, 368 (1995).
[4] N. B. Zhitenev, JETP Lett. **55**, 756 (1992).
[5] N. B. Zhitenev, R. J. Haug, K. V. Klitzing, and K. Eberl, Phys. Rev. Lett. **71**, 2292 (1993).
[6] N. B. Zhitenev, R. J. Haug, K. V. Klitzing, and K. Eberl, Phys. Rev. B **49**, 7809 (1994).
[7] V. B. Shikin, Zh. Éksp. Teor. Fiz. **95**, 1513 (1989) [Sov. Phys. JETP **68**, 873 (1989)].
[8] M. Pepper and J. Wakabayashi, J. Phys. C: Sol. St. Phys. **16**, L113 (1983).

Translated by M. E. Alferieff

Electrical properties of the solid solutions p-type $GaAs_{1-x}Sb_x$ doped with germanium

T. Yu. Allen[1)] and T. A. Polyanskaya[5)]

A. F. Ioffe Physicotechnical Institute, Russian Academy of Sciences, 194021 St. Petersburg, Russia
(Submitted August 20, 1996; accepted for publication September 16, 1996)
Fiz. Tekh. Poluprovodn. **31**, 587–593 (May 1997)

Epitaxial Ge-doped p-type $GaAs_{1-x}Sb_x$ films ($x=0-0.1$; $N_{Ge}=0.01-10$ at. % in a liquid phase; hole density at room temperature ($0.06-40\times10^{18}$ cm^{-3}), grown by liquid-phase epitaxy, were investigated. It was found that for the same Ge concentration in the liquid phase the hole density in the solid solution is approximately two times higher than in GaAs, irrespective of the Sb content. The activation energy of the germanium acceptor and the critical density for the metal–insulator transition were found: $\varepsilon_1=22\pm2$ meV and $p_c=(3.9\pm0.3)\times10^{18}$ cm^{-3} for $x=0.06$. © *1997 American Institute of Physics.* [S1063-7826(97)01905-4]

The rapid development of modern optoelectronics is largely tied to the application of III–V compounds and their solid solutions. The application of epitaxial films of the solid solutions $GaAs_{1-x}Sb_x$ ($0<x<0.2$) makes it possible, by varying the antimony content and therefore the band gap of the active layer, to obtain a set of optoelectronic devices in the wavelength range 0.9–1.13 μm. Epitaxial layers grown on GaAs substrates can be used as a wide-gap window for introducing radiation. The previously published studies[1–4] involved the use of $GaAs_{1-x}Sb_x$ films (n-type) that were not specially doped, while p-type films have been virtually ignored. In a number of devices (p–n junctions, photocathodes with a negative electron affinity) a p-type $GaAs_{1-x}Sb_x$ layer is one of the active regions. It is therefore important that the electrical properties of the p-type solid solution $GaAs_{1-x}Sb_x$ be investigated.

Typical impurities for obtaining epitaxial p-$GaAs_{1-x}Sb_x$ layers are Zn and Ge.[5,6] Germanium manifests amphoteric properties: It can form donors Ge_{Ga}^{+} at the sites of the gallium sublattice and acceptors Ge_{As}^{-} at the sites of the arsenic sublattice. In GaAs (Ref. 7) and in the solid solutions $GaAs_{1-x}Sb_x$ (Ref. 6), grown from gallium fluxed solutions, the As vacancy density is higher than the Ga vacancy density, which is what gives the p-type conductivity of these materials on doping with Ge. Since the saturated vapor pressure of germanium is lower than that of Zn, it is preferable to use Ge as a dopant for preparing p-type layers with reproducible parameters.

We investigated the solid solutions $GaAs_{1-x}Sb_x$ with Sb content in the solid phase from 0 to 10.5%. The fraction of Ge in the liquid phase varied from 0.01 to 10 at. %; this made it possible to obtain layers with a hole density from 5.6×10^{16} cm^{-3} to 3.4×10^{19} cm^{-3} at room temperature. The films were 15–20 μm thick on average. The samples for the measurements were prepared by photolithography in the form of a double Hall cross. The contacts were made by alloying indium on the contact areas of the sample. Samples for which the voltage drop measured on two pairs of potential probes did not exceed 2% were chosen for the investigations.

Figure 1 shows the room-temperature Hall hole density $p_{295}=1/eR_H^{295}$ (R_H^{295} is the Hall coefficient at $T=295$ K, $H\simeq3$ kG) as a function of the Ge content for samples with different antimony contents. We see that at the same Ge concentration in the liquid phase the hole density in GaAs ($x=0$, curve a) is approximately two times lower than in the solid solution with $x\geqslant3\%$ (curve b). Apparently, to change the hole density in the solid solution (as compared with GaAs) it is sufficient to introduce Sb at a 1% or lower level, since in the range of Sb concentrations from 3% to 10.5% the hole density is independent of x (see Fig. 1, curve b). The hole mobility decreases when Sb is introduced (Fig. 2). It is possible that these facts are explained by the effect of Sb on the ensemble of point defects in GaAs, specifically, the density of electrically active centers (Ge_{As}^{-}, Ge_{Ga}^{+}, etc.). For example, in Ref. 10 it was observed that the density of centers with energy $E_v+0.1$ eV, which associated with impurity–vacancy complexes when GaAs is doped with antimony, decreases. However, mechanism of this effect requires further study.

In studying the solid solutions we focused our attention mainly on $GaAs_{1-x}Sb_x$ layers with $x=0.06$.[2)] Some parameters of the experimental samples are presented in Table I. The experimental hole density $p=1/eR_H$ (ignoring the Hall factor) versus the reciprocal of the temperature is shown in Fig. 3 for the most weakly doped samples $GaAs_{0.94}Sb_{0.06}$. Analysis of these curves with the aid of the neutrality equation by computer fitting makes it possible to determine the thermal ionization energy ε_1, the acceptor impurity density N_A, and the degree of compensation $K=N_D/N_A$ (N_D is the donor density). We employed the neutrality equation, well known from statistics, for a nondegenerate carrier gas:[11]

$$p+N_D=\frac{N_A}{1+\beta\,(p/N_v)\exp(\varepsilon_1/kT)}. \tag{1}$$

Here $\beta=4$ is the spin degeneracy factor, and N_v is the effective density of states in the valence band with mass $m_d=m_{hh}$ (just as for GaAs), where m_{hh} is the mass of the heavy holes. Equation (1) was solved by the method of iterations. The values of ε_1, N_A, and K were found in such a way as to obtain the best fit between the computed and experimental curves $p(T)$. The degree of compensation K for a sample with the lowest hole density was found to be 0.68; as the density increases, the degree of compensation decreases to 0.5. The same value of K was found for films obtained by

TABLE I. Basic characteristics of $GaAs_{0.94}Sb_{0.06}$ samples.

Sample	Ge, at. %	d, μm	$T=295$ K: $\mu_H=R_H\sigma$, cm/(V·s)	$T=295$ K: $p_{295}=1/eR_H$, 10^{18} cm^{-3}
1	0.01	15	153	0.056
2	0.05	12	118	0.35
3	0.1	18	158	0.45
4	0.2	18	110	0.67
5	0.2	21	83.8	1.17
6	0.3	20	85.6	1.20
7	0.5	18	87.6	2.20
8	0.6	19	79.8	2.74
9	0.7	20	66.7	2.59
10	1	16	55.6	6.0

the same growth technology with hole density (at $T=295$ K) above 6×10^{18} cm^{-3}. It was determined by comparing the experimental values of the low-temperature mobility (at $T=4.2$ K) with the values calculated according to the theory of galvanomagnetic phenomena in semiconductors with degenerate bands (Ref. 12).[3)] Therefore, it can be assumed that in our samples the degree of compensation $K=0.5$ for $p>10^{17}$ cm^{-3}. The values obtained for the background donor density $N_D=KN_A$ agree with the values of N_D determined in the investigation of p–n junctions[3] and Schottky barrier[4] on n-type $GaAs_{1-x}Sb_x$ films grown under the same technological conditions and not specially doped.

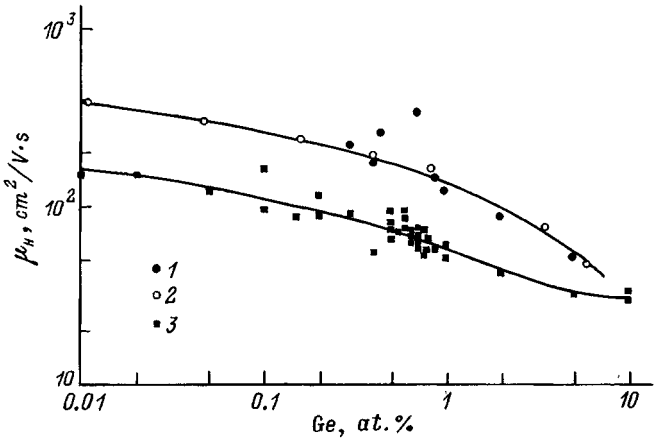

FIG. 2. Room temperature Hall hole mobility μ_H in $GaAs_{1-x}Sb_x$ ($x=0$ and $x=0.06$) versus the Ge content in the liquid phase. *1* — GaAs; *2* — GaAs;[8] *3* — $GaAs_{0.94}Sb_{0.06}$.

The values obtained for the ionization energies are shown in Fig. 4 as a function of the hole density at $T=295$ K $p_{295}=1/eR_H^{295}$ (which approximately corresponds to the value of N_A-N_D) and as a function of $p_{295}^{1/3}$. The value $\varepsilon_1=22\pm2$ meV, determined for a sample with the lowest hole density, was found to be very close to the value $\varepsilon_1^{PL}=24$ meV, presented in Ref. 13 in a study of the photoluminescence spectra of a Ge-doped solid solution

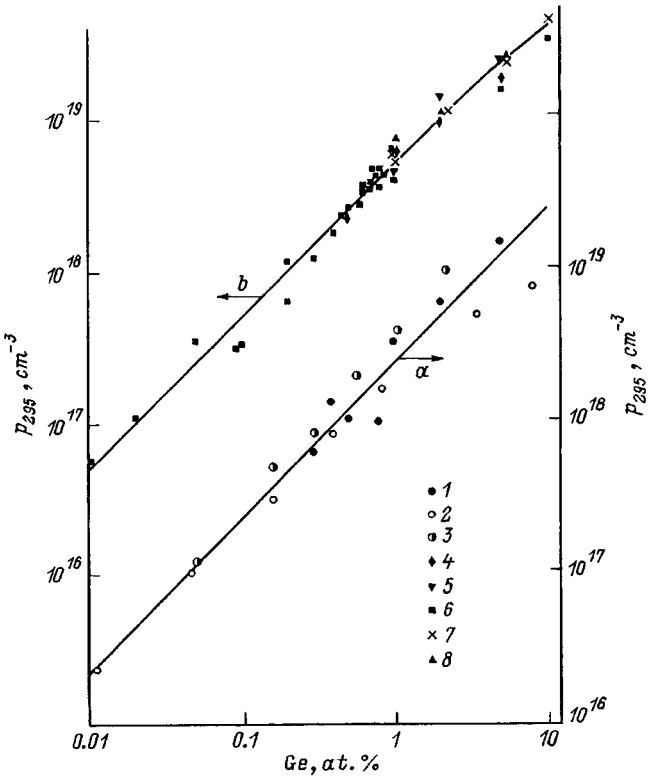

FIG. 1. Room temperature Hall hole density p_{295} in $GaAs_{1-x}Sb_x$ versus the Ge concentration in the liquid phase. Sb content, at. %: *1–3* — 0; *4* — *3*; *5* — 4.5; *6* — 6; *7* — 8.5; *8* — 10.5. The data for GaAs ($x=0$) are supplemented with the results from: *2* — Ref. 8 and *3* — Ref. 9.

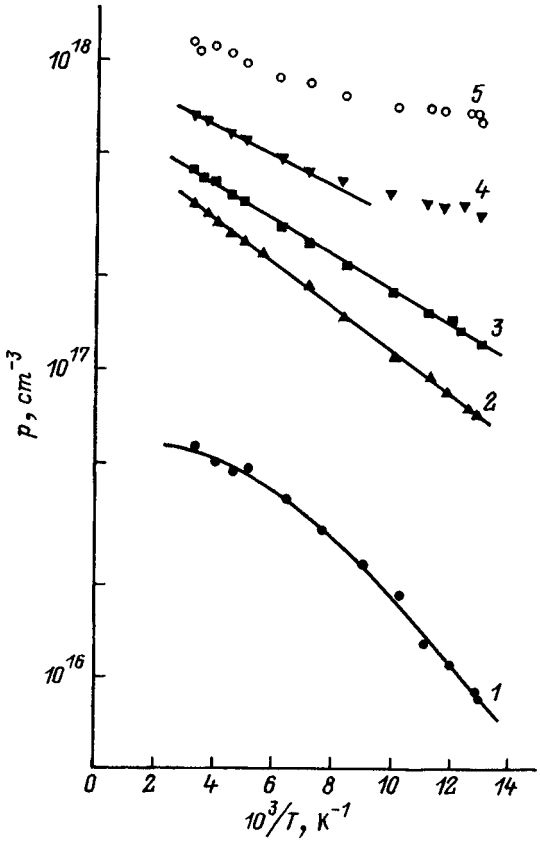

FIG. 3. Hole density p versus the reciprocal of the temperature for $GaAs_{1-x}Sb_x$ with different Sb contents. The numbers on the curves correspond to the numbers of the samples in Table I. Solid lines — Eq. (1).

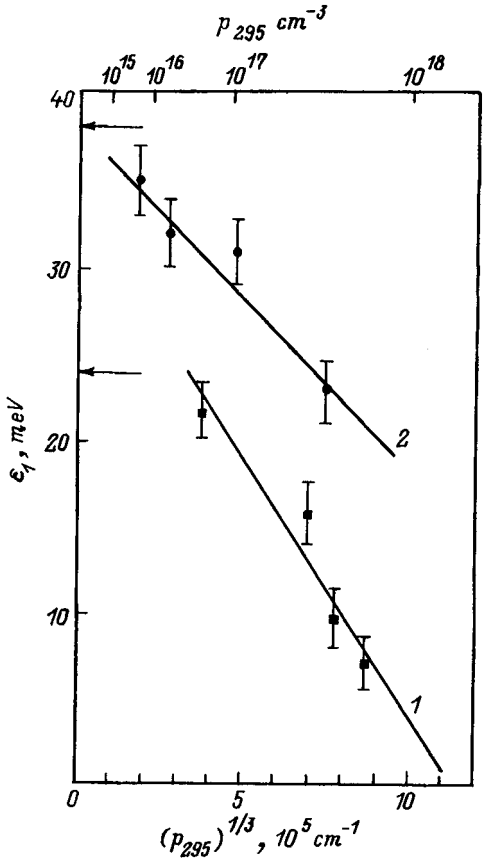

FIG. 4. Ge ionization energy versus carrier density in the samples: *1* — $GaAs_{0.94}Sb_{0.06}$; *2* — GaAs.[8] The arrows indicate the values obtained from photoluminescence investigations.[8,13]

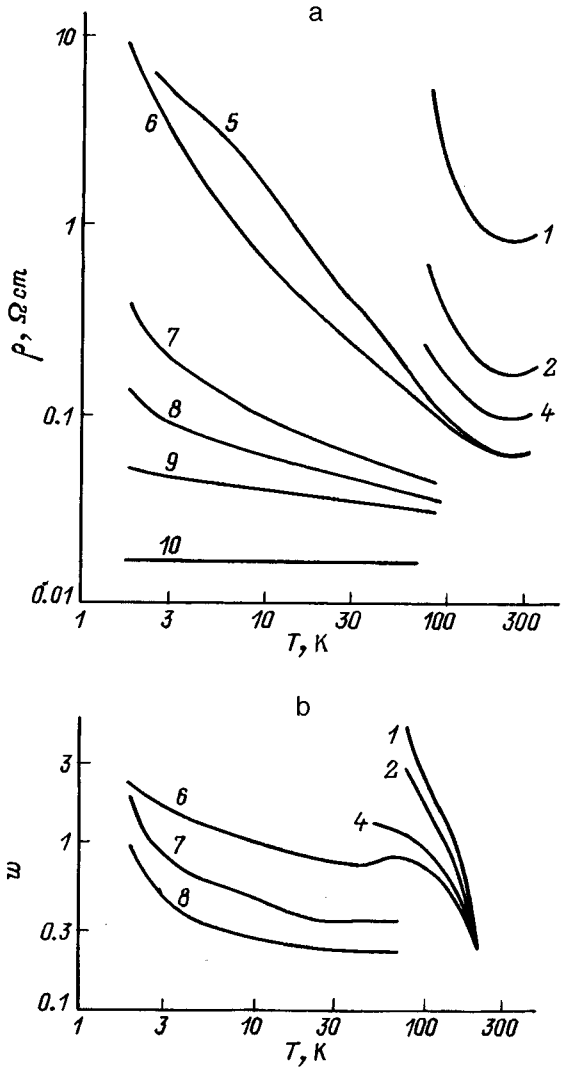

FIG. 5. Temperatures dependences: a — Resistivity of *p*-type $GaAs_{0.94}Sb_{0.06}$; b — reduced activation energy *w* (2). The numbers on the curves correspond to the numbers of the samples in Table I.

$GaAs_{0.94}Sb_{0.06}$. Figure 4 also shows the values of the thermal ionization energy of Ge in epitaxial GaAs according to the data of Ref. 8. The value $\varepsilon_1 = 35 \pm 2$ meV (found by analyzing the temperature dependences of R_H) and $\varepsilon_1^{PL} = 38$ meV (photoluminescence investigations) are presented in Ref. 8. A linear dependence of $\varepsilon(p_{295}^{1/3} \cong N_A^{1/3})$ is characteristic of hydrogen-like impurity states in semiconductors and is manifested in the range of electron or hole densities where screening of localized impurity states by carriers and by the charge of ionized impurities is appreciable. This dependence is clearly seen for GaAs (curve *2*) and for $GaAs_{0.94}Sb_{0.06}$ (curve *1*). Extrapolating the GaAs data to $p_{295}^{1/3} = 0$, we obtain $\varepsilon_1^{as} = 38.3$ meV, and for $GaAs_{0.94}Sb_{0.06}$ we obtain $\varepsilon_1^{as} = 34$ meV.

The temperature dependences of the resistivity ρ are shown for a number of samples in Fig. 5a. By differentiating these curves using the method developed in Refs. 14 and 15, we determined the temperature dependence of the reduced activation energy

$$w = \varepsilon / kT = T^{-1} \partial \ln \rho / \partial T^{-1} \tag{2}$$

(see Fig. 5b) in order to make an attempt to separate the region $\varepsilon = \text{const}$ (where $w \sim T^{-1}$) and the region $w \sim (T_0/T)^{-1/4}$ with variable hopping length. Unfortunately, we had too few samples at our disposal on the insulator side of the metal–insulator transition in order to draw any general conclusions about the laws of variation of the temperature dependence $\rho(T)$ which are characteristic of the insulator regime as well as about the temperature limits within which these laws are valid. Only the transitional region between the energies ε_1 and ε_3 is clearly seen in Fig. 5b;[16] in addition, this region does not increase in size with increasing impurity density as $N^{1/3}$, but rather it decreases (see curve *5* in Fig. 5a and curves *6–8* in Fig. 5b), as should happen with increasing overlapping of the acceptor wave functions as the metal–insulator transition is approached.[16]

Figure 6 shows the conductivity σ and the mobility $\mu_H = R_H \sigma$ at $T = 4.2$ K versus the hole density $p_{295} \cong N_A - N_D$. By analogy with the well-studied semiconductors (see, for example, the data in Ref. 17 for Ge⟨Sb⟩) the critical hole density p_c for a metal–insulator transition in $GaAs_{0.94}Sb_{0.06}$ can be estimated from the dependence $\mu_H(p)$: $p_c = (3.9 \pm 0.3) \times 10^{18}$ cm^{-3}.

This value can be compared with the critical concentration which should be estimated using the relation

$$p_c^{1/3} a_B^* = \alpha, \tag{3}$$

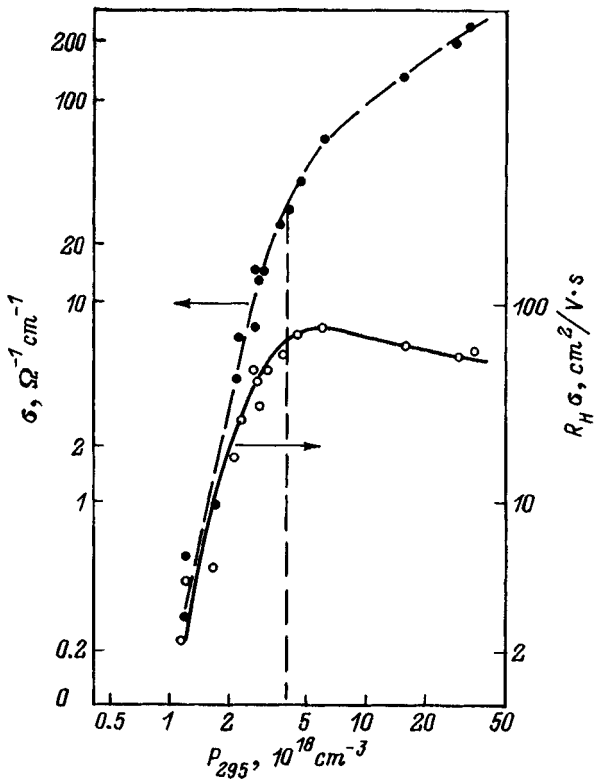

FIG. 6. Conductivity σ and hole mobility μ_H ($T=4.2$ K) versus the hole density p_{295} in the solid solution $GaAs_{0.94}Sb_{0.06}$.

where a_B^* is the effective Bohr radius of the impurity state with energy ε_1 and $\alpha \cong 0.26$ is a numerical factor. The relation (3) is based on the simple assumption that the transition to metallic conductivity occurs when the screening radius R_s becomes of the order of a_B^* and therefore the charge carriers cannot remain in localized orbits of the impurity states because of the electron-electron interaction. The quantity R_s in the approximation linear in the screening is given by the relation

$$R_s^2 = \frac{\varkappa}{4\pi e^2 p}\frac{F_{1/2}(\eta)}{F_{-1/2}(\eta)} = \begin{cases} L_D^2, & \eta < -4, \quad (4a) \\ \pi a_B^*/4k_{F0}, & \eta \gg 10, \quad (4b) \end{cases}$$

where $\eta = \varepsilon_F/kT$, ε_F is the Fermi energy, $\varkappa$ is the permittivity of the semiconductor, $F_j(\eta)$ are the Fermi integrals,[11] L_D is the Debye length, and $k_{F0}=(3\pi^2 p)^{1/3}$ is the magnitude of the wave vector for $\eta > 10$, i.e., $T \to 0$. If it is assumed that

$$R_s|_{p=p_c} = R_{sc} = a_B^*,$$

then a relation of the type (3)

$$p_c^{1/3} a_B^* = \frac{1}{4}\left(\frac{\pi}{3}\right)^{1/3} \cong 0.254$$

follows from Eq. (4b) (i.e., in the region of metallic conductivity). In Ref. 18 it was shown on the basis of an analysis of a wide spectrum of experimental data that for $\alpha = 0.26 \pm 0.01$ the relation (3) does indeed hold in a wide range of materials, including materials doped with different semiconductor impurities, despite the simplified hydrogen-like model of the impurity state. To estimate the radius a_B^* of a localized impurity state we employ a relation recommended in Ref. 16

$$a_B^* = \hbar/\sqrt{2m^*\varepsilon_1}\,. \quad (5)$$

We also note that when the masses of the light and heavy holes differ strongly, the asymptotic behavior of the charge-carrier wave functions at large distances is determined by the light mass and the energy ε_1 is determined mainly by the heavy mass (Ref. 16).[4)] Indeed, the effective Bohr energy $\varepsilon_B^* = m^* e^4/2\varkappa^2\hbar^2$ for heavy holes in GaAs (for $\varkappa = 12.79$, $m^* = m_{hh} = 0.46 \pm 0.05$) equals 38 ± 4 meV, which corresponds to the energies presented above:

$$\varepsilon_1^{PL} = 38 \text{ meV}, \quad \varepsilon_1^{as} \cong 38.3 \text{ meV}.$$

For $GaAs_{0.94}Sb_{0.06}$ the variance of the corresponding values of the ionization energy of Ge is much larger:

$$\varepsilon_1^{PL} = 24 \text{ meV}, \quad \varepsilon_1^{as} \cong 34 \text{ meV}, \quad \varepsilon_B^*|_{GaAsSb} \cong 36 \text{ meV}.$$

The last quantity was calculated for $m^* = m_{hh}|_{GaAs}$ and under the assumption that the permittivity $\varkappa$ exhibits a linear dependence on switching from GaAs to $GaAs_{0.94}Sb_{0.06}$: $\varkappa = (1-x)\varkappa|_{GaAs} + x\varkappa|_{GaSb}$ for $\varkappa|_{GaAs} = 12.8$ and $\varkappa|_{GaSb} = 15.7$. Assuming for GaAs the activation energy of acceptor states of Ge to be $\varepsilon_1|_{GaAs} = 38.2 \pm 0.2$ meV and using Eq. (5) and the values presented above for $m^* = m_{hh}|_{GaAs}$, we obtain

$$a_B^*|_{GaAs\langle Ge\rangle} = (14.7 \pm 1.2)\text{Å},$$

and for $GaAs_{0.94}Sb_{0.06}$, assuming $\varepsilon_1|_{GaAsSb} = 29 \pm 5$ meV and $m^* = m_{hh}|_{GaAs}$, we obtain

$$a_B^*|_{GaAsSb\langle Ge\rangle} = (17 \pm 2.4)\text{Å}.$$

As a result, the critical hole density estimated in accordance with Eq. (3) gives

$$p_c = (0.26/a_B^*)^3 = \begin{cases} (5.5 \pm 1.6)\times 10^{18}\text{cm}^{-3} & \text{for GaAs}\langle Ge\rangle, \\ (3.6 \pm 2)\times 10^{18}\text{cm}^{-3} & \text{for } GaAs_{0.94}Sb_{0.06}\langle Ge\rangle. \end{cases}$$

Here the error in determining p_c is large, since it consists of three terms:

$$\frac{\Delta p_c}{p_c} = 3\frac{\Delta\alpha}{\alpha} + \frac{3}{2}\left(\frac{\Delta m^*}{m^*} + \frac{\Delta\varepsilon_1}{\varepsilon_1}\right).$$

The metal–insulator transition in the solid solutions $GaAs_{1-x}Sb_x$ has not been studied previously. The value $p_c = 2\times 10^{18}$ cm^{-3} obtained for p-type gallium arsenide doped with Zn is presented in Ref. 19. In Ref. 19 anomalies of the tunneling conductivity of Pb/GaAs contacts were studied, p_c was estimated as the density at which the half-width of the differential current-voltage characteristic had a minimum, and strong dependence of the low-temperature bulk conductivity of the samples on the concentration measured at room temperature appeared. The authors also observed that a nonvanishing activation energy existed at temperatures below 10 K for hole densities below 2×10^{18} cm^{-3}. We note that in our investigations of the zero anomalies of the tunneling contacts[20] Au/p-$GaAs_{0.94}Sb_{0.06}$ (the solid solution was

doped with Ge) a maximum appeared on the curve of the relative tunneling anomaly as a function of p at $T=4.2$ K in the concentration range near 3.7×10^{18} cm^{-3}.

In summary, our estimate for the critical hole density for a metal–insulator transition in the solid solution $GaAs_{0.94}Sb_{0.06}$ gives the value $p_c\cong(3.9\pm0.3)\times10^{18}$ cm^{-3}.

[1)]Present address: Physics Department, University of Tennessee at Chattanooga, TN 37403, USA; e-mail: tbilgild@utcvm.utc.edu

[2)]This stems from the fact that in not specially doped n-type films ($GaAs_{1-x}Sb_x$, $(0.01<x<0.13)$), grown in the technological apparatus, maxima as a function of the composition of the electron mobility at $T=77$ K and the quantum yield of photoluminescence at $T=4.2$ K were observed at $x=0.06$. This was explained by the fact that the number of structural defects has a minimum in $GaAs_{1-x}Sb_x$ with $x=0.06$.[1,10]

[3)]The flattening of the curves $p(1/T)$ for samples 4 and 5 (Fig. 3) at $T<140$ K ($1000/T>7$ K^{-1}) could be due to the temperature dependence of the Hall factor. But this effect could be an indication of the onset of ionization of a shallower level (see, for example, Ref. 11).

[4)]The first of the indicated assumptions has been confirmed in our investigations of the anomalous magnetic resistance at $T=4.2$ K in $GaAs_{1-x}Sb_x$ for $0<x<0.085$.[12]

[5)]Electronic-mail: pta@nano.ioffe.rssi.ru

[1] Yu. F. Biryukin, V. N. Karyaev, I. Yu. Novikov, T. A. Polyanskaya *et al.*, Fiz. Tekh. Poluprovodn. **15**, 2288 (1981) [Sov. Phys. Semicond. **15**, 1330 (1981)].

[2] S. B. Demichev, V. N. Karyaev, S. V. Myasnikov, Kh. G. Nazhmudinov, T. A. Polyanskaya *et al.*, Élektron. tekhn., ser. 2, Poluporovodn. prib., No. 5 (164), 19 (1983).

[3] A. Ya. Vul' and S. V. Kidalov, Fiz. Tekh. Poluprovodn. **20**, 451 (1966) [Sov. Phys. Semicond. **20**, 285 (1966)].

[4] Kh. G. Nazhmudinov and T. A. Polyanskaya, Fiz. Tekh. Poluprovodn. **21**, 1737 (1987) [Sov. Phys. Semicond. **21**, 1053 (1987)].

[5] K. Sigiyama and H. Saito, Jpn. J. Appl. Phys. **11**, 1057 (1972).

[6] R. E. Nahory, M. A. Pollak, J. C. SeWinter, and B. F. Williams, J. Appl. Phys. **48**, 1609 (1977).

[7] D. N. J. Hurle, J. Phys. Chem. Sol. **40**, 647 (1979).

[8] F. E. Rosztoczy, F. Ermanis, I. Hayashi, and B. Schwartz, J. Appl. Phys. **41**, 264 (1970).

[9] C. Constantinescu and I. Petrescu-Prahova, J. Phys. Chem. Sol. **28**, 2397 (1967).

[10] V. F. Biryulin, N. V. Ganina, V. V. Chaldyshev, and Yu. V. Shmartsev, in *Abstracts of Reports at the 5th All-Union Conference on the Investigation of Gallium Arsenide* [in Russian], Tomsk, 1982, p. 62.

[11] J. S. Blakemore, *Semiconductor Statistics*, Pergamon Press, N. Y., 1962 [Russian trans., Mir, Moscow, 1964, Chap. 3, Secs. 2–5].

[12] T. Yu. Bil'gil'deeva, V. N. Karyaev, and T. A. Polyanskaya, Fiz. Tekh. Poluprovodn. **22**, 381 (1988) [Sov. Phys. Semicond. **22**, 235 (1988)].

[13] V. V. Chaldyshev, Author's Abstract of Candidate's Dissertation, Physicotechnical Institute, Leningrad, 1984.

[14] A. G. Zabrodskiĭ, Fiz. Tekh. Poluprovodn. **11**, 595 (1977) [Sov. Phys. Semicond. **11**, 345 (1977)].

[15] A. G. Zabrodskiĭ and K. N. Zinov'eva, Zh. Éksp. Teor. Fiz. **86**, 727 (1984) [Sov. Phys. JETP **59**, 425 (1984)].

[16] B. I. Shklovskiĭ and A. L. Éfros, *Electronic Properties of Doped Semiconductors*, Springer-Verlag, N. Y., 1984 [Russian orig., Nauka, Moscow, 1979].

[17] I. V. Dakhovskiĭ, T. A. Polyanskaya, L. G. Samoĭlovich, and Yu. V. Shmartsev, Fiz. Tekh. Poluprovodn. **4**, 2165 (1970) [Sov. Phys. Semicond. **4**, 1857 (1970)].

[18] P. P. Edwards and M. I. Sienko, Phys. Rev. B **17**, 2575 (1978).

[19] N. A. Mora, S. Bermon, and J. J. Loferski, Phys. Rev. Lett. **27**, 664 (1971).

[20] T. Yu. Bil'gel'deeva, Candidate's Dissertation in Physicomathematical Sciences, Leningrad Polytechnical Institute, Leningrad, 1988; T. Yu. Bil'gel'deeva, V. N. Karyaev, T. A. Polyanskaya, Kh. G. Nazhmudinov, and S. G. Yastrebov, in *Abstracts of Reports at the 5th All-Union Conference on Ternary Semiconductors and Their Applications* [in Russian], Kishenev, 1987, p. 173.

Translated by M. E. Alferieff

Photoluminescence in porous silicon produced as a result of intense laser excitation

E. Shatkovskiĭ and Ya. Vertsinskiĭ

Institute of Semiconductor Physics, 2600 Vil'nyus, Lithuania
(Submitted March 9, 1996; accepted for publication October 9, 1996)
Fiz. Tekh. Poluprovodn. **31**, 593–596 (May 1997)

The integrated photoluminescence in porous p-type silicon produced as a result of intense excitation with second harmonic ($\lambda = 532$ nm) pulses from a YAG:Nd^{3+} laser has been investigated. It was established that in the intensity range corresponding to quasistationary excitation conditions the radiation is characterized by a power-law dependence $I_{rad} \sim I^{2/3}$. As the excitation intensity increases, the quantum yield β decreases $\sim I^{-1/3}$. It is shown that the main radiation of porous silicon is due to a bimolecular recombination process. © *1997 American Institute of Physics.* [S1063-7826(97)02005-X]

Despite intensive investigations of porous silicon (*por*-Si), there is still no unequivocal answer to the question of the nature of the visible-range luminescence observed in this material. There are two main controversial models. According to the first one, the visible-range luminescence appears as a result of quantum-size effects[1,2] which are a consequence of the characteristic nanometer sizes of the porous structure. According to the second one, the visible-range radiation of *por*-Si is due to Si:O:H and H:Si:H complexes formed in the process of anodic etching and siloxen $Si_6H_3O_6$ and its modifications.[3–7] The first hypothesis is confirmed by investigations of the shift of the absorption band edge.[2,3,8–10] However, it cannot explain adequately the behavior of the luminescence spectrum. First, the luminescence arises only in samples with a substantial porosity. Second, there is no definite relation between the form and position of the luminescence spectrum and the sizes of the nanoparticles[10,11] even though, as follows from the shift of the absorption edge, there should be such a dependence. Recently, however, these two models have been converging. For example, in Ref. 12 it was established that spherical silicon nanoparticles coated with silicon oxide emit in the same region of the spectrum as *por*-Si. It was shown that this radiation can be explained by annihilation of an exciton, spatially bounded (trapped) in an intermediate region between the core of a sphere and the oxide layer on the surface. On the other hand, it is shown in Ref. 13 that clusters of planes of silicon atoms can form in complicated siloxen-type complexes. Quantum confinement occurs in these clusters. It has not been ruled out, that the two mechanisms, and possibly an even more complex system of transitions, form the integrated radiation of *por*-Si in the visible range. This assumption is based on the presence of only a very extended surface with a quantum-confinement effect. Furthermore, at low temperatures a complex structure of the spectrum appears[14,15] and a shift of the radiation band in time, formally described by a three-level scheme in Ref. 6, occurs.

Recombination models of different multiplicity are invoked to describe the characteristics of radiation from *por*-Si on the basis of the quantum-confinement mechanism. One of them, as mentioned above, is the model of three-level monomolecular recombination.[6] Monomolecular recombination, limited by tunneling through a potential barrier, is also proposed in Refs. 16 and 17. Authors of other works adhere to the opinion that the radiation of *por*-Si is due to a bimolecular process, i.e., it is the result of a recombination of free electrons or holes or electrons and holes bound in an exciton.[12,14,18,19] Nonetheless, the results and conclusions in this model are inconsistent. This is most clearly seen by comparing Refs. 14 and 18, where direct interband tansitions are studied in one case and indirect interband transitions are studied in the other.

In this study we determined the multiplicity of the radiative process in *por*-Si. We have accordingly measured the intensity of the integrated radiation as a function of the excitation intensity. Porous silicon was obtained by anodic etching of p-type single-crystal silicon wafers with $\rho = 10$ $\Omega \cdot$cm and {111} orientation for 15 min in a current of 50 mA/cm^2 at room temperature.[23] Excitation was performed by pulses of the second harmonic radiation ($\lambda = 0.532$ μm) from a Q-switched YAG:Nd^{3+} laser. The pulse duration was $\tau \cong 16$ ns. The maximum excitation intensity reached $I = 10^{24}$ photons/cm$^2 \cdot$s. The photoluminescence pulses were detected with a FÉU-28 photomultiplier operating in a linear regime and shielded by KS-11 and -12 light filters. The radiation was detected in the spectral range 1.2–0.6 μm, limited by the spectral sensitivity characteristic of the photomultiplier, on the one hand, and the transmission of the light filters, on the other. Detection occurred at the peak of the photoluminescence pulse. An optical fiber was used for optical coupling between the photomultiplier and the sample. The photoresponse signals were recorded with a wideband oscilloscope (transmission band $\Delta f = 250$ MHz). The measurements were performed at room temperature.

The dependence of the radiation intensity on the excitation power is shown in Fig. 1. As expected, excitation is nonstationary up to excitation intensities $I_1 = 10^{-2} I_0$. Since this region provides little information, we will consider below only the range of intensities $I > I_1$ in which the excitation is quasistationary.[22,23] As one can see from Fig. 1, in this range of intensities the radiation is characterized by a power-law dependence $I_{rad} \sim I^{2/3}$. We give here the quantum yield β of the radiation versus the excitation intensity calculated according to the relation

$$\beta = I_{rad}/I. \tag{1}$$

 1063-7826/97/050503-03$10.00

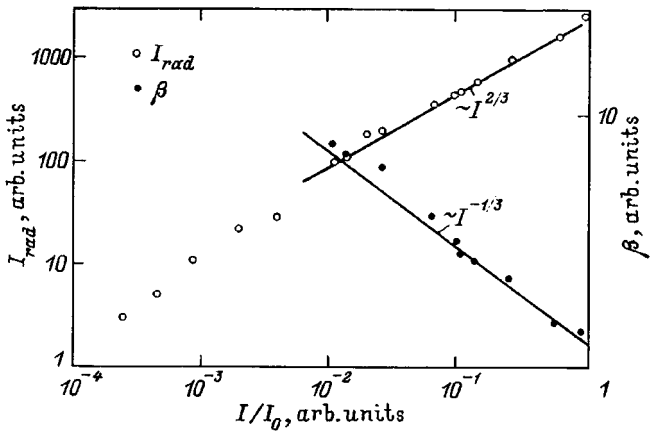

FIG. 1. Integrated intensity I_{rad} and quantum yield β versus the excitation intensity I ($I_0 = 10^{24}$ photons/cm$^2 \cdot$ s).

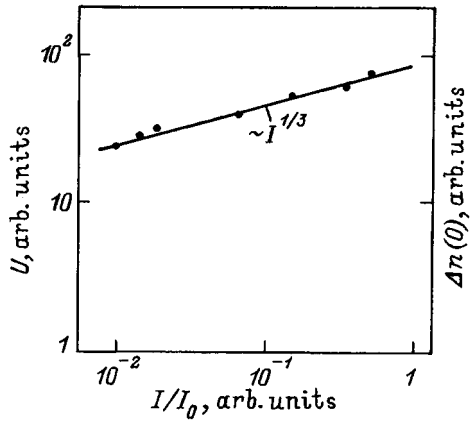

FIG. 2. Dependence of the voltage U of the photomagnetoelectric effect and of the nonequilibrium charge carrier density $\Delta n(0)$ on the excited surface of porous silicon on the intensity of the exciting laser radiation.

As one can see from Fig. 1, the quantum radiation yield decreases with increasing excitation intensity. In accordance with the measurements of the photoconductivity and photomagnetoelectric effect,[23] the density of nonequilibrium charge carriers is therefore controlled not by a radiative process, but rather by a more strongly concentration-dependent nonlinear nonradiative process. This conclusion is confirmed by the relatively low ($\sim 3\%$) numerical value of the quantum radiation yield.[17,18]

The conditions of our experiments differ fundamentally from most other experiments by the extremely high excitation intensity. The pulsed excitation regime chosen by us also serves this purpose. It is well known that under similar conditions, the density of nonequilibrium charge carriers in semiconductors usually is $\Delta n = \Delta p \gg n_0,\ p_0$. Here n_0 and p_0 are the equilibrium electron and hole densities. In this case we can write the total recombination rate r of charge carriers, taking into account the standard models of mono-, bimolecular, and three-particle interband Auger recombination, in the form

$$r = \sum_{i=1}^{3} A_i (\Delta n)^i. \tag{2}$$

Here i are the exponents (multiplicities) of the recombination processes, and A_i are the corresponding recombination coefficients. One or another process can predominate, depending on the ratio of the coefficients A_i and the density Δn. By measuring the dependence $r = r(\Delta n)$ it is possible to determine uniquely the multiplicity and therefore the model which the dominant recombination process satisfies. Furthermore, if the predominant recombination process is known, then the character of the radiative process can be established by measuring under stationary conditions the dependence of the rate of the radiative process $r_{\text{rad}} = I_{\text{rad}}$ on the generation rate. We showed in a previous study[23] that in porous silicon, just as in single-crystalline silicon, interband Auger recombination predominates under strong-excitation conditions. Its characteristic feature is a cubic dependence of the recombination rate r_A on the density Δn:

$$r_A = C_A (\Delta n)^3. \tag{3}$$

Here $C_A \equiv A_3$. As an illustration, Fig. 2 shows the voltage U of the photomagnetoelectric effect of the same samples of porous silicon as a function of excitation intensity; the curve is analogous to that obtained in Ref. 23. In our experiment the voltage is determined by the density $\Delta n(0)$ of nonequilibrium charge carriers on the excited surface, so that

$$U \sim \Delta n(0). \tag{4}$$

The generation rate of the nonequilibrium charge carriers is $g(\chi) \sim I(\chi)$. The curve of $U(I)$ therefore reflects the dependence of the density of nonequilibrium charge carriers on the generation rate. Taking into account the conditions of quasistationarity of excitation, which occurs for $I > 10^{-2} I_0$, the dependence $\Delta n(0) \sim I^{1/3}$ observed in Fig. 2 corresponds to the cubic density dependence of the recombination rate of the charge carriers. As is well known, it is realized in the case of interband Auger recombination. In the same study we showed that diffusion can be ignored in the continuity equation describing the kinetics of the charge carriers. Under stationary conditions, the recombination and generation rates will then be equal to one another: $r(\chi) = g(\chi)$. Using expression (3), we obtain

$$\Delta n(\chi) = \left[\frac{g(\chi)}{C_A}\right]^{1/3} \sim I^{1/3}. \tag{5}$$

In the case of a monomolecular radiative process we have for the radiation

$$I_{\text{rad}} = r_{\text{rad}} = A_r \Delta n \sim I^{1/3}, \tag{6}$$

and from Eqs. (1)–(3) follows the quantum yield β

$$\beta = I_{\text{rad}} / r_A \sim I^{1/3}/I = I^{-2/3}. \tag{7}$$

In the case of a bimolecular radiative recombination, when $r_{\text{rad}} \sim \Delta n^2$, we have

$$I_{\text{rad}} = B_{\text{rad}} (\Delta n) 62 \sim I^{2/3}. \tag{8}$$

Here, as usual, $A_2 \equiv B_{\text{rad}}$. The quantum yield is

$$\beta \sim I^{2/3}/I \sim I^{-1/3}. \tag{9}$$

Comparing expressions (6)–(9) with the experimental dependence which we obtained (Fig. 1), we see that the experimen-

tal dependence confirms that bimolecular radiative process was observed against the background of a predominant interband Auger recombination. In our opinion, such a process could be either band–band recombination or recombination via exciton states. Considering the indirect character of the transitions in silicon between conduction- and valence-band extrema and the low oscillator strength for such transitions,[24] recombination via a state of an exciton which is spatially confined in the intermediate layer of nanoparticles, as proposed by Kanemitsu in Ref. 12, seems more likely. We do not rule out, however, a more complex scheme of radiative transitions. We note in this connection that we performed spectrum-integrated measurements of the main emission channel. The observed shift of the position of the spectrum in time after removal of excitation,[6] the complicated structure of the spectrum at low temperatures,[14] and the radiation kinetics which we observed suggest that other, secondary, radiation channels could also be present. As the excitation intensity approaches the maximum intensity ($I > 0.1I_0$), along with a fast component 40–60 ns, we observed the appearance of a slower (150–200 ns) relaxation component. We note that the fast relaxation component corresponds to the nonequilibrium charge carrier lifetimes in silicon determined by interband Auger recombination.[22]

In summary, measurements of the dependence of the intensity of radiation from porous silicon on the excitation intensity have established the following: a) The main radiation from porous silicon is due to a bimolecular recombination process; b) most likely, recombination occurs through quantum-confined excitonic states, although interband transitions should not be ruled out; c) radiation is observed against the background of a predominant interband Auger recombination; and d) the quantum radiation yield in the spectral range 1.2–0.6 μm decreases with decreasing excitation. The fast relaxation component corresponds to the lifetime of nonequilibrium charge carriers in silicon, as determined by Auger recombination.[22]

[1] L. T. Canham, Appl. Phys. Lett. **57**, 1046 (1990).
[2] V. Lehmann and U. Goselle, Appl. Phys. Lett. **58**, 856 (1991).
[3] D. J. Ljjckwood, A. Wong, and B. Bryskiewicz, Solid Status Commun. **89**, 587 (1994).
[4] M. Stutzmann, M. S. Brandt, M. Rosenbauer, J. Weber, and H. D. Fuchs, Phys. Rev. B **47**, 4806 (1993).
[5] S. Banerjee, K. L. Narasimhan, P. Ayyub, A. K. Srivastava, and A. Sardesai, Solid Status Commun. **84**, 691 (1992).
[6] R. Laiho, A. Pavlov, and O. Nori, Appl. Phys. Lett. **63**, 275 (1993).
[7] A. Roy, A. Channani, D. D. Sarma, and A. K. Sood, Appl. Phys. Lett. **61**, 1655 (1992).
[8] H. Koyama, M. Araki, Y. Yamamoto, and N. Koshida, Jpn. J. Appl. Phys. **30**, 3606 (1991).
[9] I. Sagnes, A. Halimaoui, G. Vincent, and P. A. Badoz, Appl. Phys. Lett. **62**, 1155 (1993).
[10] Y. Kanemitsu, H. Uto, and Y. Masumoto, Phys. Rev. B **48**, 2827 (1993).
[11] S. M. Prokes, J. Appl. Phys. **73**, 407 (1993).
[12] Y. Kanemitsu, T. Ogawa, R. Shirashi, and K. Takeda, Phys. Rev. B **48**, 4883 (1993).
[13] P. Deak, M. Rosenbauer, M. Stutzmann, J. Weber, and M. S. Brandt, Phys. Rev. Lett. **69**, 2531 (1992).
[14] G. W.'tHooft, Y.A.R. R. Kessener, G. L. J. A. Rikken, and A. H. J. Venhuizen, Appl. Phys. Lett. **61,** 2344 (1992).
[15] S. Sinha, S. Banerjee, and B. M. Arora, Phys. Rev. B **49**, 5706 (1994).
[16] L. R. Tessler, F. Alvarez, and O. Teschke, Appl. Phys. Lett. **62**, 2381 (1993).
[17] J. C. Vial, S. Billat, G. Fishman, F. Gaspard, R. He'rino, M. Ligeon, F. Made'ore, I. Michlcescu, F. Muller, and R. Romenstain, Physica B **185**, 593 (1993).
[18] P. Maly', F. Troja'nek, A. Hospodkova', V. Kohlova', and I. Pelant, Solid Status Commun. **89**, 709 (1994).
[19] J. P. Proot, C. Delerue, and G. Allan, Appl. Phys. Lett. **61**, 1948 (1992).
[20] S. M. Ryvkin, *Photoelectric Phenomena in Semicondutors* [in Russian], Fizmatgiz, Moscow, 1963, p. 494.
[21] L. Dapkus, D. Gulbinaite, V. Jasutis, D. Leščinskas, and I. Šimkjeene, Liet. Fiz. Žurnalas **33**, 145 (1993).
[22] L. M. Blinov, E. A. Bobrova, V. S. Vavilov, and G. N. Galkin, Fiz. Tverd. Tela (Leningrad) **9**, 3221 (1967) [Sov. Phys. Solid State **9**, 2537 (1967)].
[23] E. Shatkovskiĭ, Ya. Vertsinskiĭ, and I. Shmikene, Liet. Fiz. Žurnalas **35**, 222 (1995).
[24] Y. H. Xie, Hybertsen, and William L. Wilson, Phys. Rev. B **49**, 5386 (1994).

Translated by M. E. Alferieff

The Schottky barrier at a junction between a metal and silicon carbide

S. Yu. Davydov, A. A. Lebedev, and S. K. Tikhonov

A. F. Ioffe Physicotechnical Institute, Russian Academy of Sciences, 194021 St. Petersburg, Russia
(Submitted March 26, 1996; accepted for publication October 20, 1996)
Fiz. Tekh. Poluprovodn. **31**, 597–599 (May 1997)

A simple model is proposed for a metal–semiconductor junction. It is assumed that a Schottky barrier is formed by states of defects localized at the interface. The experimental data on the ⟨metal (Au, Cr, Mo, and Al)⟩−⟨hexagonal siliconcarbide (6*H*−SiC)⟩ systems, where SiC has an *n*-type conductivity, are analyzed. © *1997 American Institute of Physics.* [S1063-7826(97)02103-0]

1. The study of Schottky barrier formation on a metal–semiconductor contact is an old but still important problem in semiconductor physics.[1] It is important to understand how the characteristics of the surfaces in contact and the method for producing a contact influence the parameters of the barrier that appears. Surface-barrier structures based on silicon carbide are undoubtedly of interest.[2] In Ref. 3 Schottky diodes formed on contacts between metals (Au, Mo, Cr, and Al) and *n*-6*H*-SiC were investigated. The effect of the uncompensated donor impurity density, the density of surface states, the work function of the metal, and the parameters of the insulator layer at the metal–semiconductor boundary on the barrier height was investigated experimentally. The generalized Bardeen and Schottky–Mott theory was used to analyze the experimental data.[4] It was found, specifically, that the Schottky barrier height Φ_b is the same for all metallic components investigated, and that it corresponds to half the band gap E_g in silicon carbide ($E_g \cong 3$ eV). These results are at variance with the data of Refs. 5–7, where a comparatively strong dependence of the barrier height Φ_b on the work function of the metal Φ_m was observed. This dependence was explained in Ref. 8 in a model of states induced by metal atoms. It was assumed that states formed by defects were not present in the contact region. As analysis of the published data[1] and discussion of the obtained results in Ref. 3 show, the weak dependence of Φ_b on Φ_m (we are talking about stabilization (pinning) of the Fermi level at energies corresponding to the states of the defects) is due to the presence of such states localized in the contact region. A simple model, taking into account the presence of defects in the contact region, was recently proposed for describing Schottky barriers in a metal–GaAs system.[9,10] In the present paper a modified variant of this model is used to describe the system metal–(silicon carbide).

2. We shall study the interaction of the defect state $|i\rangle$ localized on the surface of the semiconductor with a metal. The energy E_i of this state lies in the band gap. The interaction of $|i\rangle$ with the metal in contact with the semiconductor can be described by a Hamiltonian of the form

$$H=\sum_k \varepsilon_k c_k^+ c_k + E_i a_i^+ a_i + V\sum_k (c_k^+ a_i + \text{h.c.}), \tag{1}$$

where ε_k is the electron energy in the metal, V is the hybridization energy of the metallic and localized states, c_k^+ is the operator creating an electron in the state $|k\rangle$, and a_i^+ is the analogous operator for an electron in the state $|i\rangle$. The Hamiltonian (1) is a simplified version of the Anderson Hamiltonian,[11,12] where it is assumed that the level E_i can be occupied by not more than one electron (this makes it possible to drop the correlation term and the spin indices). Assuming that the level of the localized state $|i\rangle$ overlaps with the wide conduction band of the metal, it is easy to find its occupancy number n_i as

$$n_i=\frac{1}{\pi}\,\text{arccot}\,\frac{E_i-E_F}{\Gamma}, \tag{2}$$

where $\Gamma=\pi\rho V^2$ is the half-width (at half-height) of the quasilevel E_i, ρ is the density of states of the metal (assumed to be constant), and E_F is the Fermi level.

The solution (2) corresponds to an isolated state of a defect or, equivalently, a set of such states but not interacting with one another. We shall study the latter situation, making the assumption that the density of such states (per unit surface layer) equals N_i. As a result of electron tunneling between the metal and the quasilevels $|i\rangle$, a potential barrier

$$\Delta\Phi=-4\pi e^2\lambda N_i q_i, \tag{3}$$

where λ is the thickness parameter of the double layer (see below) and q_i is the charge localized in the state $|i\rangle$, arises at the contact. If prior to contact the level $|i\rangle$ was empty, then $q_i=-n_i$ and the resulting work function of the metal changes from Φ_m to $\Phi_m+\Delta\Phi$. If, however, the initially localized level was filled, then $q_i=+(1-n_i)$. The position of the Fermi level relative to the top of the valence band of the semiconductor is determined by the relation

$$E_F=I_{sc}-\Phi_m-\Delta\Phi. \tag{4}$$

Here $I_{sc}=\chi+E_g$, where χ is the electron affinity. The height of the Schottky barrier Φ_b equals E_F for a *p*-type semiconductor and E_g-E_F for a *n*-type semiconductor.

3. Let us now examine the general properties of the model. We rewrite Eqs. (2) and (4) in the form

$$\cot\,\pi n_i=\varepsilon_i-\Delta-A_i q_i, \tag{5}$$

$$\varepsilon_f=\Delta+A_i q_i, \tag{6}$$

where

$$\varepsilon_i=E_i/\Gamma,\quad \Delta=(I_{sc}-\Phi_m)/\Gamma,$$
$$A_i=4\pi e^2\lambda N_i/\Gamma,\quad \varepsilon_f=E_F/\Gamma. \tag{7}$$

The following relations can be obtained from expressions (5) and (6)

$$\frac{dn_i}{d\Delta}=\frac{\sin^2\pi n_i}{\pi}R_i, \tag{8}$$

$$\frac{d\varepsilon_f}{d\Delta}=R_i, \tag{9}$$

where

$$R_i=\left(1+A_i\frac{\sin^2\pi n_i}{\pi}\right)^{-1}. \tag{10}$$

Since the two derivatives are positive, as the work function Φ_m of the metal increases, the occupancy N_i of the level and the Fermi energy decrease. In the absence of states related to the defects, $dn_i/d\Delta=0$ and $d\varepsilon_f/d\Delta=1$. The latter equality corresponds to the Schottky–Mott case.[1] In the limit $N_i\to\infty$ we have $dn_i/d\Delta\to 0$ and $d\varepsilon_f/d\Delta\to 1$. Therefore, when the density of states of the defects is high, neither the occupancy of the defects nor the position of the Fermi level (and therefore the barrier height) depends on the work function of the contact metal.

Let us now examine the dependence of dn_i and ε_f on the position of the defect level ε_i. For arbitrary $dn_i/d\Delta$ and $d\varepsilon_f/d\Delta$ we obtain the expressions (8) and (9) but with a minus sign on the right-hand side. Therefore, a change in ε_i leads to the same consequences as a change in Φ_m. Finally, the dependence of the occupation numbers and Fermi level on the density of states N_i of the defects has the form

$$\frac{dn_i}{dA_i}=q_i\frac{\sin^2\pi n_i}{\pi}R_i, \tag{11}$$

$$\frac{d\varepsilon_f}{dA_i}=q_iR_i. \tag{12}$$

4. Let us analyze the results of Ref. 3 on the basis of the proposed model. For simplicity, let $E_i=E_g/2$, which corresponds approximately to the situation at hand (see also the data on other metal–semiconductor contacts[1,13]). We will then have

$$\cot\pi n_i=\omega-A_iq_i, \tag{13}$$

$$\varepsilon_f=\frac{1}{2}\varepsilon_g-\omega+A_iq_i, \tag{14}$$

where $\omega=(\Phi_m-\chi-E_g/2)/\Gamma$, and $\varepsilon_g=E_g/\Gamma$. According to the data presented in Ref. 3 , for the 6*H*-SiC modification of silicon carbide the band gap $E_g=3$ eV and $\chi=4.4$ eV. The work functions of metals are presented, for example, in Ref. 14 . The parameter A_i is quite difficult to calculate, since we know nothing, in principle, about the nature of the boundary defects in the system under study. Estimates presented in Refs. 9 and 10 also seem unconvincing to us, since we believe that it is unacceptable to use the concept of permittivity on atomic scales. In our view, the methods of chemisorption theory should be used to estimate λ and Γ.[15] As a result of the fact that the Schottky barriers in the system metal–6*H*-SiC correspond approximately to half the band gap, we obtain in Eq. (14) $\varepsilon_f=\varepsilon_g/2$. We then find from Eqs. (13) and (14) $n_i=-q_i=0.5$ and therefore

$$\chi=E_g/2-\Phi_m=2\pi e^2\lambda N_i. \tag{15}$$

We note that Eqs. (13) and (14) show that it must be assumed that the defect level is initially empty.

Assuming λ to be of the order of the lattice constant of the metal, i.e., $\lambda\cong 3$ Å, we find the corresponding defect densities (in units 10^{13} cm^{-2}): $N_i=3.0$, 5.9, 3.7, and 6.1 for Au, Mo, Cr, and Al, respectively. These results are completely reasonable.

We shall now find the value of the parameter R_i (see Table I), making the assumption that the width of the quasilevel of a defect $2\Gamma=1$ eV. Since $d\Phi_b^n/d\Phi_m=d\varepsilon_f/d\Delta$, we can calculate the increment to the Schottky barrier height $\Delta\Phi_b^n\cong R_i\Delta\Phi_m$, Using as a basis the parameters corresponding to the system Al/*n*-6*H*-SiC ($\Phi_b^n=1.26$ eV, $\Phi_m=4.25$ eV). Switching to molybdenum, we have $\Delta\Phi_m=0.05$ eV and, correspondingly, $\Phi_b^n\simeq 1.29$ eV, which agrees well with experiment. Switching from molybdenum to chromium, we obtain a positive increment $\Delta\Phi_b^n=0.14$ eV, which is at variance with experiment ($\Delta\Phi_b^n=-0.08$ eV). Switching from chromium to gold gives $\Phi_b^n=1.50$ eV. With the exception of chromium, which does not follow the general trend, the agreement with experiment is satisfactory. The result for chromium can be refined by, for example, displacing the defect level E_i upwards ($d\Phi_b^n/d\Phi_m=-d\Phi_b^n/d\varepsilon_i$).

TABLE I. Values of Φ_m, Φ_b^n, and the parameter R_i for $E_i=E_F=E_g/2$.

	Au	Cr	Mo	Al
Φ_m, eV	5.10	4.58	4.30	4.25
R_i	0.66	0.54	0.50	0.49
Φ_b'', eV (Ref. 3)	1.40	1.22	1.29	1.26

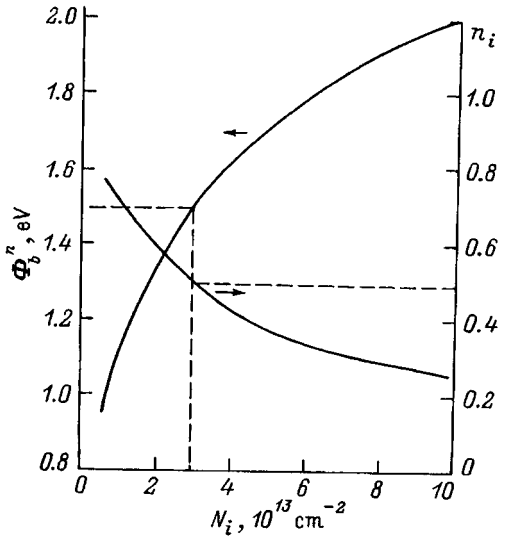

FIG. 1. Schottky barrier height Φ_b^n and occupation numbers n_i of defect states versus the density N_i of boundary defects for the system Au/*n*-6*H*-SiC with $E_i=E_g/2$. The dashed lines represent the values $d\Phi_b^n=E_g/2=1.5$ eV and $n_i=0.5$, which correspond to the value $N_i=3\times 10^{13}$ cm^{-2}.

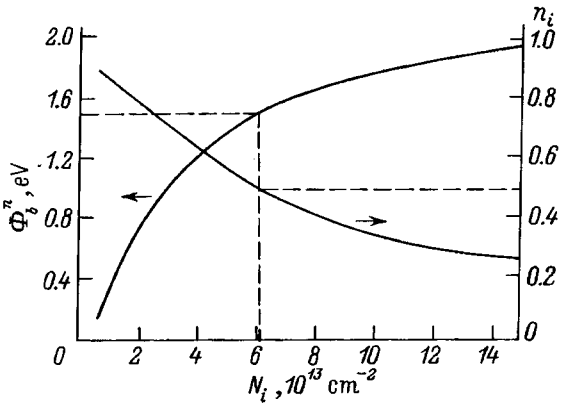

FIG. 2. Schottky barrier height Φ_b^n and occupation numbers n_i of defect states versus the density N_i for the system Al/*n*-6*H*-SiC with $E_i = E_g/2$. The dashed lines represent the same values as in Fig. 1 but for $N_i = 6.1 \times 10^{13}$ cm^{-2}.

The occupation numbers n_i of the defect levels and the Schottky barrier heights Φ_b^n versus the density of states N_i of defects for the system Au/*n*-6*H*-SiC are shown in Fig. 1. The dashed lines denote the values of $\Phi_b^n = E_g/2 = 1.5$ eV and $n_i = 0.5$, which correspond to $N_i = 3 \times 10^{13}$ cm^{-2}.

Figure 2 shows the same curves for the system Al/*n*-6*H*-SiC . Comparison of the results shows that the Schottky barrier height for a contact with Al increases much more rapidly with N_i than in the system Au/*n*-6*H*-SiC . The same tendency was established in Ref. 3 . Therefore, the proposed model is suitable for describing Schottky barriers on silicon carbide.

5. In this paper we have formulated a simple model that makes it possible to describe semiquantitatively the Schottky barrier parameters for the system metal–SiC. The most difficult problem is to determine adequately the parameters (mainly N_i and Γ), which are governed by the density and nature of the boundary defects. The fact that these defects can be generated during the process of producing a contact, which greatly complicates the investigation of the defects, introduces an additional difficulty. The fact that the Fermi level in most Schottky diodes is pinned approximately at the center of the band gap suggests that the defect density is close to N_i . Here, however, additional investigations are required.

This work was supported, in part, by Arizona State University (USA).

[1] W. Mönch, Rep. Progr. Phys. **53**, 221 (1990).
[2] *Technical Digest of Int. Conf. on Silicon Carbide and Related Materials*, ICSCRM-95 (Kyoto, Japan, 1995).
[3] A. N. Andreev, A. A. Lebedev, M. G. Rastegaeva, F. M. Snegov, A. L. Syrkin, V. E. Chelnokov, and L. N. Shestopalova, Fiz. Tekh. Poluprovodn. **29**, 1828 (1995) [Semiconductors **29**, 955 (1995)].
[4] S. M. Sze, *Physics of Semiconductor Devices*, Wiley, N. Y., 2nd Ed., 1981 [Russian translation, Mir, Moscow, 1984].
[5] J. R. Waldrop, R. W. Graut, J. C. Wang, and R. F. Davis, J. Appl. Phys. **72**, 4757 (1992).
[6] J. R. Waldrop and R. W. Graut, Appl. Phys. Lett. **62**, 2685 (1993).
[7] J. R. Waldrop, J. Appl. Phys. **75**, 4558 (1994).
[8] S. Yu. Davydov and S. K. Tikhonov, Fiz. Tverd. Tela (St. Petersburg) **37**, 2221 (1995) [Phys. Solid State **37**, 1212 (1995)].
[9] R. Ludeke, G. Jezequel, and A. Tabel-Ibrahimi, Phys. Rev. Lett. **61**, 601 (1988).
[10] R. Ludeke, Phys. Rev. B **40** (1989).
[11] P. W. Anderson, Phys. Rev. **124**, 41 (1961).
[12] C. Kittel, *Quantum Theory of Solids*, Wiley, N. Y., 1963 [Russian translation, Nauka, Moscow, 1967].
[13] F. Bechstedt and R. Enderlein, *Semiconductor Surfaces and Interfaces: Their Atomic and Electronic Structures*, Akademie-Verlag, Berlin, 1988 [Russian translation, Mir, Moscow, 1990].
[14] I. S. Grigor'ev and E. Z. Meĭlikhov [Eds.], *Handbook of Physical Quantities* [in Russian], Énergoatomizdat, Moscow, 1991.
[15] J. R. Smith [Ed.], *Theory of Chemisorption*, Springer-Verlag, N. Y., 1980.

Translated by M. E. Alferieff

Polarization anisotropy of optical interband transitions in strained InGaAs/GaAs quantum wires

S. A. Gurevich, D. A. Zakheim,[1)] and S. A. Solov'ev

A. F. Ioffe Physicotechnical Institute, Russian Academy of Sciences, 194021 St. Petersburg, Russia
(Submitted September 23, 1996; accepted for publication October 21, 1996)
Fiz. Tekh. Poluprovodn. **31**, 600–605 (May 1997)

The optical properties appearing in strained quantum wires as a result of the inhomogeneity of the elastic deformations distribution inside the wires and in the surrounding barrier material are investigated. An analytical approximation is used to calculate this distribution. It is shown that the short-wavelength shift of the photoluminescence and the polarization anisotropy of photoluminescence in a direction normal to the plane of the wires are determined mainly by the difference of the elastic deformations from the biaxial deformations. This result is confirmed by comparing the computed polarization–dependent photoluminescence spectra with the experimental data obtained for InGaAs/GaAs quantum wires with a 7×60-nm cross section.
 [S1063-7826(97)02205-9]

1. INTRODUCTION

Many papers involving calculation of the spatial distribution of the elastic mechanical deformations in buried structures with quantum wires (QWs), based on materials which are not lattice-matched, have recently appeared in the literature.[1,2] It has been shown that the elastic deformations in these structures differ substantially from a simple biaxial compression existing in the two-dimensional objects — quantum wells (QWs). This affects the band structure of QWs and results in a number of characteristic differences in the optical properties of strained QWs as compared with unstrained wires.

One of the most important manifestations of size quantization of charge carriers in QWs is the short-wavelength shift of the photoluminescence (PL) spectra as compared with the spectra of the initial quantum well. In Ref. 2 it was shown that for strained QWs this short-wavelength shift is determined mainly by the difference in the components of the elastic-deformation tensor from the values characteristic of biaxial compression of a quantum well, and only a small part of it is due to the additional quantization of electrons and holes in the plane of the initial quantum well.

It is well known[1] that a modification of the spatial dependence of the components of the elastic-deformation tensor in QWs changes primarily the structure of the valence band of the semiconductor, giving rise to mixing of the heavy- and light-hole subbands. This should result in an appreciable polarization anisotropy of the matrix elements of optical interband transitions associated with the absorption and emission of linearly polarized light. On the other hand, some experimental data show a substantial ($>5\%$) PL polarization anisotropy for structures with strained QWs of width 50–60 nm.[3] The nature of this polarization anisotropy in the case of strained QWs is substantially different from the case of unstrained structures, where it is a consequence of the additional quantization of the charge carriers in the plane of the initial quantum well.[4,5]

In the present paper we calculate the polarization-dependent PL spectra for strained InGaAs/GaAs QWs with a rectangular shape. In calculating the dispersion and the wave functions of the electrons and holes, we take into account the nonuniformity of the distribution of the elastic deformations along the cross section of the QW and the surrounding material. The computed spectra are compared with the experimental data obtained for buried structures with InGaAs/GaAs QWs.

2. BAND STRUCTURE AND MATRIX ELEMENTS OF INTERBAND TRANSITIONS IN INGAAS/GAAS QUANTUM WIRES

2.1. *Calculation of elastic stresses.* We consider first the distribution of elastic deformations in a heterostructure with an InGaAs/GaAs quantum well sandwiched between infinitely thick GaAs barriers (Fig. 1a). As is well known, the difference in the lattice constants of $In_xGa_{1-x}As$ and GaAs causes the quantum well to be uniformly biaxially compressed:

$$\epsilon_{xx}^{in}=\epsilon_{yy}^{in}=(a_0-a(x))/a_0, \quad \epsilon_{zz}^{in}=-\frac{2\nu}{1-\nu}\epsilon_{xx}^{in};$$

$$\epsilon_{xx}^{\text{out}}=\epsilon_{yy}^{\text{out}}=\epsilon_{zz}^{\text{out}}=0, \tag{1}$$

where $a(x)$ and a_0 are the lattice constants of $In_xGa_{1-x}As$ and GaAs, and ν is Poisson's ratio.

In the case of a one-dimensional structure — a quantum wire (Fig. 1b) — the situation becomes more complicated. In this case the components of the elastic deformation tensor in the xz plane become substantially spatially nonuniform, and the barrier material is elastically deformed. To calculate the components of the tensor ϵ we shall employ the analytical approximation[1]

$$\epsilon_{xx}=\left(\frac{1+\nu}{1-\nu}\frac{\theta}{2\pi}-\frac{2\nu}{1-\nu}\right)\epsilon_0-F(x,z)\,\nu\epsilon_0,$$

$$\epsilon_{zz}=\left(\frac{1-\nu}{1-\nu}\frac{\theta}{2\pi}-\frac{2\nu}{1-\nu}\right)\epsilon_0-F(x,z)\,\nu\epsilon_0,$$

 1063-7826/97/050509-06$10.00

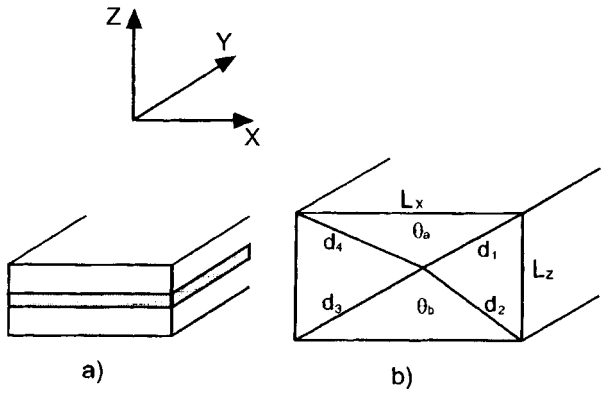

FIG. 1. Schematic diagram of a structure with a quantum well (a) and quantum wire (b).

$$\epsilon_{yy}=F(x,z)\epsilon_0, \quad \epsilon_{xz}=\frac{1+\nu}{\pi(1-\nu)}\ln\left|\frac{d_1 d_3}{d_2 d_4}\right|\epsilon_0;$$

$$\epsilon_0=\frac{a_0-a}{a_0}, \tag{2}$$

where the function $F(x,z)$ equals 1 everywhere inside the QW and 0 outside. The distances d_1, d_2, d_3, and d_{14} and angles θ_a and θ_b are shown in Fig. 1b, $\theta=\theta_a+\theta_b$. Equations (2) were obtained in Ref. 1 under the following basic assumptions: The QW and barrier materials were assumed to be continuously isotropic and to obey Hooke's law. Furthermore, Poisson's ratio of the QW and the barrier were assumed to be equal.

2.2. *Structure of the valence and conduction bands.* A distinguishing feature of expressions (2) for the components of the deformation tensor is that the hydrostatic compression $\delta=\epsilon_{xx}+\epsilon_{yy}+\epsilon_{zz}$ is constant inside the wire and equals zero outside the wire:

$$\delta^{in}=\left(2-\frac{2\nu}{1-\nu}\right)\epsilon_0; \quad \delta^{\text{out}}=0. \tag{3}$$

The quantity δ (3) is equal to the value for the quantum well. Since the Hamiltonian of the conduction-band electrons depends only on the hydrostatic compression δ, the relaxation of the elastic deformations which is described by Eqs. (2) has no effect, to a first approximation, on the quantization of the electrons. Disregarding the interaction of the conduction band with other bands, we write the Schrödinger equation for the electrons in the effective mass approximation in the form

$$\left[\frac{\hbar^2}{2}\left(-\partial_x\frac{1}{m^*}\partial_x-\partial_z\frac{1}{m^*}\partial_z\right)+\frac{\hbar^2 k_y^2}{2m^*}+a_c\delta+V^c(x,z)\right]\times f^c(x,z)=E^c f^c(x,z), \tag{4}$$

where $f^c(x,z)$ are the envelopes of the electron wave functions, $V^c(x,z)$ is the profile of the conduction-band bottom, and a_c is the deformation potential of the electrons.

To calculate the energy levels and the envelopes of the wave functions of the holes, we shall employ Luttinger's formalism[6] with a 4×4 Hamiltonian, i.e., we take into account the interaction of the two top subbands of the valence band. We write Schrödinger's equation in the form

$$[\hat{H}_L+H_s]f^\nu(x,z)=Ef^\nu(x,z), \tag{5}$$

where $f^\nu(x,z)$ is a four-component envelope wave function of the holes, and $\hat{H}_L$ is the Luttinger Hamiltonian, which in the basis of the eigenfunctions of the projection operator of the total angular momentum has the form

$$\hat{H}_L=\begin{bmatrix} H_{hh} & c & b & 0 \\ c^+ & H_{lh} & 0 & -b \\ b^+ & 0 & H_{lh} & c \\ 0 & -b^+ & c^+ & H_{hh} \end{bmatrix}\begin{bmatrix} \frac{3}{2} \\ -\frac{1}{2} \\ \frac{1}{2} \\ -\frac{3}{2} \end{bmatrix};$$

$$H_{hh}=\frac{\hbar^2}{2m_0}[(\gamma_1+\gamma_2)(\partial_x^2-k_y^2)+(\gamma_1-2\gamma_2)\partial_z^2]+V^\nu(x,z),$$

$$H_{lh}=\frac{\hbar^2}{2m_0}[(\gamma_1-\gamma_2)(\partial_x^2-k_y^2)+(\gamma_1+2\gamma_2)\partial_z^2]+V^\nu(x,z),$$

$$b=-\frac{\hbar^2\sqrt{3}}{2m_0}\gamma_3(\partial_x+k_y)\partial_z, \quad c=-\frac{\hbar^2\sqrt{3}}{2m_0}\frac{\gamma_2+\gamma_3}{2}(\partial_x+k_y)^2, \tag{6}$$

where γ_1, γ_2, and γ_3 are the Luttinger parameters, m_0 is the free-electron mass, and $V_\nu(x,z)$ is the profile of the valence-band edge. The second term in Eq. (5) is the so-called Pikus–Bir Hamiltonian,[7] which in the same basis as the Hamiltonian (6) has the form

$$H_S=-\begin{bmatrix} p+q & r & -s & 0 \\ r^* & p-q & 0 & s \\ -s^* & 0 & p-q & r \\ 0 & s^* & r^* & p+q \end{bmatrix}$$

$$p=a_\nu\delta, \quad \delta=\epsilon_{xx}+\epsilon_{yy}+\epsilon_{zz},$$

$$q=-b_\nu\left[\frac{1}{2}(\epsilon_{xx}+\epsilon_{yy})-\epsilon_{zz}\right],$$

$$r=-\frac{\sqrt{3}}{2}b_\nu(\epsilon_{xx}-\epsilon_{yy})+id_\nu\epsilon_{xy},$$

$$s=-id_\nu(\epsilon_{xz}-i\epsilon_{yz}). \tag{7}$$

Here a_ν, b_ν, and d_ν are the deformation potentials of the valence band, and the components of the deformation tensor ϵ depend on the coordinates according to Eq. (2). It should be noted that the Hamiltonian (6) is written in the axial approximation. The values of the parameters for GaAs and InGaAs employed in the calculation are presented in Table I.

TABLE I. Values of the parameters for GaAs and $In_{0.2}Ga_{0.8}As$.

Parameter	GaAs	$In_{0.2}Ga_{0.8}As$	Parameter	GaAs	$In_{0.2}Ga_{0.8}As$
m_c/m_0	0.067	0.059	a_ν, eV	–	−1.1
γ_1	6.85	9.56	b_ν, eV	–	−2
γ_2	2.1	3.34	d_ν, eV	–	−5
γ_3	2.9	4.14	a_0, Å	5.65	5.73
α_0, eV	–	−7	η	–	0.32

To solve to Eq. (5) numerically, we employed a Fourier expansion of the envelope wave functions of the electrons and holes:[8]

$$f^c(x,z)=\frac{1}{\sqrt{XZ}}\sum_{m=-n_x}^{n_x}\sum_{n=-n_z}^{n_z} f^c(m,n)e^{2\pi imx/X}e^{2\pi inz/Z},$$

$$f^\nu_\nu(x,z)=\frac{1}{\sqrt{XZ}}\sum_{m=-n_x}^{n_x}\sum_{n=-n_z}^{n_z} f^\upsilon_\nu(m,n)e^{2\pi imx/X}e^{2\pi inz/Z}, \tag{8}$$

where X and Z are the periods of a formal superlattice of QWs in the directions of the x and z axes. These periods must be chosen to be large enough so as to ensure negligible overlapping of the wave functions of the electronic and hole states of the neighboring QWs. Substitution of the expansions (8) into Eqs. (5) and (4) reduces the latter to an algebraic problem of finding the eigenvalues and eigenvectors of the matrices. The results of the calculation of the short-wavelength shift of the first interband transition e_1-h_1 relative to its position in a quantum well are presented in Fig. 2 for different widths of the QWs. The dashed curve was obtained without regard for the spatial nonuniformity of the distribution of the elastic deformations, i.e., upon substitution of the values of ϵ (1) into the Hamiltonian (7). It is evident from the figure that even for wide QWs the spatial dependence of the components of the elastic-deformation tensor cannot be ignored. In addition, in wide enough QWs the modification of ϵ_{ij}, compared with their values in the initial quantum well, is the main source of the short-wavelength shift of the transition e_1-h_1 and, together with it, the PL band. The results presented in Fig. 2 are in good qualitative agreement with the results obtained in Ref. 2 on the measurements of the magnetoluminescence, as well as with their calculation, performed using algorithms for solving numerically the equations of the theory of elasticity.

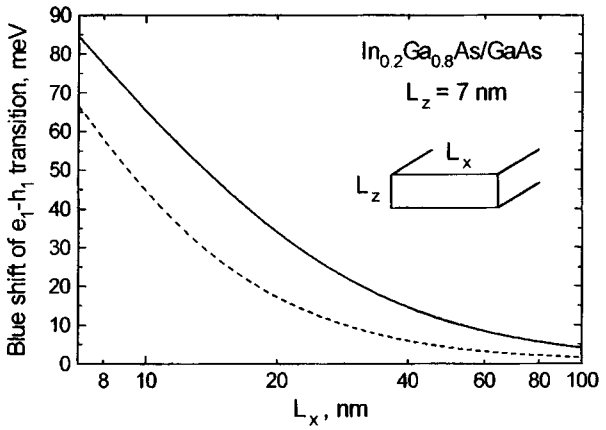

FIG. 2. Short-wavelength shift of the transition e_1-h_1 versus the width of a QW taking into account (solid line) and neglecting (dashed line) the spatial dependence of the components of the tensor of elastic deformations.

2.3. *Matrix elements and their polarization anisotropy.* Besides the short-wavelength shift of the PL, another characteristic manifestation of the one-dimensional nature of the electron-hole gas in QWs is thought to be the polarization anisotropy of PL and the absorption of light. We shall show below that in the case of strained QWs the magnitude of this anisotropy is determined mainly by the modification of the components of the tensor ϵ.

Using the expansion (8), we can calculate the overlap integrals of the envelopes of the wave functions of electrons and holes:

$$J^\nu_{i,j}=\int f^c_i(x,z)f^{\nu *}_{\nu,j}(x,z)dxdz=\sum_{m,n} f^c_i(m,n)f^{\nu *}_{\nu,j}(m,n), \tag{9}$$

where $f^c_i(m,n)$ and $f^{\nu *}_{\nu,j}(m,n)$ are the eigenvectors of the Hamiltonians (4) and (5); the indices i and j enumerate the electron and hole states, respectively; and the index $\nu=\{3/2,\ -1/2,\ 1/2,\ -3/2\}$ enumerates the components of the hole wave function. For linearly polarized light incident in a direction normal to the plane of the QWs, the matrix element of a radiative transition between states i, k_y and j, k'_y of the valence and conduction bands can be written in the form

$$|M_{i,j}|^2=F_{ij}(1+\alpha_{i,j}\cos 2\phi)\,\delta(k_y-k'_y), \tag{10}$$

where ϕ is the angle between the polarization vector of the light and the y axis (i.e., the axis of the quantum wire), and the δ function ensures that the law of conservation of quasi-wave vector in the direction of the y axis is satisfied. The amplitude F_{ij} and degree of polarization α_{ij} of a transition are related with the overlap integrals (9) by the relations (see, for example, Ref. 4)

$$F_{ij}=\frac{1}{2}\left[\ |J^{\frac{3}{2}}_{i,j}|^2+|J^{-\frac{3}{2}}_{i,j}|^2]+\frac{1}{6}[J^{\frac{1}{2}}_{i,j}|^2+|J^{-\frac{1}{2}}_{i,j}|^2\right],$$

$$\alpha_{i,j}=\frac{1}{F_{i,j}}\frac{1}{2\sqrt{3}}\left[\ J^{\frac{3}{2}}_{i,j}J^{-\frac{1}{2}*}_{i,j}+J^{\frac{3}{2}*}_{i,j}J^{-\frac{1}{2}}_{i,j}+J^{\frac{1}{2}}_{i,j}J^{-\frac{3}{2}*}_{i,j}\right]. \tag{11}$$

It should be kept in mind that the overlap integrals, and therefore the quantities $\alpha_{i,j}$ and $F_{i,j}$, are functions of k_y.

The computational results for the degree of polarization of the transition e_1-h_1 at the point $k_y=0$ are presented in Fig. 3 as a function of the width of the QW. The dashed line in this figure shows the results of such a calculation in the approximation of spatially uniform biaxial mechanical deformations. As one can see from the figure, the polarization anisotropy of the matrix elements of interband optical transitions in strained QWs is determined virtually completely by the difference of the elastic deformations from biaxial deformations. Biaxial compression, as is well known, splits the valence band, shifting the heavy-hole subband upward and the light-hole subband downward in energy. At the same time, the polarization anisotropy in the plane of the QWs is

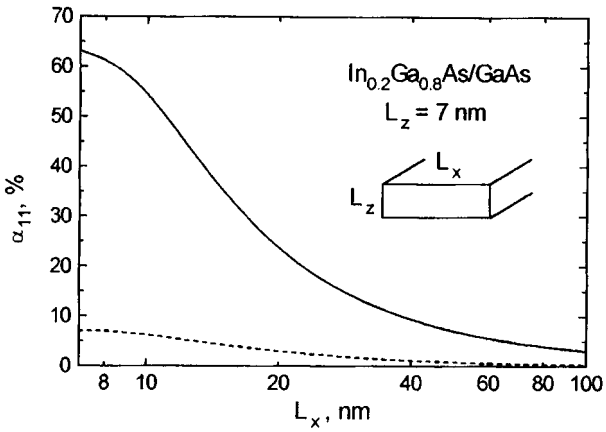

FIG. 3. Degree of polarization of the transition e_1-h_1 versus the width of a QW taking into account (solid line) and neglecting (dashed line) the spatial dependence of the components of the tensor of elastic deformations.

determined by the mixing of the states of these two subbands, which are associated with the additional size quantization in the plane of the initial quantum well. This mixing is found to be suppressed by the splitting caused by the biaxial compression. Therefore, the degree of polarization of the interband transitions in the plane of the QW approaches zero (dashed curve in Fig. 3). The difference of the elastic deformations inside a QW and in the surrounding barrier from biaxial deformations results in indirect mixing, which is not associated with size quantization, of the heavy- and light-hole subbands. The resulting polarization anisotropy of the matrix elements of interband transitions is substantial (see Fig. 3) and even exceeds the similar values for unstrained InGaAs/GaAs QWs of the same width.[4]

3. POLARIZATION ANISOTROPY OF PL

3.1. *Calculation of the PL spectra.* To calculate the PL spectra, in addition to the dispersion laws for electrons and holes, calculated in Sec. 2, and the matrix elements of interband transitions, it is also necessary to know the parameters of the homogeneous and inhomogeneous broadening of the energy levels, as well as the distribution of charge carriers over these levels.

We shall write the one-dimensional density of states in the conduction and valence bands in the form

$$D^{c,\nu}(E)=\frac{2}{\pi}\sum_n \int_{k_y} G(E-E_n^{c,\nu}(k_y))dk_y, \tag{12}$$

where $E_n^{c,\nu}(k_y)$ are the electron and hole dispersion branches, and $G(E)$ is a Gaussian function that describes in Eq. (12) the inhomogeneous broadening of energy levels. Knowing the density of states and the matrix elements of the interband transitions, we can calculate the interband light absorption spectrum

$$\alpha(\hbar\omega)=\frac{\pi e^2}{\epsilon_0 cnm_0^2}\frac{1}{\omega}\sum_{i,j} \int_{k_y}\int_{E_c}\int_{E_\nu} G(E_c-E_i^c(k_y)) \times G(E_\nu-E_j^\nu(k_y))|M_{i,j}(k_y)|^2\Gamma(E_c-E_\nu -\hbar\omega)dk_y dE_c dE_\nu, \tag{13}$$

where n is the index of refraction, ϵ_0 is the vacuum permittivity, m_0 is the free-electron mass, and ω is the frequency of the light. The Lorentzian $\Gamma(E)$, which replaces the law of conservation of energy, takes into account the homogeneous broadening of the optical transitions.

Denoting the integrand in Eq. (13) as $d\alpha$, we write the spectral dependence of the luminescence in the form

$$L(\hbar\omega)=\frac{e^2 n}{\epsilon_0\pi c^3 m_0^2}\omega^2\sum_{i,j} \int_{k_y}\int_{E_c}\int_{E_\nu} d\alpha \times F(E_c-E_F^c)F(E_\nu-E_F^\nu)dk_y dE_c dE_\nu, \tag{14}$$

where $F(E)$ is the Fermi distribution, and E_F^c and E_F^ν are the Fermi quasilevels of the electrons and holes, respectively. We underscore again that the polarization dependence of the luminescence and absorption spectra (13) and (14) is incorporated in the matrix element $M_{i,j}(k_y)$. Knowing the PL intensity for two directions of linear polarization of light (parallel and perpendicular to the axis of the QW), we can calculate the PL polarization spectrum as

$$\rho(\hbar\omega)=\frac{L_\parallel(\hbar\omega)-L_\perp(\hbar\omega)}{L_\parallel(\hbar\omega)+L_\perp(\hbar\omega)}. \tag{15}$$

Equation (14) describes the shape of the luminescence spectrum when the scale of the inhomogeneities of the QW, which result in broadening of the carrier energy levels, is less than the carrier diffusion length, i.e., when there is enough time for the carriers to be thermalized during their lifetime. However, another possible case is when the scale of the inhomogeneities is greater than the carrier diffusion length and when the luminescence of different sections of a QW occurs independently.[9] In this case the unbroadened luminescence contour must be determined first and then its convolution with the static distribution must be calculated:

$$L(\hbar\omega)=\tilde{L}(\hbar\omega,s)\times P(s-\overline{s}), \tag{16}$$

where s is a parameter, with a variance, on which the luminescence spectrum depends, $\overline{s}$ is the average value of this parameter, and $P(s-\overline{s})$ is the statistical distribution of the ensemble of QWs with respect to this parameter.

3.2. *Experimental data. Comparison with calculations.* The measurements of the PL spectra and polarization were performed on QWs obtained by reactive ionic etching followed by burying of the initial structures with a single 70-Å-thick-$In_{0.2}Ga_{0.8}As$/GaAs quantum well. A detailed description of the fabrication technology is given in Ref. 10 . Transmission microscopy data showed that the width of a QW was equal to 600 ± 100 Å.

The experimental PL spectra of a QW and of the initial structure with a quantum well, as well as the computed PL spectrum of the quantum well are shown in Fig. 4. The computed spectrum was obtained by the method described in the preceding section. The adjustable parameters were as follows:

— the position of the Fermi quasilevel E_c^F in the conduction band relative to the bottom E_{c1} of the first electron quantization subband;

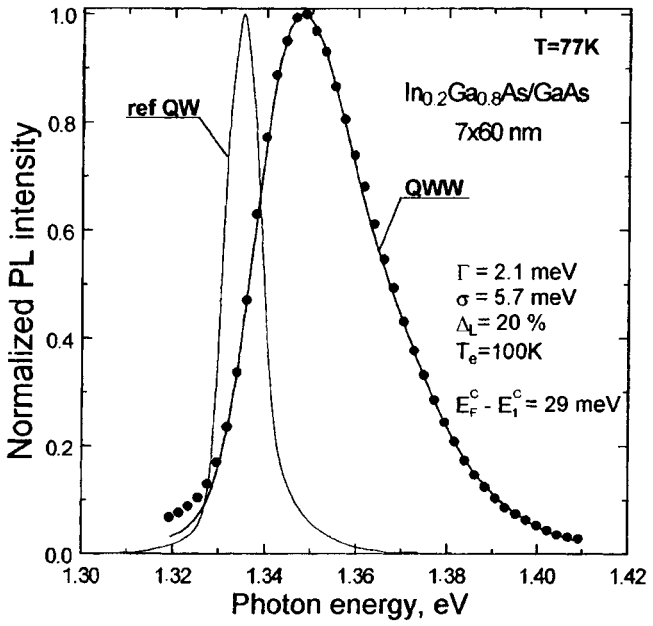

FIG. 4. PL spectra of a QW and the initial quantum well. For QW the dots show the experimental spectrum and the solid curve is the computed spectrum.

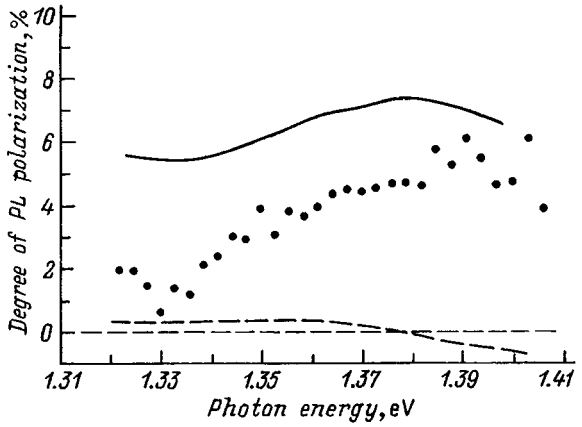

FIG. 5. PL polarization spectrum. Solid curve — calculation taking into account the spatial modulation of the components of the tensor ϵ; dashed line — in the approximation of uniform biaxial deformation; dots — experimental values. $T=77$ K.

— the magnitude Γ of the homogeneous broadening of the transitions, which appears in the Lorentzian in Eq. (13); for simplicity, this parameter was assumed to be energy-independent;

— the electron-hole gas temperature T_e;

— the magnitude of the inhomogeneous broadening σ of the levels of the initial quantum well that is associated with fluctuations of the width and composition of the quantum well, and so on; since the scale of these fluctuations is less than the carrier diffusion length, we employed Eqs. (12)–(14) to calculate them; and

— the fluctuations of the width of the QW; since the scale of these fluctuations, which are associated with the nonideality of the technological process, is much greater than the carrier diffusion length, this mechanism of broadening of the PL line must be taken into account in accordance with Eq. (16). For the distribution P we employed the normal Gaussian distribution

$$G(L-\overline{L})=\frac{1}{\sqrt{2\pi}\Delta_L}\exp\left[-\frac{(L-\overline{L})^2}{2\Delta_L^2}\right], \tag{17}$$

where L is the width of the QW, $\overline{L}$ is the average value of this width, and Δ_L is the rms fluctuation of the width.

The values of the parameters which give the best agreement between the computed shape of the PL spectrum and the experimental spectrum are presented in Fig. 4. We employed as the adjustable parameter the Fermi quasilevel of the electrons and not the holes, since these measurements of the voltage dependence of the capacitance attest to n-type conductivity near the QW. From the results of the fit (Fig. 4), one can see that the Fermi quasilevel of the electrons lies 29 meV above the bottom of the first quantization subband; i.e., the electron gas is strongly degenerate. Such a high electron density in a material that has not been specially doped can be explained by accumulation of a background n-type impurity at the boundary.[11] The position of the Fermi quasilevel of the holes in this case does not appreciably influence the shape of the PL line, since for the pump densities employed the holes are far from being degenerate.

The experimental and computed spectra of the degree of polarization of PL are presented in Fig. 5. The values of the parameters obtained from fitting the shape of PL line, as described above, were used in the calculation. The figure also shows the PL polarization spectrum calculated in the approximation of uniform biaxial deformations (dashed line). As one can see from the figure, in this approximation the calculation gives a degree of polarization that does not exceed 1%, and it does not describe the experimentally observed spectrum. At the same time, the calculation performed with allowance for the spatial modulation of the components of the tensor ϵ gives much better, though incomplete, agreement with experiment. Near the maximum of the PL line, as one can see from Fig. 5, the computed value of the degree of polarization is 1.3–1.5 times greater than the experimental value.

This discrepancy cannot be attributed only to the experimental error in the measurement of the degree of polarization of PL or the approximate nature of the algorithms for numerical calculation of these spectra. In our opinion, it can be attributed to the crystallographic nonideality of the boundaries of the QW and the presence of point defects on it. Partial inelastic relaxation of the mechanical stresses, resulting in a decrease of the spatial modulation of the components of the deformation tensor, can occur on such defects. At the present time, we are investigating the boundaries of QWs with the aid of different methods of high-resolution microscopy, and we are working on imposing boundary conditions on the components of the tensor ϵ that take into account the partial plastic relaxation of the stresses on point defects. The results of this work will be the subject of our subsequent publications.

4. CONCLUSIONS

In summary, in the present work we examined, theoretically and experimentally, the reasons for the polarization anisotropy of PL in strained structures with QWs with a rectangular cross section. The calculation was performed on the basis of the Luttinger formalism with a 4×4 Hamiltonian for the valence band. An analytical approximation was used to take into account the spatial dependence of the components of the tensor of elastic mechanical deformations. The experimental data were obtained for InGaAs/GaAs QWs prepared by reactive ionic etching.

The calculations and comparison of the computational results with experimental results showed that in the case of strained QWs the main mechanism for the appearance of polarization anisotropy of PL and light absorption is the difference of the elastic mechanical deformations by biaxial deformations. This anisotropy is found to be very large even for wide QWs and exceeds the corresponding values for unstrained structures.

[1)]Electronic mail: mitya@quantum.ioffe.rssi.ru

[1] J. R. Downes, D. A. Faux, and E. P. O'Reilly, Mater. Sci. Eng. B **35**, 357 (1995).
[2] M. Notomi, J. Hammerdberg, H. Weman, S. Nojima, H. Sugiura, M. Okamoto, T. Tamamura, and M. Potemski, Phys. Rev. B **52**, 11 147 (1995).
[3] S. A. Gurevich, D. A. Zakheim, S. A. Solov'ev, A. E. Fedorovich, V. N. Mikhajlov, S. I. Nesterov, I. V. Kochnev, and V. I. Skopina, Phys. Low-Dim. Structur. **12**, 141 (1995).
[4] U. Bockelmann and G. Bastard, Phys. Rev. B **45**, 1688 (1992).
[5] T. Sogawa, S. Ando, and H. Kanabe, Appl. Phys. Lett. **68**, 364 (1996).
[6] J. M. Luttinger and W. Kohn, Phys. Rev. **97**, 869 (1955).
[7] G. E. Pikus and G.L. Bir, Fiz. Tverd. Tela (Leningrad) **1**, 1642 (1960) [Sov. Phys. Solid State **1**, 1502 (1960)].
[8] G. A. Baraff and D. Gershoni, Phys. Rev. B, **43**, 4011 (1991).
[9] M. A. Herman, D. Bimberg, and J. Christen, J. Appl. Phys. **70**, R1 (1991).
[10] S. A. Gurevich, D. A. Zakheim, S. A. Solov'ev, A. E. Fedorovich, V. V. Komin, I. V. Kochnev, S. I. Nesterov, and V. I. Scopina, Mater. Sci. Eng. B **35**, 47 (1995).
[11] M. Notomi, M. Okamoto, and T. Tamamura, J. Appl. Phys. **75**, 4161 (1994).

Translated by M. E. Alferieff

Photoresponse of $Cd_xHg_{1-x}Te$ crystals due to composition inhomogeneities

I. S. Virt and D. I. Tsyutsyura

I. Franko Drogobych State Pedagogical Institute, 293720 Drogobych, Ukraine
(Submitted February 19, 1996; accepted for publication October 25, 1996)
Fiz. Tekh. Poluprovodn. **31**, 606–608 (May 1997)

It is shown that when $Cd_xHg_{1-x}Te$ crystals are irradiated with light with photon energy less than the band gap, photoconductivity due to generation of electron-hole pairs on inhomogeneities with a lower value of x is possible. The inhomogeneities are modeled in the form of a cluster network of small-angle boundaries of blocks with a high rate of recombination of nonequilibrium charge carriers. The magnitude of the photoresponse ($\overline{\Delta p}$) versus the size (r_c) of the cluster network is estimated. © *1997 American Institute of Physics.* [S1063-7826(97)02305-3]

The photoconductivity of $Cd_xHg_{1-x}Te$ crystals with photon energies $h\nu$ greater than the band gap E_g is due to interband absorption and formation of electron-hole pairs. In the case $h\nu<E_g$ several processes are possible — intraband and two-photon absorption[1] as well as absorption on inhomogeneities.

In this paper we report the results of an experimental study of the photoelectric properties of $Cd_xHg_{1-x}Te$ crystals ($x>0.20$) illuminated with CO_2 laser pulses ($\lambda=10.6$ μm, $h\nu<E_g$). Samples with the composition $x=0.23-0.27$ and dimensions of $7\times2\times1$ mm were employed. The samples possessed electronic conductivity with electron density $n=(5-0.5)\times10^{14}$ cm^{-3} and mobility $\mu_n=(1-0.1)\times10^5$ cm^2/(V·s). The photoresponse was recorded with a S 8–13 oscilloscope. Excitation was performed with $\Delta t\approx10^{-7}$ s laser pulses. The effect of heating of the electron gas was decreased by using low radiation powers, obtained with the aid of filters. To determine E_g in the crystals, we measured the spectral dependences of the photoconductivity at 77 K.

Light absorption can occur on spherical inhomogeneities as well as on dislocations,[2] but the most common defect in $Cd_xHg_{1-x}Te$ crystals are small-angle boundaries (SABs) of mercury-enriched blocks;[3] this determines the local decrease in E_g in their vicinity. The comparatively large area of the network of SABs in crystals makes SABs the most active defects in photoprocesses as compared with all other defects. The recombination action of extended defects was investigated in Refs. 4 and 5.

In calculating the induced photoconductivity, the cluster network of SABs can be represented by spherical grains of a semiconductor with a high rate of recombination of nonequilibrium charge carriers (NCCs) at the boundary s. Nonequilibrium charge carriers are generated in regions on the boundaries of the blocks (with $E_{gs}<h\nu$) and subsequently diffuse into the semiconductor grains (Fig. 1).

For a n-type semiconductor, in the chosen model the continuity equation for nonequilibrium charge carriers (NCCs) (Δp)has the form

$$D_p\left(\frac{d^2\Delta p}{dr^2}+\frac{2}{r}\frac{d\Delta p}{dr}\right)-\frac{\Delta p}{\tau_p}=0 \tag{1}$$

with the boundary conditions

$$\left\{D_p\frac{d\Delta p}{dr}\right|_{r=r_s}=C_s-s\cdot\Delta p\Big|_{r=r_c},\quad D_p\frac{d\Delta p}{dr}\Big|_{r=0}=0, \tag{2}$$

where D_p is the diffusion coefficient of the nonequilibrium holes, τ_p is the bulk lifetime of NCCs, and C_s is the rate of generation of NCCs at the boundaries of the blocks. The solution of Eq. (1) with the boundary conditions (2) is an expression describing the coordinate distribution of the density of NCCs inside the blocks:

$$\Delta p(r)=\Delta p_s(r_c)\frac{r_c}{r}\frac{\sinh\left(\frac{r}{L_p}\right)}{\sinh\left(\frac{r_c}{L_p}\right)}, \tag{3}$$

where $\Delta p_s(r_c)$ is the surface density of NCCs, which depends on the size of the SAB network,

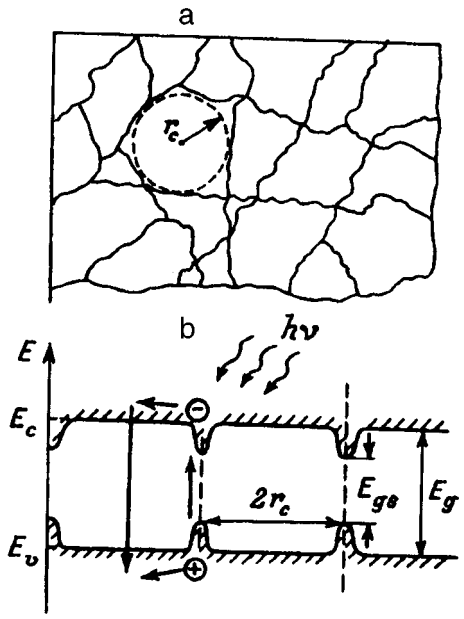

FIG. 1. SAB network (a) and energy diagram of a $Cd_xHg_{1-x}Te$ sample with SABs (b).

 1063-7826/97/050515-02$10.00

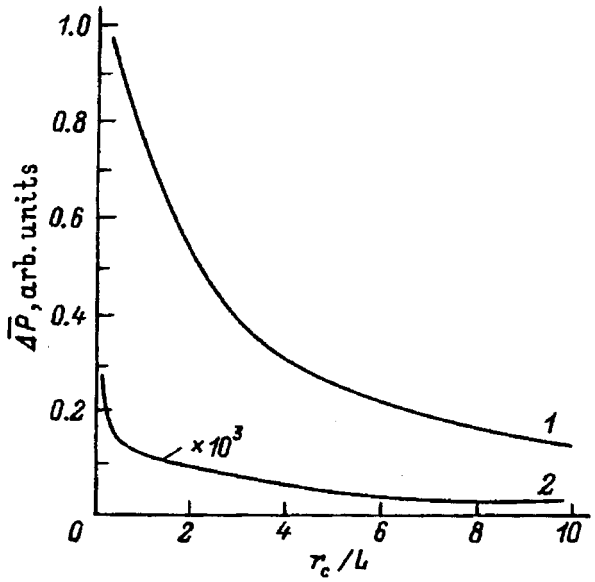

FIG. 2. Average density of nonequilibrium holes versus the relative size of a cluster network of SABs with relative surface recombination rate *1* — $s/\nu=1$, *2* — $s/\nu=100$.

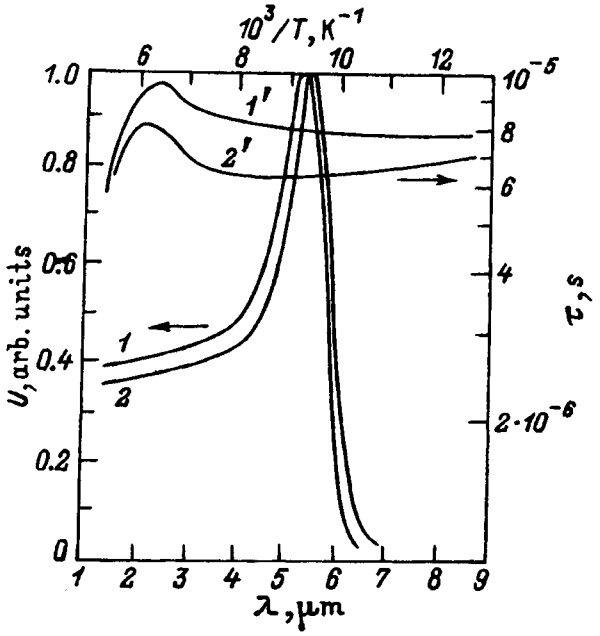

FIG. 3. Spectral characteristics of the photoconductivity (*1*, *2*) and temperature dependences of the lifetime of NCCs (*1′*, *2′*) for two *n*-type samples with composition $x=0.24$.

$$\Delta p_s(r_c)=\frac{G_s\tau_p/L_p}{\coth\left(\frac{r_c}{L_p}\right)+\frac{s\tau_p}{L_p}-\frac{L_p}{r_c}}, \tag{4}$$

and $L_p=\sqrt{D_p\tau_p}$ is the diffusion length of NCCs.

Photoconductivity is produced by the average density of NCCs within the blocks:

$$\overline{\Delta p}=\frac{3G_s\tau_p}{r_c}\left\{1+\frac{s\tau_p}{L_p}\Big/\left[\coth\left(\frac{r_c}{L_p}\right)-\frac{L_p}{r_c}\right]\right\}^{-1}. \tag{5}$$

The dependence of the relative magnitude of the photoconductivity ($\overline{\Delta p}$) on the size r_c of a cluster network of SABs is shown in Fig. 2 for different relative values of the surface recombination rate s/ν (where $\nu=L_p/\tau_p$ is the rate of diffusion of NCCs). It follows from these relations that for a sufficiently extended network of inhomogeneities, the inhomogeneities can make an appreciable contribution to the photoresponse, especially if the sizes r_c of the subblocks of SABs are comparable to the diffusion length L_p.

The experimental results for two samples of $Cd_xHg_{1-x}Te$ with composition $x=0.24$ are shown in Fig. 3. The band gap estimated according to the long-wavelength shoulder of the spectral characteristic of the photoconductivity is $E_g\approx0.20$ eV. The NCC lifetime τ_p, measured according to the relaxation of the photoresponse induced by the CO_2 laser pulse ($h\nu\approx0.11$ eV), is $(7-8)\times10^{-6}$ s. Evidently, nonequilibrium electron-hole pair production is possible in the regions of composition x_s in which the band gap is $E_{gs}\lesssim0.11$ eV (at the block boundaries). Since the relaxation time observed experimentally is much longer than that in samples with composition $x_s=0.20$, where the band gap equals the photon energy, it can be assumed that τ_p is determined by the recombination of NCCs not on inhomogeneities but rather in the volume of the blocks. The lifetimes of nonequilibrium holes in weakly doped material, which were calculated for these compositions[6] ($x=0.24$ and 0.20), differ by approximately a factor of 3, which agrees with the data obtained.

It should be noted that the high density of mercury atoms at the grain boundaries not only decreases the composition x but also forms a high density of donors. In samples with electronic conductivity this improves the natural sink of nonequilibrium holes from grain boundaries in the volume, whose energy barrier is approximately 45 meV. In InSb crystals with the same band gap E_g photoconductivity under lower-power excitation with a CO_2 laser is not observed.

On this basis it can be expected that the sensitivity to CO_2 laser radiation will increase as a result of an increase in the lifetime of NCCs, if inhomogeneities with composition $x=0.20$ are introduced into the wide-gap material $Cd_xHg_{1-x}Te$.

[1] S. Ashmontas, I. Gradauska, K. Naudzhyus, and É. Shirmulis, Fiz. Tekh. Poluprovodn. **28**, 1975 (1994) [Semiconductors **28**, 1089 (1994)].
[2] N. N. Grigor'ev, A. V. Lyubchenko, and E. A. Sal'kov, Ukr. Fiz. Zh. **34**, 1088 (1989).
[3] A. I. Elizarov, V. I. Ivanov-Omskiĭ, A. A. Korniyash, and V. A. Petryakov, Fiz. Tekh. Poluprovodn. **18**, 201 (1984) [Sov. Phys. Semicond. **18**, 125 (1984)].
[4] N. N. Grigor'ev, V. K. Ergakov, L. A. Karachentseva, K. R. Kurbanov, A. V. Lyubchenko, and É. A. Malovichko, Fiz. Tekh. Poluprovodn. **25**, 1649 (1991) [Sov. Phys. Semicond. **25**, 995 (1991)].
[5] M. G. Andrukhiv, I. S. Virt, D. I. Tsyutsyura, and P. S. Shkumbatyuk, Élektron. Tekhn., Ser. Materialy **257**, 62 (1991).
[6] V. C. Lopes, A. Y. Syllaios, and M. C. Chen, Semicond. Sci. Technol. **8**, 824 (1993).

Translated by M. E. Alferieff

Transient space-charge-limited current in porous silicon

L. P. Kazakova, A. A. Lebedev, and É. A. Lebedev

A. F. Ioffe Physicotechnical Institute, Russian Academy of Sciences, 194021 St. Petersburg, Russia
(Submitted October 14, 1996; accepted for publication October 25, 1996)
Fiz. Tekh. Poluprovodn. **31**, 609–610 (May 1997)

The transient space-charge-limited current in porous Si prepared from *n*-type crystalline Si has been investigated. The values of the electron and hole drift mobilities were determined from the charge-carrier transit times through the sample and from the magnitude of the initial photocurrent. © *1997 American Institute of Physics.* [S1063-7826(97)02405-8]

In recent years a great deal of attention has been devoted to porous silicon. This material is interesting because it exhibits intense photoluminescence and appreciable electroluminescence in the visible region of the spectrum. Until now, the characteristics of the luminescence and the optical and photoelectric properties of porous Si have been studied.[1–7] Much less attention has been devoted to the characteristics of charge-carrier transport, despite the fact that information about electron and hole drift mobilities is very important for clarifying the mechanism of electroluminescence. Data on charge-carrier mobility in porous Si prepared from *p*-type crystalline Si are available in the literature.[8] However, it is known that the most interesting results on electroluminescence have been obtained on samples prepared from *n*-type crystalline Si.[5] In this connection, in the present work we conducted investigations to determine the electron and hole drift mobilities in porous Si obtained from *n*-type crystalline Si.

Polished wafers of phosphorus-doped, *n*-type (111) crystalline Si with a resistivity of 4.5 $\Omega\cdot$cm were used to fabricate porous silicon. The porous layers were obtained by electrolytic etching of silicon in an electrolyte with the composition (% by volume) 50%HF (48%) + 50%C_2H_5OH (90%) + 0.1%KNO_2 (unimolar solution) under illumination from an incandescent lamp. The duration of the etching with current density 7–10 mA/cm^2 was equal to 25–30 min. Intense photoluminescence in the red-orange region of the spectrum was observed from samples prepared in this manner.

The investigation of charge-carrier transport was conducted on samples with a sandwich-type structure. A crystalline silicon wafer served as the bottom electrode. The top electrode consisted of a half-transmitting Au film which was deposited on the porous Si by the thermal sputtering in a vacuum. The resistance of the samples in an electric field of 10^3 V/cm was equal to about 10^8 Ω with the top electrode area $S=7\times10^{-2}$ cm^2. The thickness of the porous-Si layer, measured with an optical microscope, was $L\simeq8$ μm.

The time-of-flight method was used for the investigations.[9] Nonequilibrium charge carriers were injected into the sample by means of a light pulse from a LGI-21 laser with a wavelength of 0.337 μm and a pulse duration of the order of 8 ns.

The measurements were performed in the strong injection regime, in which a space-charge-limited transient current (SCLTC) was observed. Under SCLTC conditions the injected charge $Q\simeq CV$, where C is the capacitance of the sample, which was regarded as a flat capacitor, and V is the voltage applied to the sample.[10] The characteristic features of the SCLTC are that the current I is independent of the intensity of the injecting radiation and the current is a quadratic function of the voltage $I\sim V^2$.[10]

The measurements of the transient SCLTCs were performed with a pulsed voltage with a duration of the order of 1 ms applied to the samples and with a holding time of $\sim$100 μs between the moments of application of the voltage

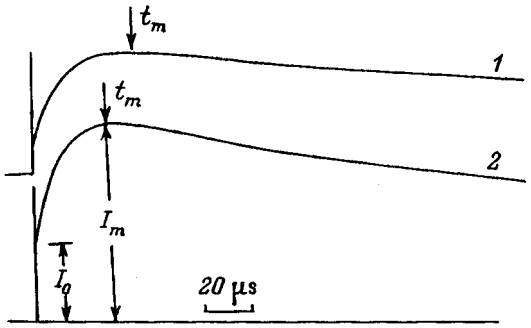

FIG. 1. Oscilloscore traces of transient space-charge-limited photocurrents corresponding to hole drift in porous Si. Applied voltage V, V: *1* — 2, *2* — 3. The sweep time is 20 μs/division.

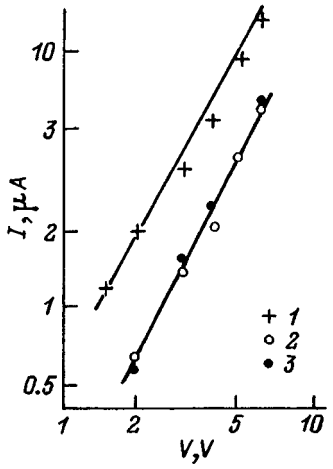

FIG. 2. Values of the currents I_m (*1*) and I_0 (*2*, *3*) versus the voltage V for space-charge-limited transient currents corresponding to hole drift (*1*, *2*) and electron drift (*3*) in a layer of porous Si.

 1063-7826/97/050517-02$10.00

and photoinjection. Figure 1 shows oscillograms of the photocurrent pulses observed during hole drift. The form of the oscillograms of the transient current $I(t)$is typical of a SCLTC. The time dependences $I(t)$ are characterized by initial I_0 and maximum I_m currents. The ratio I_m/I_0 is close to 2.7. The time t_m corresponding to the current maximum varied as the reciprocal of the voltage applied to the sample. The quantities I_0 and I_m increased almost quadratically as a function of the voltage: $I \sim V^2$ (Fig. 2). The value of the hole drift mobility μ_h was determined as the time of flight $t_T = L^2/\mu_h V$, which is related to t_m by the relation $t_m = 0.8 t_T$, as well as from the initial current density[10]

$$j_0 = I_0/S = \mu_h \varepsilon V^2/2.25 \times 10^{13} L^3,$$

where ε is the relative permittivity. The value $\mu_h = 5.7 \times 10^{-3}$ cm^2/(V·s) was obtained from the time of flight. This value of μ_h also follows from the initial current, if one sets $\varepsilon = 4.8$. It is interesting that the close value $\varepsilon \simeq 5$ was obtained in the measurements of the capacitance of the samples at a frequency of 1 MHz.

In contrast to hole transport, current pulses whose form consisted of a continuous drop of the current in time were observed during electron drift. The independence of the signal from the intensity of the injecting radiation and the quadratic dependence of its magnitude on the voltage (Fig. 2) attested to the presence of space-charge limited current. The electron drift mobility μ_e was determined from the current amplitude, which was taken as I_0, and it was assumed that $\varepsilon = 5$. This gave the value $\mu_e \simeq 6 \times 10^{-3}$ cm^2/(V·s). We note that in restructuring the time dependences of the electronic photocurrent in a double logarithmic scale, a kink appeared on the curves $I(t)$ and the time of flight was determined according to this kink. The value of the electron mobility found from the time of flight was found to be close to the value obtained from the initial current.

In summary, the investigations performed in layers of porous Si prepared from *n*-type crystalline Si gave close values of the hole and electron drift mobilities: $\mu_e \simeq \mu_h \simeq 6 \times 10^{-3}$ cm^2/(V·s). This result is different from that obtained in Ref. 8 ; this attests to the strong difference in the values of $\mu_e = 1-2$ cm^2/(V·s) and $\mu_h = 6 \times 10^{-3}$cm^2/(V·s), determined in porous Si prepared from *p*-type crystalline silicon. The high values of μ_e evidently stem from the fact that in Ref. 8 they were determined from the fast component of the current, although a slow component was also observed. The value of μ_e which we found could correspond to this component.

The fact that nearly identical values were obtained for μ_h in layers of porous Si prepared from *p*- and *n*-type crystalline Si shows that the type of conductivity in the initial material does not strongly affect hole transport in porous silicon. Another important result of this work is that it has been shown that space-charge-limited currents can be used effectively to study charge-carrier transport in porous Si.

[1] L. T. Canham, Appl. Phys. Lett. **57**, 1046 (1990).
[2] F. Koch, MRS Symp. Proc. **298**, 319 (1993).
[3] N. Koshida and H. Koyama, Appl. Phys. Lett. **60**, 347 (1992).
[4] N. Koshida, H. Mizuno, H. Koyama, and G. J. Collins Jpn. J. Appl. Phys. **34**, 92 (1995).
[5] P. Steiner, F. Kozlovski, and W. Lang, MRS Symp. Proc. **538**, 665 (1995).
[6] J. P. Zheng, K. L. Jiao, W. P. Shen, W. A. Anderson, and H. S. Kwok, Appl. Phys. Lett. **61**, 459 (1992).
[7] E. V. Astrova, S. V. Belov, O. A. Zaĭtsev, and A. A. Lebedev, Pis'ma Zh. Tekh. Fiz. **19**, 50 (1993).
[8] É. A. Lebedev, G. Polisskiĭ, and V. Petrova-Kokh, Fiz. Tekh. Poluprovodn. **30**, 1648 (1996) [Semiconductors **30**, 1099 (1996)].
[9] W. E. Spear, J. Non-Cryst. Sol. **1**, 197 (1969).
[10] M. A. Lampert and P. Mark, *Current Injection in Solids*, Academic Press, N. Y., 1970 [Russian translation, Mir, Moscow, 1973].

Translated by M. E. Alferieff

Effect of transverse pump current nonuniformity and field distribution on the dynamical characteristics of strip injection lasers

S. A. Gurevich, G. S. Simin, and M. S. Shatalov

A. F. Ioffe Physicotechnical Institute, Russian Academy of Sciences, 194021 St. Petersburg, Russia
(Submitted December 9, 1996; accepted for publication December 19, 1996)
Fiz. Tekh. Poluprovodn. **31**, 611–615 (May 1997)

A new model that makes it possible to describe in detail the static and dynamic characteristics of strip injection lasers, taking into account the transverse nonuniformity of the pump current and optical field, is proposed. For the example of a strip ridge-guide laser, it is shown that the ''hole-burning'' effect in the transverse distribution of the optical gain determines the frequency of relaxational oscillations at high power levels. The computed dependence of the rates of decay of the relaxational oscillations on the squared resonance frequency agree well with the experimental data, which previously could not be adequately explained in existing models.
 [S1063-7826(97)02505-2]

Strip injection lasers, in which the pump current flow and distribution of the optical field are concentrated in a narrow channel — a strip several microns wide — are now the most widely used lasers. In calculating the static and dynamic characteristics of such lasers, useful results can be obtained in many cases on the basis of models in which the pump current density, the nonequilibrium carrier density, and the photon density in the cavity are assumed to be constant within the strip channel.[1–3] A number of approaches, which account for the spreading of the pump current in a plane parallel to the p–n junction, charge-carrier diffusion, and the effect of the field of a laser mode on the carrier density distribution profile, have been proposed to describe the static operating regime of the laser, taking into account the transverse nonuniformity.[4–6] However, a calculation of the dynamical characteristics of strip lasers is a much more difficult problem, since the nonuniform capacitance of the diode and the inductance, which is stimulated by radiation and which is of a nonlocal character,[7] must be taken into account in this case. Several methods for solving this problem were proposed in Refs. 8–12. However, the proposed analytical approaches, as a rule, are applicable only for model structures[8–10] and numerical methods do not permit following the effect of important physical parameters on the dynamical characteristics of lasers.[11,12] The present paper proposes a new model for calculating the static and dynamic characteristics of strip injection lasers that can be applied to lasers of arbitrary construction.

For definiteness, we shall study a ridge-guide-type strip injection laser, shown schematically in Fig. 1a. In our model the laser is represented as a distributed chain, consisting of cells arranged in the transverse direction in the plane of the

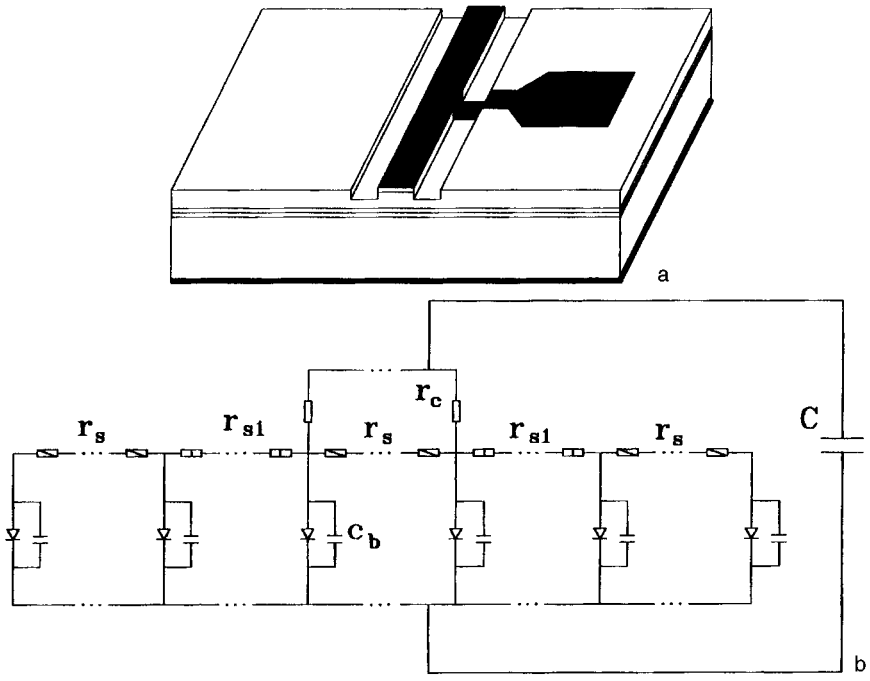

FIG. 1. Schematic diagram of a ridge-guide strip laser (a) and the equivalent circuit (b).

 1063-7826/97/050519-04$10.00

p–n junction (Fig. 1b). As shown in Fig. 1b, the sections of the structure under the ridge, the grooves, and the side regions are represented by cells of different type, so that the size Δx of each cell is small and the parameters of the structure are constant within a cell. Since the structure of the laser is symmetric with respect to the center of the ridge, the calculations were performed for half the chain shown in Fig. 1b, but the final results are presented for the complete structure. The resistances r_c, arranged in the central cells, correspond to the specific contact resistance referred to the area of a cell (the transverse size of a cell, as indicated above, equals Δx and the length of a cell equals the length of the laser cavity). The resistors r_s describe the resistance to spreading under the ridge and in the side regions, and the resistors r_{s1} describe spreading in regions under the grooves. The magnitudes of these resistances are determined on the basis of the thicknesses, the composition, and the doping level of the upper layers in the structure. It is assumed that the resistance to spreading in the thick bottom layers is small and for this reason all cells are connected to a common ''ground.''

The elementary diodes located in each cell represent the inner part of the laser structure, whose impedance depends on the pump current, and the spontaneous and stimulated radiation. The capacitances c_b describe the barrier capacitance of the p–n junction and C describes the parasitic capacitance of the contact area. The diffusion capacitance of the p–n junction, which dominates at high injection levels, is taken into account when calculating the currents in the elementary diodes.

The properties of the elementary diodes are described by the rate equations for the laser, written in the one-mode approximation in the local form:[8]

$$\frac{\partial n(x,t)}{\partial t}=\frac{J(x,t)}{ed}+D\frac{\partial^2 n(x,t)}{\partial x^2}-R_{\rm sp}(n)-\nu g(n)\Psi^2(x)N(t), \tag{1a}$$

$$\frac{\partial N(t)}{\partial t}=N(t)\Gamma_t\nu\int_{-\infty}^{\infty}g(n)\Psi^2(x)dx-\frac{N(t)}{\tau_p}+\beta\int_{-\infty}^{\infty}R_{\rm sp}(n)dx, \tag{1b}$$

where $n(x,t)$ is the density of nonequilibrium carriers in the active layer (it is assumed that the neutrality condition $n=p$ holds), x is the transverse coordinate, and t is the time. In Eqs. (1a) and (1b) $J(x,t)$ is the local pump current density, d is the thickness of the active layer, $R_{\rm sp}(n)$ is the spontaneous recombination rate, D is the ambipolar diffusion coefficient, $g(n)$ is the optical gain, Γ_t is the optical confinement factor in a plane perpendicular to the p–n junction, and ν is the speed of light in the material. As usual, $\tau_p$is the photon lifetime and β is the spontaneous emission coefficient in a mode.

The photon density $S(x,t)$ in the cavity is represented in the form

$$S(x,t)=\Psi^2(x)N(t), \tag{2}$$

where $\Psi^2(x)$ is the squared field of the transverse mode and $N(t)$ is a time-dependent coefficient. It is assumed that $\Psi^2(x)$ corresponds to the main transverse mode, which has a maximum that peaks at the center of the strip and does not depend on time, and

$$\int_{-\infty}^{\infty}\Psi^2(x)dx=1. \tag{3}$$

The radiation power through one mirror of the laser, $P_{1/2}(t)$, can then be expressed as

$$P_{1/2}(t)=\frac{1}{2}N(t)\hbar\omega\nu\frac{d}{\Gamma_t}\ln\frac{1}{R}, \tag{4}$$

where $\hbar\omega$ is the photon energy, and R is the reflection coefficient of the laser mirrors. In solving the rate equations (1a) and (1b) it was assumed that $R_{\rm sp}(x,t)=An(x,t)+Bn^2(x,t)$, where A and B are the nonradiative and radiative recombination coefficients. The following representation of the gain was also used:

$$g(n)=\frac{g'[n(x,t)-n_g]}{1+\varepsilon S(x,t)}, \tag{5}$$

where g' is the differential gain, n_g is the density at the inversion point, and ε is a coefficient that describes the gain saturation at high optical power levels.

The carrier density $n(x,t)$ at each point x is related to the voltage $U(x,t)$ across an elementary diode:

$$n(x,t)=n_0\left[\exp\frac{U(x,t)}{U_0}\right]. \tag{6}$$

The parameters n_0 and U_0 are phenomenological material parameters of the structure and can be determined from the initial exponential section of the experimental current-voltage characteristic of the laser diode. The voltage $U(x,t)$ is in turn related to the current $i(x,t)$ that flows through each unit cell. Enumerating all nodes of the equivalent circuit (Fig. 1b) and using the method of nodal voltages,[13] we write this relation in the form of the matrix equation

$$i_m=U_kG_{mk}. \tag{7}$$

In the expression (7) the matrix G_{mk} is a matrix of the nodal conductances; its diagonal elements G_{mm} are the sum of the conductances connected directly to the node m and the off-diagonal elements G_{mk} are the sum of the conductances connected between the nodes m and k with the reverse sign.[13] It is important to note that in Eq. (7) the ''barrier capacitance–diode'' pair is regarded as a source of the current I_m which is present in each cell. Since the conductances of the current sources equal zero, they do not appear in the matrix G_{mk}. Such an approach is convenient, since in the present case there is no need to describe the elementary diode as a nonlinear conductance taking into account spontaneous and stimulated emission and the diffusion capacitance.

In the structure under study the horizontal component of the current (along the x axis) consists of two parts: an ohmic current flowing along the top layer and a diffusion current flowing between the neighboring cells along the active layer.

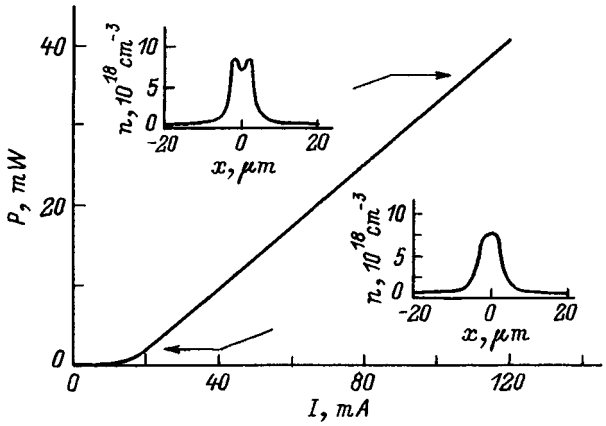

FIG. 2. Computed static power versus current characteristic of the laser. Inserts: Profiles of the nonequilibrium carrier density distribution in the active region for different radiation power levels.

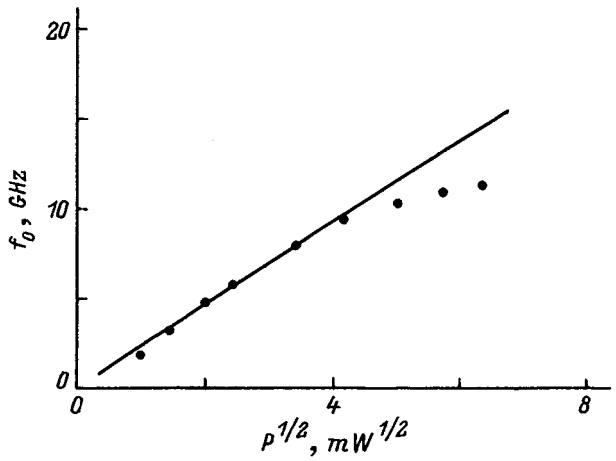

FIG. 3. Computed frequency of the relaxational oscillations versus the square root of the static power. Solid curve — calculation by the standard model, dots — calculation according to the proposed model.

It is easy to show that for reasonable doping levels and thicknesses of the layers the diffusion component of the current is much smaller (by one to two orders of magnitude) than the ohmic component. Therefore, the change in density $n(x,t)$ occurs as a result of recombination processes in the active layer and as a result of injection and extraction of carriers through the p–n junction with carrier transport along the top and bottom conducting layers. The ohmic component of the current in the present model is taken into account when the solving the matrix equation (7) and the diffusion term was dropped when solving the rate equations (1).

The computational procedure consists of solving simultaneously Eqs. (1) and (7) with the appropriate boundary and initial conditions. The external voltage or the total current through the laser must be prescribed as the boundary condition. In calculating the stationary regime of the laser, the initial conditions can be chosen arbitrarily to a certain extent. The stationary state obtained is used as an initial condition in modeling the transient processes.

The static power versus current characteristic of the laser, calculated by the procedure described above, is shown in Fig. 2. The parameters of standard InGaAsP/InP laser structures (radiation wavelength $\lambda = 1.55$ μm) with separate confinement, which contain several quantum wells in the active region, were used in the calculations.[12,14,15] The cones and grooves (Fig. 1) were assumed to be 5 μm wide and the laser cavity was assumed to be 150 μm long. The values of the main parameters in the expressions (1) and (4)–(6) were chosen to be as follows: $g' = 6\times10^{-16}$ cm^2, $\varepsilon = 2.5\times10^{-17}$ cm^3, $\tau_p = 1.6$ ps, and the parasitic capacitance $C = 0.22$ pF. As one can see in Fig. 2, the threshold current of the laser is 18 mA and the efficiency is 0.37 mW/m, which corresponds to the actually observed characteristics of such lasers. The nonequilibrium carrier density distributions in the active layer, calculated for two radiation power levels, are shown in the insets. At low power (of the order of several milliwatts) the density profile is determined by the spreading of the pump current under the ridge and the grooves. At a radiation power level of $\sim$15 mW a dip due to depletion of the carrier density under the action of the stimulated radiation (spatial hole burning[8]) appears at the center of the ridge.

Taking account of the spatial nonuniformity made it possible to explain a number of experimentally important features of the dynamics of strip lasers. The computed dependences of the frequency f_0 of the relaxational oscillations on the square root of the static radiation power P are presented in Fig. 3. The solid curve corresponds to the calculation according to the standard ''average'' model in which the pump current density and the photon density are assumed to be constant (average) within the strip. The dots in Fig. 3 represent the results of the calculation performed in a model which takes into account the spatial nonuniformity. In this case the stationary state was calculated first, after which the laser pump current I was changed by a jump by an amount $\delta I \ll I$ (weak signal). In this case damped relaxational oscillations, whose frequency f_0 is plotted along the ordinate in Fig. 3, were observed in the time dependence of the output power P. We note that the main parameters of laser structure were taken to be the same in the calculation by the average and ''nonuniform'' models. As one can see, the results of the two calculations are identical for low optical powers. At power levels exceeding $\sim$15 mW the calculation according to our model gives a sublinear dependence of f_0 on $P^{1/2}$. The same dependence is also observed experimentally.[16] To explain the saturation of f_0 in the average model it would have been necessary to increase substantially the value of the parameter ε. The observed discrepancy is explained by the above-noted burning of a spatial hole in the transverse direction (see Fig. 2).

An appreciable difference of the results is also observed in calculations of another important dynamical parameter — the decay rate γ of the relaxational oscillations. As one can see in Fig. 4, at low frequencies our model gives comparatively high values of the decay rate while at frequencies exceeding $\sim$6 GHz (radiation power exceeding $\sim$6 mW) γ is less than that predicted by the average model. It is interesting to note that this behavior of the decay at low frequencies was observed experimentally in a number of studies,[14–16] but this

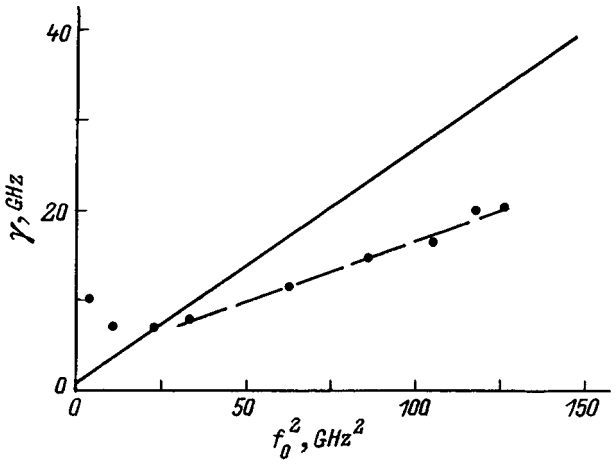

FIG. 4. Computed rate of decay of relaxational oscillations versus the squared relaxational frequency. Solid line — calculation according to the standard model, dots — calculation according to the proposed model.

has not been adequately explained in the average model. As one can see from Fig. 4, at high frequencies our computed curve of the decay versus the squared resonance frequency is nearly linear. The small variance of the points is due to the computational error. The value of the K factor,[15] obtained from the slope of this line, equals 0.14 ns. Close values of K have been obtained in experimental studies of structures of this type.[2,14,16] As our calculations show, the parasitic capacitance of the contact area in this case does not appreciably affect the character of the dependence of f_0 on $P^{1/2}$, but the presence of this capacitance increases γ slightly.

In summary, the model proposed in the present paper, taking into account the spatial nonuniformity of the pump current, the optical field, and the gain, makes it possible to describe in detail the static and dynamic characteristics of strip injection lasers. This model can be used to calculate the characteristics of different types of laser structures with a fixed profile of the optical mode.

We are deeply grateful to R. A. Suris for many helpful discussions.

This work was supported by the Nortel Company, the International Science Foundation (Grant No. NU9000), and the Fund of the European Economic Society (Grant No. 93-0049 INTAS).

[1] R. Nagarajan, M. Ishikawa, T. Fukushima, R. S. Geels, and J. E. Bowers, IEEE J. Quant. Electron. **28**, 1990 (1992).
[2] R. Nagarajan, M. Ishikawa, and J. E. Bowers, Electron. Lett. **28**, 846 (1992).
[3] J. E. Bowers, Solid–State Electron. **30**, 1 (1987).
[4] J. E. A. Whiteaway, IEE Proc. **129**, 89 (1982).
[5] N. Chinone, J. Appl. Phys. **48**, 3237 (1977).
[6] B. W. Hakki, J. Appl. Phys. **46**, 292 (1975).
[7] R. A. Suris, private communication.
[8] W. W. Ng and E. A. Sovero, IEEE J. Quant. Electron. **20**, 1008 (1984).
[9] N. Chinone, K. Aiki, M. Nakamura, and R. Ito, IEEE J. Quant. Electron. **14**, 625 (1978).
[10] J. D. Evans, G. J. Letal, G. P. Lee, and I. G. Simmons, in *LEOS'95 Conf. Proc.* **1**, 278 (1995). [IEEE Lasers and Electro-Optic Society 1995 Annual Meeting, San Francisco, CA, USA, 1995].
[11] R. F. Kazarinov and M. R. Pinto, IEEE J. Quant. Electron. **30**, 49 (1994).
[12] R. Bonello and I. Montrosset, J. Lightwave Techn. **10**, 1890 (1992).
[13] L. A. Bessonov, *Theoretical Prinicples of Electronics* [in Russian], Vyssh. Shkola, Moscow, 1978.
[14] J. D. Ralston, S. Weisser, I. Esquivais, E. C. Larkins, J. Rosenzweig, P. J. Tasker, and J. Fleissner, IEEE J. Quant. Electron. **29**, 1648 (1993).
[15] R. Olshansky, P. Hill, V. Lanziera, and W. Powazinik, IEEE J. Quant. Electron. **23**, 1410 (1987).
[16] S. Weisser, P. J. Tasker, I. Esquivias, J. D. Ralston, and J. Rosenzweig, IEDM'93 Conf. Proc., IEDM 93-601 [Int. Electron Dev. Meeting, Washington, DC, USA, Dec. 5–8, 1993].

Translated by M. E. Alferieff

Luminescence properties of gallium nitride layers grown on silicon carbide substrates by gas-phase epitaxy in a chloride system

A. S. Zubrilov,[1)] Yu. V. Mel'nik, D. V. Tsvetkov, V. E. Bugrov, A. E. Nikolaev, S. I. Stepanov, and V. A. Dmitriev

A. F. Ioffe Physicotechnical Institute, Russian Academy of Sciences, 194021 St. Petersburg, Russia
(Submitted December 3, 1996; accepted for publication January 15, 1997)
Fiz. Tekh. Poluprovodn. **31**, 616–620 (May 1997)

The luminescence properties of undoped epitaxial layers of gallium nitride grown on silicon carbide substrates by gas-phase epitaxy in a chloride system have been investigated. An edge band (361 nm, 96 K) and defect bands (380, 430, 560 nm, 96 K) were recorded in the photo- and cathodoluminescence spectra. It was observed that the parameters of the edge and defect luminescence bands for the GaN layers studied do not depend on the crystalline perfection of the substrate, but rather they are determined by the growth conditions, specifically, the position of the sample in the reactor. It is shown that there exists a characteristic symmetry of the distribution of the luminescence properties of a layer along the surface of the samples relative to the direction of the gas flow in the reactor. A correlation is established between the parameters of the edge and blue luminescence bands and the density of the electrically-active impurity in the epitaxial layer. © *1997 American Institute of Physics.*
[S1063-7826(97)02605-7]

1. INTRODUCTION

The production of highly efficient blue and green light emitting diodes[1] and the development of a violet injection laser[2] based on gallium nitride have made this material one of the most intensively studied semiconductors. The development of epitaxial methods for growing GaN is being pursued very actively. These studies are impeded by the fact that GaN substrates are virtually nonexistent,[3] and the methods being developed are heteroepitaxial.

We reported in a previous paper the possibility of growing high quality epitaxial layers of AlN on sapphire substrates[4] and GaN layers on silicon carbide substrates[5] modified during gas-phase epitaxy by a chloride-hydride method (CHM) without the use of a buffer layer. An advantage of silicon carbide as a substrate for GaN over the widely used sapphire is the smaller lattice mismatch and the possibility of passing an electrical current through the substrate, which is important for a number of device applications. Furthermore, GaN/SiC heterojunctions are of interest for device applications.[6,7] It is natural to expect that in the case of epitaxy without a buffer the parameters of the substrate will have a much stronger effect on the structural quality and properties of the epitaxial layer than in the case of epitaxy on a pregrown buffer.[1–3]

In Ref. 8 we presented the properties of the crystalline structure of epitaxial layers grown by CHM on silicon carbide substrates. It was found that the quality of the crystalline structure of the GaN epitaxial layers is determined mainly by the crystalline perfection of the substrate. Experiments in which the half-width of the x-ray rocking curve from a definite section of the SiC substrate was compared with the half-width of the rocking curve from the GaN layer grown on the same section of the substrate showed that as the half-width of the rocking curve from the silicon carbide structure increases, the rocking curve from the gallium nitride layer increases in width. The range of variation of the half-width of the x-ray rocking curve for different sections of the SiC substrate ranged in these experiments from 17 to 74 angular seconds. The existing range of values for a GaN-layer was equal to 69 to 149 angular seconds. In the present paper we report the results of an experimental study of the optical characteristics of these layers.

2. EXPERIMENTAL SAMPLES AND MEASUREMENT METHODS

The GaN layers were grown at atmospheric pressure in a horizontal reactor placed in a multizone furnace with resistive heating. Silicon carbide crystals were used as substrates. Gallium nitride was deposited without a buffer layer. The layers were grown on the (0001) Si face of the SiC substrates of the $6H$ and $4H$ polytypes. The substrates were both n- and p-type. The layers were not doped during growth. The growth temperature was in the range 950–1050 °C. The layers ranged in thickness from 0.2 to 7 μm. For samples 30 mm in diameter the variance of the GaN layer thickness over the area did not exceed 5%. The growth rate ranged from 0.1 to 60 μm/h, depending on the technological regimes. The layers possessed electronic-type conductivity. The density of uncompensated donors N_D-N_A, determined with a mercury probe by the $C-V$ method, was in the range $10^{17}-10^{18}$ cm^{-3}. A description of the characteristic features of the technology can be found in Refs. 5 and 8 .

The luminescence properties of the samples were investigated by photo- (PL) and cathodoluminescence (CL) in the temperature range 96–300 K. A nitrogen laser operating at a wavelength of 337.1 nm was used for photopumping. The parameters of the laser were as follows: pulse power — 2 kW, pulse duration ~10 ns, and pulse repetition frequency — 100 Hz. A 4 to 15-keV electron beam was used for the cathodoluminescence investigations. The beam current was

 1063-7826/97/050523-04$10.00

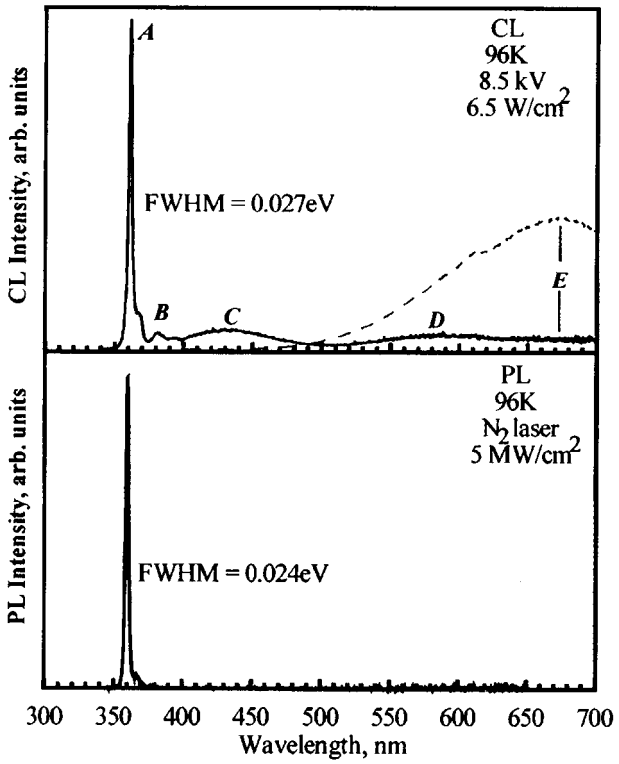

FIG. 1. Cathodoluminescence (top figure) and photoluminescence (bottom figure) spectra of GaN layers grown on 6*H*-SiC substrates. The dotted line is the cathodoluminescence spectrum of the substrate.

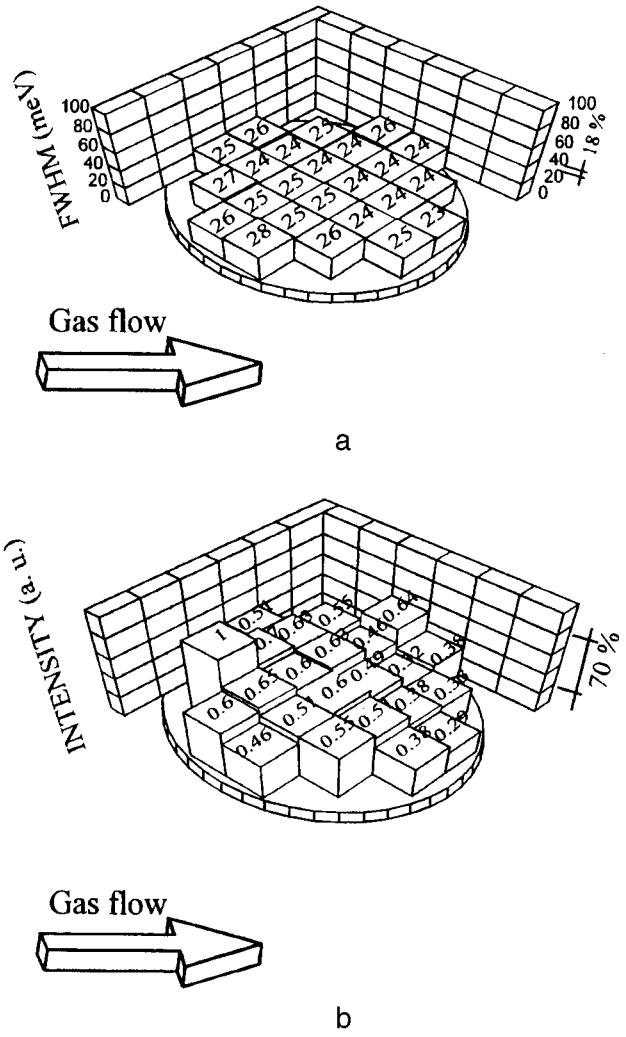

FIG. 2. Histograms of the distribution of the half-widths of the edge peak (a) and intensities of the edge peak (b) for the GaN epitaxial layer over the area of a plate 30 mm in diameter. The arrow marks the direction of gas flow of the reagents relative to the substrate in the reactor.

equal to 0.01–0.05 mA. The diameter of the electron beam on the surface of the sample was varied in the range 0.5–50 mm. The luminescence spectra were recorded with a monochromator (MDR-23) with a dispersion of 1.3 nm/mm. The spectral resolution of the apparatus was no worse than 0.1 nm. After being recorded with a photomultiplier (FÉU-100), the signal was automatically corrected for the spectral sensitivity of the apparatus. A chart of the distribution of the intensity values and the half-width of the luminescence bands, measured in 24 regions of the structure by analogy with previous x-ray studies,[8] was constructed for a layer grown on a SiC substrate 30 mm in diameter.

3. EXPERIMENTAL RESULTS AND DISCUSSION

The characteristic luminescence spectra of the GaN layers grown at low and high excitation levels are shown in Fig. 1. We note that the excitation method does not greatly influence the spectra. Four bands are typically present for the measured spectra: an edge band *A* ($\lambda_{max}\sim$361 nm, 96 K), previously interpreted as an excitonic band,[9] and three longer wavelength bands *B*, *C*, and *D* in the near-UV, blue, and yellow-green regions of the optical spectrum, respectively. The *B* band ($\lambda_{max}\sim$380 nm, 96 K) and the *C* band ($\lambda_{max}\sim$430 nm, 96 K) can be attributed to self-doping during growth. The nature of the *D* band ($\lambda_{max}\sim$560 nm, 96 K), which is apparently attributable to vacancies in the nitrogen sublattice, is being vigorously discussed in the literature.[3] An *E* band with a radiation intensity peak in the edge region of the spectrum was recorded in some samples; this band is apparently due to reemission in the SiC substrate (the cathodoluminescence spectrum of the substrate has a wide band with a maximum at the wavelength ~670 nm). In some samples the *C* and *D* bands were not recorded. At very high excitation levels (of the order of 1 MW/cm^2) the edge band *A* was observed to dominate the bands *B*, *C*, and *D* as result of saturation of the recombination channels via defects. We note that the previously measured correlations[8] between the half-width of the x-ray rocking curves and the luminescence characteristics (the half-width of the luminescence bands and the ratios of the intensities of different bands) were not observed. The type of conductivity and polytype of SiC substrates had no effect on the luminescence of the GaN layers.

In studying the distribution of the luminescence properties over the area of a layer grown on a SiC substrate 30 mm in diameter, it was found that the position of the sample relative to the direction of the gas flow affected the luminescence properties (Figs. 2–4). The intensity of the edge peak of the photo- and cathodoluminescence and also the *C* and *D* band intensities were distributed symmetrically relative to

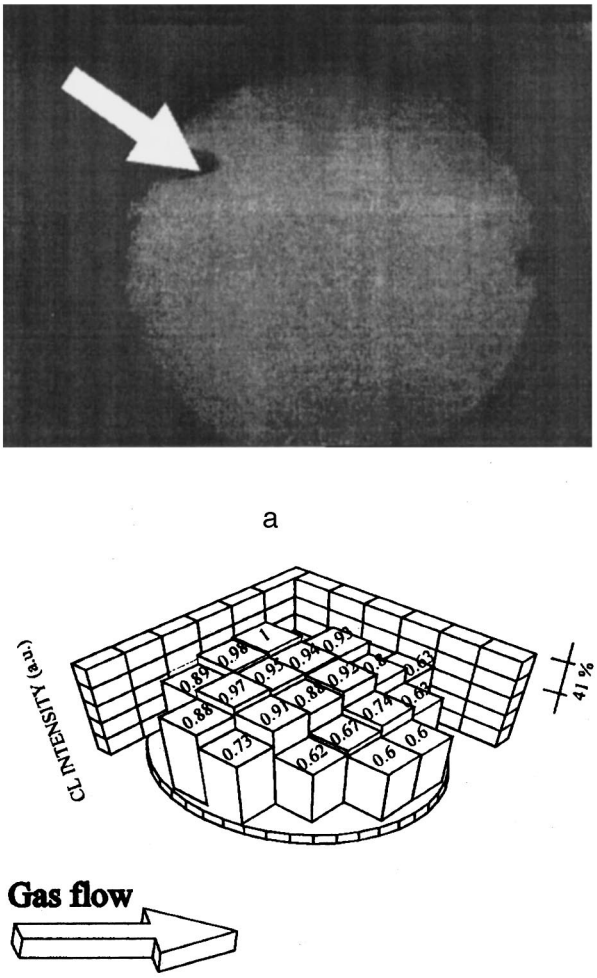

FIG. 3. Analysis of the distribution of the intensities of the *C* luminescence band over the area of the plate. Topogram (a) and histogram (b): distribution of the intensity of the blue band (optical filter with a transmission band 380–460 nm). The arrows show the direction of gas flow of the reagents relative to the substrate in the reactor.

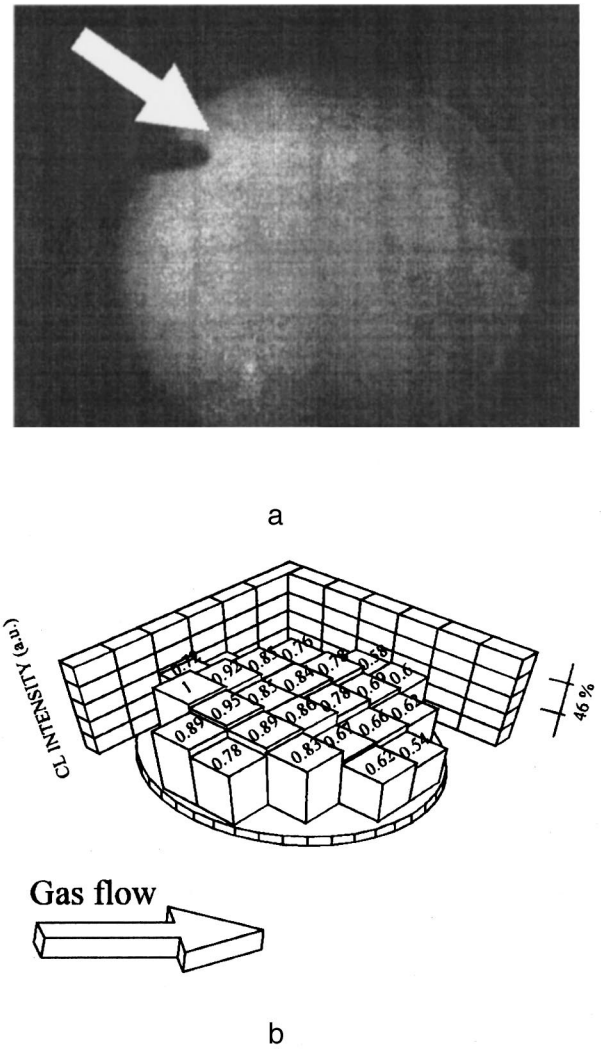

FIG. 4. Analysis of the distribution of the intensities of the *D* luminescence band over the area of the plate. Topogram (a) and histogram (b): distribution of the intensity of the green band (optical filter with a transmission band 500–580 nm). The arrows show the direction of gas flow of the reagents relative to the substrate in the reactor.

a line passing through the center of the sample parallel to the direction of the gas flow. This symmetry was not observed in the x-ray measurements in Ref. 8 . The density N_D-N_A, constant over the entire area of the sample, was equal to 2×10^{17} cm^{-3}.

The results obtained can be explained as follows. The nonuniform distribution of the intensity of the luminescence bands over the area of the sample is due, in our opinion, to the nonuniform introduction of point defects into the layer: impurities and (or) intrinsic defects of the structure (here a correlation is possible between the luminescence and electrical properties over the area of the sample). In turn, the nonuniformity of the distribution of point defects could be due to at least two factors: the nonuniform distribution of the contaminating uncontrollable impurity along the growth zone of the reactor and the dependence of the trapping coefficients for these impurities and (or) point defects on the technological conditions on the growth surface (pressure of the reagents, temperature) and the properties of the surface itself. In this connection, the appearance of mirror symmetry in the distribution of the intensity of the luminescence bands is not unexpected and is determined by the geometry of the reactor at a fixed position of the substrates during growth. This effect is quite weakly expressed in one sample (which is the fundamental advantage of the technology employed for growing GaN). For this reason, it was not possible to observe on one sample a correlation with the density N_D-N_A. However, such a correlation could be observed in samples from different growth experiments with substantially different intensity of the blue defect band *C*. As a rule, more intense *C* band and greater broadening of the edge band *A* were observed in samples with a large value of N_D-N_A (Fig. 5).

Here a different reason is given for the absence of a sharp correlation between the luminescence and x-ray measurements. In strongly mismatched heterostructures, such as GaN/SiC, the main type of structural defects, whose density and distribution determine the broadening of the x-ray rocking curves in the ω-scan geometry, are dislocations. For a

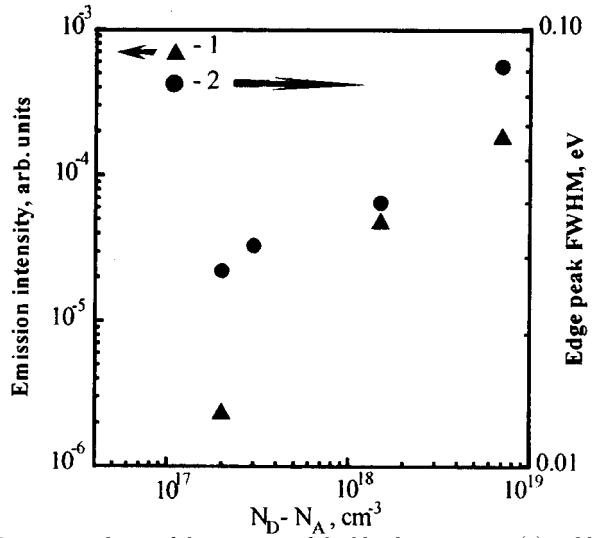

FIG. 5. Dependence of the intensity of the blue luminescence (*1*) and half-width of the edge peak (*2*) on the density $N_D - N_A$ for a number of epitaxial GaN layers grown by CHM under different technological regimes.

dislocation density of $10^8 - 10^9$ cm^{-2} (Ref. 8) in the experimental layers the effect of point defects on the x-ray rocking curves is negligible. On the other hand, it is well known that such a high dislocation density in III–V nitrides, nonetheless, makes it possible to prepare highly efficient light-emitting diodes and injection lasers based on them.[1,2] This means that the luminescence properties of these materials are largely determined by point defects and local mechanical stresses, i.e., the short-range order in the crystal (even in the free states, for example, free excitons, which contribute to the edge luminescence in GaN, are strongly localized because of the large effective masses of the charge carriers[3]). This is apparently attributable to the fact that the diffusion lengths for nonequilibrium charge carriers in this material are short[10] compared with the average distance between dislocations. There is therefore enough time for most nonequilibrium charge carriers to recombine before being trapped by dislocations. However, in the case of a strong interaction of the systems of point and extended (for example, impurity atmosphere of dislocations) defects, correlations are, in principle, also possible between the luminescence (electrical) properties and the spatial distribution of the extended defects. The fact that we were not able to observe such correlations in the experimental layers indicates that the interaction of the systems with one another is not strong enough to cause an appreciable change in the luminescence and electric properties along the area of the GaN samples.

As indicated above, the edge band *A* is of an excitonic nature and consists of a superposition of two bands[9] — a band associated with the annihilation of an exciton localized on a neutral donor and a band of a free exciton. The broadening of the *A* band is determined by two effects: temperature and inhomogeneous broadening, which could be caused by defects and local mechanical stresses. As one can see in Fig. 2, the half-width (FWHM) of the *A* band is small and the variance in the values of the half-width of the *A* band over the area is also small (18%). This attests to the fact that the contribution of inhomogeneous broadening is relatively small in this case. For samples obtained under nonoptimal technological conditions and possessing a large *A*-band half-width (>100 meV, 300 K), inhomogeneous broadening makes a substantial contribution; this is confirmed by the weaker temperature dependence of the half-width for this band.

The nature of the defect luminescence bands in our samples is unknown. Analysis of the composition of the samples by Auger electron spectroscopy showed that the samples do not contain chemical impurities with concentrations exceeding 0.1 at. %. Analysis of the GaN layers by secondary-ion mass spectrometry revealed the presence of traces of a number of elements which could form electrically active centers. However, this question requires additional investigation.

In summary, a strong effect of substrate properties on the luminescence properties of a layer were not observed for gallium nitride layers of high structural perfection on silicon carbide substrates without a buffer layer; i.e., the substrate does not make a substantial contribution (at least for layer thicknesses greater than 0.2 μm) to the formation and distribution of point structural defects over the area of the layer, which largely determine the luminescence properties of gallium nitride.

We wish to thank A. I. Babanin for performing the investigations of the composition of the layers grown. We also thank N. I. Kuznetsov for performing the electrical measurements and I. P. Nikitina for valuable discussions.

This work was supported, in part, by Arizona State University (USA).

[1)]Electronic mail: asz@shuttle.ioffe.rssi.ru; fax: (812) 247-6425.

[1] S. Nakamura, M. Senoh, and T. Mukai, Appl. Phys. Lett. **62**, 2390 (1993); H. Morkoc, S. Strite, G. B. Gao, M. E. Lin, B. Sverdlov, and M. Burns, J. Appl. Phys. **76**, 1363 (1994); S. Nakamura, M. Senoh, N. Isawa, and S. Nagahama, Jpn. J. Appl. Phys. Lett. **34**, L797 (1995).

[2] S. Nakamura, in *Proc. Int. Symp. On Blue Laser and Light Emitting Diodes*, Chiba University, Japan, 1996, p. 119.

[3] S. Strite and H. Morkoc, J. Vac. Sci. Technol. B **10**, 1237 (1992).

[4] A. O. Lebedev, Yu. V. Melnik, and A. M. Tsaregorodtsev, in *Inst. Phys. Conf. Ser.* **137**, Chap. 4 (1994), p. 405.

[5] Yu. Melnik, I. P. Nikitina, A. S. Zubrilov, A. A. Sitnikova, Yu. G. Musikhin, and V. A. Dmitriev, Inst. Phys. Conf. Ser. **142**, Chap. 5 (1996) p. 863.

[6] A. E. Nikolaev, Yu. V. Melnik, M. N. Blashenkov, N. I. Kuznetsov, I. P. Nikitina, A. S. Zubrilov, D. V. Tsvetkov, V. I. Nikplaev, V. A. Dmitriev, and V. A. Soloviev, MRS Internet J. Nitride Semicond. Research, **1**, 45 (1996) (http://nsr. mij. org/1/45).

[7] J. I. Pankove, S. S. Chang, H. C. Lee, R. J. Molnar, T. D. Moustakas, and B. Van Zeghbroeckin, in *Proc. Int. Electron. Dev. Meeting* (1994) p. 389.

[8] Yu. Melnik, I. P. Nikitina, A. E. Nikolaev, D. V. Tsvetkov, A. A. Sitnikova, and V. A. Dmitriev, in *Abstracts 1st European Conf. On Silicon Carbide and Related Mater*, Heraklion, Greece, 1996, p. 79.

[9] D. K. Nelson, M. A. Jakobson, Yu. Melnik, and A. V. Selkin, in *Abstracts Topical Workshop on III–V Nitrides*, Nagoya, Japan, 1995, P-4.

[10] V. Dmitriev, K. Irvine, J. Edmond, A. Sitnikova, Yu. Musikhin, N. Bert, A. Zubrilov, V. Nikolaev, I. Nikitina, Yu. Melnik, A. Babanin, and A. Tsaregorodtsev, in *Abstracts 11th Int. Conf. On Crystal Growth*, Hague, Netherlands, 1995, p. 135; V. Dmitriev, K. Irvine, G. Bulman, J. Edmond, A. Zybrilov, V. Nikolaev, I. Nikitina, D. Tsvetkov, A. Babanin, A. Sitnikova, Yu. Musikhin, N. Bert (to be published).

Translated by M. E. Alferieff

Mechanism of multivalued electrical conductivity anisotropy in double heterostructure wells and superlattices

Z. S. Gribnikov

Institute of Semiconductor Physics, Ukrainian National Academy of Sciences, 252650 Kiev, Ukraine
(Submitted July 4, 1996; accepted for publication July 8, 1996)
Fiz. Tekh. Poluprovodn. **31**, 621–625 (May 1997)

A new mechanism is proposed for the multivalued anisotropy of the longitudinal electrical conductivity in double and multiple heterostructures based on multivalley semiconductors. The mechanism is based on the assumptions that when the electron gas is heated, the interwell thermionic emission through a low potential barrier becomes the dominant channel for electronic transitions between wells and that interwell transitions with the valley remaining the same can occur more often than intervalley transitions. The internal electrical voltages arising on the barriers as a result of different intervalley redistribution in the wells are taken into account.
 [S1063-7826(97)02705-1]

1. The multivalued anisotropy of electrical conductivity (MAE) (or the multivalued Sasaki effect — MSE) is most clearly manifested in the form of a spontaneous breaking of the symmetry of the electron distribution along equivalent valleys of a multivalley semiconductor in the case of a current directed along one of the symmetry axes of the crystal. This effect, which leads to domain (layered) structure of the transverse electrical field and valley densities,[1] has been investigated in great detail, both theoretically and in experiments with bulk *n*-Si samples (see the monograph in Ref. 2 and the more recent review articles[3,4]). The ''standard'' mechanism of MAE is a rapid increase in the probability of an intervalley transition with the emission of an intervalley phonon at low lattice temperatures as the heating of the electron gas in a valley increases.

When bulk samples are replaced by layered structures with potential barriers separating the conducting channels, the domain structure of the transverse electric field should change appreciably as a result of the field effect on the barriers.[5]

Here we give the first exposition of a new mechanism of the MAE which differs from the standard phonon mechanism and is characteristic only of layered heterostructures with two or more current channels separated by potential barriers. The proposed mechanism is impossible in bulk samples. We shall show the essence of this mechanism for the simplest example of a double symmetric heterostructure well (Fig. 1) whose current-conducting channels (wells), just as the barrier separating them, consist of materials whose electronic spectrum can be described in a double-valley model.

Let us assume that in each of two wells a and b the electrons in each of two valleys 1 and 2 form a single level ε_I (the lowest subbands). (In view of the assumed weakness of the tunneling coupling between wells, we disregard the splitting of these levels.) Let us also assume that the upper-lying quantization levels ε_{II}, ε_{III}, etc., lie at the height of or above the barrier and are therefore collective. Since the tunneling coupling between the wells in the lowest subbands is assumed to be weak, a different mechanism of interwell electron transistions predominates in the range of longitudinal electric fields of interest to us — well-to-well thermionic emission. In the process of such emission an electron from, for example, valley 1 in well a (i.e., from state $a1$) should be heated up to an energy in its own well such that as a result of scattering it is transferred into one of the higher subbands (while remaining in the same valley) and then again is scattered by the lowest quantization level but now in the well b (i.e., it is transferred into the state $b1$), where it cools.

We shall assume below that a interwell valley-conserving thermionic transition in the range of fields studied is a much more likely process than intervalley scattering of electrons within a well. This is possible if elastic intervalley scattering (by impurities or composition fluctuations of the alloy) is suppressed, the emission of intervalley phonons is very small, i.e., the temperature is low, and the height of the thermoelectric interwell barrier $\varepsilon_{ab}=\varepsilon_{II}-\varepsilon_I$ is much lower than the energy $\hbar\omega_M$ of an intervalley phonon

$$\varepsilon_{ab}<\hbar\omega_M. \tag{1}$$

At equilibrium the initially uniform distribution of carriers over valleys and wells is present, i.e., $n_{a1}=n_{a2}=n_{b1}=n_{b2}=n_0$. The applied electric $E_x=E$ is directed along the x axis and there is no transverse component: $E_y=0$. Because of the anisotropy of the valleys 1 and 2, each valley contains transverse current components $j_{ya1}=j_{yb1}=-j_{ya2}=-j_{yb2}$, which, because of the absence of the field component E_y, do not lead to an average heating or cooling of the carriers in the valleys.

Let us now assume that a fluctuation intervalley redistribution of carriers arises in the well a with the appearance of a positive correction δn_{a1} and a negative correction $\delta n_{a2}=-\delta n_{a1}$. As a result, the conductivity of the well a acquires anisotropy, so that this well produces a small transverse field δE_a, directed so that type $a1$ electrons are cooled as a whole and type $a2$ electrons are heated. Since there is no such field in the well b, the thermionic emission equilibrium breaks down and an excess transition of type $a2$ electrons into the state $b2$ and also a transition of type $b1$ electrons into the cooled state $a1$ arise. Now, an electric field δE_b of opposite sign compared with the field δE_a, giving rise to the additional heating of type $b1$ electrons and cool-

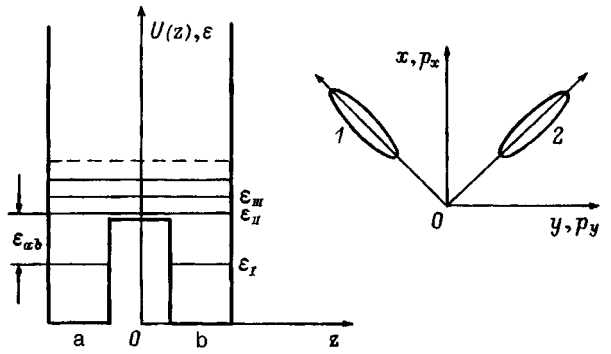

FIG. 1. Double heterostructure well (left side) and arrangement of valleys in the two-dimensional p space of the lowest size-well subbands (right side).

ing of type $b2$ electrons, i.e., (taking into account the thermionic emission process into the well a) intensifying the initial concentration fluctuation in the well 1, arises in well b also.

As a result, when the dissipative fluctuation-intensifying effects described above predominate over many other effects which suppress it, one of two stationary states, shown schematically on the right side of Fig. 2, arises. Such a state is characterized by the presence of transverse electric fields $E_y^{(a)}$ and $E_y^{(b)}$, equal in magnitude and opposite in direction in wells a and b, as well as by a different filling of the valleys in the wells; here the asymmetry of filling is the same in magnitude but different in sign $n_{a1}-n_{a2}=n_{b1}-n_{b2}$ (however, $n_{a1}+n_{b1}=n_{a2}+n_{b2}$). As a comparison, states with broken symmetry which arise in the bulk of the material in the standard MAE scheme are shown on the left side of Fig. 2.

2. The schematic picture of MAE, shown in Fig. 2, in a double well cannot be realized in pure form, since the presence of the fields of different sign $E_y^{(a)}$ and $E_y^{(b)}$ results in the appearance of a voltage $V(y)=-\int_0^y[E_y^{(a)}(y')-E_y^{(b)}\times(y')]dy'$ on the potential barrier separating the wells. This voltage has two consequences which radically change the picture described above.

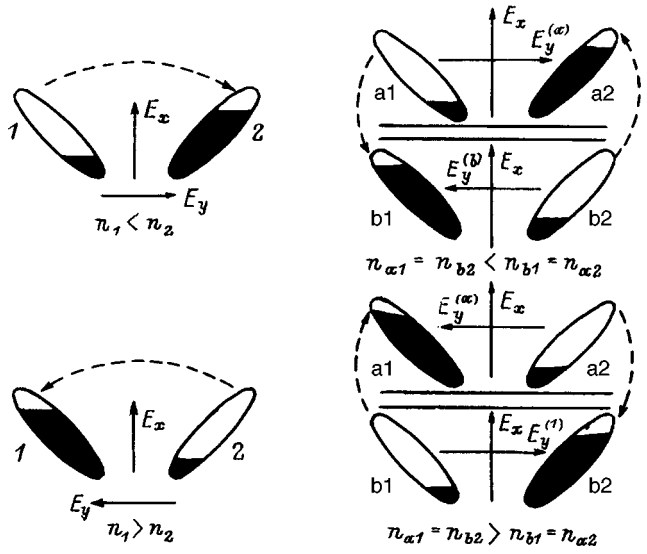

FIG. 2. Schematic picture of MAE in the ''standard'' bulk variant (left side) and in the proposed variant for a double well (right side).

First, there is a charge exchange of the wells, for which

$$e(n_a-n_b)=2\int_0^{V(y)}C(V')dV', \tag{2}$$

where $n_a=n_{a1}+n_{a2}$, $n_b=n_{b1}+n_{b2}$, and $C(V)$ is the effective differential interwell capacitance. Second, the shape of the potential barrier and the wells changes. Now, in view of the strong asymmetry which has appeared, we cannot introduce a single lowest, doubly degenerate, level and we must examine different levels in the wells and introduce two different thermionic emission energies. Therefore, the probabilities of thermionic emission from well a into well b and vice versa are different not only because of the different heating of the electrons in these wells, but also because of the presence of the voltage $V(y)$.

As a result of the two effects acting together, the region of space containing a transverse field $E_y^{(a,b)}$ and the corresponding valley redistribution of electrons in the wells is bounded and separates two wide regions where $E_y^{(a,b)}=0$, but between the wells there is a voltage $V(\infty)$ and $V(-\infty)=-V(\infty)$. The presence of these voltages is due, according to Eq. (2), to the asymmetric filling of the wells: $(n_a-n_b)|_{y=\infty}=-(n_a-n_b)|_{y=-\infty}$. Actually, these wide regions also play the role of layers — domains in the MAE mechanism under study, while the comparatively narrow layers that separate them with transverse fields and intervalley repopulation of electrons serve as domain walls. Therefore, the MAE occurs in these walls.

The qualitative features of the domains and domain walls with the standard MAE in bulk samples and in the double-well case studied here are summarized in Table I.

3. We shall write a simplified (phenomenological) system of equations that makes it possible to describe qualitatively the effect which we are studying. These equations also elaborate and generalize the analogous equations for the standard MAE effect (their viability was later confirmed by many numerical calculations). They include Eq. (2) and four continuity equations for all four groups of electrons introduced above:

$$\frac{\partial n_{\gamma k}}{\partial t}+\frac{\partial j_{\gamma k}}{\partial y}=-n_{\gamma k}[\nu(F_{\gamma k},V_{\gamma\gamma'})+\nu_0(F_{\gamma k})]+n_{\gamma' k}\nu(F_{\gamma' k},V_{\gamma'\gamma})+n_{\gamma k'}\nu_0(F_{\gamma k'}), \tag{3}$$

where $\gamma=a, b$, $k=1, 2$, $\gamma'\neq\gamma$, $k'\neq k$, $V_{ab}=-V$, and

$$F_{\gamma k}=e\mu E^2[1+\zeta_\gamma^2-2A\zeta_\gamma(-1)^k]. \tag{4}$$

Here $\zeta_\gamma=E_y^{(\gamma)}/E$.

Here it is assumed that the components of the valley mobility tensors, which by definition do not depend on the heating, are $\mu_{xx}^k=\mu_{yy}^k=\mu$ and $\mu_{xy}^k=\mu_{yx}^k=-A\mu(-1)^k$, and it is assumed that the heating dependence of the probabilities $\nu(F_{\gamma k},V_{\gamma\gamma'})$ and $\nu_0(F_{\gamma k})$ can be much stronger. The probabilities, introduced in Eqs. (3) (inverse times), of intervalley scattering $\nu_0(F_{\gamma k})$ are assumed to be functions only of some effective powers (per electron) $F_{\gamma k}$ given by Eq. (4) (in com-

TABLE I.

Bulk sample with standard (phonon) MAE mechanism	Double well with thermoelectron MAE mechanism
Domain properties	
Constant transverse field, intervalley population redistribution, anisotropic conductivity	No transverse fields, constant voltage on the barrier, no intervalley population redistribution, interwell population redistribution, isotropic conductivity
Properties of double walls	
Transverse field passes through zero, intervalley population redistribution occurs through zero, domain walls are polarized: thin and thick (forward and reverse)	Transverse fields in wells, voltage on barrier passes through zero, intervalley population redistribution in wells, interwell population redistribution passes through zero, domain walls are not polarized
Symmetry relations	
$E_y(y)=-E_y(-y)$	$E_y^{(a)}(y)=-E_y^{(b)}(-y)$, $V(y)=-V(-y)$
$n_1(y)=n_2(-y)$	$n_a(y)=n_b(-y)$, $n_{a1}(y)=n_{b2}(-y)$, $n_{a2}(y)=n_{b1}(-y)$

plete analogy with the standard theory of the MSE[2]), and the probabilities of interwell thermoelectronic transition $\nu(F_{\gamma k},V_{\gamma\gamma'})$ depend also on the voltages $\pm V$ across the potential barrier. The electron fluxes $j_{\gamma k}$ in the y direction are

$$j_{\gamma k}=-D\frac{\partial n_{\gamma k}}{\partial y}-\mu E n_{\gamma k}[\zeta_\gamma-A(-1)^k]. \tag{5}$$

Finally, it is assumed that the quasineutrality condition holds:

$$\sum_{\gamma=a,k=1}^{b,2} n_{\gamma k}=4n_0. \tag{6}$$

From this condition [and also from Eqs. (3) and (5)] follows the condition

$$n_a\zeta_a+n_b\zeta_b+A(n_{a1}-n_{a2}+n_{b1}-n_{b2})=0, \tag{7}$$

where the zero on the right side corresponds to the assumption of a Hall configuration of the sample in the xy plane.

The solution of the system (2)–(6) falls outside the scope of the present paper. Here we confine our attention only to some of its simplest consequences.

a) For all values of E there exists a trivial solution $n_{\gamma k}=n_0$, $\zeta_a=\zeta_b=0$, $F_{\gamma k}=e\mu E^2$, $V=0$.

b) The system considered above describes the standard MAE:

$$n_{a1}=n_{b1}=n_1;\quad n_{a2}=n_{b2}=n_2\neq n_1;$$
$$\zeta_a=\zeta_b=\zeta\neq 0;\quad V=0. \tag{8}$$

Here $F_{a1}=F_{b1}=F_1\neq F_{a2}=F_{b2}=F_2$.

The possibility for the existence of the solutions (8) does not mean that these solutions are necessary. They occur only in some range of electric fields $E\in(E_l,E_h)$ at sufficiently low temperatures, where sufficiently rapid growth of $\nu_0(F)$ with F occurs. The solutions in the domain walls depend on whether or not the direction of the field flux of the majority carriers in a domain [which appears in Eq. (5)] is the same as or opposite to that of their diffusion flux.[1] As a result, we have two types of domain walls, alternating with one another: thick walls, where these directions are identical on both sides, and thin walls, where these fluxes are antiparallel on both sides.

c) There exist solutions with symmetric properties:

$$n_{a1}(y)=n_{b2}(-y);\quad n_{a2}(y)=n_{b1}(-y);\quad n_a(y)=n_b(-y);$$
$$\zeta_a(y)=-\zeta_b(-y);\quad V(y)=-V(-y). \tag{9}$$

These solutions are the new solutions whose existence is due to the rapid growth of $\nu_0(F,V)$ with F. These solutions are identical to those shown in Fig. 2 (on the right side of the figure) only at the point $y=0$, which must be taken as the center of the domain wall. We note that in this case there is no polarization of the domain walls that occurs in the case of the standard bulk effect, since the densities $n_{\gamma k}$ in these walls do not change sharply and the values of the fields $E_y^{(a,b)}$ do not pass through zero (and, conversely, are close to their maximum values).

In the domains separated by this wall the voltages on the barrier saturate up to the values $V_s=V(\infty)$ and $-V_s=V(-\infty)$; the densities also saturate: $n_{as}=n_a(\infty)=n_b(-\infty)$ and $n_{bs}=n_b(\infty)=n_a(-\infty)$; and the fields $E_y^{(a)}$ and $E_y^{(b)}$ approach zero. The intervalley redistribution in each well also vanishes together with the fields. The saturated value V_s of the voltage is determined from Eqs. (2) and (6) and also from the equation that follows from Eq. (3),

$$n_{as}\nu(V_s)=n_{bs}\nu(-V_s), \tag{10}$$

where $\nu(\pm V_s)=\nu(e\mu E^2,\pm V_s)$. From these equations we have

$$2\int_0^{V_s}C(V)dV=2en_0\frac{\nu(-V_s)-\nu(V_s)}{\nu(-V_s)+\nu(V_s)}, \tag{11}$$

$$n_{as}=4n_0\frac{\nu(-V_s)}{\nu(-V_s)+\nu(V_s)}, \tag{12}$$

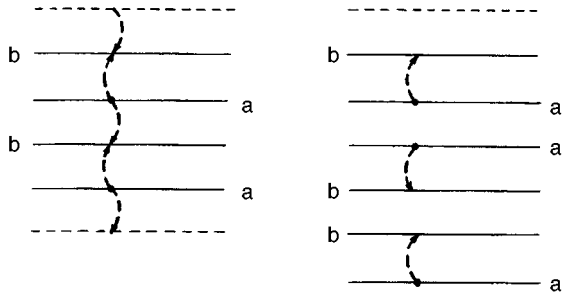

FIG. 3. Possible variants of interwell population redistribution in a multiwell heterostructure. Left — symmetric population redistribution, right — population redistribution by means of pairing.

$$n_{bs}=4n_0\frac{\nu(V_s)}{\nu(-V_s)+\nu(V_s)}. \tag{13}$$

It is easy to show that the existence of nontrivial solutions of Eq. (11) requires a sharp function $\nu(V_s)$. Otherwise, the only domain solution is $V_s=0$. In the case of a very sharp function $\nu(V_s)$ we find that all electrons are transferred into one of the wells because of complete emptying of the other well.

In addition to walls where fields are realized, for example, in the sequence $E_y^{(a)}>0$, $E_y^{(b)}<0$, it is also possible to have analogous walls with fields with opposite signs. The alternation of these two types of walls leads to the existence of multidomain (multilayer) structures with domains of different extent. There arise in this connection the problems of periodicity, stability, pinning, chaos, and so on.

4. The satisfaction of the condition (1) shifts the region of existence of the standard MSE in the structures under study in the direction of stronger fields. Domains with interwell voltage and interwell charge exchange must be unstable with respect to intervalley redistribution by the phonon mechanism. Depending on the combination of parameters, the appearance of an additional redistribution can both completely destroy the structure arising in the weak field region and be incorporated into it (with the formation of a hybrid structure).

Thus far we have studied only double-well structures. Similar effects should also arise in multiwell periodic structures. The closest analog to the double-well problem would be structures in which wells with an even number could be similar to the well *a* and wells with odd numbers similar to the well *b* (Fig. 3a). However, besides the structure ... *bababa* ..., it is entirely possible to have a structure ... *baabbaabba* ... (Fig. 3b). In the latter structure the position of the walls corresponding to one pair of layers is much more easily decoupled and therefore the collection of possible domain structures is enriched substantially, which facilitates transition to chaos.

The most obvious material systems in which the effects described above should be sought are the heterostructures $Si/Si_{1-x}Ge_x$ and Ge/Si_xGe_{1-x}. We shall examine the first of these structures, grown on a Si (100) substrate.

As is well known, in this case the main change in the gap width occurs as a result of offsets in the valence band. However, according to the estimates made in Ref. 6 in a wide range of values of x (0.2–0.5), we are still dealing with a type-I heterostructure, i.e., the $Si_{1-x}Ge_x$ layers also form potential wells in an electronic band with an offset of the order of 0.02 eV, and the deformation of these layers is such that the indicated wells contain only two pairs of Δ valleys ([010] and [001]), and the [100] valley is substantially raised upward. Accordingly, a band structure that is optimal in the sense of the studied effect is realized here. Unfortunately, the unavoidable alloy scattering in $Si_{1-x}Ge_x$ wells can greatly increase ν_0 and liquidate the expected effect.

In this sense, the advantages of the Ge/Si_xGe_{1-x} structure on a (100) Ge substrate with Ge wells has noticeable advantages. For $x=0.02-0.03$ it is also easy to obtain in these structures barriers with $\varepsilon_{ab}\simeq 0.02$ eV. Here alloy scattering is transferred into the barriers, where the residence time of an electron (equal to the ballistic transit time between two elastic scatterings) is short. We note that the structures on Ge substrates have been attracting increased attention in recent years (see, for example, Refs. 7–9).

Although the experimental observation of the effect in double and multiply repeating wells requires cooling to or near the temperature of liquid helium, here (in contrast to bulk Si) carrier freeze-out and dielectrization of the samples do not occur, since under selective doping of the barriers electrons will always fill the wells (if the ionization energy of the impurity in the barrier is sufficiently low, as is the case with the structure Ge/Si_xGe_{1-x} for small x).

I thank V. L. Borblik for invaluable assistance in preparing the manuscript. This work was supported by the Fund for Fundamental Research of the Ukrainian State Committee on Science and Technology (Grant No. 2.3/122 (''Prostir'')).

[1] Z. S. Gribnikov and V. V. Mitin, JETP Lett. **14**, 182 (1971).
[2] A. Asche, Z. S. Gribnikov, V. V. Mitin, and O. G. Sarbeĭ, *Hot Electrons in Multivalley Semiconductors* [in Russian], Nauk. Dumka, Kiev, 1982.
[3] M. Asche, in *Hot Electron Transport in Semiconductors*, edited by L. Reggiani, Springer-Verlag, Berlin, 1985, p. 149.
[4] M. Asche, Solid–State Electron. **32**, 1633 (1989).
[5] Z. S. Gribnikov and A. N. Korshak, Fiz. Tekh. Poluprovodn. **28**, 963 (1994) [Semiconductors **28**, 558 (1994)].
[6] R. People and J.C. Bean, Appl. Phys. Lett. **48**, 538 (1986).
[7] V. I. Gavrilenko, I. N. Kozlov, O. A. Kuznetsov, M. D. Moldavskaya, V. V. Nikanorov, L. K. Orlov, and A. L. Chernov, JETP Lett. **59**, 348 (1994).
[8] V. J. Aleshkin, N. A. Bekin, I. V. Erofeeva, V. I. Gavrilenko, Z. F. Krasil'nik, O. A. Kuznetsov, M. D. Moldavskaya, V. V. Nikonorov, and V. M. Tsvetkov, Lithuan. J. Phys. **35**, 368 (1995).
[9] E. Murukami, K. Nakagava, A. Nishida, and M. Miyao, IEEE Electron. Dev. Lett. **12**, 71 (1991).

Translated by M. E. Alferieff

Positive magnetoresistance in films of the ferromagnetic semiconductor $Eu_{1-x}Sm_xO$

V. F. Kabanov and A. M. Sverdlova

Saratov State University, Saratov, Russia
(Submitted May 12, 1996; accepted for publication July 8, 1996)
Fiz. Tekh. Poluprovodn. **31**, 626–628 (May 1997)

The positive magnetoresistance effect in a film of the ferromagnetic semiconductor $Eu_{1-x}Sm_xO$ has been studied; this effect is not characteristic of materials of this class. The effect of the external magnetic and electric fields and temperature on the positive magnetoresistance was investigated. It is shown that the magnitude of the magnetoresistance $\Delta\rho/\rho_0$ is determined by scattering of free charge carriers by spatial fluctuations of the magnetization which are due to the nonuniform distribution of defects in the structurally disordered system (quasiamorphous film). © *1997 American Institute of Physics.* [S1063-7826(97)02805-6]

It is well known that some oxide compounds of rare-earth elements, specifically, europium monoxide EuO and the solid solutions $Eu_{1-x}Sm_xO$ based on it, are ferromagnetic materials. In this paper we report the results of an experimental study of positive magnetoresistance observed in $Eu_{1-x}Sm_xO$ films, which is not characteristic of magnetic semiconductors of this class.

We investigated the properties of films of the oxide of a solid solution of europium with samarium. The films were obtained on a *n*-type single-crystal silicon substrate by vacuum thermal evaporation of a corresponding base alloy and subsequent oxidation. The films were 0.1 μm thick. Aluminum contacts were used for the electrodes. The transverse current through the structure was measured in the enrichment regime at the ⟨rare-earth oxide⟩–silicon boundary. The resistance measurements were performed in the temperature range 77–300 K in magnetic fields $H=3.0-7.6$ kOe and electric fields $E=10^3-10^6$ V/cm.

The results obtained are presented in Figs. 1–4. Positive magnetoresistance was observed in the ferromagnetic temperature range. As one can see from Figs. 1 and 2, the specific magnetoresistivity $\Delta\rho/\rho_0$ is a linear function of the intensity of the magnetic field in the range investigated. This form of the characteristic was virtually independent of the orientation of the magnetic field vector relative to the electric field vector (Fig. 2). The magnitude of the effect at $H=7.6$ kOe ordinarily reached several percent and much higher (up to 20%) with individual samples.

The magnetoresistivity as a function of the intensity of the electric field (for fixed values of the temperature and magnetic field intensity; see Fig. 3) for different samples has a maximum at $E\simeq(2-3)\times10^5$ V/cm, it increases for fields in the region $(0.7-2)\times10^5$ V/cm, and it drops off gently in the range $(4-10)\times10^5$ V/cm. A curve of the electric conductivity σ versus the intensity of the electric field is shown in Fig. 3 for comparison.

The quantity $\Delta\rho/\rho_0$(Fig. 4) drops off rapidly near the Curie temperature T_c and at $T>T_c$ it decreases virtually to zero. The curve $\sigma(T)$ is also plotted here.

We employed the model of magnetic clusters to explain the positive magnetoresistance in films of magnetic semiconductors.[1] This model has been used to analyze scattering mechanisms at temperatures near the paramagnetic region.[2] A region (magnetic cluster) with an anomalously high magnetic moment **K**, much greater than the magnitude of the spin of a europium ion $\mathbf{S}_{Eu}$, forms around different kinds of imperfections because the stronger ferromagnetic coupling between defects and regular magnetic ions Eu^{2+}. The experimental films are strongly defective quasiamorphous structures[3] in which magnetic clusters can exist.

The moment of a cluster is a geometric sum of the corresponding projections of the constituent ions of the clusters onto a chosen direction of magnetization. Therefore, the existing magnetization fluctuations can be dominant scattering centers of free charge carriers (in this case electrons).

In samples with a negative magnetoresistance (characteristic of ordinary ferromagnetic semiconductors of the type EuO) at temperatures $T\leqslant T_c$ an external magnetic field suppresses the magnetization fluctuations. This is accompanied by an increase in the carrier mobility and a decrease of the resistance in a magnetic field.

In our case the suppression of fluctuations should also occur in an external magnetic field. However, under the conditions of a high density of defects, nonuniformity of the magnetic properties of the films can play a large role in the experimental films at low temperature $T\leqslant T_c$. In a weak magnetic field, magnetization fluctuations (of nonuniformly arranged clusters) can be intensified because of the spatially nonuniform magnetization. This makes it possible to explain the positive magnetoresistance, which is attributable to the scattering by the magnetic-field-enhanced magnetic moments of clusters and which increase linearly with the intensity of the field, as follows from experiment.

This point of view is confirmed by the fact that a change in the direction of the magnetic field **H** with respect to the carrier current density vector **j**, which coincides in direction with the vector **E**, does not affect the characteristics. The observed differences in the values of $\Delta\rho/\rho_0$, depending on the whether the vectors **H** and **j** are parallel or perpendicular to one another, are explained by the well-known magnetic anisotropy in the experimental films.[4]

The positive magnetoresistance was previously observed in samples of the antiferromagnets EuSe and EuTe. The following explanation of this effect was given for strongly defective materials. In an antiferromagnet a weak magnetic field gives rise to the formation of ferromagnetic clusters,

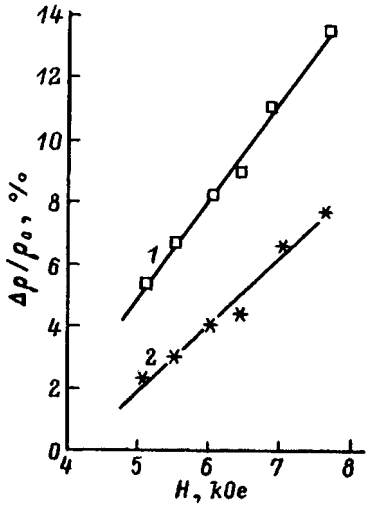

FIG. 1. Magnetoresistivity $\Delta\rho/\rho_0$ versus magnetic field intensity H. *1, 2* — Different samples. $T=77$ K, $E=2.5\times10^5$ V/cm.

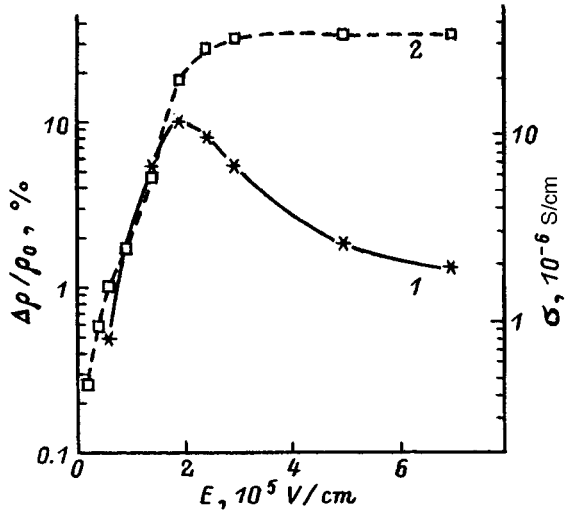

FIG. 3. Magnetoresistivity $\Delta\rho/\rho_0$ (*1*) and electrical conductivity σ (*2*) versus electric field intensity E. $T=77$ K, $H=7.6$ kOe.

scattering by which increases the resistance,[5] which we used in our discussion.

To analyze the dependence of the magnetoresistivity on the intensity of the electric field in the sample, it is necessary to take into account the fact that the electric field in the magnetic materials changes not only the electric properties but also the magnetic ordering. It is well known[1] that in order for a magnetoelectric effect to exist, an electric field must be nonuniform. In our experimental samples this situation is conveniently realized, since our samples contain intercrystalite barriers of different magnitude distributed throughout the sample. It has been shown[6] that the Poole–Frenkel' effect, which is associated with lowering of the barriers in the indicated voltage range, makes the main contribution to the mechanism of electrical conductivity in $Eu_{1-x}Sm_xO$ films. In electric fields up to $\sim3\times10^5$ V/cm a sharp increase of the free electron density is observed (increase of σ in Fig. 3), and when the electric barriers are conserved, one can legitimately say that the distribution of the free electron density over the sample is substantially nonuniform. The increase in the electron density near a defect intensifies the ferromagnetic coupling near it and results in a local increase of the magnetization. Carrier scattering increases, the mobility decreases, and the positive magnetoresistivity increases.

The barriers decrease in electric fields exceeding 3×10^5 V/cm. This results in a more uniform distribution of the charge carrier density, and the magnetization fluctuations also corrrespondingly become weaker, the scattering by the magnetization fluctuations decreases, and the quantity $\Delta\rho/\rho_0$ decreases.

As one can see, the dependence of the magnetoresistivity on the intensity of the electric field has a maximum at $E\simeq3\times10^5$ V/cm under the experimental conditions ($T<T_c$ and weak magnetic fields). We obtained this value of E previously in Ref. 6 , and it corresponds to the voltage at which

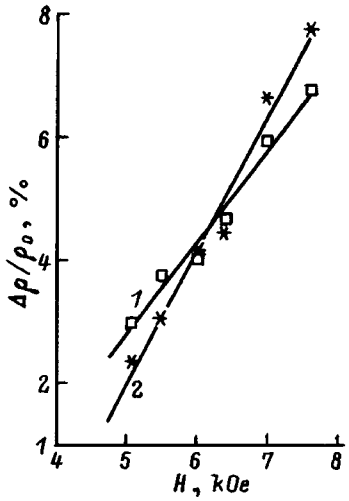

FIG. 2. Magnetoresistivity $\Delta\rho/\rho_0$ versus magnetic field intensity H. *1* — $\mathbf{H}\perp\mathbf{j}$, *2* — $\mathbf{H}\parallel\mathbf{j}$. $T=77$ K, $E=2.5\times10^5$ V/cm.

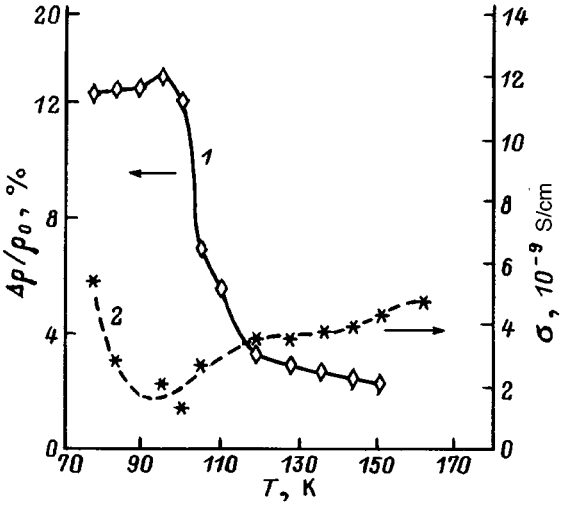

FIG. 4. Temperature dependence of the magnetoresistivity $\Delta\rho/\rho_0$ at $E=3\times10^5$ V/cm. $H=7.6$ kOe (*1*) and electric conductivity σ at $E=10^3$ V/cm (*2*).

the mechanism of current passage in the experimental films changes. The mechanism of thermionic ionization of traps dominates in stronger fields.

The temperature dependence of $\Delta\rho/\rho_0$ (Fig. 4) obtained by us exhibits a sharp drop at $T \geqslant T_c$, which occurs because the magnetic moment of a cluster decreases with increasing temperature $|\mathbf{K}| \sim 1/T$. This occurs in connection with the temperature-related decrease of the magnetic ion density inside a cluster and possibly destruction of the cluster itself at higher values of T. In the range $T \leqslant T_c$ the quantity $\Delta\rho/\rho_0$ remains virtually constant, although it was found that at these temperatures the electrical conductivity of the samples increases as a result of an increase in mobility due to spontaneous magnetization.

This indicates that the positive magnetoresistance occurs only at temperatures on the order of T_c and below, when the spontaneous magnetization existing in this temperature range reflects the nonuniformity of the properties in the sample. The nonuniformity of magnetization is increased by an external magnetic field, which increases carrier scattering, decreases mobility, and gives rise to a positive magnetoresistance. At high temperatures, $T > T_c$, the spontaneous magnetization vanishes and, correspondingly, the positive magnetoresistance vanishes.

In summary, we have examined the positive magnetoresistance in a film of the ferromagnetic semiconductor $Eu_{1-x}Sm_xO$; this effect is not characteristic of materials of this class. The influence of external magnetic and electric fields and temperature on the positive magnetoresistance was investigated. It was shown that $\Delta\rho/\rho_0$ is determined by the scattering of free charge carriers by the spatial fluctuations of the magnetization, which arise due to the nonuniform distribution of defects in a structurally disordered system (quasiamorphous film).

[1] É. L. Nagaev, *Physics of Magnetic Semiconductors* [in Russian], Nauka, Moscow, 1979.
[2] V. F. Kabanov, Fiz. Tekh. Poluprovodn. **26**, 1837 (1992) [Sov. Phys. Semicond. **26**, 1032 (1992)].
[3] O. S. Vdovin, V. N. Kotelkov, V. A. Rozhkov *et al.*, *Films of the Oxides of Rare Earth Elements in MIM and MIS Structures* [in Russian], Saratov University Press, Saratov, 1983.
[4] V. G. Bamburov, A. S. Borukhovich, and A. A. Samokhvalov, *Introduction to the Physical Chemistry of Ferromagnetic Semiconductors* [in Russian], Metallurgiya, Moscow, 1988.
[5] V. G. Kashin and E. L. Nagaev, JETP Lett. **21**, 126 (1975).**21**, 56 (1975).
[6] V. F. Kabanov and A. M. Sverdlova, Fiz. Tekh. Poluprovodn. **25**, 1388 (1991) [Sov. Phys. Semicond. **25**, 837 (1991)].

Translated by M. E. Alferieff

Photoacoustic spectroscopy of porous silicon

A. N. Obraztsov and V. Yu. Timoshenko

Department of Physics, M. V. Lomonosov Moscow State University, 119899 Moscow, Russia

H. Okushi and H. Watanabe

Electrotechnical Laboratory, Tsukuba, Japan

(Submitted June 13, 1996; accepted for publication September 10, 1996)
Fiz. Tekh. Poluprovodn. **31**, 629–631 (May 1997)

The results of a photoacoustic spectroscopy investigation of the optical absorption in porous-silicon films in the range 300–1500 nm are reported. It was found that the fundamental absorption edge due to the porous layer lies in the range 350–500 nm for the experimental samples. It was determined from the dependence of the photoacoustic signal on the light modulation frequency that the thermal conductivity of porous silicon is 0.25×10^{-3} W/cm·deg.
 [S1063-7826(97)02905-0]

1. INTRODUCTION

The possible use of porous silicon (*por*-Si) for the fabrication of optoelectronic devices (see, for example, Ref. 1) has been attracting investigators from the moment that the unique properties of this material were discovered.[2,3] However, the nature of the most remarkable properties of *por*-Si — the shift of the fundamental absorption edge and photoluminescence in the short-wavelength direction (with respect to the values characteristic of crystalline silicon) — until now has not been conclusively established. The existing models give this phenomenon different mutually exclusive explanations, including the following: quantum-mechanical effects associated with the spatial confinement of the electrons; presence of siloxens and polysilicon compounds in the layer of porous silicon; manifestation of ''tails'' of the density of states in the band gap of silicon, and others (see the review in Ref. 4). Therefore, despite the enormous number of studies devoted to *por*-Si, the need for further investigations of this material remains.

Some of the most important, from the practical and fundamental standpoints, properties of porous silicon are its optical properties, and especially the optical absorption. As a rule, measurements of the optical absorption spectra are performed on free films of *por*-Si, obtained by sharply increasing the current at the final stage of electrochemical formation of a film,[5] etching of a silicon substrate in NaOH solution,[6] or with the help of other methods (see the review in Ref. 7). However, the separation of the porous film from the silicon substrate can substantially alter the properties of *por*-Si. At the same time, the published optical absorption data, which were obtained by nondestructive methods of investigation, are limited to only several studies.[8,9]

In the present paper we report the results of an experimental study of *por*-Si layers by photoacoustic (PA) spectroscopy, similar to the methods employed in Refs. 8 and 9. The improved experimental technique which we emplyed made it possible not only to confirm the basic results of our predecessors, but also to obtain new experimental data on optical absorption in the range 300–1500 nm and to estimate the thermal conductivity of *por*-Si from the dependence of the photoacoustic effect on the light modulation frequency (in the range from 45 to 1500 Hz).

2. EXPERIMENTAL CONDITIONS

The *por*-Si layers were prepared on KDB-10 silicon plates (boron-doped silicon with (100) orientation and resistivity $\rho=10\ \Omega\cdot$cm). To ensure a good ohmic contact, prior to anodization an aluminum layer was deposited on the backside of the plate (vacuum sputtering followed by alloying at a temperature of 400 °C). The composition of the electrolyte was HF(50%):C_2H_5OH in a 1:1 ratio. The anodization process was conducted in the dark at room temperature with a current density of 30 mA/cm^2 for a period of 5 min. After the electrochemical treatment the samples were washed in ethanol and dried in air. To stabilize the properties of the porous silicon, the samples were held in air for several weeks before the measurements were started.

The thickness of the porous layer of the prepared samples, measured by optical and electronic microscopy, was equal to about 15 μm. The porosity was determined by gravimetric measurements and was equal to about 80%.

The measurements of the photoluminescence and Raman scattering of light in the porous films were performed under standard conditions[10] using the 488-nm line radiation from an argon laser.

An upgraded Princeton Applied Research Corporation spectrometer (Model 6001) was used to obtain the PA spectra in the range from 300 to 1500 nm. The amplitude of the PA signal from a sensitive microphone placed in an air-filled measuring cell was recorded at room temperature. The light from a 1-kW xenon lamp was passed through a monochromator and modulated with a mechanical chopper with a frequency from 40 to 1500 Hz. In recording the spectra the scan step was equal to 4 nm with a monochromator slit width of 2 mm; this corresponded to a spectral width of 8 nm in the UV and visible regions of the spectrum and 32 nm in the IR region. To take into account the spectral distribution of the intensity of the light source, all PI spectra were normalized to the spectrum of the xenon lamp, recorded with the aid of a pyroelectric detector simultaneously with the PA spectra.

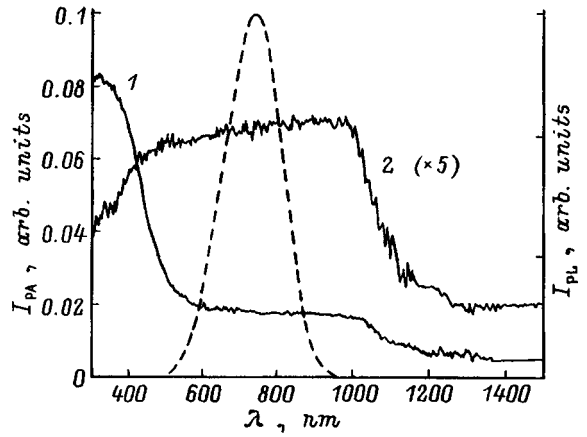

FIG. 1. PA spectra of layers of porous silicon (*1*) and a crystalline Si substrate (*2*) with light modulation frequency 45 Hz. *2* — Scale enlarged by a factor of 5. Dashed line — photoluminescence spectrum for the same sample of porous silicon.

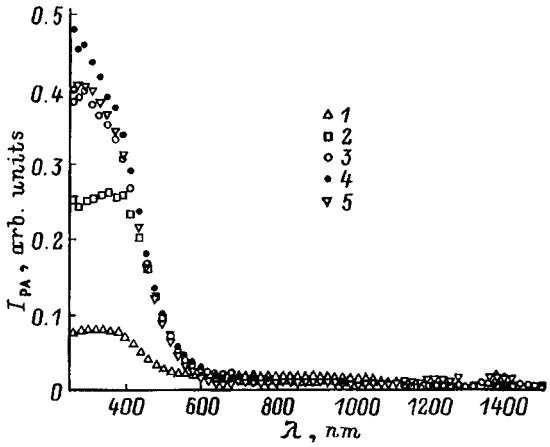

FIG. 2. PA spectra obtained for porous silicon with different light modulation frequencies, Hz: *1* — 45, *2* — 275, *3* — 500, *4* — 1000, *5* — 1500. For clarity, only 20% of the experimental points are presented.

The effectiveness of such a normalization was confirmed by measuring the PA spectra of amorphous carbon (carbon black standard). In accordance with the published data,[11] this material is characterized by an absorption spectrum similar to that of an absolutely blackbody.

3. RESULTS AND DISCUSSION

The prepared *por*-Si samples possessed an optically smooth surface and a uniform brown color over the entire surface. The typical photoluminescence spectrum $[I_L(\lambda)]$ of the samples, represented in Fig. 1 by a dashed line, is similar to the spectrum described previously in Refs. 10 and 12. The maximum of the photoluminescence line was located near 750 nm at room temperature. The half-width of the line was equal to about 200 nm. The Raman scattering (RS) spectra were also typical of such films and consisted of asymmetric lines shifted by 2 cm^{-1} into the low-frequency direction relative to the line at 520 cm^{-1} characteristic of crystalline silicon. As indicated previously, this form of the RS spectra can be explained with the aid of the model of spatial confinement of phonons and attests to the presence of silicon particles with an average size of 4–5 nm in the porous layer.[7,10,12]

The solid lines in Fig. 1 show the spectral dependences of the amplitude of the PA signal $I_{PA}(\lambda)$ measured at a modulation frequency of 45 Hz for *por*-Si and an initial Si plate (curves *1* and *2*, respectively). Since the experimental conditions for the Si plates and *por*-Si samples were nearly identical, the corresponding PA spectra can be compared not only with respect to shape, but also with respect to the absolute values of the PA signal and therefore the light absorption coefficient.

Two features attesting to the large change in the light absorption coefficients in the region 400–500 and 1050–1150 nm are clearly seen in the *por*-Si spectra (see Fig. 1, curve *1*). These features evidently correspond to the fundamental absorption edge in a porous silicon film and in a single-crystal substrate. This is confirmed by the fact that the amplitude of the PA signal for the initial Si plate (Fig. 1, curve *2*) is actually identical to that of the *por*-Si samples (Fig. 1, curve *1*) in the IR range. In both cases a sharp decrease in the amplitude of the PA signal is observed for light with photon energy close to the band gap in silicon (1.1 eV). The variation of the spectral dependence of the PA signal for crystalline silicon in the UV and visible parts of the spectrum is evidentally due to the change in the reflection coefficient, whose increase results in a decrease of the fraction of the light absorbed in the sample and hence a decrease in the amplitude of the PA signal.[13] These spectral features are in good agreement with the known optical properties of silicon.[14]

Increasing the modulation frequency of the light resulted in a relative decrease, due to the absorption of light in the crystalline silicon, of the PA signal (Fig. 2). As is well known, the effective thickness of the sample, which determines the amplitude of the photoacoustic signal, is identical to the thermal diffusion length; it is $\mu=(2\alpha/\omega)^{1/2}$, where ω is the light modulation frequency, $\alpha=k/\rho C$ is the thermal diffusivity, k is the thermal conductivity, ρ is the density, and C is the specific heat of the material of the sample.[11] At relatively low frequencies (up to 700 Hz) the thermal diffusion length in porous silicon does not exceed the thickness of the porous layer (for our samples 15 μm) and the obtained PA signal is determined by light absorption in both the *por*-Si film and in the crystalline substrate. At frequencies above 700 Hz the thermal diffusion length in porous silicon is less than the film thickness. As a result, the characteristic feature in the crystalline substrate, which is associated with light absorption, vanishes completely in the PA spectra.

The spectra shown in Fig. 2 illustrate the considerations. The small decrease in the amplitude of the signal at frequencies above 1 kHz could be due to a variation in the properties of porous silicon over the thickness of the film: a decrease in the fraction of nonradiative recombination of photoexcited charge carriers or a relative increase in the reflection and scattering of light in the surface layers of the porous film.[8]

Our experimental data (80% porosity, thermal diffusion length $\mu=15$ μm for modulation frequency $\omega=700$ Hz) and tabulated data for silicon [density $\overline{\rho}=2.328$ $g\cdot cm^{-3}$,

$C = 0.7$ J/g·deg (Ref. 15)], make it possible to estimate the thermal conductivity for porous silicon as $k = 0.25 \times 10^{-3}$ W/cm·deg. This value is three orders of magnitude lower than the thermal conductivity of crystalline silicon (1.5 W/cm·deg) and even more than an order of magnitude lower than the thermal conductivity of quartz SiO_2 (0.014 W/cm·deg).[15] This estimate is confirmed by the previously described experiments on Raman scattering, during which a substantially larger heating of the samples of porous silicon by laser radiation compared with crystalline silicon was observed.[7,10,12] It is obvious that this parameter of *por*-Si (thermal conductivity) depends strongly on the porosity of the film and it is important from the standpoint of practical applications of *por*-Si.

An interesting features of our PA spectra is the relatively ''sharp'' fundamental absorption edge corresponding to porous silicon. The spectral dependences described in the literature (see, for example, Refs. 5–7 and 16) indicate a ''more even'' variation of the absorption coefficient in nearly the entire visible range. Such a discrepancy could be due to the method used for preparing the experimental samples. As a rule, even when using methods similar to PA spectroscopy,[16,17] films prepared by separating a porous layer from the substrate are employed. In the course of the procedure for separating the film, and also during the subsequent oxidation of the film in air, substantial changes in the properties of *por*-Si can occur. Thses changes are manifested as a change in the optical characteristics. For example, substantial changes in the photoluminescence properties of *por*-Si as a result of separation of the film from a substrate were described in Ref. 5.

In summary, the method of photoacoustic spectroscopy employed in the present work made it possible, because of its nondestructive character, to obtain fundamentally new data on the spectral dependence of the absorption coefficient of layers of porous silicon.

We wish to thank the International Matsumae Foundation for awarding a stipend to A. N. Obraztsov for work at the Electrotechnical Laboratory (Sukuba, Japan), which made this work possible.

[1] W. Lang, P. Steiner, and F. Kozlowski, J. Luminesc., **57**, 341 (1993).
[2] L. T. Canham, Appl. Phys. Lett. **57**, 1046 (1990).
[3] V. Lehmann and U. Gosele, Appl. Phys. Lett. **58**, 856 (1991).
[4] S. M. Prokes, Interface, **4**, 341 (1994).
[5] Y. H. Xie, M. S. Hybertsen, W. L. Wilson, S. A. Ipril, G. E. Carver, W. L. Brown, E. Dons, B. E. Weir, A. R. Kortan, G. P. Watson, and A. J. Liddle, Phys. Rev. B **49**, 5386 (1994).
[6] E. Massone, A. Foucaran, and J. Camassel, J. Luminesc. **57**, 51 (1993).
[7] D. J. Lockwood, Solid State Commun. **92**, 101 (1994).
[8] G. Amato, G. Spagnolo, L. Boarino, R. Gavioso, and G. Benedetto, J. Physique IV, Col. 7, **4**, C7 (1994).
[9] B. S. Brodin, I. V. Blonskiĭ, and V. A. Tkhorik, Pis'ma Zh. Tekh. Fiz. **20**, 41 (1994) [Tech. Phys. Lett. **20**, 151 (1994)].
[10] A. N. Obraztsov, V. G. Pirogov, V. Yu. Timoshenko, and Th. Ditrich, Phys. Low-Dim. Structur. **2**, 95 (1994).
[11] A. Rosencwaig, *Photoacoustics and Photoacoustic Spectroscopy*, Wiley, N. Y., 1980, p. 95.
[12] V. A. Karavanskiĭ and A. N. Obraztsov, Fiz. Tekh. Poluprovodn. **29**, 582 (1995) [Semiconductors **29**, 302 (1995)].
[13] H. Tokumoto, M. Tokumoto, and T. Ishiguro, J. Phys. Soc. Jpn. **50**, 602 (1981).
[14] H. W. Verleur, J. Opt. Soc. Amer. **58**, 1356 (1968).
[15] H. W. Sze, *Physics of Semiconductor Devices*, Wiley, N. Y., 1981, p. 850.
[16] F. Koch, V. Petrova-Koch, and T. Muschik, Luminesc. **57**, 271 (1993).
[17] A. C. Boccara, D. Fournier, and J. Badoz, Appl. Phys. Lett. **36**, 130 (1980).

Translated by M. E. Alferieff

Exciton scattering by concentration fluctuations and projection of the spins of magnetic impurities in quantum wells in semimagnetic semiconductors

A. V. Vertsimakha and V. I. Sugakov[1)]

Institute of Nuclear Research, Ukrainian National Academy of Sciences, 252028 Kiev, Ukraine
(Submitted July 4, 1996; accepted for publication October 23, 1996)
Fiz. Tekh. Poluprovodn. **31**, 632–634 (May 1997)

Exciton scattering by fluctuations of the concentration and the orientation of the spins of magnetic impurities and the associated broadening of excitonic bands in a quantum well with semimagnetic barriers CdMnTe/CdTe/CdMnTe have been investigated. The relaxation time is found as a function of the exciton energy and thickness of the well. The relaxation time depends strongly on the magnetic field. The dependence is different for excitons that form the σ_+ and σ_- components of the optical transition. © *1997 American Institute of Physics.* [S1063-7826(97)03005-6]

The optical properties of quantum wells and superlattices based on semimagnetic semiconductors have been widely investigated in recent years.[1–3] The giant spin splitting of the bands, which arises in heterostructures consisting of alternating magnetically mixed and nonmagnetic layers as a result of the exchange interaction of charge carriers with magnetic impurities,[4] makes it possible to change the depth of the quantum wells by means of an external magnetic field and leads to splitting of the excitonic lines in a magnetic field.

An important question in the study of heterostructures is the investigation of the effect of structural imperfections on their physical properties. The imperfections could be associated with the conditions under which the crystal is grown and with fluctuations of the composition. Imperfections of the second type are always present, irrespective of the method used for growing the structure. One way to study structural defects is to investigate the shape of the excitonic spectra. Scattering of excitons by imperfections results in broadening of the bands. The effect of composition fluctuations on the excitonic spectra in heterostructures with nonmagnetic impurities was investigated in Ref. 5. Such an influence should be substantial in semimagnetic semiconductors, since the magnetic impurities, because of the exchange interaction with the carriers, largely determine the energy spectrum of the excitons. Furthermore, it can be expected that the line broadening in them will depend on the magnetic field, which is not the case in crystals with nonmagnetic impurities. In bulk crystals such broadening was studied in Ref. 6 . In heterostructures, characteristic features associated with the two-dimensional nature of the system and with the redistribution of the exciton wave function between wells and barriers accompanying a change in the dimensions of the heterostructures, should be observed. In our study we examine the scattering of excitons by fluctuations of the concentration and orientation of the spins of impurities in a quantum well with semimagnetic barriers CdMnTe/CdTe/CdMnTe.

To study scattering by fluctuations of the impurity we write the exciton Hamiltonian in the form

$$H = H_0 + H_{\text{int}}, \tag{1}$$

$$H_{\text{int}} = \sum_{\mathbf{n}} \frac{1}{N_0}[(\Delta_e - J_e \mathbf{S}_e \cdot \mathbf{S}_{\mathbf{n}})\,\delta(\mathbf{r}_e - \mathbf{n}) + (\Delta_h - J_h \mathbf{S}_h \cdot \mathbf{S}_n)\,\delta(r_h - \mathbf{n})]X_{\mathbf{n}}, \tag{2}$$

where H_0 is the typical Hamiltonian of a free exciton in a crystal with no impurities[7] and H_{int} is the Hamiltonian of the interaction of an electron and hole with Mn^{2+} ions, which includes the exchange interaction described by the exchange integrals J_e and J_h and the interactions caused by the deformation of the lattice accompanying the introduction of an impurity ion, which are described by the terms Δ_e and Δ_h. The latter interactions lead to an offset of the bands and form a quantum well in the absence of a magnetic field. The magnetic field is directed perpendicular to the layers of the system. The quantities $\mathbf{S}_e$, $\mathbf{S}_h$, and $\mathbf{S}_{\mathbf{n}}$ are the spins of the electron, hole, and impurity, respectively; N_0 is the density of cationic sites in the lattice and $\mathbf{r}_e$ and $\mathbf{r}_h$ are the electron and hole coordinates. The diamagnetic effects, which are small in the magnetic fields studied, are ignored in the Hamiltonian (1); the masses of the particles are assumed to be isotropic and identical in the different layers of the heterojunction. The quantity $X_{\mathbf{n}}$ gives the distribution of the impurities: $X_{\mathbf{n}}=0$ if a Cd^{2+} ion is present at the site $\mathbf{n}$ and $X_{\mathbf{n}}=1$ if the main ion is replaced by a Mn^{2+} ion. We represent $X_{\mathbf{n}}$ and $S_{\mathbf{n}}$ in the form

$$X_{\mathbf{n}} = X + \delta X_{\mathbf{n}}, \tag{3}$$

$$\mathbf{S}_{\mathbf{n}} = \langle \mathbf{S}_{\text{Mn}} \rangle + \delta \mathbf{S}_{\mathbf{n}}, \tag{4}$$

where $\langle \mathbf{S}_{\text{Mn}} \rangle$ and $\delta \mathbf{S}_{\mathbf{n}}$ are the average value and the fluctuation of the spin of an impurity, and X and $\delta X_{\mathbf{n}}$ are the average value and fluctuation of the relative density. Using expressions (3) and (4), we can transform the Hamiltonian into the form

$$H = \widetilde{H}_0 + \Delta H,$$

$$\widetilde{H}_0 = H_0 + X(\Delta_e - J_e \mathbf{S}_e \cdot \langle \mathbf{S}_{\text{Mn}} \rangle)\Theta(|z_e| - L/2) + X(\Delta_h - J_h \mathbf{S}_h \cdot \langle \mathbf{S}_{\text{Mn}} \rangle)\Theta(|z_h| - L/2),$$

where

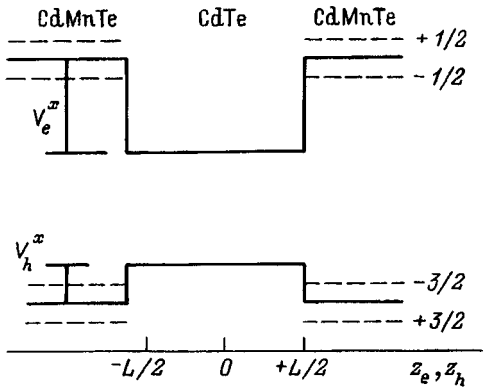

FIG. 1. Energy level diagram of the heterojunction. The dashed lines show the splitting of the bands in a magnetic field. $V_e^x = X\Delta_e$, $V_h^x = X\Delta_h$.

$$\mathbf{V} = -\frac{1}{N_0}(J_e\mathbf{S}_e\delta(\mathbf{r}_e-\mathbf{n}) + J_h\mathbf{S}_h\delta(\mathbf{r}_h-\mathbf{n})),$$

$$V_1 = \frac{1}{N_0}((\Delta_e - J_e\mathbf{S}_e\cdot\langle\mathbf{S}_{\mathrm{Mn}}\rangle)\,\delta(\mathbf{r}_e-\mathbf{n}) + (\Delta_h - J_h\mathbf{S}_h\cdot\langle\mathbf{S}_{\mathrm{Mn}}\rangle)\,\delta(\mathbf{r}_h-\mathbf{n})),$$

$\Theta(z)$ is the unit step (Heaviside) function. The term $\widetilde{H}_0$ is the Hamiltonian of the interaction of an exciton with the magnetic impurities in the mean-field approximation (Fig. 1), and ΔH takes into account the fluctuations of the distribution of the impurities and orientations of their spins.

Let us examine the probability of elastic scattering of an exciton by fluctuations of the distribution and orientation of the impurity spins. In the zeroth approximation the states of an exciton are determined by the Hamiltonian $\widetilde{H}_0$, found in the mean-field approximation. Since the interaction energy of an exciton with an impurity is much smaller than the width of the excitonic band, the scattering can be studied in the Born approximation by perturbation theory with the perturbation Hamiltonian ΔH. We shall ignore the processes associated with spin flipping in the process of scattering. For calculations we chose the often employed form of the wave functions of excitons localized in a quantum well:[2,8]

$$\Psi_{\mathbf{k}}(\mathbf{r}_e,\mathbf{r}_h) = \phi_e(z_e)\,\phi_h(z_h)\,\Phi_{\mathbf{k}}(\boldsymbol{\rho}_e,\boldsymbol{\rho}_h),$$

$$\Phi_{\mathbf{k}}(\boldsymbol{\rho}_e,\boldsymbol{\rho}_h) = 1/\sqrt{S}\,\exp(i\mathbf{k}\cdot\mathbf{R})\,\phi_{\mathrm{ex}}(\rho),$$

where $\mathbf{r}_{e(h)} = (\boldsymbol{\rho}_{e(h)}, z_{e(h)})$, $\boldsymbol{\rho}_{e(h)}$ are the coordinates of an electron (hole) in the plane of the layer, $\mathbf{R}$ are the coordinates of the center of mass of the exciton in the plane of the layer, $\boldsymbol{\rho} = \boldsymbol{\rho}_e - \boldsymbol{\rho}_h$, S is the area of the layer, $\phi_{\mathrm{ex}}(\rho) = \sqrt{2\pi}\exp(-\rho/\lambda)/\lambda$, λ is a variational parameter, and $\phi_e(z_e)$ and $\phi_h(z_h)$ are the wave functions of the lowest-lying states of an electron and hole in the quantum well.[2,8] The probability for the scattering of an exciton from a state $\mathbf{k}$ into a state $\mathbf{k}'$ is determined by the standard perturbation theory. We obtain the reciprocal of the relaxation time after summing the probability of scattering over the final states $\mathbf{k}'$ and averaging over the distribution of impurities and the orientation of their spins. For low impurity concentrations these distributions can be assumed to be uncorrelated. Then

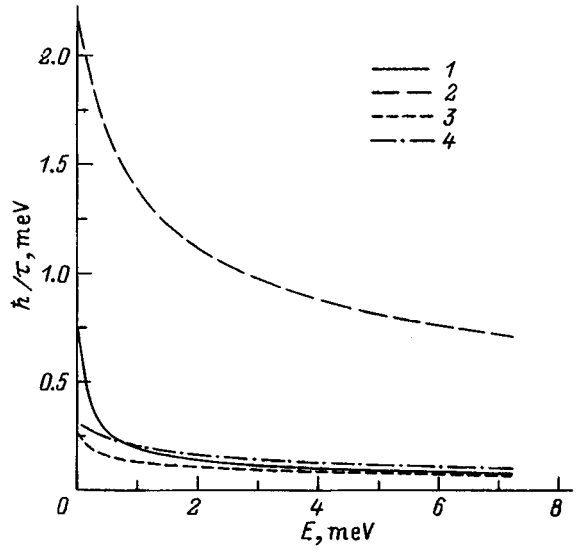

FIG. 2. $\hbar/\tau_E$ versus the wave vector of an exciton in a field $H = 0.25$ T. *1* — $L = 15$ Å, σ_{E+}; *2* — $L = 15$ Å, σ_-; *3* — $L = 60$ Å, σ_+; *4* — $L = 60$ Å, σ_-.

$$\langle \delta X_{\mathbf{n}}, \delta X_{\mathbf{m}}\rangle = X(1-X)\,\delta_{\mathbf{n},\mathbf{m}},$$

$$\langle \delta S_{\mathbf{n},z}, \delta S_{\mathbf{m},z}\rangle = \langle \delta S_{\mathrm{Mn}}^2\rangle\,\delta_{\mathbf{n},\mathbf{m}},$$

$$\langle \delta S_{\mathbf{n},z}, \delta X_{\mathbf{n}}\rangle = 0.$$

Finally, for the reciprocal of the relaxation time of an exciton we obtain

$$\tau_E^{-1} = \frac{2\pi}{\hbar}\sum_{\mathbf{k}'}\left\{\langle\delta S_{\mathrm{Mn}}^2\rangle X^2\sum_{\mathbf{n}}|\langle\mathbf{k}'|V_z|\mathbf{k}\rangle|^2 + X(1-X)\times\sum_{\mathbf{n}}|\langle\mathbf{k}'|V_1|\mathbf{k}\rangle|^2 + \langle\delta S_{\mathrm{Mn}}^2\rangle X(1-X)\times\sum_{\mathbf{n}}|\langle\mathbf{k}'|V_z|\mathbf{k}\rangle|^2\right\}\delta(E_{\mathbf{k}'}-E_{\mathbf{k}}),$$

where $E_k = \hbar^2k^2/2M$ is the kinetic energy of an exciton, M is the mass of an exciton, and $\langle\mathbf{k}'|V_i|\mathbf{k}\rangle = \int d\mathbf{r}_e d\mathbf{r}_h \Psi_{\mathbf{k}'}^*(\mathbf{r}_e,\mathbf{r}_h) V_i \Psi_{\mathbf{k}}(\mathbf{r}_e,\mathbf{r}_h)$, $i = 1$, 2, and 3. One manifestation of exciton scattering by impurities should be broadening of the excitonic bands. The contribution of scattering by fluctuations of the impurity concentration to the half-width of the excitonic absorption band is $1/\tau_{E(\omega)}$, where $E(\omega)$ is the energy of an exciton at the frequency ω.[9] Calculations of the quantity $1/\tau_{E(\omega)}$ were performed numerically for CdMnTe/CdTe/CdMnTe heterostructures with $X = 0.05$, temperature $T = 2$ K, and the following parameters:[2,10] $X\Delta_e = 0.85\Delta E_g$ and $X\Delta_h = 0.15\Delta_{Eg}$, where $\Delta E_g = 1.587X$ is the offset of the bandgap at the boundary of the layers; the effective masses of the carriers are $m_e = 0.96m_0$ and $m_h = 0.5m_0$ (m_0 is the electron mass), $J_e = 0.22$ eV, $J_h = 0.83/3$ eV, and the dielectric constant $\varepsilon = 9.7$. The computational results for $\hbar/\tau_E$ as a function of the kinetic energy E of an exciton in the plane of the layer in a magnetic field $H = 0.25$ T are presented in Fig. 2. In contrast with a bulk crystal, the reciprocal of the relaxation time, due to scattering

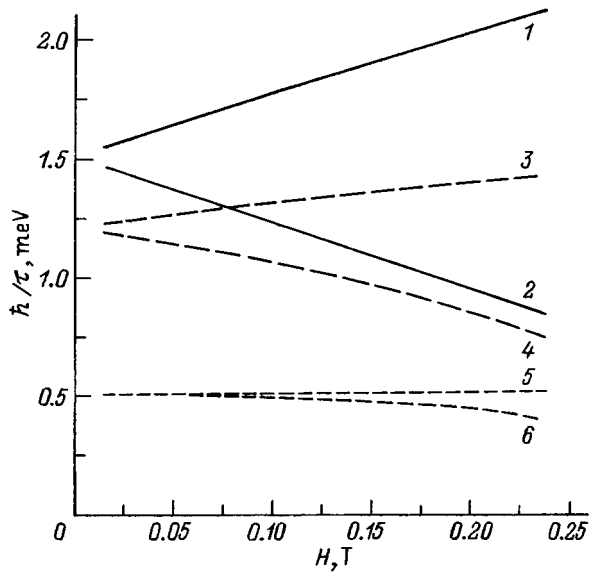

FIG. 3. $\hbar/\tau_g$ versus magnetic field at $E=0$. *1* — $L=15$ Å, σ_-; *2* — $L=15$ Å, σ_+; *3* — $L=30$ Å, σ_-; *4* — $L=30$ Å, σ_+; *5* — $L=50$ Å, σ_-; *6* — $L=50$ Å, σ_+.

by an impurity, of an exciton in a quantum well remains finite in the limit $E\to 0$ because of the two-dimensional nature of the problem, and because the density of final states is different from zero in the limit $E\to 0$. Since excitons with $E=0$ participate in the reflection of light incident on the heterojunction in a direction along the normal, the scattering mechanism under study can cause the fluctuations-associated broadening of the excitonic bands in heterostructures to be different from that in bulk crystals. Figure 3 shows $\hbar/\tau_E$ versus the magnetic field for $E=0$ of excitons with polarizations σ_+ and σ_- (states with $s_e=-1/2$, $s_h=-3/2$ and $s_e=1/2$, $s_h=3/2$, respectively). The scattering probability for different transitions has a different dependence on the magnetic field: For the σ_+ transition $\hbar/\tau_E$ increases with the field and for the σ_- transition it decreases. The different dependence, are attributable to the fact that for the same orientation of the spins the nonexchange and exchange parts of the interaction with an exciton with an impurity add and for the other orientation they subtract. Note the strong dependence of the broadening (narrowing) of the bands on the magnetic field. The reciprocal of the relaxation time increases with decreasing width of the quantum well, since the probability for the penetration of an exciton into the barriers, in which the magnetic impurities are located, is high.

In this study we examined a very simple mechanism, yet one which is always present in mixed crystals, of broadening of excitonic bands — scattering of excitons by concentration fluctuations. It gives a larger contribution to the broadening than the fluctuations-induced change in the exciton spectrum. The latter contribution in bulk crystals results in broadening which depends on the relative impurity concentration as $X^2(1-X)^2$,[11] and it is much smaller than that observed experimentally.[6] Real heterostructures contain nonuniformities of the distribution of impurities and defects of a technological origin, whose presence can substantially change the exciton spectrum. In this case the change in the spectrum, rather than the scattering, determines the broadening of the bands. However, calculations of such broadening require a knowledge of the character of such technological imperfections and cannot generally be performed. Furthermore, the calculations performed in this paper show that composition fluctuations, which are always present in a crystal, give to the broadening a contribution which can be observed experimentally.

We thank S. M. Ryabchenko for a helpful discussion.

This work was supported by the International Soros Program for Education in the Exact Sciences of the International Renaissance Fund, Grant ISEEP SPU 042065.

[1)]E-mail: kinr@sovam.com; Fax: +(380) 44 265–44–63.

[1] E. Deleporte, J. M. Berroir, G. Bastard, C. Delalande, J. M. Hogh, and L. L. Chang, Phys. Rev. B, **42**, 5891 (1990).
[2] E. L. Ivchenko, A. V. Kavokin, and V. P. Kochereshko, Phys. Rev. B, **46**, 7713 (1992).
[3] J. Warnock, B. T. Jonker, A. Petrou, W. C. Chou, and X. Liu, Phys. Rev. B, **48**, 17 321 (1993).
[4] A. V. Komarov, S. M. Ryabchenko, O. V. Terletskiĭ, I. I. Zheru, and R. D. Ivanchuk, Zh. Éksp. Teor. Fiz. **73**, 608 (1977) [Sov. Phys. JETP **46**, 318 (1977)].
[5] S. D. Baranovskii, U. Doerr, P. Thomas, A. Naumov, and W. Gebhart, Phys. Rev. B **48**, 17 149 (1993).
[6] S. M. Ryabchenko, Yu. G. Semenov, and O. V. Terletskiĭ, Fiz. Tverd. Tela (Leningrad) **27**, 2901 (1985) [Sov. Phys. Solid State **27**, 1746 (1985)].
[7] R. S. Knox, *Theory of Excitons*, Academic Press, N. Y., 1963 [Russian trans., Mir, Moscow, 1996].
[8] A. V. Naumenko and V. I. Sugakov, Ukr. Fiz. Zh. **41**, 228 (1996).
[9] E. Skaistys, V. I. Sugakov, and O. S. Zinets, Phys. Status Solidi B **58**, 415 (1973).
[10] J. K. Furdyna and J. Kossut, *Semimagnetic Semiconductors* [Russian trans., Mir, Moscow, 1992].
[11] N. N. Ablyazov, M. É. Raĭh, and A. L. Éfros, Fiz. Tverd. Tela (Leningrad) **25**, 353 (1983) [Sov. Phys. Solid State **25**, 199 (1983)].

Translated by M. E. Alferieff

Optical absorption edge and its modification due to the decomposition of cadmium telluride and cadmium sulfide solid solution films

A. P. Belyaev, V. P. Rubets, and I. P. Kalinkin

St. Petersburg Technological Institute, 198013 St. Petersburg, Russia
(Submitted July 8, 1996; accepted for publication October 25, 1996)
Fiz. Tekh. Poluprovodn. **31**, 635–638 (May 1997)

The spectral dependences of the transmission and absorption of metastable CdS_xTe_{1-x} films before and after thermally activated decomposition have been studied. A model is proposed for the transmission processes in disordered multiphase systems. The correlations between characteristic points on the transmission curves and the composition of the solid solution are determined. © *1997 American Institute of Physics.* [S1063-7826(97)03105-0]

For many reasons, light absorption is generally analyzed in the overwhelming majority of scientific studies involving the optical properties of a given system. The transmission is ordinarily not analyzed. In this connection, it is helpful to make such an analysis for films of the solid solutions (SSs) CdS_xTe_{1-x} and to compare the results with the standard approach.

The choice of the model is made mainly for two reasons. First, the solid solutions of II–VI compounds possess a wide spectrum of properties, which are always of interest to investigators and practitioners. Second, a pronounced metastable system is easy to model. The metastable system is achieved by synthesizing under sharply nonequilibrium conditions, for example, synthesis on a substrate cooled to a temperature close to that of liquid nitrogen.[1,2] The metastability of the system makes it a convenient object for investigating phase transformations and, correspondingly, for investigating the correlations between the transmission and the composition.

1. EXPERIMENTAL PROCEDURE AND SAMPLES

The films were prepared by the thermal-screen method[3] from a mechanical mixture of CdS and CdTe powders. The mixture was placed in a reactor and heated up to the sublimation temperature, and the substrate was cooled with liquid nitrogen. The reactor with the powder heated up to the sublimation temperature ($T=1020$ K) and the cooled substrate were brought together by a manipulator only for the synthesis time (not more than several seconds). Synthesis was realized in a 10^{-3} Pa vacuum on a muscovite-mica substrate.

According to x-ray phase and electron diffraction analysis, the structure of the films was close to polycrystalline. Thermally activated decomposition of the solid solutions was conducted in a vacuum by heating up to a temperature of 600 K and holding at this temperature for 2 h. The substrate and reactor temperatures were monitored with copper–constantan and chromel–aluminum thermocouples, respectively. The thickness of the samples did not exceed 1 μm. The thickness was estimated with a MII-4 microinterferometer. Electron diffraction investigations were performed on an EMR-100 electron diffraction camera and x-ray phase analysis was performed on a DRON-2 diffractometer. The optical measurements were performed on a SF-26 spectrophotometer at room temperature.

2. EXPERIMENTAL RESULTS

The results of the investigations of the transmission coefficient of the CdS_xTe_{1-x} solid solution are shown in Fig. 1. Curve *1* corresponds to the transmission of the sample immediately after preparation; curve *2* corresponds to the same sample after thermal action. The same figure also shows for comparison the transmission curves of CdS (curve *3*) and CdTe (curve *4*) films.

As one can see from the figure, the spectral transmission curve of the freshly prepared film of solid solution can be represented, to a first approximation, as a linear superposition of the transmission curves of cadmium telluride and cadmium sulfide films, where a weakening of the wavelength dependence of the transmission coefficient occurs in the wavelength intervals 570–800 nm.

After the sample is annealed, the stepped character of the transmission curve is smoothed out (curve *2*). Transmission increases in the wavelength interval 570–800 nm.

The typical experimental results for the absorption coefficient in films of the solid solutions CdS_xTe_{1-x} are presented in Fig. 2. Curve *1* was obtained from a freshly prepared sample and curve *2* was obtained from the same sample after annealing. The results correspond to the sample whose transmission was examined above (Fig. 1).

As one can see from the figure, the absorption coefficient α of the sample before and after annealing gradually increases in an interval of several eV. In both cases the curves contain an exponential section of growth (Urbach edge) satisfying the empirical relation[4]

$$\alpha=\alpha_0 \exp[-\gamma(E-\hbar\omega)/kT], \tag{1}$$

where α_0 and γ are constants, E is the band gap, and $\hbar\omega$ is the photon energy.

The absorption curve for the annealed sample was characterized by a lower value of the parameter γ.

3. DISCUSSION

As is well known, transmission, in general, is not a self-averaging physical quantity. It depends multiplicatively on the size of the object and the ''tails'' of the probability distribution of the scatterer configurations make the main contribution to its average value. For this reason, the theoretical

 1063-7826/97/050540-03$10.00

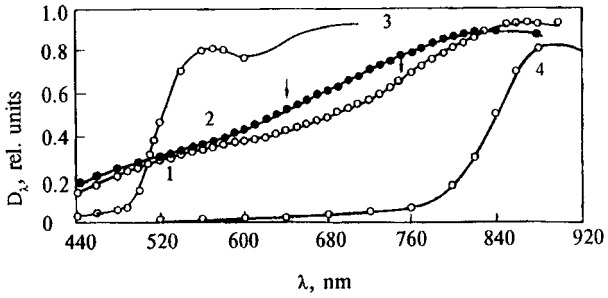

FIG. 1. Spectral dependences of the transmission of films of the solid solutions CdS_xTe_{1-x} before (*1*) and after (*2*) thermally activated decomposition and of CdS (*3*) and CdTe (*4*) films.

description of such quantities is a very difficult problem, whose solution even in a one-dimensional case is known at present only approximately.

According to current theory, the transmission of a disordered system is determined by the so-called representative scatterer configurations, which are thought to account for the transmission to be within a small neighborhood of its average value.[5] The composition of the representative configurations is not, in general, the most likely composition, but together with the concentration of representative configurations it determines the properties of the transmission coefficient of the object.

The experimental films of the solid solutions were synthesized from the vapor phase by vacuum condensation on a substrate. Films grow in such a synthesis method by nucleation and layerwise. The composition of the solid solution therefore fluctuates over the volume. Since CdS_xTe_{1-x} are variable-gap solutions, fluctuations of the absorbing properties of the volume of the film occur along with the composition fluctuations. According to what we have said above, one or another set of absorbing regions (scatterers) in the path of the light can be regarded as typical or a representative configuration.

In the experiment under discussion the transverse cross-sectional area of the sample was exponentially large compared with the thickness of the sample. This means that the results obtained for a one-dimensional model can be used to interpret the data.[5] In this case the experimentally observed transmission can be regarded as

$$D_\lambda \approx S^{-1} \sum \langle D_L \rangle, \tag{2}$$

where D_λ is the experimentally observed transmission, S is the area of the film, and $\langle D_L \rangle$ is the transmission of a representative configuration (average value of the transmission of a linear chain).

For a one-dimensional chain[5]

$$\langle D_L \rangle = \exp[-\overline{nL}(1-D)], \tag{3}$$

where L is the chain length, n is the scatterer density, and D is the transmission of one scatterer in a chain.

Since the short-wavelength photons are absorbed by all regions of the inhomogeneous CdS_xTe_{1-x} films, and since the long-wavelength photons are absorbed only by regions with composition giving a small band gap, the quantity $\overline{n}$ can

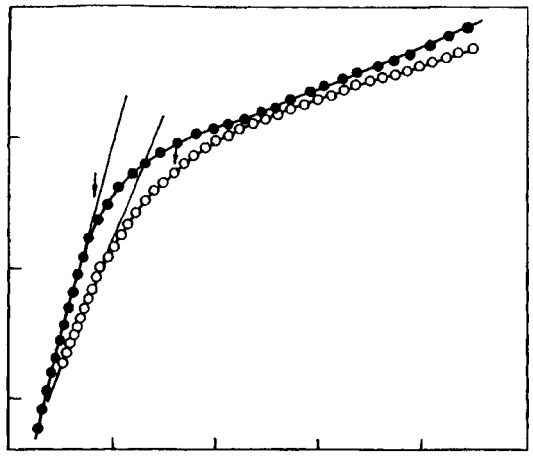

FIG. 2. Spectral dependences of the absorption coefficient of the solid solutions CdS_xTe_{1-x} before (*1*) and after (*2*) thermoreactive decomposition.

assume a different value for each wavelength. This means that the spectral curves presented in Fig. 1 can be regarded as being the result of a functional coupling between the scatterer density and the wavelength of the incident light.

In Fig. 1 curve *1*, which corresponds to a freshly prepared sample, demonstrates low transmission in the region 570–800 nm. According to (2) and (3), this indicates that the scatterer density increases substantially in this region, and that a maximum of the variation of the density occurs at the inflection point λ_m of the spectral curve. This means, in turn, that the sample contains predominantly regions with a band gap corresponding to photon energy λ_m, which makes it possible to determine the composition of the solid solution in terms of the functional relation between the width of the band gap and the composition of the solid solution.

The composition of the solid solution determined in this manner for the sample represented by curve *1* in Fig. 1 was found to be $x=0.60$, which is close to the result obtained from x-ray phase and electron diffraction analysis ($x=0.58$).

According to the x-ray phase and electron diffraction analysis, the freshly prepared CdS_xTe_{1-x} samples are single-phase samples. It can be assumed, however, from the fact that their spectral transmission curves are close to a linear superposition of the spectral curves for CdS and CdTe that they contain representative configurations with composition close to the indicated binary compounds. Their concentration in the experimental samples is evidently low; for this reason, they are not detected either by x rays or electron diffraction. As indicated above, however, the transmission is due to the ''tails'' of the probability distribution and it is therefore very sensitive to the relative fluctuations.

The existence of composition fluctuations is confirmed by electrical investigations, according to which the potential well of the zones of films of the solid solutions of II–VI compounds grown by the method of vapor condensation on a substrate is determined mainly by fluctuations of the composition of the solid solution.[6]

After the samples are annealed, the variation of their transmission coefficient becomes more monotonic. The re-

gion with a low transmission vanishes (Fig. 1, curve *2*). In the proposed model this means that their representative configurations with good transmission in the indicated spectral region appear in the volume, and hence the concentration of regions with the most characteristic composition decreases (for the sample studied $x=0.60$). X-Ray phase and electron diffraction analysis confirms this conclusion and detects the decomposition of solid solutions into two phases.

According to the proposed model, one would think that the spectral curves of such samples should contain two characteristic points. However, graphical differentiation can separate only one point — at short wavelengths. The composition of the phase estimated according to this point was identical to the results obtained by electron diffraction and x-ray phase analysis for one of the detected phases ($x=0.78$).

The absence of a second characteristic point is due, in our opinion, to the smearing of the absorption curve of each scattering region and by the increase in the relative rms deviation Δ_λ of the transmission. According to Ref. 5, the relative rms deviation Δ is

$$\Delta = N^{-0.5}\delta, \tag{4}$$

where N is the number of linear chains in the sample, and δ is the rms deviation of the transmission of one linear chain

$$\delta = \{\exp[\overline{nL}(1-D)]-1\}^{0.5}. \tag{5}$$

Since the wide-gap regions are transparent to long-wavelength radiation, it can be assumed that in this spectral region the number of effective scatterers in the sample decreases and therefore $\overline{n}$ decreases, which, according to Eqs. (4) and (5), results in a smoothing of the spectral dependence of the transmission.

The spectral dependences of the absorption coefficient have a form that is characteristic of disordered semiconductors.[4] This behavior of the materials has still not been explained unequivocally. It is well known, however, that as the degree of disorder increases, the absorption edge becomes increasingly more smeared, and correspondingly the parameter γ decreases.[7] This correlates with the data from our investigations of CdS_xTe_{1-x}. After the sample is annealed, which, according to the results presented above, results in decomposition of the solid solution, γ decreases.

The ''knee'' on the spectral absorption curve is used to estimate the optical band gap in the case of the Urbach absorption edge. This is a rather crude method, and ordinarily it gives a result that is somewhat less than the band gap obtained in other measurements.[4]

Our results also show a similar relation, as one can see from Fig. 2. The arrows on the curves in the figure mark the gaps which we calculated from the spectral curves of the transmission coefficient.

In many cases, for disordered systems beyond the exponential absorption edge there follows a dependence[4]

$$\alpha = B(\hbar\omega - E)^2/\hbar\omega, \tag{6}$$

where B is a constant.

Extrapolating this quadratic dependence, we find the band gap.

The quadratic region in the CdS_xTe_{1-x} systems investigated is found to be very narrow, and its extrapolation gives a substantially underestimated result. For the samples, whose spectral curves are shown in Figs. 1 and 2, $E=1.45-1.55$ eV.

Such a discrepancy can be explained, in our view, by the atypical character of the density of states in the CdS_xTe_{1-x} solutions. The theoretical derivation of the quadratic dependence of $\alpha\hbar\omega$ on $\hbar\omega$ is based on the assumption of parabolic bands. In the systems investigated, however, strong fluctuations of the bands occur. It seems to us that this can substantially alter the density of states. The energy E determined by extrapolating the experimental curve (6) should therefore be regarded only as a characteristic energy, which is related in some way with the band gap.

In conclusion, we note that we checked the correlation found between the characteristic points on the transmission curve and the composition of the solid solution for other systems as well. Specifically, good agreement of the results for CdS_xTe_{1-x} films was obtained by using the functional relation between the composition and the band gap determined from photoluminescence measurements.

4. CONCLUSIONS

1. The absorption edge of films of the solid solutions CdS_xTe_{1-x}, synthesized under strongly nonequilibrium conditions, before and after thermally activated decomposition, has the form characteristic of disordered systems — the Urbach edge.

2. Transmission processes in systems of the type CdS_xTe_{1-x} can be satisfactorily interpreted on the basis of the model of representative configurations in the form of linear chains.

3. The spectral dependences of the transmission coefficient are a sensitive indicator of the phase composition of the system, making it possible to identify the phase composition under certain conditions.

This work was supported by the Russian Fund for Fundamental Research (No. 96-02-19138).

[1] J. Mendolia and D. Lemoine, Phys. Status Solidi A **97**, 601 (1986).
[2] A. P. Belyaev, V. P. Rubets, and I. P. Kalinkin, Fiz. Tekh. Poluprovodn. **31**, 635 (1997) [Semiconductors **31**, 540 (1997)].
[3] A. P. Belyaev and I. P. Kalinkin, Thin Sol. Films **158**, 25 (1988).
[4] N. F. Mott and E. A. Davis, *Electronic Processes in Non-Crystalline Materials*, Clarendon Press, Oxford, 1979, 2nd edition [Russian translation, Mir, Moscow, 1982, Part 1].
[5] I. M. Lifshits, S. A. Gredeskul, and L. A. Pastur, *Introduction to the Theory of Disordered Systems*, Wiley, N. Y., 1988 [Russian original, Nauka, Moscow, 1982].
[6] A. P. Belyaev, V. P. Rubets, Kh. A. Toshkhodzhaev, and I. P. Kalinkin, Fiz. Tekh. Poluprovodn. **18**, 1975 (1984) [Sov. Phys. Semicond. **18**, 1234 (1984)].
[7] A. P. Belyaev, V. P. Rubets, Kh. A. Toshkhodzhaev, and I. P. Kalinkin, Fiz. Tekh. Poluprovodn. **26**, 1755 (1992) [Sov. Phys. Semicond. **26**, 982 (1992)].

Translated by M. E. Alferieff

The A. G. Aronov Prize

[S1063-7826(97)03205-5]

The A. G. Aronov prize for the best published article on condensed matter physics was founded by the Foundation for Intellectual Cooperation in memory of the first President of the Foundation. A committee of well-known Russian and foreign scientists has been assembled to judge the papers.

The prize was won the first time in 1994 by S. L. Ginzburg for his paper ''Self-organization of the critical state in Josephson lattices and granular superconductors,'' which was published in *Zhurnal Eksperimental'noĭ i Teoreticheskoĭ Fiziki* **96**, 607 (1994) [JETP **79**, 334 (1994)].

After assessing the papers submitted for the 1995 prize, the committee decided not to award the prize, but in 1997 to hold the competition for papers published in 1995 and 1996. The papers submitted to the competition in 1995 will be judged together with the new submissions.

The committee is now accepting papers published in 1995–1996 into competition for the A. G. Aronov prize.

According to the terms of the A. G. Aronov prize:

1. The competition for the prize is open to Russian citizens on the permanent staff of a Russian scientific or scholarly organization, whose name must appear in the heading of the paper.

2. Eligible papers must have been published in the years indicated, in a Russian or foreign journal. Series of papers are not eligible.

3. The paper must be nominated by a Doctor of Sciences specializing in the particular field. The nominating specialist should cite three of his or her own papers in the given field. The letter of nomination should indicate which of the results presented in the paper nominated for the prize represent new findings.

4. The author (or authors) will send to the Prize Committee an application for entry in the competition, the letter of nomination, three copies (reprints or xerographic copies) of the published article, and brief information about the author(s)—education, academic degrees and titles, and places and lengths of employment.

5. Each author or group of authors may present only one paper for the competition.

6. The deadline for the submission of entries for the A. G. Aronov prize for 1995–1996 is September 1, 1997, and the prize will be awarded on December 1, 1997. The results of the competition will be published in *Fizika Tverdogo Tela* (St. Petersburg) [*Physics of the Solid State*].

7. The papers submitted for the competition should be sent to the address: 194021 St. Petersburg, Ulitsa Politekhnicheskaya 26, A. F. Ioffe Physicotechnical Institute, Russian Academy of Sciences, to the attention of G. E. Pikus, Committee Chairman.

Board of Trustees of the Foundation for Intellectual Cooperation

Translated by J. R. Anderson

